LAMDA

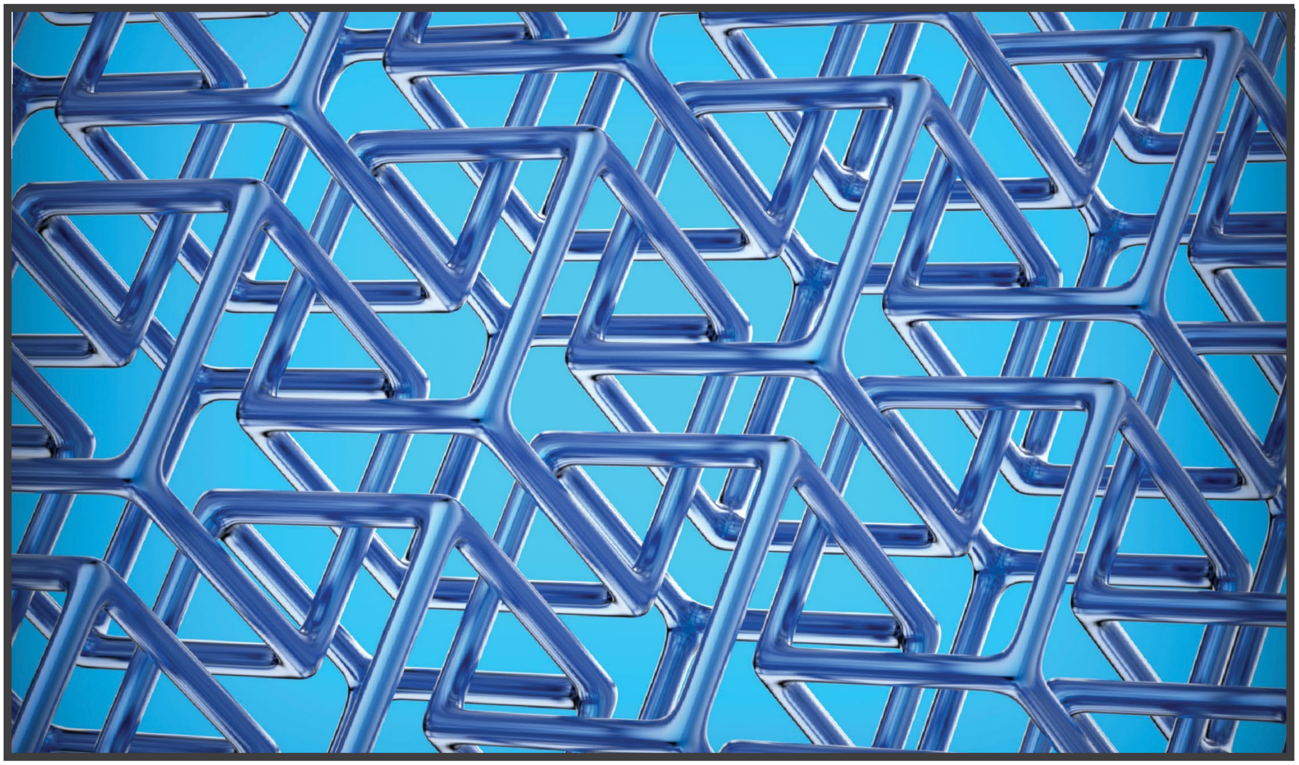

Proceedings

LOUISIANA MATERIALS DESIGN ALLIANCE

RII LAMDA Symposium • August 2, 2024

Welcome to the RII Symposium!

On behalf of Louisiana EPSCoR, I would like to welcome you to the 2024 LA EPSCoR RII LAMDA Symposium. This is a great opportunity for everyone to become engaged in this trend-setting research/education initiative supported under the auspices of the National Science Foundation and the Louisiana Board of Regents. The objective of the project is to propel the State to a nationally/internationally competitive position in advanced manufacturing and materials, with the goal of securing a federally funded center of excellence.

We are very proud of this multidisciplinary initiative, in which undergraduate/graduate students, post-doctoral researchers, and university research faculty from five institutions across the State participate. I also welcome our distinguished participants and guests—NSF program officer, individuals serving on our External Review Board, Industrial Advisory Board, EPSCoR Committee members, and university research administrators.

This virtual Symposium features presentations on LAMDA's achievements and plenty of opportunities to network with your colleagues.

Thank you for participating in this Symposium, and I wish you all a productive and enjoyable meeting.

Michael Khonsari,
Louisiana EPSCoR Project Director and
Associate Commissioner for Sponsored Programs R&D, Louisiana Board of Regents

This work is supported by the U.S. National Science Foundation under grant number OIA-1946231 and the Louisiana Board of Regents for the Louisiana Materials Design Alliance (LAMDA).

Louisiana Board of Regents
P.O. Box 3677
Baton Rouge LA 70821-3677
225-342-4253
https://lamda.rsi.laregents.edu/

What is EPSCoR?

The Established Program to Stimulate Competitive Research (EPSCoR) is a federal/state partnership established in 1978 by the National Science Foundation (NSF) with the goal of stimulating sustainable improvements in the research & development (R&D) capacity of states—like Louisiana—that historically have not received significant federal R&D funding. Since its initial establishment, EPSCoR programs are now supported by seven federal agencies.

Louisiana has participated in NSF EPSCoR since 1987, and has been the recipient of several competitively awarded Research Infrastructure Improvement (RII) awards. LA EPSCoR has served as the catalyst for transforming the way large-scale collaborative research is conducted in the State—from individual campuses competing for limited federal resources to one in which increased collaboration has enabled Louisiana to become more competitive for major R&D funding at the national level.

The scientific vision of LAMDA is to build the design framework for new complex concentrated alloys (CCAs) and thermoset shape memory polymers (TSMPs) for AM with desired performance and structural integrity (reliability and durability). To realize this vision, a common ML-guided approach will be employed to navigate extended compositional spaces towards the design goals and, in the process, generate new fundamental insights into composition-processing-structure-properties relationships in these two classes of AM materials. Tightly integrated with science are strategic broader impact initiatives to enhance STEM education in the jurisdiction through new courses and course modules, an industry supported technology demonstration testbed, programs to engage students in research at national labs and industries, and multiple statewide initiatives to ensure the development of a skilled and diverse workforce.

Tightly integrated with LAMDA are a suite of programs offered by LA EPSCoR to the entire State's higher education and K-12 community. These programs are designed to improve Louisiana's research competitiveness, train a highly-educated workforce, and promote greater public awareness and participation in science, technology, engineering, and mathematics (STEM). These programs include:

- LAMDA Seed Awards
- Links with Industry, Research Centers, and National Labs (LINK)
- Supervised Undergraduate Research Experiences (SURE)
- Speaking of Science (SoS) speakers' bureau
- STEM Outreach grants

Louisiana EPSCoR Committee Members

- **Henry Chu (Chair)**, Professor, Center for Advanced Computer Studies, University of Louisiana at Lafayette
- **Kaneisha Akinpelumi**, Associate Vice President for Research and Sponsored Programs, Xavier University
- **Connie Fabré**, Executive Director, Greater Baton Rouge Industry Alliance
- **Kimberly Foster**, Dean, School of Science and Engineering, Tulane University
- **T. Gregory Guzik**, Professor, Louisiana State University and NASA EPSCoR Project Director
- **Paul Helton**, Executive Director, LED FastStart
- **Chris Kevil**, Vice Chancellor for Research, LSU Health Sciences Center – Shreveport
- **Michael Khonsari**, Associate Commissioner for Research & Sponsored Initiatives and LA EPSCoR Project Director and Dow Chemical Endowed Chair Professor of Mechanical Engineering, Louisiana State University
- **Ramesh Kolluru**, Vice President for Research, University of Louisiana at Lafayette
- **Barry LeBlanc**, President, CEO, Pamlab, L.L.C.
- **Andrew Maas, Associate Vice President for Research, Louisiana State University**
- **Deborah Marshall**, Assoc. Vice President of Research and Sponsored Programs, Xavier University of Louisiana
- **Patrick Mensah**, Associate Dean of Research and Graduate Programs, Southern University and A&M College
- **Christopher Morrison**, Associate Executive Director of Basic Science, Pennington Biomedical Research Center
- **Giovanni Piedmonte**, Vice President for Research, Professor of Pediatrics, Tulane University
- **Ramu Ramachandran,** Associate Vice President for Research, Louisiana Tech University
- **Carrie Robison**, Deputy Commissioner for Research & Sponsored Initiatives, Louisiana Board of Regents

LAMDA Leadership Team Members

- **Les Butler**, Professor, Chemistry, Louisiana State University
- **William Chirdon**, Associate Professor, Graduate Coordinator, Department of Chemical Engineering, University of Louisiana at Lafayette
- **Henry Chu,** Professor, Executive Director, Informatics Research Institute, School of Computing & Informatics, University of Louisiana at Lafayette
- **Cindi Dunn,** Office of Educational Innovation and Evaluation – Kansas State University (member-at-large)
- **Shengmin Guo,** Co-PI, Associate Professor Mechanical and Industrial Engineering, Louisiana State University
- **Jihun Hamm**, Co-PI, Associate Professor, Department of Computer Science, Tulane University
- **Michael Khonsari,** PI**,** Louisiana EPSCoR Project Director, Louisiana State University
- **Xiali Hei**, Co-PI, Assistant Professor, School of Computing & Informatics, University of Louisiana at Lafayette
- **Wynton Johnson,** Coordinator, Graduate School Strategic Initiatives, Louisiana State University
- **Ahmed Khattab**, Dean and Professor, College of Engineering, University of Louisiana at Lafayette
- **Guoqiang Li**, Co-PI, Professor, Department of Mechanical Engineering, Southern University
- **Wen Jin Meng**, Professor, Department of Mechanical Engineering, Louisiana State University
- **Patrick Mensah**, Professor, Department of Mechanical Engineering, Southern University
- **Arden Moore**, Co-PI, Associate Professor, Mechanical Engineering Department, Institute for Micromanufacturing, Louisiana Tech University
- **Erica Murray**, Research Assistant Professor, Mechanical Engineering Department, Institute for Micromanufacturing, Louisiana Tech University
- **Dimitris Nikitopoulos**, Department of Mechanical and Industrial Engineering, Louisiana State University
- **John A. Pojman,** Department Head and Chair, Chemistry, Louisiana State University
- **Ramu Ramachandran,** Professor of Chemistry, Associate Dean for Research College, College of Engineering and Science**,** Louisiana Tech University
- **Phillip Sprunger,** Professor Physics, Louisiana State University

National Science Foundation EPSCoR

- **Jeanne Small**, NSF EPSCoR Program Director, Arlington, VA

External Review Board (ERB)

- **Joseph Beaman**, Professor, University of Texas, Austin, TX
- **Jian Cao,** Assistant Vice President for Research and Professor of Mechanical Engineering and Civil and Environmental Engineering, Northwestern University, Evanston, IL
- **John Gillespie, Jr.,** Director and Professor of Civil and Environmental Engineering, University of Delaware, Newark, DE
- **Alan Needleman,** Professor, Texas A&M University, College Station, TX
- **Harold Silverman**, Baton Rouge, LA, retired Senior Vice Provost, State University of New York System
- **Susan Sinnott,** Department Head and Professor, The Pennsylvania State University, University Park, PA

Industrial Advisory Board (IAB)

- **Paul Gradl,** NASA Marshall Space Flight Center
- **R. Scott Hyde,** Timken Company
- **Andrew Mallow,** LSU National Center for Advanced Manufacturing
- **Tom McGaughy,** EWI
- **Jerry Peck,** Bascom Hunter
- **Subhash Singhal,** Pacific Northwest National Laboratory, retired
- **John Williams,** Boeing Research and Technology

External Evaluator

- **Cindi Dunn**, Office of Educational Innovation and Evaluation - Kansas State University
- **Besangie Sellars**, Office of Educational Innovation and Evaluation - Kansas State University

Participating Institutions

- Louisiana State University
- Louisiana Tech University
- Southern University
- Tulane University
- University of Louisiana at Lafayette

Louisiana EPSCoR Staff

- **Michael Khonsari**, Project Director
- **Jessica Patton**, Project Administrator
- **Shannon Domingue**, Director of Communications and Outreach

TABLE OF CONTENTS

3D Printable Regolith-Filled Shape Memory Vitrimer Composite for Extraterrestrial Application

Kingsley Yeboah Gyabaah[1], Maryam Jahan[2]

[1]Department of Mechanical Engineering, Southern University, & A&M College
[2]Department of Chemistry, Southern University and A & M College

Abstract: The Moon naturally lends itself as the first location for extraterrestrial colonization. After the first stage of colonization, it will be necessary to construct the fundamental lunar infrastructure rapidly, safely, and simply. These three conditions can be realized if we utilize lunar resources in outer space. In missions of extended extraterrestrial sites on the Moon, Mars, and other planetary, in situ resource utilization is necessary to maximize scientific returns and minimize costs. This study investigates a neoteric approach in the manufacture of lunar regolith-filled shape memory vitrimer (SMV) composites for extraterrestrial applications. A high-performance SMV with robust mechanical properties was combined with locally available lunar regolith to form a composite material exhibiting 3D printability. The 3D-printed SMV regolith composite exhibited a good thermomechanical property with a compressive and tensile strength of 139.16MPa and 13.99MPa, respectively. The shape memory properties of the composite were also examined. This study shows that in-situ utilization of locally available lunar regolith to form advanced composite material is possible. High-performance SMV regolith composite is a promising material for lunar base applications due to the simple manufacturing process, excellent mechanical properties, and low energy consumption.

Keywords: Shape memory vitrimer; Regolith; 3D printing; Self-healing.

1. **Introduction**

Developing an independent extra-terrestrial settlement has for decades been a staple of science fiction literature [1]. Being the nearest celestial body to Earth [2], the moon is abundant in a variety of minerals and energy sources, including sunlight and helium-3, metals, and ilmenite, which appear to be ideal locations for additional deep space exploration and settlement [3]. Space agencies like NASA, ESA, and CNSA have all demonstrated a long-term commitment to lunar base construction and inhabited space exploration [4–6]. The purpose of establishing extraterrestrial bases and possibly permanent residence on the moon is to protect from meteorite impacts, solar and cosmic radiation, and extreme temperature fluctuations [7,8], which will create the foundation and optimum environment for further deep space colonization. However, one of the biggest obstacles to lunar colonization is the exorbitant cost of shipping raw materials from Earth to construct both temporary and permanent structures on the moon [9]. Based on current research, the development of lunar construction has been severely limited by the high cost of transferring source materials and the substantial payload transported from Earth [10– 12]. To continue our exploration and advancement of space, humans will need to identify, extract, and use local resources, much as the exploration of our globe requires us to adapt and learn how to use resources that vary by continent, region, and climate. For this reason, in-situ resource utilization (ISRU) technology offers a potential remedy for building lunar bases [13]. In-situ resource utilization will enable the affordable establishment of extraterrestrial exploration and operations by minimizing the materials carried from Earth [2]. Formed from the breakdown of large rocks into smaller particles due to meteorites and micrometeorites impacts, and space weathering, lunar regolith is the main finer fractions of the unconsolidated fragments and material that covers the surface of the moon [14,15]. Lunar regolith has two potential applications, first as a building material or as raw material for construction or industrial-based processes. It has now been demonstrated by numerous researchers to be an easy, feasible, and economical feedstock for lunar construction [16–18]. Polymer concrete is used to produce non-hydraulic concrete for space construction. Appropriate polymer binders such as unsaturated polyester, methyl methacrylate, epoxy, polyurethane, and urea-formaldehyde resins [19] are used to prepare mortar-type, three- dimensional network structures with silicate-based materials. Nevertheless, the use of thermosets as the binder for polymer concrete raises major problems regarding their reprocessability and recycling as they are intrinsically insoluble and infusible. The introduction of reversible covalent adaptable networks (CANs) into polymer structures has led to a third class of polymers called vitrimer [20]. Vitrimer combines the mechanical resilience of thermosets and the recyclable, and reprocesseable properties of thermoplastics [21]. Developing sustainable materials for space applications is very important since materials used for various applications can be reprocessed and reused again for long periods. Hence the use of vitrimer as the matrix binder in the polymer regolith concrete is highly desired. In this work, we explore the use of recyclable and reprocesseable UV curing shape memory vitrimer (SMV) as the binder for lunar regolith to form a high-performance composite that exhibits 3D printability for extraterrestrial applications. The use of SMV as the matrix of the composite combines the attractive properties of thermoset such as chemical resistance, and good mechanical, and thermal properties with thermoplastics' reprocessability, self- healing ability, and recyclability.

2. Materials and Methods

In this study, 3D printable and recyclable SMV-regolith composite resin was prepared by mixing Bisphenol A glycerolate dimethacrylate (BPAGMA), Ethyl (2,4,6-trimethyl benzoyl) phenylphosphinate as the photoinitiator, and the lunar regolith simulant as fillers. In this work, 3 % of the photo-initiator Ethyl (2,4,6-trimethylbenzoyl) phenylphosphinate was dissolved in Bisphenol A glycerolate dimethacrylate (BPAGMA). Triethylamine (0.5wt.%) and 1-4-butanediol dimethacrylate (20wt.%) were added to the BPAGMA as a diluent to obtain a resin of good viscosity for 3D printing. The mixture was stirred in a silicon bath at 90 ˚C for 2 h. 20wt.% of 200 meshed-sized regolith was used in the preparation of the resin for the 3D printing. Anycubic Photon Mono 3D Printer was used for the Digital Light Processing.

3. Properties of 3D Printed SMV-Regolith Composites

.

Figure 1. 3D printed SMV-regolith composite samples using digital light processing (DLP) printer.

The shape memory effect of the 3D-printed SMV-regolith composite was evaluated. Shape memory properties of the composite were investigated via its shape fixity ratio and free shape recovery ratio. The 3D printed composite was first programmed by following 4-step procedures, including (1) Heating the system; (2) Loading at rubbery temperature; (3) Cooling to glass state while holding the stress constant; and (4) Unloading. The composite exhibited a good shape recovery property, with a shape fixity ratio (F) of 67.696% and a shape recovery ratio (R) of 87.65%. Figure 9 shows the various heights were measured using a caliber.

3.1 Mechanical properties of the 3D printed SMV-regolith composites.

3D-printed cylindrical and dogbone-shaped samples were used for the tensile and compressive tests, respectively. From the compressive tests, the printed composite showed a compressive strength of 139.16MPa. The tensile strength was about 14 MPa, suggesting that the SMV-regolith composite is brittle under tension.

4. Conclusion

In summary, a high-performance shape memory vitrimer regolith composite was synthesized using lunar regolith simulant and shape memory vitrimer as the constituent materials. 3D printing of the SMV-regolith composite samples was also manufactured using a digital light processing (DLP) printer. The printed samples exhibited good thermomechanical properties which is very essential considering the harsh lunar environment. Future space exploration and colonization call for the use of lunar resources and modern technology as ways to establish temporary and permanent settlements in the lunar environment. This work explored the use of sustainable materials and technology to achieve this goal in a resource-starved environment.

5. Acknowledgments

This work is supported by the U.S. National Science Foundation under grant number OIA-1946231 and the Louisiana Board of Regents for the Louisiana Materials Design Alliance (LAMDA).

6. References

[1] A.E. Jakus, K.D. Koube, N.R. Geisendorfer, R.N. Shah, Robust and Elastic Lunar and Martian Structures from 3D-Printed Regolith Inks, Sci. Rep. 7 (2017) 1–8. https://doi.org/10.1038/srep44931.

[2] M. Fateri, A. Gebhardt, Process Parameters Development of Selective Laser Melting of Lunar Regolith for On-Site Manufacturing Applications, 52 (2015) 46–52. https://doi.org/10.1111/ijac.12326.

A Laminated Flame-retardant Hybrid Hemp/glass High Temperature Shape Memory Photopolymer Composite for Engineering Applications

John Konlan[1], Sakil Mahmud[1], Jenny Deicaza[1], Guoqiang Li[1,]

[1]Mechanical & Industrial Engineering Department, Louisiana State University

Abstract: Cultivated natural fibers are promising for green and sustainable polymer reinforcement, but their low load-bearing capacity and flammability limit their use in composites. Beam theory indicates normal stress peaks at outer layers and shear stress at the mid-plane during bending. To enhance performance, a laminated composite with hybrid fiber-reinforced shape memory photopolymer was developed, featuring strong synthetic glass fibers over a core of natural hemp fibers. This design achieved mechanical properties similar to composites reinforced solely with glass fibers, along with excellent shape memory and flame retardancy. The hybrid composites demonstrated a 52% shape fixity ratio, a 71% shape recovery ratio, and 24 MPa recovery stress. After 40 seconds of burning, they retained 83.53% of their load-carrying capacity. This approach enables the use of low-strength, flammable natural fibers in multifunctional composites with enhanced load-bearing, shape memory, and flame-retardant properties.

Keywords: Natural fiber, Shape memory, Flame retardancy, Low velocity impact, Structural integrity

1. Introduction

Recent concerns about the recyclability of synthetic fibers highlight their high energy consumption and environmental impact [1]. Producing and recycling carbon and glass fibers is energy-intensive and generates substantial waste. Natural fibers offer an environmentally friendly alternative, reducing plastic use and pollution. However, challenges exist in recycling diverse plastics, producing bio-based plastics, and integrating natural fibers due to their limited load-carrying capacity [2]. For example, adding 10 wt% cellulose fiber to polylactide reduces tensile strength by 30%. Fiber hybridization enhances the sustainability, cost-effectiveness, and performance of natural fiber-reinforced polymer (FRP) composites by combining natural fibers with superior synthetic or natural fibers [3]. This method significantly improves tensile and impact strengths. For instance, hybridizing jute with glass fibers tripled tensile strength and increased impact strength six-fold, while carbon fiber hybridization improved tensile strength ten-fold and impact strength five-fold. Though hybridizing natural fibers alone doesn't match these mechanical gains, it boosts sustainability. Performance factors include fiber content, hybrid ratio, orientation, and stacking sequences. This study developed a gradient hybrid reinforcement approach using strong glass fibers on the outer layers and a weak natural hemp core, enhancing mechanical properties and fire resistance through a high-temperature shape memory polymer (HTSMP) reinforced with UV-curable Triacrylate monomer and phosphine oxide. The HTSMP exhibited high glass transition, mechanical strength at high temperatures, and remarkable shape recovery stress.

The objective of this study is to create a new multifunctional laminated composite using natural fibers alongside synthetic fibers, achieving high impact tolerance and shape memory properties. Beam theory is employed to integrate weak natural fibers while maintaining mechanical integrity. An innovative UV-curing polymer allows rapid curing in 20 seconds for plant-based composites, enhancing flame retardancy without chemical treatments. This method delays natural fiber burning and preserves structural integrity, contributing to reduced plastic consumption and aligning with sustainability goals for high-performance hybrid composites.

2. Experimental methods

A mold release agent and unidirectional glass fibers were purchased from Fiberglast, USA, and 100% natural hemp fabric was donated by Ag Center, Louisiana State University. The hemp fabric weighed around 200 g/m². Tris[2-(acryloyloxy) ethyl] isocyanurate (TAI) and photo-initiator Diphenyl(2,4,6-trimethylbenzoyl) phosphine oxide (TPO) were obtained from Sigma-Aldrich. A solution was prepared by mixing 93 wt% TAI and 7 wt% TPO at 100 °C for 2 hours, then degassed at 80 °C. Hemp fibers were dried at 100 °C for 4 hours to remove moisture before the prepreg process. The solution was used to wet glass and hemp fabric, and composites were produced using a hand layup technique, resulting in 5.05 mm thick laminates. These were cured in a UV chamber for 20 seconds on each side and thermally post-cured for 1 hour at 200 °C. The composite boards were cut to size using a water-jet cutting machine. The FRP composite laminates made with eight layers of natural hemp and six layers of synthetic glass fibers were labeled hFRP and gFRP, respectively. Hybrid laminates with natural fiber cores and glass fiber outer layers were labeled hFRP-G1 and hFRP-G2. The number of layers was chosen to fill the mold thickness while maintaining a constant fiber volume fraction.

3. Results and Discussions

3.1 Composite design and structural characterizations

Numerous studies have confirmed that polymers demonstrating elevated glass transition temperatures (Tg) exhibit enhanced dimensional stability and retain their mechanical properties when exposed to high temperatures. Tg recorded for the pure polymer, and its FRP composite laminates are given in Table 1 [3].

Samples	T_g (°C)	Wt% loss @ 200 °C	$T_{5\%}$ (°C)	T_{max} (°C)	Residue wt% @ 800 °C
Pure polymer	218.47	0.001	395.25	421.33	10.07
hFRP	224.38	0.207	313.07	446.29	7.27
hFRP-G1	227.37	0.146	327.57	441.83	21.66
hFRP-G2	224.11	0.118	334.29	441.71	25.93
gFRP	228.98	0.136	393.78	444.25	51.40

Table 1. Thermal properties of the pure polymer and FRP composites. Tg was recorded from the second heating scan of DSC, and the material's weight loss as a function of temperature was derived from TGA.

As depicted in Fig.1a, thermogravimetric analysis (TGA) was used to evaluate the thermal degradation of the FRP composite laminates. Figure1b illustrates the weight loss and the first derivative of the mass ratio (DTG) against temperature. The key parameters, such as the temperature of 5% weight loss (T5%) and the temperature of maximum degradation (T_{max}), are summarized in Table1

Fourier Transform Infrared (FTIR) spectra were analyzed to study the chemical composition of materials and the interaction between fibers and polymer. As shown in Fig.1c and 1d, the pure polymer does not contain any peak around 810 cm^{-1} of C=C groups, implying the polymerization of C=C groups of TAI monomers. The absence of a peak of the C=C bonds suggest the polymer was successfully synthesized with full curation [4]. The pure glass fibers exhibited various oxides (at 1392 cm^{-1}), such as boron oxide and aluminum oxide. The spectra also displayed the presence of an oxygen-silicon bond in the Si–O–Si group at a frequency of 990 cm^{-1} and an asymmetric deformation vibration of the –CF3 group at a frequency of 682 cm^{-1} 50.

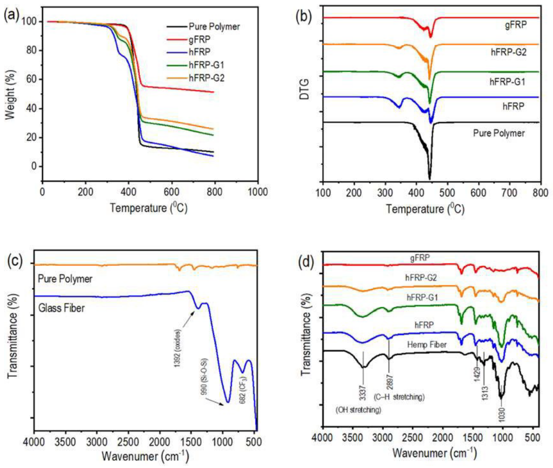

Figure1. (a) TGA curves, (b) DTG curves, and (c-d) FTIR spectra of FRP polymer composite laminates.

3.2 Mechanical properties, Shape memory and flame retardancy

The load versus time plots for all FRP composite laminates showed similar patterns with at least two major peaks. The first peak indicates the incipient damage point, marked by delamination and stiffness reduction, which increases with more glass fibers. The highest load point, representing the maximum impact load before significant fracture, also rose with additional glass fiber layers in hFRP laminates. Figure 2 (ii) gives a summary of the load versus energy traces. The flame retardancy of the various laminates is presented in Figure 2 (i). Mechanical properties based on 3-point bending tests of virgin and bent specimens is given in Table 2. The laminates demonstrated shape memory. The shape fixity ratios of the gFRP, hFRP-G1, and hFRP-G2 are found to be 52.80%, 58.28% and 53.99%, and the shape recovery ratios are 71.58%, 86.02%, and 70.28%, respectively. However, the pure polymer demonstrates a similar level of shape fixity ratio (~58.0 %), but in terms of shape recovery ratio, it shows a higher percentage (~93.1 %) compared to the polymer composite. A similar phenomenon was observed in metallic open-cell foam composites with another SMP. The reason is that the fiber itself has no shape memory effect.[5]

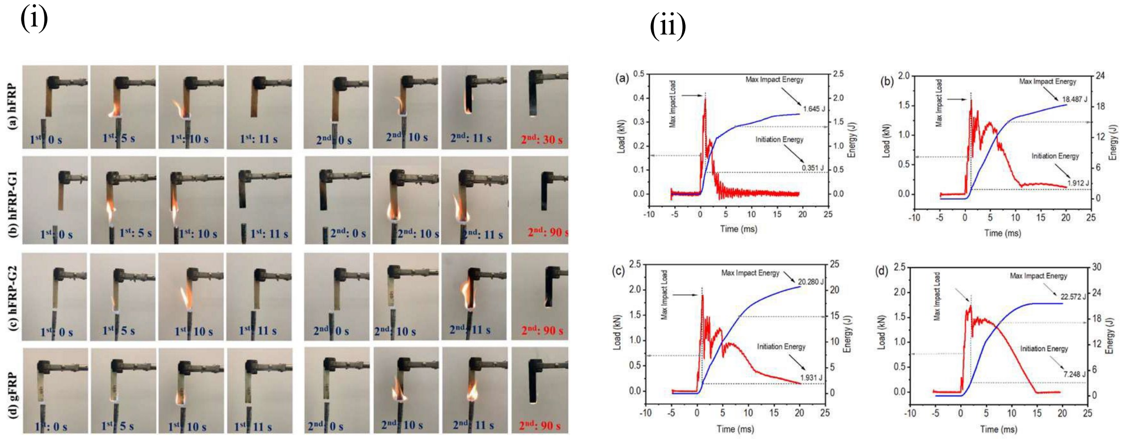

Figure .2(i) (a) Vertical ignition test of (a) hFRP, (b) hFRP-G1, (c) hFRP-G2, and (d) gFRP composite laminates. (ii) The load and energy traces of LVI of the various laminates

Samples	Max bending stress (MPa)$^{\alpha}$	Max recovery stress (MPa)$^{\alpha}$	Max bending stress (MPa)$^{\beta}$	Residual bending stress (%)$^{\gamma}$
hFRP	10.49 ± 1.16	–	–	–
hFRP-G1	75.92 ± 8.26	16.65 ± 2.19	50.70 ± 4.36	66.78
hFRP-G2	73.63 ± 7.11	24.17 ± 1.43	61.50 ± 12.09	83.53
gFRP	94.25 ± 5.89	21.39 ± 4.11	90.57 ± 0.44	96.10

Table 2. Mechanical properties based on three-point bending tests of the various samples

4. Conclusion

This study used a high-temperature shape memory polymer to create hybrid glass and hemp fiber composites. The hybrids showed a sevenfold increase in bending strength, higher impact force, ductility, and effective flame retardancy, maintaining 83.53% of bending strength after 40 seconds of open flame exposure. They also displayed favorable shape memory characteristics with over 52% shape fixity and 71% shape recovery ratios. This research highlights the potential of combining natural and synthetic fibers for high-performance, lightweight, multifunctional composites.

5. Acknowledgement

This work is supported by the U.S. National Science Foundation under grant number OIA-1946231 and the Louisiana Board of Regents for the Louisiana Materials Design Alliance (LAMDA), and US national Science Foundation under grant number HRD-1736136.

References

[1] Wang, B., Ma, S., Yan, S. & Zhu, J. Green Chem. 21, 5781–5796 (2019)
[2] Ribeiro, M. C. S. et al. Recycling 1, 178–193 (2016)
[3] Li, M. et al. Compos. Part B Eng. 200, 108254 (2020)
[4] Feng, X. & Li, G. Appl. Mater. Today 23, 101056 (2021
[5] Abedin, R., Konlan, J., Feng, X., Mensah, P. & Li, G. Smart Mater. Struct. 31, 095009 (2022)

Advancing Additive Repair: A Novel Framework Using Point Cloud Data and Surface Reconstruction

Radif Uddin Ahmed, Iftesam Nabi, Chowdhury Sadid Alam, and M Shafiqur Rahman
Department of Mechanical Engineering, Louisiana Tech University

Abstract: This study represents an additive repairing method for solid bodies through the accurate scanning and reconstruction of three-dimensional (3D) surfaces inspired by the additive manufacturing (AM) technique. The proposed methodology utilizes a laser profiler (Keyence LJX 8200) and a stepper motor driven gantry mechanism to scan an arbitrary surface and obtain point cloud data (PCD). The scanned PCD data goes through various preprocessing techniques for maintaining consistent quality before exporting the final dataset. To prepare the actual surfaces effectively from the vertices and normal to the faces, several surface reconstruction techniques, including Delaunay Triangulation, Ball Pivoting Algorithm, and Poisson's Surface Reconstruction, are applied to the point cloud dataset because the preprocessed data only provides information about the vertices of scanned surface. The 3D surface produced through this process is exported in the form of a Standard Tessellation Language (STL) file, which can be printed via any 3D printers. The precision of the surface reconstruction algorithm is experimentally evaluated by comparing the dimensions of the scanned item with that of the 3D-printed item.

Keywords: Laser Scanning, Point Cloud Data, Surface Reconstruction, Standard Tessellation Language, 3D Printing.

1. Introduction

Additive manufacturing (AM) can significantly contribute to damaged surface restoration. Precise 3D surface scanning is crucial for meeting the growing demand for additive repair methods. Laser scanning efficiently obtains key surface property information by creating a virtual copy of the physical object. A 2D laser profiler integrated with a gantry system can generate 3D point cloud data (PCD). Effective surface preparation involves recreating a surface by creating a triangular mesh from the PCD dataset. This complex task is taken care of by different surface reconstruction algorithms.

Researchers have explored various sensing techniques and algorithms for surface reconstruction. Parde et al. [1] developed a cost-effective IR sensor-based 3D scanning system, limited by transparent and reflective surfaces. Gurau et al. [2] proposed an advanced robotic coordinate measuring machine with light detection and ranging for PCD collection, using forward kinematics and LabView for synchronization. Walecki et al. [3] introduced a custom 3D laser scanner with the ILSTA algorithm for super-resolution scanning. Guo et al. [4] addressed large-scale reconstruction using parallel processing with the Delaunay triangulation algorithm, though it faced challenges with unevenly distributed point clouds and mesh merging. These studies highlight the ongoing efforts to improve 3D scanning and surface reconstruction techniques, each with unique advantages and limitations.

From the literature survey it is evident that surface scanning and surface reconstruction have been a matter of interest to many for surface property analyses. However, extending the application of surface scanning and reconstruction to additive repair is yet to be pursued. Therefore, the goal of this study is to create a systematic framework for accurate 3D laser scanning to surface reconstruction so that additive repairs can be performed using the 3D printing methodology. The study holds promise to open new doors to freeform (conformal) AM and repairing applications.

2. Methodology

The proposed framework (presented in Fig. 1a) scans a surface with the help of a LASER scanning head and a gantry mechanism connected to a computer which synchronizes the movement of the gantry system and data acquisition of the LASER scanner. 3D scanned data is exported as extracting Point Cloud Data (PCD) which is later converted to a Stander Tessellation Language (STL) file by utilizing various surface reconstruction algorithms. The synchronization of the gantry mechanism and the LASER scanning head is carried out by a python program running in the computer, the algorithm of that python program is presented in Fig. 1b.

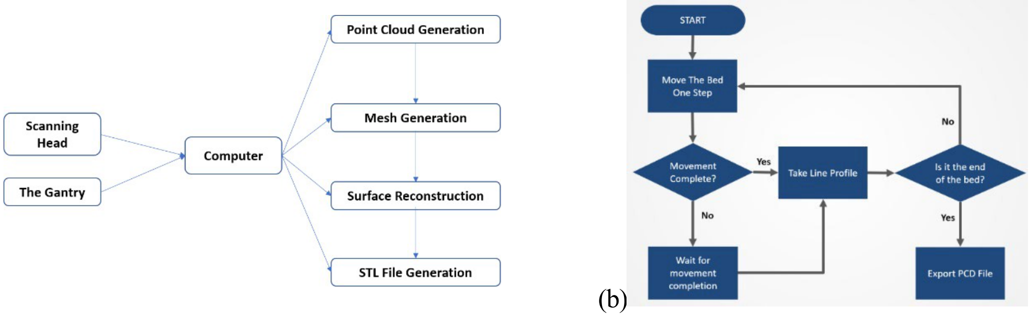

(a) (b)

Figure 1: (a) LASER scanning framework, (b) Algorithm for exporting PCD file.

In this study, the Keyence LJ-X 8200 laser profiler is used (Fig. 2a), which provides 3200 data points across a 72 mm-wide line profile. As the sensor is stationary, a gantry mechanism is constructed to extend the scanning capabilities from a line to an area. The gantry system consists of one bed (14.5 mm × 21.5 mm) which is placed on top of two guide rods and driven using a stepper motor controlled by a microcontroller. Measuring resolution of the LASER scanning head and the gantry system are0.0225 mm and 0.0003125 mm respectively.

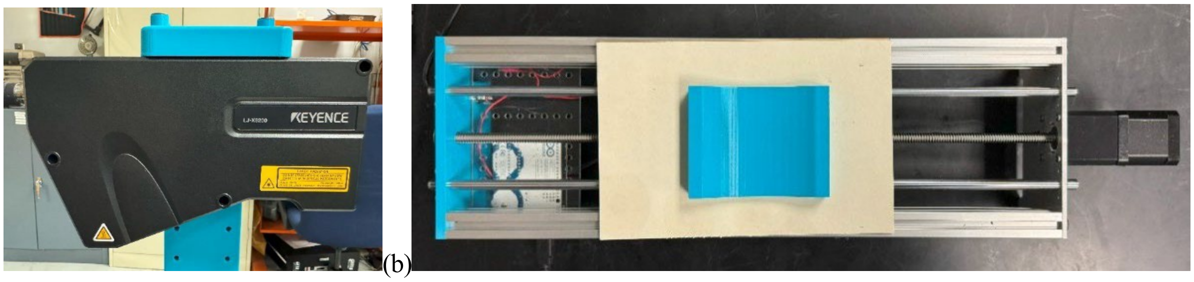

(a) (b)

Figure 2: (a) Keyence LJ-X 8200 LASER profiler sensor head, (b) Top view of the custom fabricated gantry mechanism.

The perform a scanning operation a reference physical object is needed. In this study, a custom object is modeled using SolidWorks. The 3D model is presented in Fig. 3(a) with its dimensions. The reference object is printed using the Ultimaker3 Fused Deposition Modeling (FDM) 3D printer with Polylactic Acid (PLA) filament.

The 3D Printed version of the reference object is presented in Fig. 3(b). This model is later scanned using the proposed method and the PCD data of the scanned surface containing 2,061,686 datapoints is presented in Fig. 3(c).

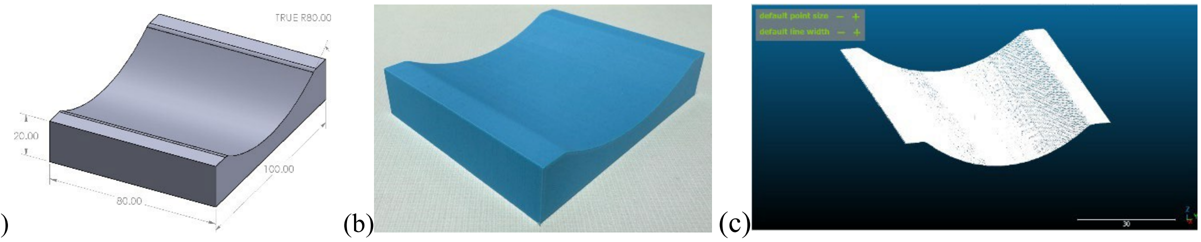

(a) (b) (c)

Figure 3: (a) 3D model, (b) 3D printed reference object, (c) PCD data of the conformal surface.

3. Results and Discussion

After surface scanning, the raw PCD dataset contains only the vertices and to recreate a complete surface, different surface reconstruction algorithms such as Alpha Shapes, Ball Pivoting, and Poisson Surface Reconstruction algorithm are used [5−7]. The reconstructed surfaces are presented in Fig. 4.

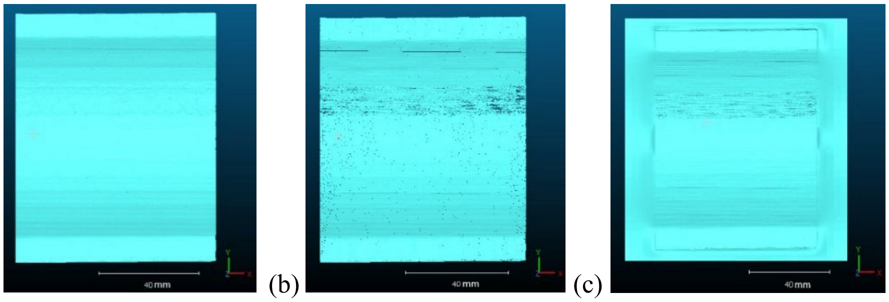

(a) (b) (c)

Figure 4: Reconstructed surface using (a) Alpha Shapes, (b) Ball Pivoting, and (c) Poisson Surface Reconstruction algorithms.

Performance of different surface reconstruction models is tested with different values of their respective tuning parameter to get the best surface reconstruction from each model. Table 1 presents the comparative results for the three surface reconstruction models.

Table 1: Performance comparison of surface reconstruction algorithms.

Sl. No.	Alpha Shapes Algorithm	Ball Pivoting Algorithm	Poisson Surface Reconstruction Algorithm
Watertight	Yes	No	**Yes**
Number of Faces	1070338	4035206	**7050146**
Runtime	252.8571	189.7558	**213.4093**
File Size	53516.984	201760.384	**353429.184**
Tuning Parameter	Alpha = 5	Radius = 0.1	Depth = 11

To determine the most efficient surface reconstruction algorithm for the proposed scanning hardware, multiple criteria were evaluated. The primary requirement was the ability to generate a watertight surface, which eliminated the Ball Pivoting algorithm. Among the remaining models, the Poisson Surface Reconstruction algorithm demonstrated superior performance across several key parameters. It generated the highest number of triangular faces in the shortest time, outperforming the Alpha Shapes algorithm in runtime efficiency. Additionally, it produced a higher number of triangles while maintaining a smaller file size. Based on these comprehensive evaluations, the Poisson Surface Reconstruction algorithm emerged as the most efficient model for the proposed surface scanning hardware.

4. Conclusion

The proposed approach demonstrates high dimensional accuracy in creating digital 3D representations of physical objects. The seamless hardware integration of the sensor and gantry mechanism ensures high-density point cloud data (PCD) extraction. Three surface reconstruction algorithms–Alpha Shapes, Ball Pivoting, and Poisson Surface Reconstruction were evaluated, with the Poisson Surface Reconstruction algorithm showing superior performance. The framework successfully exports STL files suitable for additive repair procedures. Beyond repair applications, this approach has potential in manufacturing wearable sensors, protective gear, soft robotics, and customizable biomedical equipment at various length scales.

5. Acknowledgments

This work is supported by the U.S. National Science Foundation under grant number OIA-1946231 and the Louisiana Board of Regents for the Louisiana Materials Design Alliance (LAMDA), and the Board of Regents Support Fund, Contract number LEQSF (2023-26)-RD-A-19, Program: R&D, Research Competitiveness Subprogram (RCS).

6. References

[1] Parde, M., Khankal, K., and Meshram, R., 2018, "Implementation of 3D Scanner Using IR Distance Sensor," International Journal of Advance Research and Innovative Ideas in Education, 4(2), pp. 4632-4637.

[2] Gurau, V., Gerhardstein, A., Carruthers, K., and Frazer, H., 2024, "Laser Scanner-Based Robotic Coordinate Measuring Machine," International Journal of Mechanical Engineering and Robotics Research, 13(1), pp. 161–168.

[3] Walecki, P., and Taubin, G., 2020, "Super-Resolution 3-D Laser Scanning Based on Interval Arithmetic," IEEE Trans. Instrum. Meas., 69(10), pp. 8383–8392.

[4] Guo, B., Wang, J., Jiang, X., Li, C., Su, B., Cui, Z., Sun, Y., and Yang, C., 2020, "A 3D Surface Reconstruction Method for Large-Scale Point Cloud Data," Mathematical Problems in Engineering, pp. 1–14.

[5] Kirkpatrick, D. G., and Seidel, R., 1983, "On the Shape of a Set of Points in the Plane," IEEE Trans. Inf. Theory, 29(4), pp. 551–559.

[6] Bernardini, F., Mittleman, J., Rushmeier, H., Silva, C., and Taubin, G., 1999, "The Ball-Pivoting Algorithm for Surface Reconstruction," IEEE Trans. Vis. Comput. Graph., 5(4), pp. 349–359.

[7] Kazhdan, M., Bolitho, M., and Hoppe, H., 2006, "Poisson Surface Reconstruction," Proceedings of the Fourth Eurographics Symposium on Geometry Processing, Eurographics Association, Cagliari, Sardinia, Italy, pp. 61–70.

Analysis of Secondary Metabolites from the Fruiting Bodies of the American Beautyberry

Brayden Blackburn[1], TaoTao Ling[2], Fatima Rivas[3]

[1]Undergraduate Researcher, Department of Chemistry, Louisiana State University
[2]Research Assistant Professor, Department of Chemistry, Louisiana State University
[3]Assistant Professor, Department of Chemistry, Louisiana State University

Abstract: Natural products, or secondary metabolites from living organisms, are important compounds as they can be used for drug development. The American Beautyberry, or *Callicarpa americana*, contains biologically active natural products. Extracts of *C. americana* have been described as generally effective against breast cancer, but the exact molecular structure and the mode of action (MOA) of its natural products remain understudied. This study aims to isolate biologically active components of *C. americana* and conduct structural elucidation techniques as well as test them against cancer cell line models. We hypothesize that extracts of the fruiting bodies of *C. americana* will contain a previously undiscovered compound that can be characterized for its effectiveness against certain cancers. We have performed alcoholic extraction on the fruiting bodies of the *C. americana*. We then subjected this crude extract to flash column chromatography. Following chromatography, the resulting fractions were subjected to nuclear magnetic resonance (NMR) and high-resolution mass spectrometry (HRMS). In addition, we tested them against cell line models using the CellTiter-Glo® assay to evaluate their cytotoxicity and the propidium iodide assay to determine the cell death modality caused by treatment with this set of natural products. Overall, our study will produce valuable information on the molecular structure and biological activity of the natural products isolated from the fruit of *C. americana*.

Keywords: *Callicarpa americana*, fruit, natural products, breast cancer, anti-cancer properties

1. Introduction

Natural products are secondary metabolites from nature which are known for their biological activity and usefulness in drug development. Plants of the genus *Callicarpa* have been known to contain several biologically active natural products which can affect various metabolic diseases such as cancer.[1] One member of this genus is the American Beautyberry (*Callicarpa americana*). *C. americana*, like most members of *Callicarpa*, was commonly used as a remedy in traditional medicine.[1] In modern scientific research, extracts of *C. americana* have been found to affect breast cancer cell lines.[2] Natural products isolated from this plant in previous studies include various terpenoids and flavonoids.[2] Some other natural products of *C. americana* are yet to be specifically characterized, and their exact molecular structure and MOA remain elusive. In this study, we will focus on extracts from the fruiting bodies of *C. americana*. Our aim in this work is to first isolate and purify biologically active natural products of *C. americana* and then perform structural elucidation methods on them and test them against multiple different breast cancer cell line models. We hypothesize that the biologically active natural products isolated from *C. americana* will be useful as a building block for future drug-like molecules.

2. Methods

We began the process of isolating these natural products by first performing alcoholic extraction on a sample of *C. americana* berries. The sample was first dissolved in ethanol and placed in a Dionex™ ASE™ 150 Accelerated Solvent Extractor. Following use of the solvent extractor, we used a rotary evaporator to evaporate the solvent. The crude extract was then subjected to flash column chromatography. The fractions resulting from flash column chromatography were then characterized by thin-layer chromatography (TLC). Using cerium ammonium molybdate (CAM) stain on the developed TLC plates, we were able to determine which fractions showed characteristic activity of carbohydrates. Sets of fractions that showed consistent similar staining activity on TLC were combined. After these combinations dried for 24 hours, solid remained in the flask of only one combination. Once this solid sample, to be referred to as "AB-120", was dry, we began to perform structural elucidation techniques on it. To characterize their molecular structure, we used both ^{1}H NMR and ESI-TOF HRMS for AB-120. In addition to structural elucidation, the AB-120 isolate was analyzed for biological activity by two bioassays. First, AB-120 was evaluated for its cytotoxic properties with the CellTiter-Glo® assay.[3] The CellTiter-Glo® assay was performed for each of two cell lines: MDA-MB231 (a triple negative breast cancer cell line) and SUM149 (an inflammatory triple negative breast cancer cell line). Both times, the drugging period used was 72 hours. Additionally, the propidium iodide assay was conducted to determine the cell death modality of the healthy cell line BJ when treated with AB-120.[4] BJ was used for this assay in part so that cell viability data from both assays performed can be compared to simulate a diseased environment.

3. Results

We observed from the results of ^{1}H NMR that the compounds in AB-120 generally show aromatic properties, suggesting that they are similar to the previously isolated terpenoids and flavonoids. Past this, the results of ^{1}H NMR and HRMS on AB-120 did not yield conclusive information regarding its compounds' molecular structure. While structural elucidation results were inconclusive, results of the biological evaluation were far more revealing. The EC50 values, or concentrations of AB-120 at which 50% of the cells were found viable, from the CellTiter-Glo® assay were 25.09µm for MDA-MB231 and 13.04µm for SUM149. The EC50 value from the propidium iodide assay on BJ was >100µm. Also, data from the propidium iodide assay did not give clear results regarding the cell death modality induced by AB-120.

4. Conclusion

This preliminary work produced some valuable conclusions. First, the cytotoxic properties of the extracts of *C. americana* fruit have a significant effect on multiple subtypes of breast cancer cell line. Furthermore, these cytotoxic properties affect breast cancer cell lines significantly more than they affect normal cell lines. This distinction is crucial for the prospect of future drug development, because a compound with cytotoxicity that affects normal cells at the same rate as cancerous cells has no medicinal benefit. More work remains to be done in order to determine usage of *C. americana* isolates for drug development, and this work will be accomplished in future studies.

5. Limitations and Future Studies

While this study provided valuable preliminary information related to the natural products in the fruit of *C. americana*, this preliminary work was met with limitations. Primarily, this study in its current stage was limited by time. The procedures required to carry out this study take significant lengths of time. While this is sufficient time for preliminary work as this was, time hindered this study from including more than simply preliminary information. Apart from time, another limitation of this study was the lack of structural elucidation information yielded by the isolate. This lack of usable NMR and HRMS data was due to the lack of solid sample available for analysis. One other notable limitation of this study was the results of the propidium iodide assay. These results did not provide the desired information regarding cell death modality. We aim to account for all these limitations in future studies of *C. americana*.

As this topic is further explored in future studies, there will be several factors to consider which were identified by this study. First, more comprehensive structural elucidation must be performed on the compounds we isolated from *C. americana* to be able to properly characterize the molecular properties of these natural products. In addition to this, the isolated compounds should be tested against a greater array of subtypes of breast cancer cell lines. Furthermore, future studies should include more detailed work involving the cell death modality of cells treated with the isolated compounds. To accomplish that, perhaps a different biological assay such as the Annexin V binding assay should be performed.[5] Finally, future studies should do similar analysis of the rest of the plant against varying subtypes of breast cancer. Should these propositions be implemented, the information to be provided about compounds isolated from *C. americana* will be considerably more conclusive.

6. Acknowledgments

This work is supported by the U.S. National Science Foundation under grant number OIA-1946231 and the Louisiana Board of Regents for the Louisiana Materials Design Alliance (LAMDA).

Additionally, the Rivas lab is supported by Louisiana Board of Regents Support Fund Award under grant number LEQSF-RD-A-05 and the National Institute of General Medical Sciences (NIGMS) under grant number R15GM148983.

6. References

[1] Jones, W. P., & Kinghorn, A. D. (2008). Biologically active natural products of the genus *Callicarpa*. *Current Bioactive Compounds*, *4*(1), 15-32.
[2] Jones, W. P., Lobo-Echeverri, T., Mi, Q., Chai, H., Soejarto, D. D., Cordell, G. A., Swanson, S. M., & Kinghorn, A. D. (2007). Cytotoxic constituents from the fruiting branches of *Callicarpa americana* collected in southern Florida. *Journal of Natural Products*, *70*(3), 372-377.
[3] CellTiter-Glo® cell viability assay - Promega corporation. (n.d.). https://www.promega.com/-/media/files/promega-worldwide/europe/promega-france/autre/223492146dscrcelltiterglo-ds306-25.pdf?la=en
[4] Riccardi, C., Nicoletti, I. (2006). Analysis of apoptosis by propidium iodide staining and flow cytometry. *Nature Protocols, 1*, 1458–1461.
[5] Kari, S., Subramanian, K., Altomonte, I.A. et al. Programmed cell death detection methods: a systematic review and a categorical comparison. *Apoptosis 27*, 482–508 (2022).

Blockchain Application to the Processes in Materials Design: A Survey

Diego Segura Ibarra, Fan Li, Jianjun Zhu, Jinyuan Chen

Department of Electrical Engineering, Louisiana Tech University

Abstract: Data is a valuable resource that can facilitate the development of advanced products sustainably and transparently. However, issues like data manipulation, forgery, and deletion can damage data reliability, limiting its use throughout product development. An important aspect of product development that is affected by data-related issues is materials design. Moreover, this paper aims to identify and explore solutions that relieve data reliability concerns in materials design. Specifically, we investigate the implementation of blockchain to mitigate data-related problems that affect materials design. Blockchain is a decentralized and immutable ledger where information is inherently protected against tampering. This paper presents challenges in materials design that arise from data-reliability concerns and discusses blockchain-based methods to tackle these challenges. Moreover, our survey presents how blockchain can be implemented to aid materials design.

Keywords: Blockchain, Materials informatics, Data reproducibility

1. Introduction

In recent years, there has been a growing demand for more advanced, sustainable, and transparent products, driven by emerging technologies and evolving consumer expectations. To fulfill the demand for such products, it is vital to understand and address the challenges in material design. Designing new materials is important as it helps solve today's engineering problems, which advances our current society. In this work we will focus on the areas of materials informatics and data reproducibility.

A promising technology that can aid the materials informatics and data reproducibility is blockchain. Blockchain is a decentralized and immutable ledger of information. By utilizing blockchain, industries can protect information against tampering and a single point of failure. The materials design can benefit from blockchain technology. For example, researchers can store scientific data and metadata in a blockchain to protect against intellectual property theft. In what follows, Section 2 presents materials informatics challenges and blockchain implementation, while Section 3 details data reproducibility challenges and blockchain implementations.

2. Materials Informatics

Materials informatics is a field combining materials science and data science that strives to use data-driven techniques to support the design and discovery of novel materials. This field introduces a new paradigm that works in conjunction with the three paradigms of materials research, i.e., experimentation, theory, and computation [1]. The idea is to take advantage of previously collected experimental or computational data by using machine/deep learning models to predict the behavior, properties, or composition of current and novel materials [1]. By supporting data-driven techniques with substantial experimental or computational data, it is possible to accelerate the exploration of the vast chemical space for materials, enabling the rapid discovery of materials with improved properties

2.1 Challenges

Data availability, quality, and quantity are paramount for materials informatics as it relies on the performance of data-driven models. Without sufficient data, machine and deep learning models will not deliver accurate results, which burdens the use of these techniques to study materials. While there currently exists extensive data on numerous materials, this data often lacks the appropriate metadata or is not made publicly available. As a result, this area faces challenges regarding the lack of metadata and data sharing.

Metadata: Metadata refers to the information that describes scientific data. It can include the details regarding the asset from which the data was gathered, the experimental or computational methods used to obtain the data, the authors who published the data, and the characteristics of the digital file [2]. Without metadata, the scientific community would be unable to determine the dataset's relevance or provenance, which may limit its application in research. Moreover, it is beneficial for both the authors and the scientific community that scientific data is accompanied by its corresponding metadata. Nonetheless, significant scientific data lacks proper characterization and there is currently no metadata standard [3].

Adoption of data sharing practices: Encouraging researchers to share their data is important for the success of materials informatics. Since materials informatics depends on the availability and quantity of data, it will benefit from the data provided by the scientific community. The larger the amount of available data, the better the performance of data-driven models. Additionally, data sharing allows for increased collaboration within the scientific community. For instance, a researcher's experimental data can help computational scientists verify the applicability of their computational model. Moreover, through the shared data, researchers would be able to advance their work, increasing the number of valuable findings in materials science. Despite the benefits of data sharing, many researchers are reluctant to share data due to the concern of getting scooped, IP infringement, data misuse, and not getting proper credit [4].

2.2 Blockchain Implementation

Blockchain for existing material databases: Existing material databases can adopt blockchain to manage and protect metadata. It is important to keep metadata secure and immutable since it contains the authorship information of scientific data. To ensure researchers will have a verifiable and reliable way to prove their authorship to the submitted data, the dataset's metadata can be stored in a blockchain system. Then, the metadata will become unchangeable and secured against malicious activity like tampering. In this way, existing materials databases can keep their data storing and sharing infrastructure and leverage blockchain to further protect the researcher's IP. To link the scientific data stored off-chain to the metadata stored on-chain, the metadata can include the hash value of the original scientific data. In this case, if either the scientific data or metadata is modified, it can be easily identified through the blockchain. Using this blockchain application, it is possible to tackle IP infringement, one of the factors that affects data sharing. Removing the IP concern will encourage more researchers to share their data with the scientific community via open material databases. The use of blockchain to improve data sharing in material databases has also been proposed in [4,5]. In these works, data sharing platforms are developed for materials science that utilize blockchain to solve data management and security problems.

Decentralized electronic collaboration platform: Blockchain can support the creation of platforms that foster collaboration between scientists and encourage scientists to share data without an intermediate regulatory par

[5,6]. Ideally, everyone should have the opportunity to access the available materials data and contribute to the databases. To this end, a decentralized environment where no single entity controls the entire dataset is beneficial. Blockchain can enable such a decentralized environment. Additionally, in a community-driven platform, it could also be possible for researchers to help each other provide adequate scientific data or metadata. For example, Bob and Alice are materials scientists and Bob would like to use the data Alice uploaded, but Alice's data is not well characterized. In this case, the platform can allow Bob to comment on Alice's data and let her know how she can improve her metadata so that her data is useful to others.

3. Data Reproducibility

The ability to recreate scientific findings and reach similar conclusions as previous studies is an essential aspect of academic research. Such reproducibility can be achieved when research works clearly and openly describe the methodologies used to reach a set of results [7]. Further, being honest about these methods also maintains academic integrity and allows the public to trust scientific discoveries [8]. Additionally, making sure research work is reproducible and trustworthy allows future scientists to effectively build upon existing work [7].

3.1 Challenges

Currently, the importance of reproducible and trustworthy research is highlighted by the demand to use existing data to power future discoveries. However, reproducibility is not as widespread as it should be.

Unreproducible studies: The reproducibility of academic studies has come into question after it was revealed that a large amount of them could not be reproduced [9,10]. In fact, a 2016 study that surveyed researchers across various disciplines, found that more than 70% of them were unable to reproduce other researchers' studies [10]. Additionally, there have been research papers that have been punished due to having unreproducible studies or forged data [11]. There are many factors that can cause such irreproducibility. For example, the use of specialized techniques [8,10] or the use of complex computational processes [7] can affect the ability of others to replicate results in experimental and computational studies respectively. In addition to these two factors, poorly described methodologies and the absence of data, software, and tools have affected the reproducibility of both computational and experimental works [7,8,10].

3.2 Blockchain Implementation

Computational data reproducibility: It is possible to take advantage of an Etherium virtual machine to perform computational simulations [9]. The Etherium virtual machine is essentially a virtual computer powered by the various computers that contribute to the blockchain network. This type of virtual machine was developed by Ethereum to execute smart contracts that are written on a Turing-complete programming language called Solidity. Through Solidity, computational scientists can write programs that run mathematical simulations. [9] demonstrated that an Ethereum virtual machine could store and perform quantum chemistry simulations through molecular dynamics. By performing this simulation through an Ethereum virtual machine, they could store the exact parameters and code used for a molecular dynamics simulation and repeat it at the Ethereum blockchain. Because of the properties of blockchain, the work on the virtual machine is immutable and can be exactly repeated by whoever has access to the virtual machine. If researchers take part in performing simulation through an Etheriu virtual machine, it can guarantee that future computational works are reproducible by anyone who has access to the blockchain.

Experimental data reproducibility: Experimental studies are challenging to reproduce since they require a great number of tools and expertise. In experimental studies, simply uploading a description of the tools and methods used during experimentation to a blockchain system is not enough to guarantee the reproducibility of the study. Inspired by the advancement of robotics, [11] designed a physical platform where robots can automatically execute experiments based on instructions stored on a blockchain. The idea is to have researchers submit the instructions that describe how their experiment was performed to a blockchain. Then, the machine would verify the results of the experiments by following the set of instructions. Through this idea, researchers of various backgrounds could reproduce existing works, increasing the trust in experimental studies.

4. Conclusion

This study investigated how blockchain can benefit two important aspects of material design. Specifically, this work identified various challenges in materials informatics and data reproducibility. The blockchain-based solutions that can tackle these issues have been provided. This information can help researchers and practitioners understand how blockchain can be implemented to improve the area of material design. An extended version of this work can be found in [12].

5. Acknowledgments

This work is supported by the U.S. National Science Foundation under grant number OIA-1946231 and the Louisiana Board of Regents for the Louisiana Materials Design Alliance (LAMDA).

6. References

[1] D. J. Audus and J. J. de Pablo, “Polymer Informatics: Opportunities and challenges,” ACS Macro Letters, vol. 6, no. 10, pp. 1078–1082, Sep. 2017. doi:10.1021/acsmacrolett.7b00228

[2] K. Frydrych et al., “Materials Informatics for Mechanical Deformation: A review of applications and challenges,” Materials, vol. 14, no. 19, p. 5764, Oct. 2021. doi:10.3390/ma14195764

[3] M. Scheffler et al., “Fair Data Enabling New Horizons for Materials Research,” Nature, vol. 604, no. 7907, pp. 635–642, Apr. 2022. doi:10.1038/s41586-022-04501-x

[4] C. Wang, H. Su, L. Duan, and H. Li, “InterMat: A blockchain-based materials data discovery and sharing infrastructure,” Processes, vol. 11, no. 11, p. 3168, Nov. 2023. doi:10.3390/pr11113168 5 => 57

[5] R. Wang et al., “A secured big-data sharing platform for Materials Genome Engineering: State-of-the-art, challenges and architecture,” Future Generation Computer Systems, vol. 142, pp. 59–74, May 2023. doi:10.1016/j.future.2022.12.026 6=>56

[6] P. Vazquez, K. Hirayama-Shoji, S. Novik, S. Krauss, and S. Rayner, “Globally Accessible Distributed Data Sharing (Gadds): A decentralized fair platform to facilitate data sharing in the Life Sciences,” Bioinformatics, vol. 38, no. 15, pp. 3812–3817, May 2022. doi:10.1093/bioinformatics/btac362 7=>110

[7] E. National Academies of Sciences, *Reproducibility and Replicability in Science*. National Academies Press, 2019. 8 => 81

[8] P. Diaba-Nuhoho and M. Amponsah-Offeh, “Reproducibility and Research Integrity: The role of scientists and Institutions,” *BMC Research Notes*, vol. 14, no. 1, Dec. 2021. doi:10.1186/s13104-021-05875-3 9=>82

[9] M. W. Hanson-Heine and A. P. Ashmore, “Computational chemistry experiments performed directly on a Blockchain Virtual Computer,” Chemical Science, vol. 11, no. 18, pp. 4644–4647, 2020. doi:10.1039/d0sc01523g 10=>83

[10] M. Baker, “1,500 scientists lift the lid on reproducibility,” Nature, vol. 533, no. 7604, pp. 452–454, May 2016. doi:10.1038/533452a 11=>101

[11] Y. Xu, R. Liu, J. Li, Y. Xu, and X. Zhu, “The Blockchain Integrated Automatic Experiment Platform (BIAEP),” The Journal of Physical Chemistry Letters, vol. 11, no. 23, pp. 9995–10000, Nov. 2020. doi:10.1021/acs.jpclett.0c02840 12=>85

[12] D. Segura Ibarra, F. Li, J. Zhu, and J. Chen, “Blockchain application to the processes in Material Design, production, distribution, and disposal: A survey,” Journal of Industrial Information Integration, vol. 41, p. 100638, Sep. 2024. doi:10.1016/j.jii.2024.100638

Bonding of 5086 Al-Mg Alloy to Stainless Steels Using Additive Friction Stir Deposition Process

Saeid Zavari, Ehsan Bagheri, Huan Ding, Noushin Adibi, Shengmin Guo

Department of Mechanical & Industrial Engineering, Louisiana State University

Abstract: Aluminum alloys and steel are vital materials in engineering sectors such as transportation, construction, and energy. Their distinct properties pose challenges for traditional fusion welding methods due to differences in melting points, thermal expansion, and densities, leading to intermetallic compound formation that weakens dissimilar joints. Solid-state techniques like friction stir welding offer promising solutions. This study explores the feasibility of using additive friction stir deposition (AFSD) to bond Al5XXX and stainless steel, focusing on Al5086 and S.S.316. Initial attempts faced challenges, but modifications led to successful deposition. Tensile tests revealed the joint's ultimate tensile strength was 24% of the UTS of Al5086, with SEM analysis showing mechanical interlocking as the primary bonding mechanism. Future work will focus on enhancing diffusion bonding for improved joint strength.

Keywords: Solid-state joining, MELD, Additive friction stir deposition, Aluminum alloys.

1. Introduction

Nowadays, because of environmental pollution and the constraints of energy resources, the industry is obliged to reduce the fuel consumption of manufactured vehicles. One of the most effective approaches to achieve this goal is by reducing vehicle weight. This can be accomplished by using lighter materials that maintain the same mechanical properties as traditional materials, such as aluminum alloys. Aluminum alloys, like the Al5XXX series, offer an excellent combination of strength and weight reduction, making them ideal for various applications. However, joining aluminum alloys to other materials, such as stainless steel, presents significant challenges. In addition, modern vehicles, including aircraft and cars, are comprised of an extensive array of mechanical components manufactured through various processes. Cars can contain anywhere from 10,000 to 30,000 parts, while aircraft often involve millions. A prevailing trend in manufacturing these products is the increasing complexity and quantity of parts, often incorporating novel combinations of materials. Joining these components during assembly commonly involves welding, adhesive bonding, and mechanical fastening. Fusion welding, for instance, employs external heat to fuse materials at the interface, yet its widespread use may compromise the quality, precision, and dependability of joined parts due to high temperatures. Adhesive bonding and mechanical fastening typically yield joints with lower strength compared to welding. Commercial demands for enhanced performance, productivity, and cost efficiency in joining operations are escalating. Moreover, the necessity for robust joining of dissimilar materials is growing, exemplified by the need to join high-strength steel and aluminum sheets in certain car models for weight reduction purposes [1]. Consequently, there is a pressing need to explore novel joining methods to meet the requirements of evolving applications and materials. Processes for joining through plastic deformation can be categorized into two main groups:

1- Metallurgical joining: cold welding, friction welding, friction stir welding, resistance welding, etc.
2- Mechanical joining: self-pierce riveting, mechanical clinching, joining via forming techniques such as hydroforming, electromagnetic forming, and incremental forming, fastening methods including hemming, seaming, and staking.

In metallurgical joining processes like cold welding and friction welding, severe plastic deformation breaks up oxide films and contaminants at the interface between workpieces. The clean surfaces then bond under high interfacial pressure. The workpieces are internally heated by interfacial slipping and plastic work, which accelerates deformation as the workpieces soften with rising temperature. These metallurgical joining processes, which involve plastic deformation, are also known as solid-state welding processes. To achieve metallurgical bonding, significant plastic deformation is required.

In contrast, mechanical joining by plastic deformation uses interfacial pressure and interlocking without thermal effects. One example of this type of joining occurs when an inner tube inserted into an outer ring is plastically expanded by internal pressure. This pressure remains at the interface after unloading, thus mechanically joining the workpieces. The joining strength can be increased by forming beads and dimples. Another example is when workpieces are mechanically interlocked by plastic deformation. Unlike metallurgical joining processes, mechanical joining processes do not require the breaking up of oxide films or an increase in interfacial temperature. Instead, plastic deformation is controlled to generate proper pressure and interlocks. Mechanical joints can be more widely applied and are often stronger than those created by mechanical fastening processes like riveting, stitching, and crimping. These processes are commonly used in automated assembly operations to enhance productivity and reduce costs [2,3].

In the context of modern manufacturing challenges, this study investigates novel methods for joining dissimilar materials. Specifically, it explores the feasibility of utilizing additive friction stir deposition to achieve robust bonds between Al5XXX and stainless steel, addressing the growing need for efficient and effective joining techniques in diverse engineering applications. The goal is to explore the processing parameters, microstructural evolution, and mechanical properties of the resulting joints to develop predictive models that can enhance material properties and industrial applications.

2. Experimental Setup

The AFSD process involves the use of a rotating tool that moves along the interface between the aluminum feedstock rod and the stainless-steel substrate. The frictional heat generated by the rotating tool softens the aluminum, allowing it to be deposited onto the substrate without reaching its melting point. This solid-state process avoids the formation of detrimental intermetallic compounds that are typical in traditional fusion welding. The materials used in this study were Al5086 and S.S.316. To create a sample, 2 inches of Al5086 were applied onto the S.S.316 substrate, aiming to achieve a total sample height of 4 inches. The selection of these materials was based on their widespread use in industrial applications and their challenging nature when it comes to joining dissimilar metals. The experimental setup involved optimizing several tool parameters, including rotational speeds, feed rates, and travel speeds. These parameters were critical in ensuring successful deposition and achieving the desired mechanical properties of the bonded section. The rotational speed of the tool was adjusted to generate adequate frictional heat without causing excessive softening or damage to the materials. The feed rate and travel speed were optimized to control the deposition rate and ensure uniform material distribution.

3. Results and Discussion

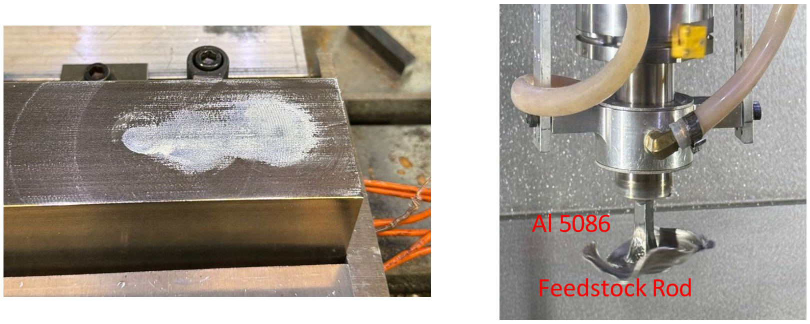

Figure 1. Initial attempt to deposit Al5086 on the S.S. substrate.

The initial attempt to deposit Al5086 onto the S.S.316 substrate faced several challenges, primarily due to the differences in thermal and mechanical properties. Figure (1) shows that it was not possible to deposit Al5086 on the S.S. substrate. These issues necessitated several modifications to the process parameters and substrate preparation techniques.

The substrate modification involved creating nine dovetail grooves on the stainless-steel surface. These grooves served to confine the deposited material and enhance mechanical bonding between the aluminum alloy and the stainless-steel substrate. After modifications, successful deposition of Al5086 onto S.S.316 was achieved. Figure (2) illustrates the modified substrate and the deposited block.

As seen in the picture (2E), the side grooves were not filled with the material, which is visually obvious. Therefore, a sample from the center of the cross-section was extracted for tensile, hardness, and microstructure analysis. The results of these tests are provided in figure (3). The ultimate tensile strength (UTS) of the bonded samples was found to be significantly lower than that of the base material, Al5086. The UTS of the joint was only 24% of the UTS of the Al5086 alloy. This decrease in tensile strength indicates that the bonding achieved through AFSD did not fully transfer the mechanical properties of the aluminum alloy to the joint. The lower tensile strength can be attributed to the challenges faced in achieving a strong bond between the aluminum and stainless steel, as well as the presence of small gaps observed in the joint. Scanning electron microscopy (SEM) images provided crucial information on the microstructural characteristics of the joint. The SEM images revealed that there was no metallurgical bonding between the Al5086 and S.S.316. Instead, the images showed the presence of small gaps at the interface, indicating that the bonding mechanism was primarily mechanical interlocking rather than diffusion bonding. The

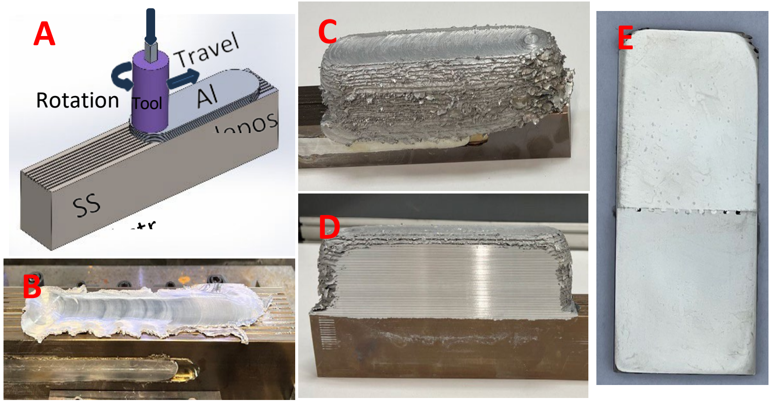

Figure 2. Al/S.S. as-deposited part.

absence of metallurgical bonding is a significant factor contributing to the reduced tensile strength of the joint. Future work will focus on introducing various interlayers and brazing materials to enhance diffusion bonding and improve joint strength.

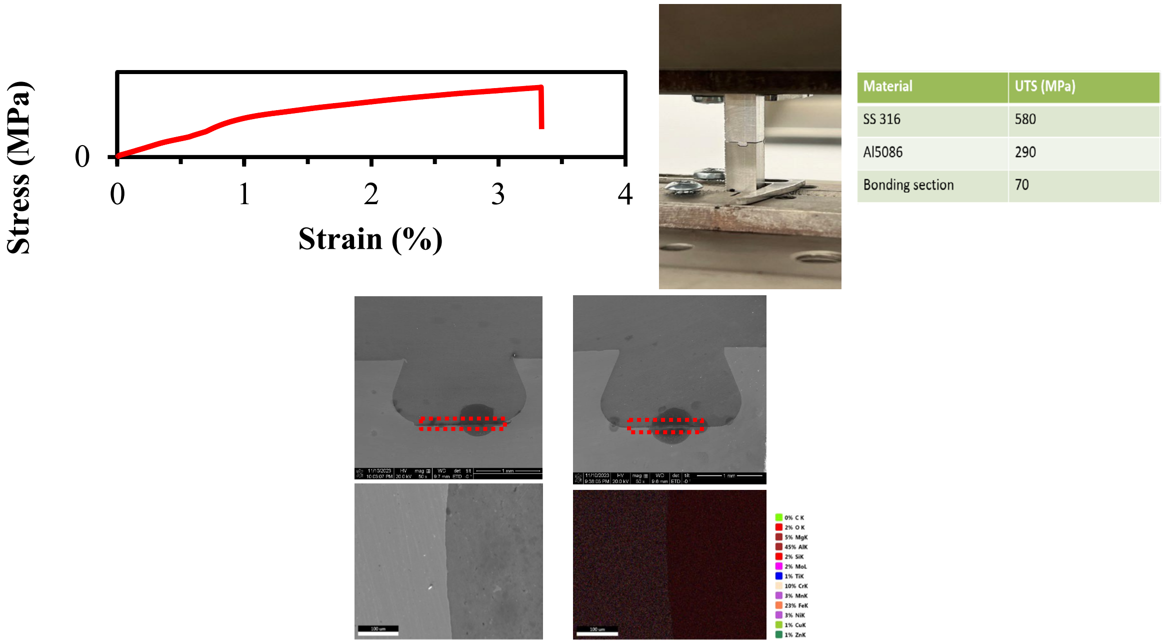

Material	UTS (MPa)
SS 316	580
Al5086	290
Bonding section	70

Figure 3. Al/S.S. Tensile and SEM results

4. Conclusion

In conclusion, this study delved into the feasibility of using additive friction stir deposition to bond Al5XXX and stainless steel. Initial attempts revealed challenges in depositing Al5086 onto the stainless-steel substrate. After modifications, deposition occurred; however, the tensile results indicated only 24% of the ultimate tensile strength (UTS) of Al5086, with SEM images revealing small gaps between the Al and SS. Therefore, it appears that mechanical bonding rather than diffusion bonding was the primary contributor to strength. Moving forward, the investigation will focus on exploring the impact of various interlayers and brazing materials in the subsequent stages of the work.

5. Acknowledgments

This work is supported by the U.S. National Science Foundation under grant number OIA-1946231 and the Louisiana Board of Regents for the Louisiana Materials Design Alliance (LAMDA).

6. References

1. Kleiner, Matthias, Manuel Geiger, and A. Klaus. "Manufacturing of lightweight components by metal forming." CIRP annals 52, no. 2 (2003): 521-542.
2. Mori, K. I., Bay, N., Fratini, L., Micari, F., & Tekkaya, A. E. (2013). Joining by plastic deformation. CIRP Annals, 62(2), 673-694.
3. Shirzadi, A. A., Zhang, C., Mughal, M. Z., & Xia, P. (2022). Challenges and latest developments in diffusion bonding of high-magnesium aluminium alloy (Al-5056/Al-5A06) to stainless steels. Metals, 12(7), 1193.

Chemical Group-Driven Generation of Multi-Monomer Thermoset Shape Memory Polymers Using Generative Conditional Variational Autoencoder

Borun Das[1], Andrew Peteres[2], Guoqiang Li[3], Xiali Hei[4]
[1,4]Department of Computer Science, University of Louisiana at Lafayette
[2]Department of Chemical Engineering, Louisiana Tech University
[3]Department of Mechanical Engineering, Louisiana State University

Abstract: The discovery of novel thermoset shape memory polymers (TSMPs) for additive manufacturing can be accelerated through the use of a deep-generative algorithm, minimizing the need for laborious traditional laboratory experiments. We are the first to introduce an innovative approach that uses a deep generative learning model, namely the conditional variational autoencoder (CVAE), to discover novel TSMPs with lower glass transition temperature (Tg) and high recovery stress values (Er). We integrate specific chemical groups, such as epoxy, amine, thiol, and vinyl, as constraints to generate novel TSMPs while preserving the essential reaction properties. To address the challenges posed by small dataset, we use the CVAE model with graph-extracted features. Unlike previous studies focused on single-polymer systems, our research extends to two-monomer samples, discovering 22 novel TSMPs. This approach has practical implications in additive manufacturing, biomedical devices, aerospace, and robotics for the discovery of novel samples from limited data.

Keywords: Thermoset Shape Memory Polymer, Chemical Group Driven, Smart Material, Conditional Variational Autoencoder (CVAE), Machine Learning, Additive Manufacturing, Monomer-Based

1. Introduction

Thermoset shape memory polymers (TSMPs) are smart materials that can restore their predefined shape when stimulated by external factors such as heat. These materials are particularly used in applications where precision control of shape change is required, such as biomedical devices, aerospace structures, robotics, and so on. TSMPs are utilized not only in specialized fields but also in common areas like textiles, consumer products, and infrastructure. For example, TSMPs enable the creation of shape-changing toys, adaptive eyewear, and self-adjusting footwear that conform to user preferences or environmental factors.

However, the main obstacle in finding TSMPs is the arduous task of finding materials with optimal properties, which is prone to errors and requires a lot of time. In the lab, TSMPs are discovered using methods such as combinatorial chemistry for rapid screening of polymers, molecular dynamic (MD) simulations to predict material behavior, and mechanical testing to evaluate properties under various conditions. Techniques such as MD simulations can alleviate certain difficulties, yet creating a comprehensive model for a novel TSMP and conducting simulations is still time-intensive. The use of generative deep learning algorithms offers a promising approach to overcome the challenges of developing new TSMPs. Algorithms such as Generative Adversarial Networks (GANs), Variational Autoencoders (VAE) and Recurrent Neural Network (RNN)/Long-Short Term Memory /(LSTM) are revolutionary tools for generating new content and realistic output across various domains. For example, GANs can create realistic images and VAEs can generate new text or images. Thus, they can be capable of learning the complex structure of polymers, generating novel polymers, and predicting new properties based on the molecular structure, providing substantial progress in the search for ideal TSMPs.

Ma and Luo have used the generative RNN[1] on a 12,000 polymer dataset collected from the existing polyInfo6 database and generated 1M polymers. In their work, they claimed that their generated chemical space is similar to the training samples they used to train the model. Kuenneth and Ramprasad developed a transformer-based multitasking chemical language model, PolyBert,[2] tailored from polymer informatics, facilitating the quick screening of polymer candidates for specific domain applications. PolyBert is capable of extracting meaningful features and predicting diverse properties with precise accuracy. Yan et al.[3] generated new TSMPs by combining two monomers that have different functional groups, such as epoxy, amine, viynyl, hydroxy cross-linkers, and so on. The researchers applied the VAE model to small drug molecules to train the model to learn chemical properties. Subsequently, they used a deep learning model to predict Tg and Er using the features extracted by the VAE model.

Consequently, deep learning has gained significant attention in polymer informatics. Although its application in property prediction has made substantial progress, there is a notable gap in its utilization to generate novel, domain-specific polymers. Although some researchers[1][4] have explored the use of deep-generative algorithms to find new polymers, there is still a lack of research that focuses specifically on the generation of TSMPs using such methodologies. This work aims to bridge the research gap in additive manufacturing by discovering new TSMPs using the proposed conditional variational autoencoder(CVAE). We successfully generate 22 novel TSMPs by training the model on two monomer-based TSMPs, focusing on specific chemical groups such as epoxy (C1OC1), amine (-N-), thiol (-SH-), hydroxyl (-OH), and vinyl (C=C). Our approach uses graph-based feature extraction to precisely represent molecular structures, with atoms as nodes and bonds as edges. By introducing constraints based on the presence and quantity of these chemical groups, our CVAE framework ensures the generation of polymers with the desired chemical compositions. In summary, our key contributions are as follows:

- Pioneering the application of generative model CVAE to discover new two-monomer based TSMPs.
- Incorporating chemical groups as constraints during model training and sample generation to preserve reaction properties between two monomers. Two-monomer TSMPs exhibit greater thermal stability, enhanced durability, and improved resistance to degradation compared to single monomer polymers.

2. Method

A CVAE is an extension of VAE that generates data conditioned on specific attributes. For example, a CVAE trained on images of handwritten digits can generate a new digit image by specifying the desired digit (e.g., generating a ’7’ by providing the label ’7’ as a condition). The encoder learns essential features from the graph-extracted data and generates latent vectors. The decoder then takes these latent vectors and generates new samples closer to the input data distribution. By incorporating graph-based input features and chemical groups as conditional features, the model learns the reaction properties between two monomers. We initiate the feature extraction process from the samples, represented in Simplified Molecular Input Line Entry System (SMILES) format. We use graph-based feature extraction techniques. Each atom is treated as a node, and the bonds between atoms are edges, considering adjacent bonds and ring structures. We extract two conditional features from each monomer, focusing on distinct chemical groups such as epoxy (C1OC1), amine (-N-), vinyl (C=C), hydroxyl (-OH), and thiol (-S-). One feature indicates the positions of these groups, and the other is their total count. If the count value is not at least 2, the two monomers will not react with each other. The two additional features assign higher weights to samples containing these groups, ensuring accurate reaction properties.

0

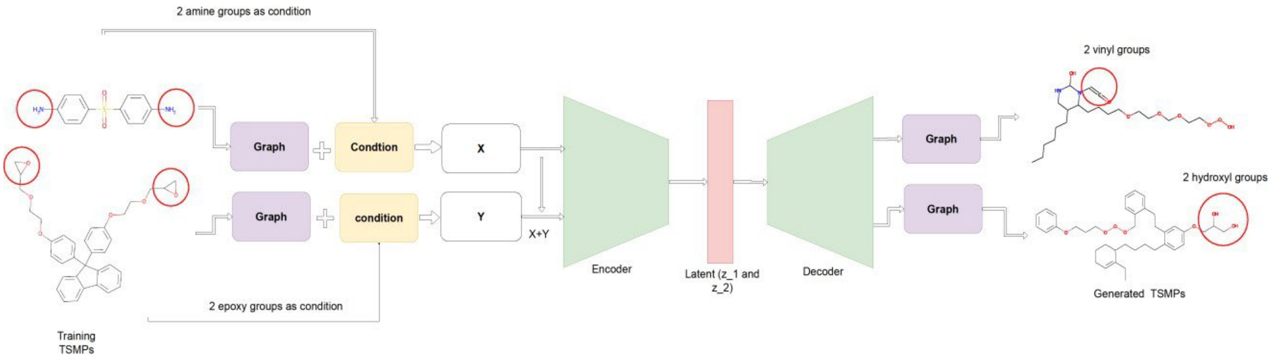

Figure 1: The proposed CVAE method to generate two-monomer-based TSMPs. Red circles indicate conditional chemical groups.

Graph input features and constraint features from the two monomers are concatenated into two sets, X and Y , corresponding to each monomer. Before giving two features to the encoder model, we update Y by the summation of X and Y to highlight the relationship between the two monomers. X and Y are then given separately to the encoder, generating two latent distributions, z1 and z2. The latent vectors are passed through the decoder to generate two graphs, which are subsequently converted into SMILES form, resembling the input data. The method architecture is illustrated in Figure 1. In addition to our main focus on generating TSMPs using a generative algorithm, we develop a CNN model to predict two important properties: Tg and Er for the generated samples.

3. Result

To generate new TSMPs, various types of noise, such as Gaussian noise and salt-and pepper noise, are added to the training data and processed through the model. This method results in the generation of 22 chemically valid novel TSMPs. Chemical validation is performed using the RDKit14 chemo-informatics library by creating valid MOL files from generated TSMPs. The chemical structures of 2 out of 22 generated TSMPs are shown in Figure 2. Not only having the right combination of the chemical groups would be sufficient, but also the number of these groups must meet the threshold value in each monomer. Our proposed method satisfies this condition as well. For example, consider sample 1 in Figure 2 which comprises three epoxy groups in the second monomer and two amine groups in the first. Despite successfully generating new TSMPs, several limitations have emerged such as dataset too small, epoxy-amine group dominated training samples, disconnected molecules while generating novel samples, and unstable Er values in training data leading to high error rate. Despite all the limitations, our study shows a significant advancement in TSMP generation. We have demonstrated the potential of generative algorithms to produce new TSMPs and characterize their properties, which is our focus in this study.

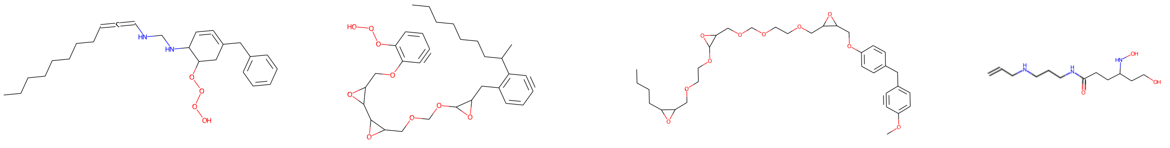

1. Tg: 194°C, Er: 29 MPa

2. Tg: 160°C, Er: 33 MPa

Figure 2: Generated TSMPs

4. Conclusion

In conclusion, our study demonstrates the potential of deep generative learning algorithms to revolutionize material discovery in additive manufacturing. By using CVAE, we have found 22 novel TSMPs, overcoming traditional time-consuming and error-prone synthesis processes. Despite limitations due to a small dataset, our success highlights the feasibility of this approach. Future research should focus on expanding datasets, refining models, and integrating advanced evaluation techniques to accelerate progress in additive manufacturing and usher in a new era of material innovation and customization using AI.

5. Acknowledgments

This work is supported by the U.S. National Science Foundation under grant number OIA-1946231 and the Louisiana Board of Regents for the Louisiana Materials Design Alliance (LAMDA).

6. References

[1] Ma, R.; Luo, T. PI1M: a benchmark database for polymer informatics. Journal of Chemical Information and Modeling 2020, 60, 4684–4690.
[2] Kuenneth, C.; Ramprasad, R. polyBERT: a chemical language model to enable fully machine-driven ultrafast polymer informatics. Nature Communications 2023, 14, 4099.
[3] Yan, C.; Feng, X.; Wick, C.; Peters, A.; Li, G. Machine learning assisted discovery of new thermoset shape memory polymers based on a small training dataset. Polymer 2021, 214, 123351.
[4] De Cao, N.; Kipf, T. MolGAN: An implicit generative model for small molecular graphs. arXiv preprint arXiv:1805.11973 2018

Designing a Heated Substrate for the Additive Manufacturing Process of Carbon Steel

Mahnaz Ensafi, Hamed Ghadimi, Selami Emanet, Shengmin Guo
Department of Mechanical & Industrial Engineering, Louisiana State University

Abstract: Additive Friction Stir Deposition (AFSD) is a solid-state additive manufacturing technique that deforms feedstock metal to build parts layer by layer. This study investigates heating a carbon steel substrate to 700 °c for AFSD process. The experimental setup includes a carbon steel substrate, copper substrate reinforced with Inconel plates and insulated with ceramics to optimize heat transfer and reduce heat loss. Six quarter-inch diameter heaters, each providing 560 watts, were used, totaling 3.3 kW of energy. The setup incorporated ceramic insulators and fixtures, with heat loss calculated at 2.88 kW. Experimental results showed a gradual temperature rise, with the substrate reaching 522 °c in 56 minutes, 606 °c in 86 minutes, and 620 °c in 99 minutes. Initial sparking issues were resolved by gradually increasing the temperature. Thermocouples placed strategically ensured accurate temperature measurements.

Keywords: Additive Friction Stir Deposition (AFSD), Heat transfer, Conduction

1. Introduction

Additive Friction Stir Deposition (AFSD) is a layer-by-layer additive manufacturing technique that operates in a solid state. This process involves thermomechanical stirring and softening the feedstock metal, integrating it with the underlying layers to create parts. AFSD is recognized for its combination of mechanical compression and friction-generated heat to deposit materials, making it a distinct thermomechanical processing method. For printing carbon steel using AFSD, it is necessary to heat the substrate to 700 °c. This paper aims to explain the project, which involves heating a carbon steel substrate with dimensions of 12×4×0.5 inches up to 700 °c. Achieving this requires a suitable heater, along with the design of appropriate ceramic insulators and fixtures to prevent heat loss. The paper details the methodology used to select and implement the heater, insulators, and fixtures to ensure efficient heating and minimal heat loss.

2. Method

The study's experimental setup, illustrated in Figure 1, investigates heat transfer through the system. It includes a carbon steel substrate and a copper substrate housing six heaters for efficient heat transmission. Inconel plates are placed under the carbon steel to reinforce the copper substrate, ensuring structural integrity and effective heat conduction. Ceramic materials surround the system to mitigate heat loss, acting as insulators to prevent heat dissipation and ensure maximum heat is directed toward the carbon steel substrate. Robust fixtures secure the entire assembly, maintaining stability during operation. The copper substrate, which houses the heaters, is the primary heat source. These heaters, embedded within the copper substrate, generate and conduct heat to the carbon steel substrate. Ceramic insulators play a crucial role in preventing heat loss, enhancing the efficiency of heat transfer. The heat conduction equation (Equation 1) was used to quantify heat loss through the ceramic's insulator.

$$q = kA\frac{\Delta T\,(T_2 - T_1)}{L} \qquad (1)$$

q is the amount of conducted heat, k is The thermal conductivity of the material, A is the cross-sectional area through which heat is conducted, ΔT is The temperature difference and l is the length or thickness of the material.

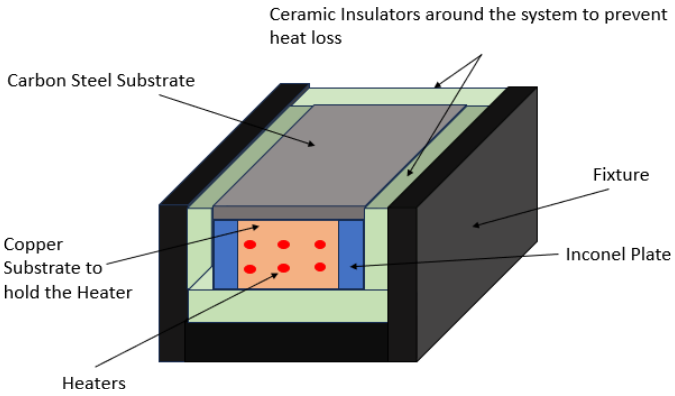

Figure 1. The schematic of experimental setup

The total heat loss was calculated at 2.54 kW, with 1.09 kW lost from the side area, 1.27 kW from the bottom area, and 0.17 kW from the back area. The thermal conductivity (k) of the ceramic is 1.46 W/m°c and the temperature difference (ΔT) is 675 °c as the temperature of carbon steel substrate is 700 °c and room temperature is considered 25 °c.

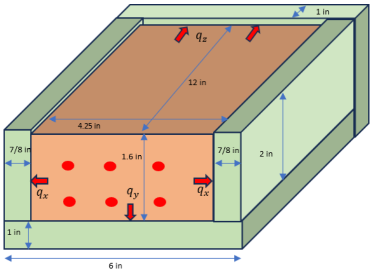

Area (m2)		Thickness of Ceramics	
		inches	meter
Bottom Area	0.03290316	1	0.0254
Side Area	0.012387072	0.875	0.022225
Back Area	0.004387088	1	0.0254

(a) (b)

Figure 2. (a) Schematic of the heat loss calculation, and (b) calculation of the cross-sectional area and thickness of each side

Six quarter-inch diameter heaters, each supplying 560 watts, provide approximately 3.3 kW of total energy. This setup ensures sufficient heat generation to compensate for heat loss and maintain the desired system temperature.

3. Experiment results

In the experiment, six heaters were inserted into designated holes, as shown in Figure 3(a). Initial tests revealed sparkling when the temperature increased, posing a risk to equipment and data reliability. To address this, the temperature gradually increased to 700 °c in controlled steps. Thermocouples were placed on the heater, the copper substrate, and beneath the Inconel substrate to monitor temperature distribution accurately. The steel entire system was secured with step clamps to prevent movement during heating. These clamps ensure the system's position and stability, facilitating consistent and reliable operation.

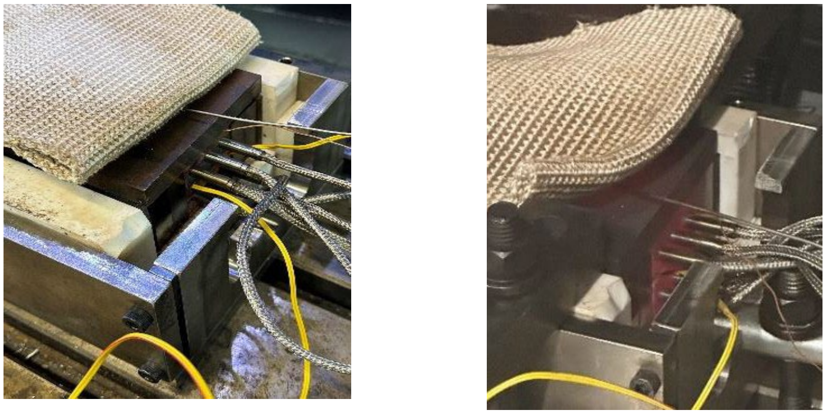

(a) (b)

Figure 3. (a) Entire system before turning the heaters on. (b) Entire system after turning the heaters on

Heaters were cycled on and off at regular intervals, staying on for 90 seconds at higher temperatures to ensure proper heat transfer. Temperature readings were taken at specific intervals, showing a steady rise: 522 °c after 56 minutes, 606 °c after 86 minutes, and 620 °c after 99 minutes. Corresponding temperatures at the copper substrate were 600 °c, 670 °c, and 674 °c (Figure 3(b)). The rate of temperature increase was faster up to 500 °c, indicating efficient heat conduction and minimal heat loss initially. The rate slowed beyond 500 °c due to increased thermal resistance. The controlled heating strategy effectively achieved high temperatures while addressing the sparking issue. Thermocouples ensured accurate temperature measurements, and secure fixation minimized errors from movement. Detailed temperature readings offered valuable insights into thermal behavior, guiding future improvements and optimizations. Overall, the experiment demonstrated the importance of careful planning and precise execution in high-temperature setups

4. Conclusion

This study explored heating a carbon steel substrate to 700 °c for Additive Friction Stir Deposition (AFSD). The setup included a carbon steel substrate, copper substrate reinforced with Inconel plates and insulated with ceramics to optimize heat transfer and minimize heat loss, utilizing six heaters providing a total of 3.3 kW of energy. Careful design and implementation of ceramic insulators and fixtures ensured efficient heating, with heat loss calculated at 2.54 kW. The substrate's temperature rose steadily, reaching 522 °c in 56 minutes, 606 °c in 86 minutes, and 620°c in 99 minutes, while the copper substrate's temperatures were slightly higher. Initial sparking issues were resolved by gradually increasing the temperature. Strategically placed thermocouples provided accurate temperature measurements, and step clamps ensured system stability. The study demonstrated the feasibility of using AFSD to heat a carbon steel substrate to high temperatures. The findings highlight the importance of meticulous planning, precise execution, and robust experimental design.

5. Acknowledgments

This work is supported by the U.S. National Science Foundation under grant number OIA-1946231 and the Louisiana Board of Regents for the Louisiana Materials Design Alliance (LAMDA).

Effect of Graphite Coating on Tensile Properties of MELD (friction stir) Printed Al6061 at High Deposition Rate

Michael Talachian[1], Nils Newhauser[1], Shengmin Guo[1], Dimitris Nikitopoulos[1], Eric Fodran[2], Eric Barnes[2]

[1]Mechanical and Industrial Engineering Department, Louisiana State University
[2]Northrop Grumman Corporation

Abstract: In this project, tensile properties of two MELD printed blocks, with and without graphite, are explored. Additive Friction-Stir Deposition (AFSD) process achieves deposition of metals with severe plastic deformation without melting. A square cross section feedstock rod is pressed against a substrate and rotates at the dictated spindle speed to create heat. The heat created by friction with existence of a 0.09" – high protrusion makes the yield strength drop which is plasticized and stirred by tool rotation. After producing 2 blocks, with and without graphite coating, at the deposition rate of 9.8 Kg/hr and performing tensile tests and hardness tests, we observed interesting changes in yield strength, maximum stress, and elongation. The conducted hardness test backed up the changes in yield strength, maximum stress, and elongation.

Keywords: MELD, Al6061, Additive Manufacturing, Additive Friction Stir Deposition

1. Introduction

Additive Friction Stir Deposition (AFSD) is a layer-by-layer thermomechanical solid-state manufacturing (AM) process. In this process, the material which has been softened and plastically deformed will be stirred to the lower layer(s) and eventually creates a three-dimensional part. In this process, plastic deformation and material flow is induced by combined mechanical force and heat generated by the friction stir process. Figure 1 shows the mechanism of AFSD and the deposition tool design.

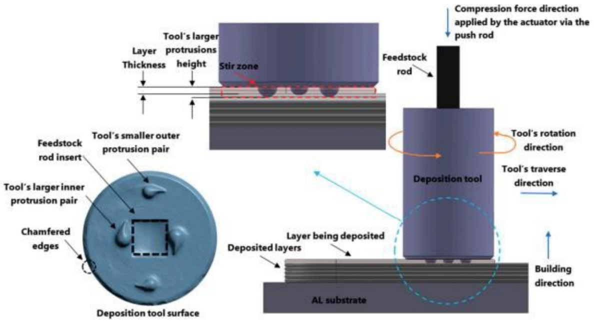

Figure 1. Mechanism of AFSD and the deposition tool design [1]

2. Materials and Methods

2.1 Feedstock Materials

In the MELD process,9.5 x 9.5 x 508 mm Al 6061-T6 rods were used. The print outcome is 2 mm (0.08 inch) in layer thickness and about 43.2 mm (1.7 inch) in width. The traverse speed and feed rate are correlated based on the conservation of mass. In order to be compliant with the next step which is cutting miniature dog-bone shaped samples out of the block for tensile tests, we printed the blocks 2 inches in height. With a simple calculation, to build a 51 mm (2 inch) by 43.2 mm (1.7 inch) by 177.8 mm (7 inches) block, ~392,000 mm^3 of Al 6061 is needed.

2.2 ASTM Standard Specimen Preparation

In this study subsize ASTM E8/EM8-22 standard specimens were used. Specimens were 100 mm in length, and 2 mm in thickness. The gauge section was 25 mm long and 6 mm in width. As shown in the figure below, 48 specimens were extracted from each block in 2 different orientations, 4 stacks and 8 columns. The first orientation is laying flat along the X direction (traverse direction) and the other orientation was perpendicular to the traverse direction. Naming format of the specimens is Column number – Stack number.

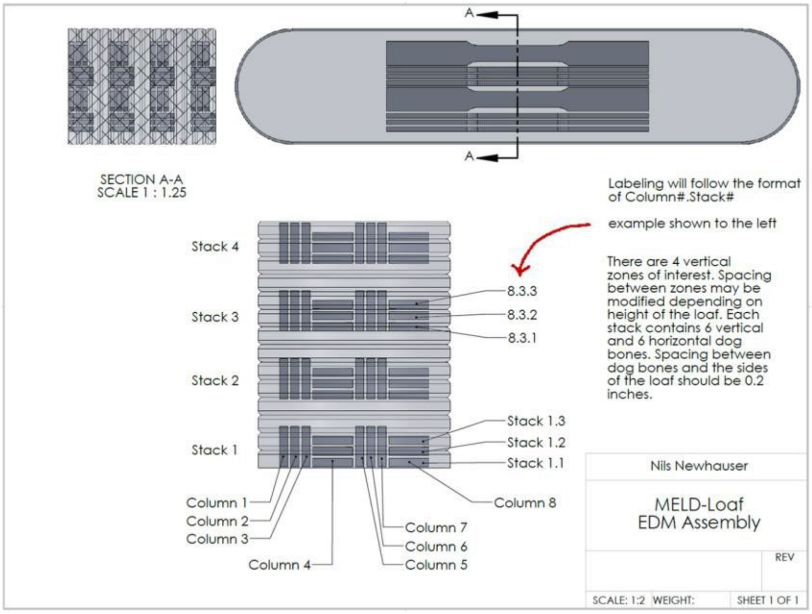

Labeling will follow the format of Column#.Stack#

example shown to the left

There are 4 vertical zones of interest. Spacing between zones may be modified depending on height of the loaf. Each stack contains 6 vertical and 6 horizontal dog bones. Spacing between dog bones and the sides of the loaf should be 0.2 inches.

Figure 2. Tensile specimen extraction map and naming format.

3. Results and Discussion

The objective of this study was to extract subsize dog-bones in two different orientations and 4 stacks and then perform tensile test and compare the results. The test resources machine used in this work generates the data that we required in the test setup such as: Date, time, direction, control rate, specimen's length, specimen's width, specimen's thickness, specimen's area, maximum load, maximum stress, elongation, modulus of elasticity, and offset yield. Based on the presented data below we can obviously see as we approach stack 4 which is the top of the block the yield stress, maximum stress and maximum load increases and the elongation decreases.

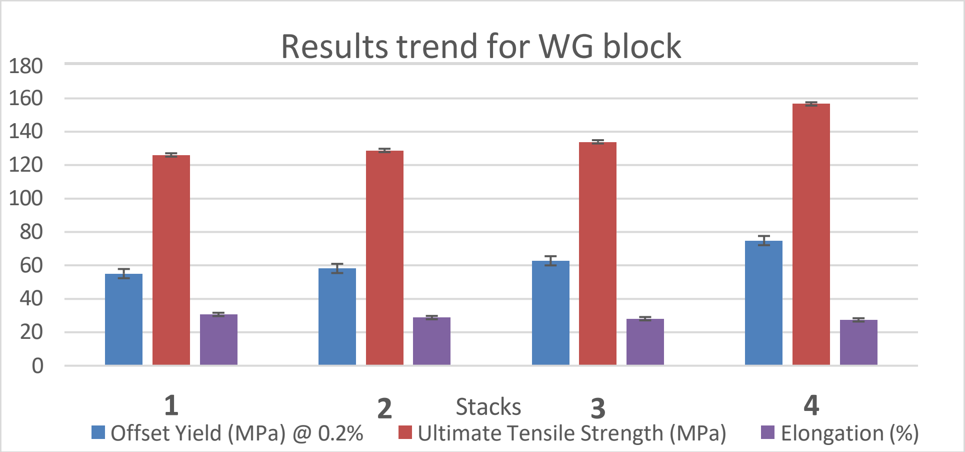

Figure 3. Results trend for With Graphite coating.

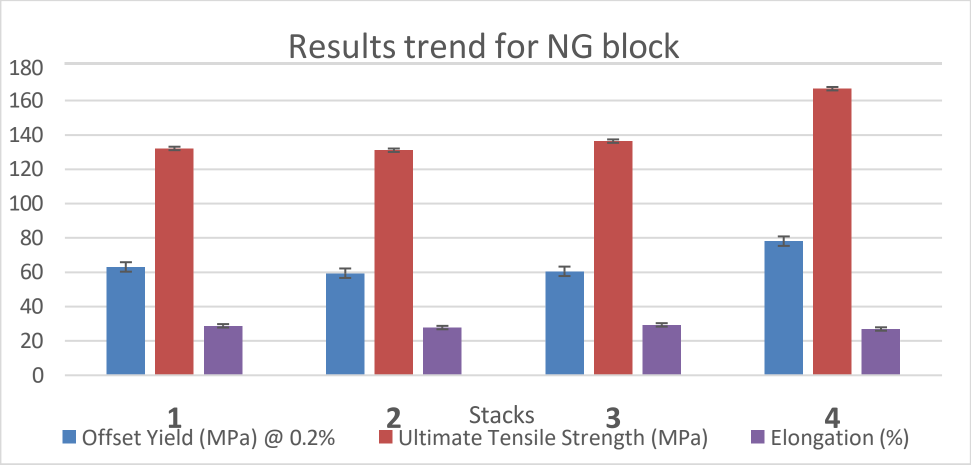

Figure 4. Results trend for No Graphite coating.

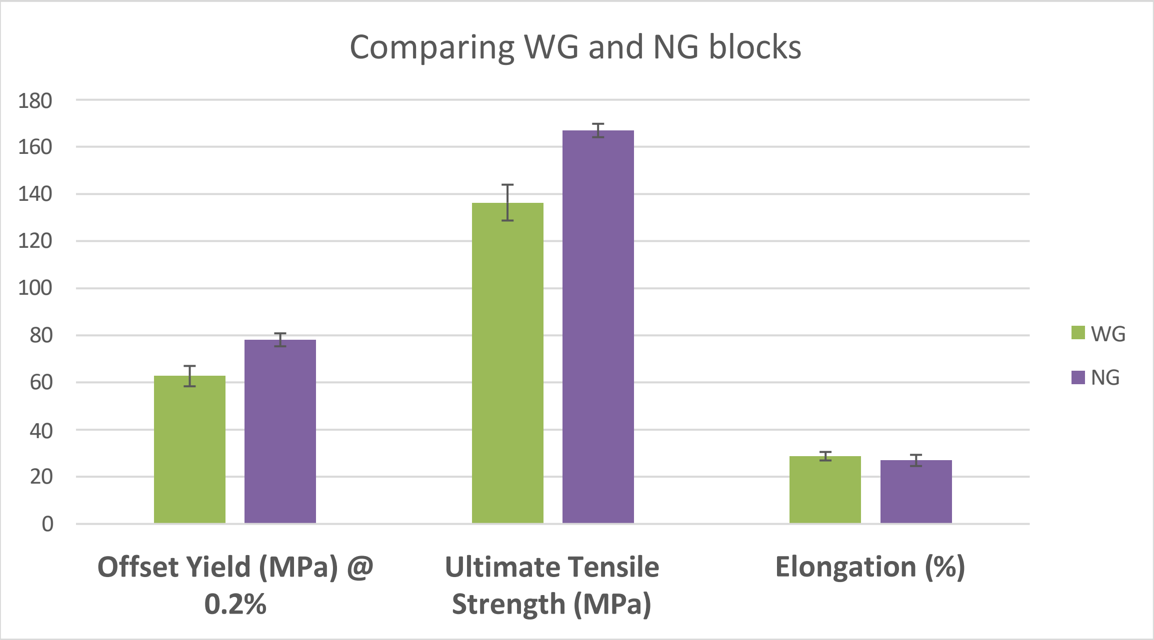

Figure 5. Comparing WG and NG blocks.

4. Conclusion

In this study tensile tests were conducted based on ASTM standard E8/E8M on subsize dog-bones and data were processed to show stress-strain curves for feedstock rods with and without graphite coatings. We observed that as we approach towards the top of the build strain decreases and stress increases which gave us an indication that the build is less annealed towards the top of the build.

5. Acknowledgments

This work is supported by the U.S. National Science Foundation under grant number OIA-1946231 and the Louisiana Board of Regents for the Louisiana Materials Design Alliance (LAMDA). This work is also supported by Northrop Grumman Corporation.

6. References

[1] Hardness Distribution of Al2050 Parts Fabricated Using Additive Friction Stir Deposition. Hamed Ghadimi, Huan Ding, Selami Emanet, Mojtaba Talachian, Chase Cox, Michael Eller and Shengmin Guo.

Effect of Heat treatment on Mechanical Properties and Electroconductivity of Al 7075 Parts Prepared by Additive Friction Stir Deposition

Ehsan Bagheri, Saeid Zavari, Noushin Adibi, Shengmin Guo

Department of Mechanical and Industrial Engineering, Louisiana State University

Abstract:
In this study, Al 7075 parts were fabricated using additive friction stir deposition, and the effect of T73 heat treatment on mechanical properties, including hardness and tensile properties, was evaluated. The results showed that the average hardness and electroconductivity of the as-fabricated Al 7075 blocks were 80.5 HV and 39.8 %IACS, respectively, which differed significantly from the feedstock material values of 175.5 HV and 33.3 %IACS. Additionally, the tensile strength decreased from 551.6 MPa to 311.7 MPa. After heat treatment, the properties were successfully recovered, with hardness and strength improving to 162 HV and 464.9 MPa, respectively, while conductivity decreased to 37.1 %IACS.

Keywords: Additive friction stir deposition; Aluminum alloy, Mechanical properties

1. Introduction

Friction-based additive manufacturing is a plasticity-driven solid-state process that has emerged as a promising alternative to fusion-based 3D printing methods. It involves severe shear deformation induced by frictional forces to build the desired shape layer-by-layer. Three common friction-based additive manufacturing methods are friction extrusion additive manufacturing, hybrid metal extrusion and bonding, and additive friction stir deposition (AFSD) [1]. AFSD, commercially known as MELD, is the most prevalent solid-state AM technique, offering significant advantages in terms of production efficiency, flexibility, and cost. In the AFSD process, a feedstock rod is fed to a substrate surface through a hollow rotating tool. The rod softens due to the heat generated by frictional forces and flows as the tool moves across the surface. The major parameters in AFSD, which control the local heat input, include material feed rate (F), tool rotational speed (ω), layer thickness (T), and tool traverse velocity (V). Higher rotational speeds and lower traverse velocities result in higher heat input, significantly influencing the part's quality and properties [2]. Common surface defects in AFSD include excessive material flash, onion ring patterns, galling, surface scratches, and edge cracking, which can be mitigated by adjusting the processing parameters [3]. Therefore, optimizing these parameters is essential to achieve defect-free deposition with the best possible properties.

The 7xxx series of aluminum alloys, known for their high specific strength, excellent fatigue properties, and machinability, have been extensively used in the aerospace industry and military sectors. Due to the challenges associated with fusion-based additive manufacturing of this series, such as hot cracking from its non-weldable nature, solid-state techniques like AFSD are essential [4]. Numerous studies have focused on single-layer deposition of 7xxx series aluminum alloys, specifically Al 7075, for repair purposes [5]. However, there is a relative scarcity of research on multilayer AFSD of these alloys. The higher hardness and strength of Al 7075 make the AFSD process more challenging. For instance, Avery et al. [6]. deposited an Al 7075 block with a feedstock feed rate of 50.8 mm/min, traverse velocity of 50.8 mm/min, and rotational speed of 250 rpm. Their results revealed a refined microstructure, but the hardness, tensile strength, and fatigue life of the printed block were lower than those of the feedstock material. They did not study the effect of heat treatment on the deposition properties and observed excessive flash due to improper selection of processing parameters. Elshaghoul et al. [7]. studied the feasibility of 3D printing Al 7075 on an Al 2024 substrate using AFSD, optimizing the deposition parameters. They successfully achieved physically defect-free depositions by pushing a rotating Al 7075 feeding rod with a diameter of 4 cm onto the Al 2024 substrate, without traverse movement, at a rotational speed of 400 rpm and material feed rates of 1, 2, 3, and 4 mm/min. In the present work, two Al 7075 blocks are deposited, with one block subjected to heat treatment. Mechanical and electrical conductivity tests are conducted on both parts to evaluate the performance of the as-deposited material at different layers and to determine if heat treatment can recover the part's performance. This study lays the groundwork for implementing AFSD in the fabrication of Al 7075 parts for engineering applications.

2. Materials and methods

Al 7075 square rods with dimensions of 9.5×9.5×457.2 mm³ were cut from Al 7075-T651 square bars (OnlineMetals) using a waterjet cutter and used as the feedstock material. A MELD L3 machine equipped with a standard tool featuring two pairs of teardrop-shaped protrusions was employed for 3D printing. These protrusions were located on the bottom surface of the tool in a centrosymmetric array; two surrounded the feedstock rod outlet, while the other pair was near the edge of the tool. They assist in material flow and heat generation by increasing frictional forces and can re-stir the previously deposited layer depending on the selected layer thickness. An Al 7075-T651 plate (304.8×101.6×12.7 mm³) was used as the substrate for 3D printing. A thermocouple was placed below the substrate to estimate the processing temperature. The substrate was preheated to 250°C to facilitate the printing of the initial layers. To prevent jamming inside the tool during AFSD, the feedstock rods were coated with a thin layer of graphite as a dry lubricant before being fed into the machine. The schematic of the process is shown in Fig. 1.a. The process began by pushing the rods against the substrate to generate sufficient heat for material flow, and the parts were deposited layer-by-layer based on a G-code. Two large blocks with the same lengths and heights of 165.1 and 40.6 mm, respectively.

Microhardness of the different layers was measured along the center line in the building plane before and after the heat treatment using a CM-803 AT microhardness tester. The load and dwell time of the machine were set at 100 gf and 15 s, respectively. Electroconductivity of the specimens was recorded by a portable instrument (Sigmascope SMP 350, Helmut Fischer GmbH) working based on eddy current principle. The device was calibrated by standard samples with similar conductivities. The results were presented as percentages according to the International Annealed Copper Standard (%IACS). Tensile properties of the as-deposited and heat-treated specimens were evaluated based on ASTM E8-E8M. Subsize flat samples were cut from the top and bottom regions in the longitudinal direction (XY plane). They were subjected to a tensile rate of 1.2 mm/min using a universal testing machine (TestResources 313) equipped with a 5 kN load cell.

3. Results and discussion

Microhardness and electroconductivity tests were conducted along the cross-sectional center line from the top to the bottom layers (Z direction), and the results are presented in Fig. 1. For the as-deposited part, hardness decreased from 84.4 HV in the second layer from the top (Z = 2.25 mm) to 76.1 HV in the bottom layer (Z = 38.25 mm). The average hardness along the center line was 80.5 HV, indicating a 54.4% decrease compared to the feedstock hardness of 176.5 HV. In contrast, conductivity exhibited an opposite trend, increasing from 38.7 %IACS to 40.6

%IACS across the same layers. The average conductivity of the as-deposited cross-section improved from 33.3 %IACS in the feedstock material to 39.8 %IACS. These changes in properties can be explained by the microstructure results and the change in the secondary phases in the matrix [8].

After heat treatment, the average hardness significantly increased to 162.0 HV, while electroconductivity changed to 37.1 %IACS. The variation in properties from the top to the bottom layers also became less pronounced. The hardness measured for the second top layer was 165.7 HV, decreasing to 160.0 HV in the bottom layer. Conductivity improved from 35.7 %IACS to 37.9 %IACS across these layers. The substantial enhancement in hardness and the decrease in electroconductivity after heat treatment can be attributed to the changes in the size and distribution of secondary phases. Similar results have been reported for the hardness and electroconductivity of Al 7075 following heat treatment [8, 9].

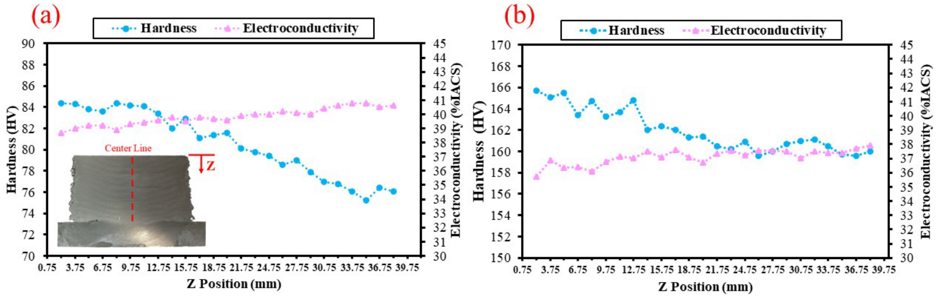

Fig. 1 Electroconductivity and hardness data along the cross-section center line for a. as-deposited, b. heat treated specimens

Figure 2 illustrates the strain-stress curves obtained from tensile testing of the specimens in the longitudinal direction before and after the heat treatment and the results are summarized in Fig. 3. According to the supplier, the ultimate stress and elongation at break for the Al 7075-T651 feedstock material were 551.6 MPa and 8.2%, respectively. The ultimate stress of the as-deposited parts decreased to 311.7 and 287.6 MPa for the top and bottom layers, respectively. However, the ductility enhanced; the elongation at break increased to 17.8 and 21.9% for the corresponding layers. However, the ultimate strength improved to about 464.9 MPa and the elongation decreased to approximately 9.4% after the heat treatment suggesting that smaller precipitates were formed uniformly. The results are in good agreement with the hardness measurements.

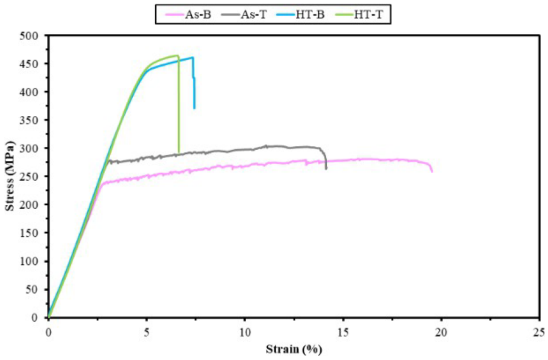

Fig. 2 Stress-strain curves for the as-deposited and heat-treated specimens

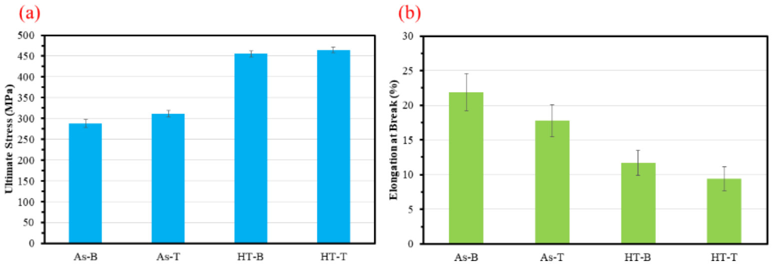

Fig. 3 Ultimate strength and elongation at break for the samples before and after heat treatment

4. Conclusion

Al 7075 parts were fabricated using additive friction stir deposition, and the effect of T73 heat treatment on their mechanical properties, including hardness and tensile strength, was evaluated. The results indicated that the mechanical properties of the as-fabricated Al 7075 blocks decreased significantly compared to the feedstock material. Following heat treatment, the properties were successfully improved.

5. Acknowledgments

This work is supported by the U.S. National Science Foundation under grant number OIA-1946231 and the Louisiana Board of Regents for the Louisiana Materials Design Alliance (LAMDA).

6. References

[1] W. Tang, X. Yang, and C. Tian, "Influence of rotation speed on interfacial bonding mechanism and mechanical performance of aluminum 6061 fabricated by multilayer friction-based additive manufacturing," *The International Journal of Advanced Manufacturing Technology,* vol. 126, no. 9, pp. 4119-4133, 2023/06/01 2023, doi: 10.1007/s00170-023-11378-1.

[2] Z. Shen *et al.*, "Local microstructure evolution and mechanical performance of friction stir additive manufactured 2195 Al-Li alloy," *Materials Characterization,* vol. 186, p. 111818, 2022/04/01/ 2022, doi: https://doi.org/10.1016/j.matchar.2022.111818.

[3] A. Mukhopadhyay and P. Saha, "A critical review on process metrics–microstructural evolution–process performance correlation in additive friction stir deposition (AFS-D)," *Journal of the Brazilian Society of Mechanical Sciences and Engineering,* vol. 44, no. 9, p. 422, 2022/08/22 2022, doi: 10.1007/s40430-022-03729-y.

[4] C. J. T. Mason *et al.*, "Process-structure-property relations for as-deposited solid-state additively manufactured high-strength aluminum alloy," *Additive Manufacturing,* vol. 40, p. 101879, 2021/04/01/ 2021, doi: https://doi.org/10.1016/j.addma.2021.101879.

[5] R. J. Griffiths, D. T. Petersen, D. Garcia, and H. Z. Yu, "Additive Friction Stir-Enabled Solid-State Additive Manufacturing for the Repair of 7075 Aluminum Alloy," *Applied Sciences,* vol. 9, no. 17, p. 3486, 2019. [Online]. Available: https://www.mdpi.com/2076-3417/9/17/3486.

[6] D. Z. Avery *et al.*, "Influence of Grain Refinement and Microstructure on Fatigue Behavior for Solid-State Additively Manufactured Al-Zn-Mg-Cu Alloy," *Metallurgical and Materials Transactions A,* vol. 51, no. 6, pp. 2778-2795, 2020/06/01 2020, doi: 10.1007/s11661-020-05746-9.

[7] Y. G. Y. Elshaghoul *et al.*, "Additive Friction Stir Deposition of AA7075-T6 Alloy: Impact of Process Parameters on the Microstructures and Properties of the Continuously Deposited Multilayered Parts," *Applied Sciences,* vol. 13, no. 18, p. 10255, 2023. [Online]. Available: https://www.mdpi.com/2076-3417/13/18/10255.

[8] C. Zeng *et al.*, "Microstructure Evolution of Al6061 Alloy Made by Additive Friction Stir Deposition," *Materials,* vol. 15, no. 10, p. 3676, 2022. [Online]. Available: https://www.mdpi.com/1996-1944/15/10/3676.

[9] H. Ghadimi *et al.*, "Hardness Distribution of Al2050 Parts Fabricated Using Additive Friction Stir Deposition," *Materials,* vol. 16, no. 3, p. 1278, 2023. [Online]. Available: https://www.mdpi.com/1996-1944/16/3/1278.

Effect of Layer Thickness on the Microstructure and Corrosion Behavior of AFS-D Processed Al 6061 in 3.5% NaCl Solutions

Md Shafayet Alam[1], Dr. Erica P. Murray[2]

[1]Institute of Micro Manufacturing, Louisiana Tech University
[2]Institute of Micro Manufacturing, Louisiana Tech University

Abstract: Additive manufacturing, often referred to as 3D printing is a cutting-edge process of creating three-dimensional objects layer by layer from a digital model, which offers various advantages like increased design freedom, reduced waste, and the ability to create complex geometries. The goal of this work is to study the corrosion behavior of Additive Friction Stir Deposition processed Al6061 alloy in 3.5% NaCl solution based on their microstructures. The microstructure is one of the primary elements that can affect the corrosion properties of the material. The corrosion properties were assessed via the impedance measurement, polarization resistance and the cyclic polarization experiments. Microstructural observations were executed before and after the experiments to recognize the changes on the microstructures of the samples during the corrosion process. By analyzing the experimental data and the supporting microstructural information, the corrosion properties of the samples were identified.

Keywords: Corrosion, AFS-D, Al6061, MELD, EIS, Cyclic Polarization, Raman Spectroscopy

1. Introduction

Additive manufacturing uses data computer-aided-design (CAD) software or 3D object scanners to direct hardware to deposit material, layer upon layer, in precise geometric shapes. [1] This technique was introduced to offer tremendous advantages in the manufacturing field, such as producing intricate and complex designs, including internal structures and features that may be challenging or impossible with traditional methods, low material usage and wastage, cost efficiency and so on. [2] The additive friction stir deposition (AFS-D) process is a solid-state process that represents an innovative thermomechanical approach engineered for the additive manufacturing (AM) of large-scale components in an open-air environment. [3] In the AFSD process, a rotating deposition tool, aided by an applied downward force on the feedstock rod, generates frictional heat, softening and plasticizing the rod. [4] The plasticized material undergoes a conversion of plastic work to thermal energy, contributing to volumetric heat generation. The molten feedstock then flows to fill the gap under the deposition tool and is deposited onto a previously laid layer or a fixed substrate. [5] This systematic deposition process allows for the continuous manufacturing of a part as the tool follows a predefined path, building up the structure layer by layer.

As the precedence, parameters cause the microstructural defects, which affect the corrosion properties, hence it is necessary to observe the microstructures of the material before and after the corrosion experiments, to understand the defects caused by the processing parameters, and the microstructural change due to the corrosion process. The electrochemical corrosion measurements were collected for verification, and various microscopy and spectroscopy techniques were used for further interpretation. After evaluating all the electrochemical and microscopic results, the impact of processing parameters on the corrosion properties of the processed material was understood.

2. Research hypothesis, methodology and result:

Material Description

Al6061 solid square rods with the composition of Al-1.63, Mg-0.44, Si-0.23, Cu-0.16 (wt.%) and a size of 9.5 × 9.5 × 508 mm^3 were used as feedstock. A MELD L3 machine was utilized to fabricate the samples. The processing parameters for the AFS-D processed Al6061 samples are shown in table 1:

AFS-D Process	Deposition Layer Thickness		Rotation Speed	Traverse Speed		Actuator Speed (Feed Rate)	
	mm	in	rpm	mm/min	in/min	mm/min	in/min
Method 1	2.032	0.08	300	127.0	5.0	152.4	6
Method 2	1.016	0.04	300	279.40	11.0	152.4	6

Result and Discussion

Electrochemical Analysis

The electrochemical experiment performed on the Al6061 samples with different process parameters showed divergent behavior. The cyclic polarization test depicts the steps during the corrosion process. In Fig. 1, the sample with the thinner deposited layer had higher corrosion potential (E_{Corr}) than the other sample, showing it to be less prone to corrosion. Besides, this sample also has higher pitting potential (E_{pit}), meaning that localized pitting is less likely to occur in this sample during corrosion process than the sample with thicker deposited layer, even though pitting is delayed in the thicker deposited layer sample after corrosion. This can be explained by the presence of less reactive elements near the pits, which requires more potential to get corroded off, thus the delayed pitting. Overall, the cyclic polarization determines the thinner deposited layer sample having better corrosion properties of the two samples.

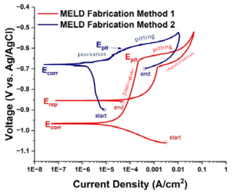

Figure 1: Cyclic polarization of Al6061 samples processed by Method 1 and 2.

Microstructural Observation

The microstructure of the sample was observed to validate the electrochemical results obtained from the cyclic polarization experiment. The confocal imaging showed the pit depths in the samples after the corrosion process. The result showed the thick deposited layer sample had a higher number of pits, having pit depths up to 67.2 µm. Whereas, the thin deposited layer sample had fewer pits with pit depth up to 5.9 µm. The higher pitting potential enables the sample with thin deposited layer to have lesser pits.

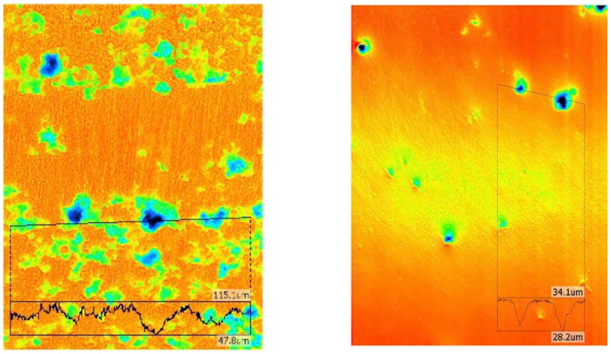

Figure 2: Confocal images of Al6061 a) Method 1, and b) Method 2

The Raman Spectroscopy was performed on the samples to identify and measure the respective oxide layers and their intensity. The oxide layer formed on the exposed surface of the sample protects the sample from corrosion. The spectroscopy in Fig. 3 showed that the protective oxide layer present on the thin deposited layer sample was more robust than the other sample, causing it less prone to corrosion. This observation validated the cyclic polarization result about the pitting potential of the two samples.

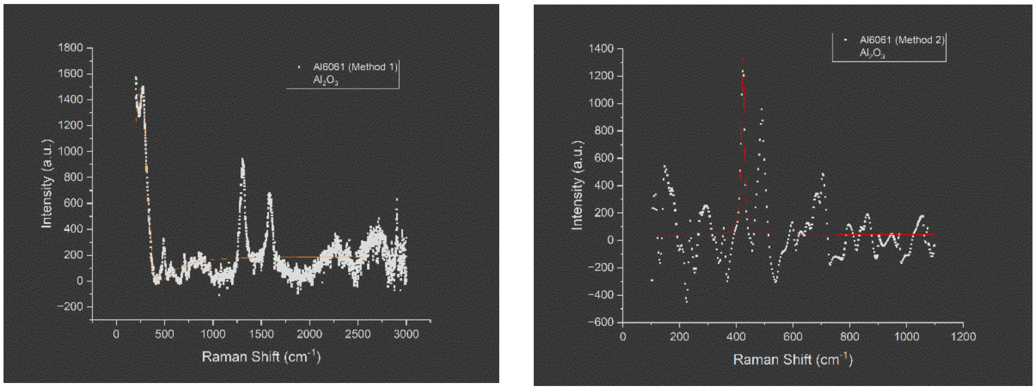

Figure 3: Raman Spectroscopy of Al6061 a) Method 1, and b) Method 2

4. Conclusion

The thickness of the AFS-D Al6061 layers significantly influenced corrosion behavior. Samples fabricated with 1 mm AFS-D layers developed thick layers which limited pitting corrosion. The cyclic polarization data suggested the samples were less prone to corrosion as the corrosion potential tended to be less negative. The microstructural observations indicated the robust oxide layer present on the sample processed with method 1. The confocal images showed fewer localized pits. Therefore, it is evident that thin AFS-D layers hinder corrosion.

5. Acknowledgments

We would like to thank Dr. Shegmin Guo and his team at Louisiana State University for providing the samples in this experiment.

This work is supported by the U.S. National Science Foundation under grant number OIA-1946231 and the Louisiana Board of Regents for the Louisiana Materials Design Alliance (LAMDA).

6. References

[1] U. M. Dilberoglu, B. Gharehpapagh, U. Yaman, and M. Dolen, “The Role of Additive Manufacturing in the Era of Industry 4.0,” Procedia Manuf., vol. 11, pp. 545–554, 2017, doi: 10.1016/j.promfg.2017.07.148.
[2] S. M. E. Sepasgozar, A. Shi, L. Yang, S. Shirowzhan, and D. J. Edwards, “Additive manufacturing applications for industry 4.0: A systematic critical review,” Buildings, vol. 10, no. 12, pp. 1–35, 2020, doi: 10.3390/buildings10120231.
[3] H. Ghadimi, M. Talachian, H. Ding, S. Emanet, and S. Guo, “The Effects of Layer Thickness on the Mechanical Properties of Additive Friction Stir Deposition-Fabricated Aluminum Alloy 6061 Parts,” Metals, vol. 14, no. 1. 2024. doi: 10.3390/met14010101.
[4] M. B. Williams et al., “Elucidating the Effect of Additive Friction Stir Deposition on the Resulting Microstructure and Mechanical Properties of Magnesium Alloy WE43,” Metals, vol. 11, no. 11. 2021. doi: 10.3390/met11111739.
[5] D. Garcia et al., “In situ investigation into temperature evolution and heat generation during additive friction stir deposition: A comparative study of Cu and Al-Mg-Si,” Addit. Manuf., vol. 34, p. 101386, 2020, doi: https://doi.org/10.1016/j.addma.2020.101386

Enhanced Mechanical Properties in 3D-printed Carbon Fiber Composites via Optimized FDM Parameters

Mohammad Rouhi Moghanlou[1], **Michael M Khonsari**[1]

[1]Department of Mechanical and Industrial Engineering, Louisiana State University

Abstract: This study uses the Taguchi method to optimize four FDM printing parameters when using chopped carbon fiber-reinforced polyamide filaments. The goal is to maximize UTS and minimize inter-layer porosities while considering printing time and part weight. Tensile test specimens and cubic samples were printed using the Taguchi model, and their cross-sectional porosities were assessed using optical micrography and image processing software. The results showed significant variations in UTS values, ranging from 91.9 to 171 MPa, with porosities between 1.4% and 17.63%. The most optimized specimen was found to have an infill line distance of 0.4 mm, layer height of 0.3 mm, printing speed of 100 mm/s, and chamber temperature of 55°C. Subsequent tensile tests validated the Taguchi optimization prediction.

Keywords: Additive manufacturing; 3D printing; FDM; Taguchi; carbon fiber composites; UTS

1. Introduction

Additive manufacturing (AM) is a revolutionary approach that offers design flexibility and precision in object fabrication, surpassing traditional methods. 3D printing via FDM is the most widely used AM method, used in various industries like automotive, aerospace, and medical [1]. This approach allows for the fabrication of complex geometries and structures while maintaining the strength-to-weight advantages of traditional CFRPs [2].

3D-printed CFRPs can be categorized into short and continuous fibers, allowing for the customization of objects to meet specific usage requirements. The combination of chopped fibers' strength and low weight with thermoplastic polymers offers significant advancements in AM. Isotropic reinforcement of chopped fibers improves performance and durability for high strength-to-weight ratios [3]. Lobov et al. showed that short CF-reinforced ABS has significantly improved mechanical properties compared to conventional ABS [4]. A separate study examined the mechanical properties of graphene blocks reinforced with chopped CF, finding that the inclusion of 0.8 wt.% CF led to a nearly 60% increase in flexural strength.

The Taguchi method, a design of experiments technique, has been used to optimize 3D printing parameters. Ahmed et al. used this method to optimize FDM printing parameters for thermoplastic composites reinforced with oil palm fiber [5]. The effects of FDM printing parameters on mechanical properties, including impact resistance and tensile strength, have become a significant area of interest. Kamaal et al. found that tensile strength is significantly influenced by infill percentage, layer height, and building direction in 3D-printed CF-reinforced PLA composite [6].

This study aims to optimize FDM printing parameters using chopped CF-reinforced polyamide in 3D printing. The goal is to maximize UTS and minimize inter-layer porosities while considering printing time and weight. The Taguchi method is used for efficient optimization, and tensile test samples and cubic samples are used. The optimal values are determined based on criteria such as maximum tensile strength, minimum porosity, and UTS/weight & UTS/time.

2. Material and Method

2.1. FDM printing

A 1.75-mm diameter filament with a density of 1207 kg/m3 was used for printing specimens. The filament had asymmetrically distributed carbon fibers with an average length of 100 ± 50 µm and a diameter of 7 ± 0.5 µm. The filament was dried at 85°C for 12 hours to reduce humidity. The Sermoon D3 pro printer from Creality3D was used to fabricate tensile and porosity samples, with hardened steel nozzles that can withstand abrasive filaments like CF-reinforced polymer. The figure below shows the filament as well as the FDM printer components.

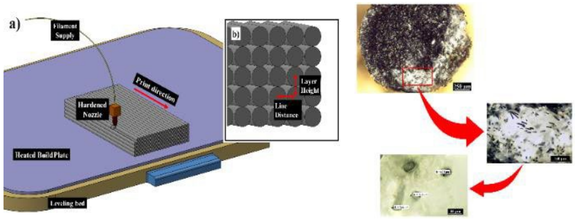

Figure 1 a) CF-reinforced filament, b) Main components of FDM printer

2.2. Taguchi method

The study investigates four main printing parameters: infill line distance, layer height, print speed, and chamber temperature. Using this method, the number of samples was reduced from 256 to 16. The Taguchi method involves three steps: DOE, analysis of the signal-to-noise ratio, and optimization. DOE involves experiments, while S/N ratio analysis evaluates performance. Optimization involves determining optimal parameter quantity and validating findings. For the case of maximized output, the equation is as follows:

$$S/N_i = -10\log\left(\frac{1}{N}\sum_{u=1}^{N_i}\frac{1}{y_u^2}\right)$$

2.3. Porosity analysis and tensile testing

As mentioned, porosity analysis was performed on cubic samples printed with the Taguchi parameters, where microscopic images of the cross-section were analyzed in ImageJ software. Tensile tests were done using an axial fatigue machine with a maximum load capacity of 25kN, as shown in the figure below.

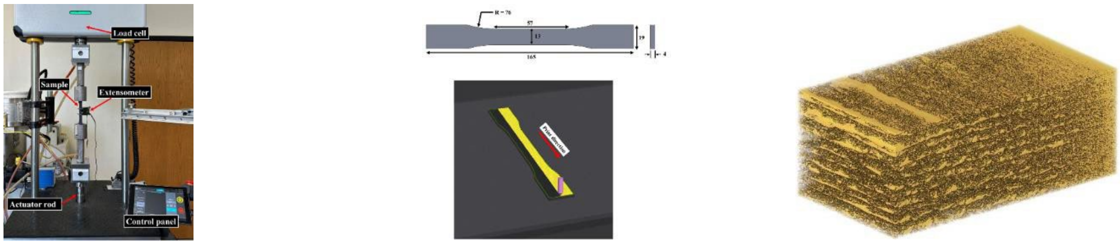

Figure 2 a) Schematic of the uniaxial device and, b) geometry and direction of print C0 X-ray tomography image of porosity sample

3. Results

3.1. Mechanical properties

Tensile experiments on 16 specimens (as shown below) illustrate varying tensile strength, with an average of 115.7 MPa. The combination of matrix and fibers enhances structural performance, resulting in composites with greater failure resistance than monolithic polymers.

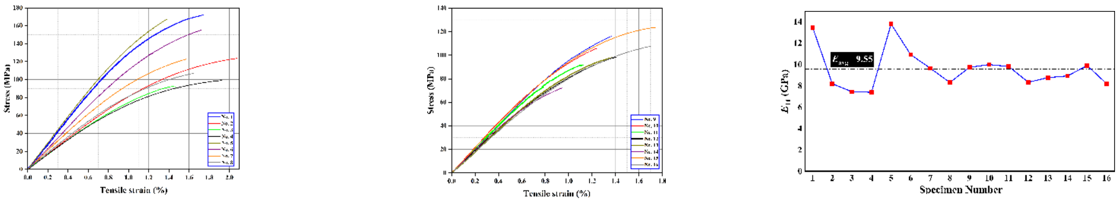

Figure 3 Elastic mechanical properties of 16 Taguchi samples

Figure 4 compares the samples using three measures, showing that specimens No. 1, No. 5, and No. 6 have superior tensile strength but weaker UTS/print time performance. The purpose of comparing these parameters is to improve the accuracy of Taguchi analysis, as the strength-to-weight ratio is more important than strength alone in various applications and manufacturing practices. Production time is also a critical factor to consider.

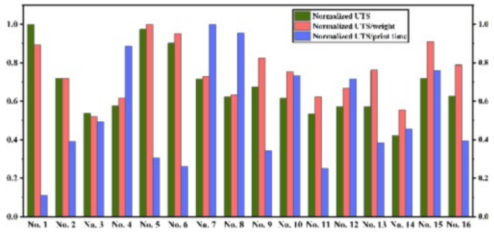

Figure 4 An analysis of the normalized UTS, UTS/ weight, and UTS/ time values for tensile samples using the Taguchi design.

3.2. Porosity analysis

The results from porosity analysis show that specimens with a 0.075 mm layer height have adjacent printed layers with minimal inter-layer porosities, while samples with 0.22 mm and 0.3 mm have discernible pores, leading to premature failure. Cubic samples were 3D printed using L16 design parameters, and their porosities were calculated using ImageJ software. Sample No. 1 had the lowest porosity of 1.44%, mainly due to its small layer height and infill line distance values. The overall upward trend can be attributed to the increase in infill line distance within each set of four samples.

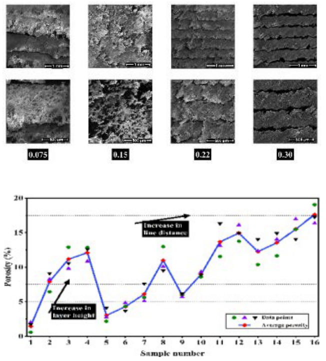

Figure 5 a) SEM images of the cross-sections of samples with different layer heights, b) variations of porosities within Taguchi sample

3.3. Taguchi optimization

The Taguchi optimization uses UTS, sample weight, and print time data to maximize UTS/sample weight and UTS/printing time. Normalized values are used in Minitab. Optimal values for infill line distance, layer height, printing speed, and chamber temperature are determined. The optimized printing properties result in a 12% improvement in UTS/weight ratio and UTS/time ratio compared to the best specimen among 16 tested samples.

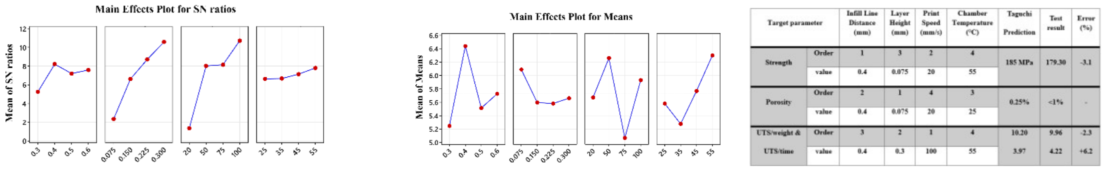

Target parameter		Infill Line Distance (mm)	Layer Height (mm)	Print Speed (mm/s)	Chamber Temperature (°C)	Taguchi Prediction	Test result	Error (%)
Strength	Order	1	3	2	4	185 MPa	179.30	-3.1
	value	0.4	0.075	20	55			
Porosity	Order	2	1	4	3	0.25%	<1%	-
	value	0.4	0.075	20	25			
UTS/weight &	Order	3	2	1	4	10.20	9.96	-2.3
UTS/time	value	0.4	0.3	100	55	3.97	4.22	+6.2

Figure 6 Taguchi design results with the maximum UTS/weight and UTS/ time objective

4. Conclusion

The study used the Taguchi method to optimize FDM printing parameters for fabricating chopped CF- reinforced polyamide. The parameters included infill line distance, layer height, printing speed, and chamber temperature. The results showed significant variation in mechanical properties among samples, with UTS ranging from 72.16 to 171.86 MPa. The optimal parameters for maximizing UTS/print weight and UTS/print time were 0.4 mm infill line distance, 0.3 mm layer height, 100 mm/s printing speed, and 55°C chamber temperature.

5. Acknowledgments

This work is supported by the U.S. National Science Foundation under grant number OIA-1946231 and the Louisiana Board of Regents for the Louisiana Materials Design Alliance (LAMDA).

References

1. Penumakala, P.K., J. Santo, and A. Thomas, *A critical review on the fused deposition modeling of thermoplastic polymer composites.* Composites Part B: Engineering, 2020. **201**: p. 108336.
2. Cole, D.P., et al., *Interfacial mechanical behavior of 3D printed ABS.* Journal of Applied Polymer Science, 2016. **133**(30).
3. Almeshari, B., et al., *Development of 3D printing short carbon fiber reinforced polypropylene composite filaments.* Journal of Materials Research and Technology, 2023. **24**: p. 16-26.
4. Lobov, E., et al., *Effect of Short Carbon Fiber Reinforcement on Mechanical Properties of 3D-Printed Acrylonitrile Butadiene Styrene.* Polymers, 2023. **15**(9): p. 2011.
5. Ahmad, M.N., et al., *Application of taguchi method to optimize the parameter of fused deposition modeling (FDM) using oil palm fiber reinforced thermoplastic composites.* Polymers, 2022. **14**(11): p. 2140.
6. Kamaal, M., et al., *Effect of FDM process parameters on mechanical properties of 3D-printed carbon fibre–PLA composite.* Progress in Additive Manufacturing, 2021. **6**: p. 63-69.

Fairness-aware Point Processes

Boyang Zhang[1], Mingxuan Sun[1]

[1]Louisiana State University

Abstract: Point processes are very popular in modeling self-exciting user-item interaction events such as online check-ins, job-seeking events, and electronic records of hospital admissions. A joint modeling of point processes with coevolving user and item interests has been shown more effective for capturing the temporal dynamics. Although current studies are promising in improving event prediction accuracy, there are still critical research challenges due to data imbalances with respect to certain event groups. Unfair predictions may be generated due to data bias and can be amplified through self-excitation. In this paper, we propose a novel point process framework that incorporates dynamic coevolutionary feature embedding into the geometric structure to tackle data sparsity. We also introduce several novel fairness metrics to penalize the event likelihood function to enforce fairness. Extensive experiments on real-world datasets demonstrate that our method improves event prediction over baselines and controls the balance between accuracy and fairness effectively.

Keywords: Point Process, Fairness, Graph Convolution

1. Introduction

Human events are often recurrent and exhibit self-exciting properties. For example, in patient diagnosis events, elevated risk exists for a patient that has been recently at risk. Time intervals between consecutive events carry rich information about specific types of user-item interaction events. Point processes, which assume certain forms of inter-event correlations, have been widely used in predicting temporal events such as online check-ins, job-seeking events, and electronic records of hospital admissions [1, 2]. Despite promising examples of point processes with coevolutionary dynamics, there are still critical research challenges due to data imbalances with respect to certain user/item groups. Firstly, the coevolving dynamics driven by the occurrence of user-item interaction would fail to achieve good performance when there are insufficient interaction events for each process. In fact, a large portion of users and items have very few interaction events in many applications. For example, Netflix movie rating dataset contains 480 k users and 17 k items and most users only rate a few movies. Secondly, unfair predictions may be generated due to data bias and can be amplified through self-excitation. For example, job seeking event prediction based on interaction data may exhibit socioeconomic bias since users with frequent interaction events on LinkedIn tend to be the communities of higher socioeconomic status. To tackle these challenges, we present a novel fairness-aware point processes to strike a balance between the accuracy and fairness. Our major contributions are: (1) We learn the joint modeling of point processes with coevolutionary feature embedding to achieve higher prediction accuracy especially for processes with insufficient observations. (2) We present some novel fairness metrics for introducing user and item parity into temporal event prediction. By addin penalty terms of fairness costs to the likelihood function, our model enforces that the expected intensity over a time period for each of the user/item groups to be equal.

2. Related Work

Point processes have been widely used in various applications such as predictive policing [3, 4] and predicting recurrent online user behaviors [1, 2, 5]. High dimensional intertwined stochastic processes have been introduced to capture coevolutionary dynamics in [6, 7] to achieve promising performance. Specifically, additional features such as user features, item features, and useritem interaction features are embedded dynamically into the intensity of point processes. However, these feature driven methods do not enforce intensity smoothness over different processes sharing similar users or items. Thus, the prediction accuracy of future event occurrences decreases for users and items with very few observed interactions. Geometric convolutional network (GCN) [8] has been applied on non-Euclidean data, e.g., graphs, to extract important features. Existing studies [9–11] apply GCN to several specific tasks such as text classification, traffic forecasting, and matrix completion. Such additional geometric information represents either explicit or implicit correlations between dimensions, and extraction of these graph related features significantly enhance the performance of several learning models.

3. Model

Formally, the ordered list of all observed q events are denoted as O = {ek = (uk, ik, tk)} q k=1 in a window [0, T], where uk ∈ {1, ..., m}, ik ∈ {1, ..., n}, tk ∈ R +, 0 ≤ t1 ≤ t2... ≤ tq ≤ T. The event sequence (e.g., browsing history) of each user-item pair (u, i) can be modeled as a point process. A point process is characterized via its conditional intensity λ u,i(t), which is the expected rate of the event occurrences given the history of all events up to time t. We assume the self exiting component of the intensity function λ u,i(t) depends on the interaction of two multivariate point processes. Specifically, the intensity function for a (u, i) pair is characterized as:

$$\lambda^{u,i}(t) = \eta^{u,i} + \boldsymbol{y}_u(t)\boldsymbol{z}_i(t)^\top. \tag{3.1}$$

where η u,i ≥ 0 is the baseline intensity, yu (t) ∈ R d and zi(t) ∈ R d are the intensity functions for the user process and the item process both with latent d dimensions. We build the intensity functions yu (t) and zi(t) by graph convolutional functions defined on user and item features, which may change over time. The convolutional filters are equivalent to the coefficients of the intensity functions. The inner product of the user process and the item process captures the compatibility between a user u and an item i.

4. Experiment

Our model is evaluated on four real world datasets which include user or item features as well as temporal interactions between them. Specifically, the IPTV dataset contains 7,100 users and 436 TV programs from January to November 2012 with several program features, and some features such as genres and countries can be regarded as sensitive feature on which we will apply fairness penalty. The Yelp1 dataset is presented by Yelp dataset challenge. It contains the time stamps of writing reviews for 17k businesses by 100 users in 11 years. The Reddit2 dataset records the time stamps of posting discussions between random selected 1,000 users and 1,403 threads in January 2014. The LinkedIn dataset contains the job hopping records between 2,439 LinkedIn users and 82 IT companies. We group the users by old and young as the fairness sensitive features. We compare the state- of-art baselines with our model using the first three datasets, and evaluate the fairness on the sensitive features of IPTV and LinkedIn datasets. Following [11], we construct a user or item graph as an unweighted k-nearest neighbor graph in the space of features such as TV features. If user and item features are not available, we can apply SVD to a two dimensional user-item matrix, which is constructed from the time sequences and each entry represents the total number of user-item interactions, to get latent feature vectors for the user and item. We split all of the events on the total time T by a proportion, e.g., p = 0.76, so the events before time T · p are the training data, and the rest of them are testing data.

In LinkedIn dataset, we treat user age as the sensitive feature. The users are divided into young and old, with a 64% and 36% split. The trade-off parameter of the fairness β or γ varies in the range [0, 1, 100, 10000] in the training stage. For each value of trade-off parameter, we obtain a model which minimizes the associated regularized loss function. As the Huber fairness incorporates the MAE fairness and MSE fairness, we only demonstrate the Huber fairness and the KL fairness on IPTV dataset for item fairness and on LinkedIn dataset for user fairness. The evaluation metric of fairness loss on test set is the same as the one used in the regularizer. The relations between test set fairness and accuracy are shown in fig. 1. In the figure, y axis is MAR repr fairness loss on test set. The model becomes more fair when the fairness loss is smaller and ideally approaches 0. The prediction performance is better when the MAR is smaller and ideally approaches 1. There are four curves in total each corresponding to the model frontier using one of the two fair metric regularizers on one of the two data sets. Four markers on each curve, approximately from left to right, indicate the models trained using different trade-off parameters changing from [10000, 100, 1, 0]. Generally, as the trade-off parameter decreases, the model becomes more accurate and less fair.

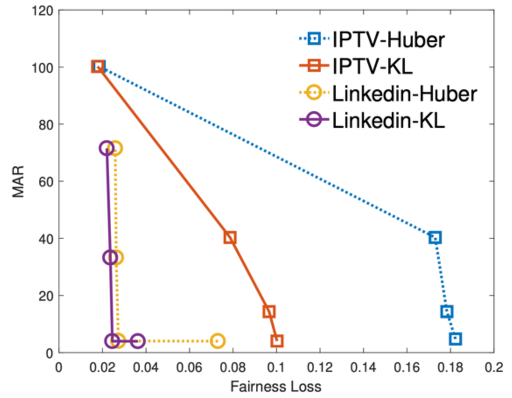

Figure 1: Trade-off between prediction and fairness of IPTV and LinkedIn datasets.

4. Conclusion

In this paper, we present an efficient point process framework that incorporates coevolving nature of feature embedding to tackle data sparsity, and introduce several novel fairness metrics that penalize the event likelihood function to enforce fairness. Extensive experiments on the real world datasets demonstrate that our method can not only benefit event prediction but also balance between accuracy and fairness.

5. Acknowledgments

This work is supported by the U.S. National Science Foundation under grant number OIA-1946231 and the Louisiana Board of Regents for the Louisiana Materials Design Alliance (LAMDA).

6. References

[1] X. Wang, R. Donaldson, C. Nell, P. Gorniak, M. Ester, and J. Bu, “Recommending groups to users using user- group engagement and time-dependent matrix factorization,” in Proc. of AAAI, 2016.
[2] H. Xu, W. Wu, S. Nemati, and H. Zha, “Patient flow prediction via discriminative learning of mutually- correcting processes,” IEEE TKDE, vol. 29, no. 1, pp. 157–171, 2017.
[3] G. Mohler, M. B. Short, P. J. Brantingham, F. P. Schoenberg, and G. E. Tita, “Self-exciting point process modeling of crime,” JASA, vol. 106, no. 493, pp. 100–108, 2011.
[4] G. Mohler, R. Raje, J. Carter, M. Valasik, and J. Brantingham, “A penalized likelihood method for balancing accuracy and fairness in predictive policing,” in Proc. of IEEE SMC, 2018, pp. 2454–2459.
[5] N. Du, Y. Wang, N. He, J. Sun, and L. Song, “Time-sensitive recommendation from recurrent user activities,” in Proc. of NeurIPS, 2015, pp. 3492–3500.
[6] M. Farajtabar, Y. Wang, M. G. Rodriguez, S. Li, H. Zha, and L. Song, “Coevolve: A joint point process model for information diffusion and network co-evolution,” in Proc. of NeurIPS, 2015, pp. 1954–1962.
[7] Y. Wang, N. Du, R. Trivedi, and L. Song, “Coevolutionary latent feature processes for continuous-time user- item interactions,” in Proc. of NeurIPS, 2016, pp. 4547–4555.
[8] M. Defferrard, X. Bresson, and P. Vandergheynst, “Convolutional neural networks on graphs with fast localized spectral filtering,” in Proc. of NeurIPS, 2016, pp. 3844–3852.
[9] Y. Li, R. Yu, C. Shahabi, and Y. Liu, “Diffusion convolutional recurrent neural network: Data-driven traffic forecasting,” in Proc. of ICLR, 2018.
[10] T. N. Kipf and M. Welling, “Semi-supervised classification with graph convolutional networks,” in Proc. of ICLR, 2017.
[11] F. Monti, M. Bronstein, and X. Bresson, “Geometric matrix completion with recurrent multi-graph neural networks,” in Proc. of NeurIPS, 2017, pp. 3697–3707.

Fracture Analysis of Additive Friction-Stir Deposited Non-Ferrous and Ferrous Alloys

Chowdhury Sadid Alam[1], Radif Uddin Ahmed[1] and M Shafiqur Rahman[1]
[1]Department of Mechanical Engineering, Louisiana Tech University, Ruston, LA 71270

Abstract: Solid-state additive manufacturing techniques like Additive Friction Stir Deposition (AFSD) are transforming metal 3D printing by enhancing efficiency, material properties, and environmental benefits. AFSD enables high-strength, fully dense non-ferrous and ferrous alloys with superior mechanical characteristics. This study examines the fatigue crack growth and fracture behaviors of AFSD-processed AA6061-T6 and 4340 steel alloys. Using numerical methods, mixed mode fracture properties and crack propagation are evaluated. Modified compact tension specimens (MCTS) subjected to tensile loads are analyzed to determine Paris Law constants. ANSYS software's SMART tool predicts crack trajectories and fatigue growth under constant amplitude loading. Numerical model results, showing stress intensity factors, crack extension, and stress deformation, are validated against experimental outcomes. A comparative analysis confirms that AFSD significantly improves mechanical properties over traditional methods, highlighting its potential for high-strength structural and repair applications in ferrous and non-ferrous alloys.

Keywords: Fracture Analysis, Crack Growth, Separative Morphing Adaptive Remeshing Technology, Finite Element, Additive Friction Stir Deposition.

1. Introduction

Additive Friction Stir Deposition (AFSD) is a cutting-edge solid-state additive manufacturing (AM) technique for creating fully dense 3D metallic structures. Unlike traditional AM methods, AFSD uses a rotating hollow tool to deposit material onto a substrate through continuous frictional interaction. The friction-generated heat plastically deforms the material without melting it, resulting in equiaxed fine microstructures and mechanical properties similar to wrought materials, with fewer defects. AFSD uniquely produces as-printed components with mechanical characteristics comparable to wrought materials. [1, 2]

Analyzing fractures and crack propagation is crucial for predicting material lifespan and safety. These studies reveal failure mechanisms under stress, helping engineers improve designs, safety standards, and prevent failures. Understanding crack initiation and propagation, especially under cyclic loading and harsh conditions, leads to more durable materials and innovative repair techniques. Recent research has focused on various aspects of metal fracture and crack propagation.

This study explores the potential of AFSD-processed ferrous and non-ferrous metals using finite element (FE) simulations. Due to the high costs of experimental fatigue analysis in different fields like aerospace and aviation, precise computational methods are needed to predict crack growth and fatigue life under static and dynamic loading [3]. A numerical model using ANSYS SMART technology was developed to analyze the influence of hole position, stress intensity factors, and fatigue life of modified compact tension specimens (MCTS) for these alloys. This research also advances the material characterization of newly developed AFSD-processed ferrous and non-ferrous metals.

2. Materials and Methods

The ferrous material analyzed is AFSD-processed 4340 steel, containing chromium, molybdenum, nickel, carbon, manganese, sulfur, and silicon. Known for its high strength, it is widely used in aerospace, defense, automotive, and manufacturing industries. The non-ferrous material is AA6061-T6 alloy, mainly composed of magnesium and silicon. This alloy is notable for its weldability, with engineering vibration during welding significantly enhancing the weld joints' hardness and tensile strength [4]. The mechanical properties of 4340 steel and AA6061-T6 alloy considered in these simulations include modulus of elasticity, Poisson's ratio, yield strength, and ultimate strength. Table 1 presents the material properties used in the fracture test simulations at room temperature (22°C) [5, 6].

The specimen selected for this study is a Modified Compact Tension Test Specimen [3]. The dimensions of the specimen (in mm) are shown in Fig. 1(a). The main hole diameter is 7 mm, positioned at horizontal and vertical distances, K and C, respectively, from the crack initiation. The simulation is performed under fatigue loading with the assumption that the tested material is isotropic and linear elastic with load ratio of R = 0.1. The SMART tool utilizes the Paris Law equation for analysing the fracture scenario in the ANSYS workbench software [3].

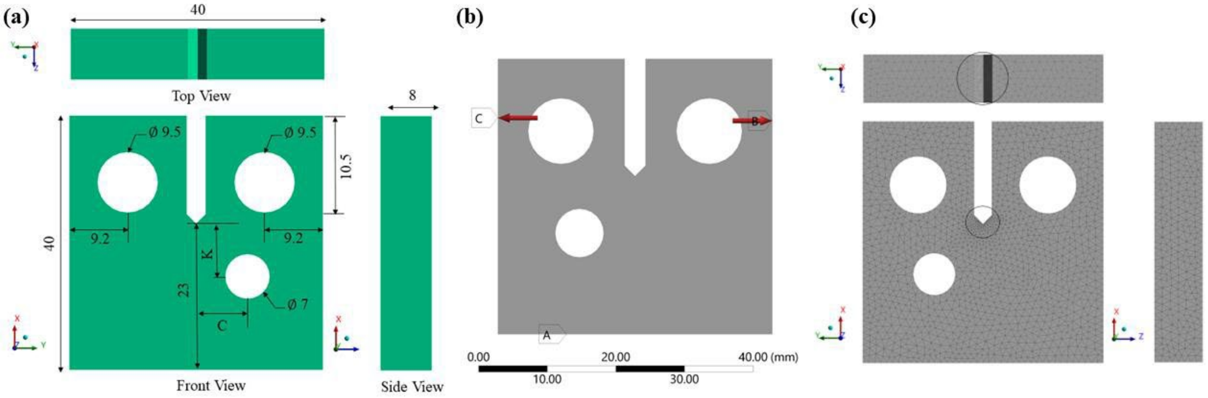

Fig. 1: (a) Modified compact tension test specimen where dimensions are in mm, (b) physical domain of the MCTS specimen, and (c) computational mesh with 1,03,431 elements

In this study, a 3-D CAD model is created in SolidWorks 2020 and imported in ANSYS Workbench 2022 R2 for the FE modeling. The physical and computational domain with the initial and boundary conditions are depicted in Fig. 1(b). Figure 3 shows the 3-D mesh of the computational domain for the ASTM E8M sub-size flat model, where 103431 quadratic elements are connected by their nodes. This is the converged mesh size which is used for the entire analysis. The mesh convergence study for the model is conducted targeting the mesh sensitivity with respect to the total deformation during fracture analysis at the room temperature.

3. Results and Discussions

The mechanical properties of metal alloys are greatly influenced by their microstructure. AFSD, as a solid-state additive manufacturing process, strain-hardens the plastic zone, producing small, equiaxed grains that improve mechanical properties. This study's FE model uses these enhanced properties to analyze fractures in 4340 steel and AA6061-T6 alloys.

3.1 Total Deformation

This study analyzes fracture and fatigue crack propagation in both regular and AFSD-processed 4340 steel and AA6061-T6 alloys. MCTS specimens are subjected to identical loads in all simulations for easy comparison. Figures 2(a) and 2(b) show the total deformation contours for AFSD-processed AA6061-T6 and 4340 steel samples.

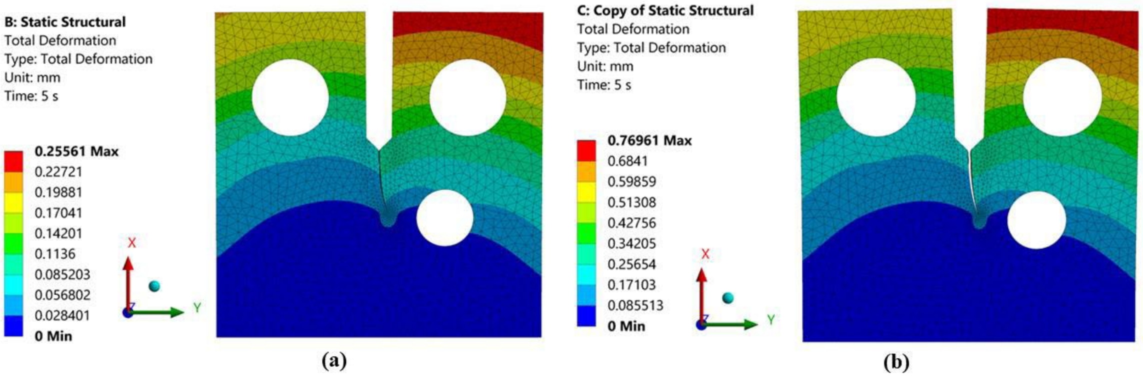

Fig. 2: Total deformation contour for AFSD processed (a) 4340 steel and (b) AA6061-T6 alloy

3.2 Crack Extension Length

The SMART fracture tool in ANSYS was used to analyze crack propagation in 4340 steel and AA6061-T6 alloy samples. Figure 3 shows the crack extensions over time using the crack extension probe feature. Under 100 MPa loads, AFSD-processed steel exhibited significantly lower crack growth, with an extension of 8.0335 mm in 5 seconds, compared AFSD-processed AA6061-T6 recording 8.1961 mm in 5 seconds with the same loading conditions. Regular metal specimens show more crack growth over time.

The AFSD process refines the microstructure into equiaxed grains, reducing defects and voids. A smaller grain size in metal alloys generally lead to a higher strength and hardness. The smaller sized grains restrict the movements of dislocation, which makes grain propagation harder and leads to enhanced mechanical properties. Moreover, equiaxed grains having similar dimensions in all direction give better isotropic mechanical properties compared to other grain shapes. Consequently, AFSD-processed specimens exhibit higher fracture strength and superior crack propagation behavior than regular ferrous and non-ferrous alloys as depicted in Fig.3.

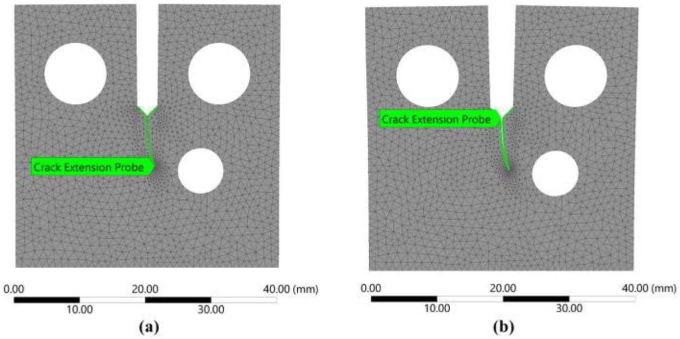

Fig. 3: Crack length extension on the AFSD-processed (a) 4340 steel and (b) AA 6061-T6 specimen

4. Conclusion

Separating Morphing Adaptive and Remeshing Technology (SMART) technique was used to create 3-D finite element model to predict crack propagation and fracture behavior of ferrous and non-ferrous alloys manufactured by the additive friction stir deposition (AFSD) process. Results for total deformation, stress intensity factor, and crack length extension with time of the AFSD-processed 4340 steel and AA6061-T6 parts provide a detailed understanding of the fracture properties of this alloy. AFSD-processed parts have higher strength and fatigue life than that of the conventionally manufactured alloys. The finite element model presented provides a faster yet reliable solution than costly experimentations. The overall study also provides a guide to investigate the mechanical and fracture properties of other high entropy materials that can be used in the AFSD process.

5. Acknowledgments

This research is supported by the National Science Foundation through cooperative agreement OIA-1541079 and the Louisiana Board of Regents.

6. References

[1] Tuncer, N. and Bose, A., 2020, “Solid-state metal additive manufacturing: A Review,” JOM, 72(9), pp. 3090–3111.
[2] Rivera, O. G., Allison, P. G., Jordon, J. B., Rodriguez, O. L., Brewer, L. N., McClelland, Z., Whittington, W. R., Francis, D., Su, J., Martens, R. L., and Hardwick, N., 2017, “Microstructures and mechanical behavior of Inconel 625 fabricated by solid-state additive manufacturing,” Materials Science and Engineering: A, 694, pp. 1–9.
[3] Alshoaibi, A.M.; Fageehi, Y.A., 2020, “Numerical Analysis of Fatigue Crack Growth Path and Life Predictions for Linear Elastic Material.” Materials, 13, p. 3380.
[4] Yogeesha, C., 2022, “Studies on Bending Properties of AA 6061-T6 Aluminium Alloy Joined By Friction Stir Welding,” ECS transactions, 107, p. 783.
[5] Kumar, A., Jayakumar, P., and Sharma, V. K., 2019, “Microstructure and properties of thermomechanically treated and bake hardened AISI 4340 steel,” Materials Today: Proceedings, 18, pp. 848–860.
[6] Sajith, S., Murthy, K., and Robi, P., 2020, “Experimental and numerical investigation of mixed mode fatigue crack growth models in aluminum 6061-T6,” International Journal of Fatigue, 130, p. 105285.

Frontal Polymerization of Thiol-Ene Free-Radical and Vinyl Ether Cationic Hybrid System

Alexandra V. Aucoin[1], Michael D. Goss[1], Jacob M. Russel[1], John A. Pojman[1]

[1]Department of Chemistry, Louisiana State University

Abstract: Frontal polymerization of mixtures containing a trithiol and a divinyl ether (in different concentrations) initiated by both a free-radical thermal initiator and a cationic superacid generator are investigated. This is the first reported study of a frontally polymerizable thiol-ene free-radical and vinyl ether cationic hybrid system. Frontal polymerization (FP) is a process in which a localized reaction zone propagates from the coupling of thermal diffusion and the Arrhenius dependence of reaction rate of an exothermic polymerization. The advantages of using FP in this system are one-pot formulations, rapid polymerization, and no additional cure times. Extremely fast fronts are produced from this reaction, and flexible polymers are formed. The reaction's kinetics and the resulting polymer's mechanical properties are studied in this report.

Keywords: frontal polymerization, thiol, vinyl ether, hybrid, copolymerization

1. Introduction

Frontal polymerization (FP) was first discovered in 1972 by Russian scientists Chechilo and Enikolopyan who defined the spreading of polymerization reactions under pressure.[1] FP is a self-sustaining exothermic polymerization reaction that proceeds directionally in a narrow reaction zone. It is a promising technique that allows the possibility of rapidly synthesizing uniform polymers and polymer networks. Pojman rediscovered FP in the early 1990s, and new studies are still emerging.[2]

Thermal frontal polymerization, the most studied form of FP, arises when thermal diffusion combines with the Arrhenius-based reaction rate dependency in exothermic polymerization. These thermal fronts can be triggered by heating devices capable of initiating initiator decomposition and subsequent heat release. Such devices include soldering irons, heat guns, and IR heaters.[3-5]

Free-radical and cationic FP hybrid polymerizations have received an abundance of attention in recent years. The principal motivation for these hybrid polymerizations has been to create a system that overcomes the boundaries of each of the individual systems.[6] A thiol-vinyl ether hybrid system would be advantageous because of the thiol's ability to produce highly uniform cross-link density networks and the vinyl ether's ability to rapidly synthesize solid polymers. In this study, we report for the first time the initial kinetic, thermal, and mechanical results for a frontally-polymerizable thiol-ene free-radical and vinyl ether cationic hybrid system.

2. Experimental

Materials - Trimethylolpropane tris(3-mercaptopropionate) (TT1) was the trithiol used in this study, and tri(ethylene glycol) divinyl ether (TEGDVE) was the divinyl ether. The thermal initiator used was Luperox 231, and the super acid generator was IOC-8. Fumed silica was added to the prepolymer to increase viscosity. These structures can be seen in Figure 1.

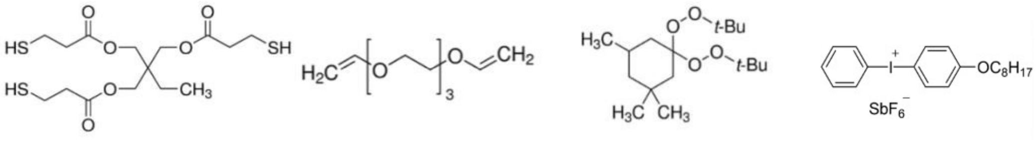

TT1 TEGDVE Luperox 231 IOC-8

Figure 1. Structures of chemicals used in this study.

Formulation Preparation - In the study of increasing thiol concentration, TT1:TEGDVE mixtures were prepared by combining the trithiol and divinyl ether based on weight percent. Each formulation was made containing a specified amount of TT1 and TEGDVE with 1 part per hundred resin (phr) of L231 and IOC-8. (Parts per hundred resin is a unit representing 1 g of material for every 100 g of resin.) IOC-8 was first dissolved in propylene carbonate in an approximate 1:1 weight ratio before adding the monomer mixture. Luperox 231 was then added to the mixture and shaken in a vortex mixture for a minute. To increase viscosity, 10 wt% fumed silica was added to the solution and hand mixed.

To prepare the formulations for the initiator studies, a 50 wt% TT1:TEGDVE solution was prepared for each sample. Varying concentrations of L231 and IOC-8 were added to the mixture, and 10 wt% fumed silica was added to increase the viscosity of the samples.

Thermally-Initiated Frontal Polymerization - The resulting resin putty was placed into a wooden mold (13.5 cm × 2 cm × 0.6 cm) lined with wax paper for easy removal. A soldering iron was heated to 200 °C and placed within the resin to initiate the front. Once the front began propagating, the soldering iron was removed, and the front propagation was observed. The fronts were recorded using a video camera placed directly above the sample with a ruler placed parallel to the sample. Front velocity was calculated from the slope of the graph of front position vs time. Front temperature was recorded using an IR camera. Triplicate experiments were performed by running three trials of three separate solutions.

Mechanical Testing – 3-point Bending - Mechanical testing was performed via 3-point bending of 50 & 60 wt% TT1:TEGDVE samples on ASTM.

3. Results

Study of Front Velocity and Temperature vs Increasing Concentration of Thiol:Vinyl Ether

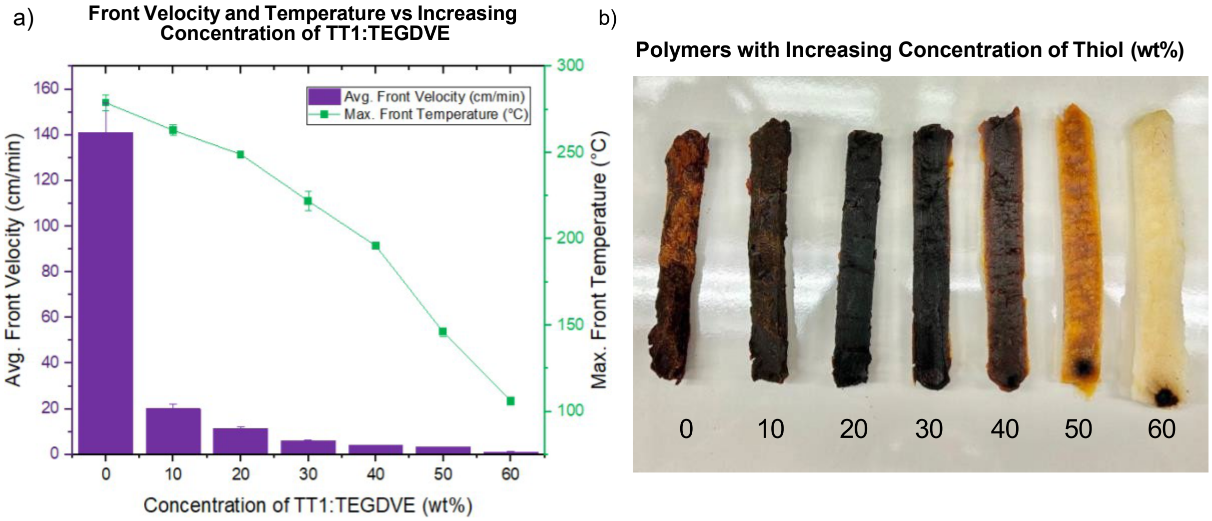
a) Front Velocity and Temperature vs Increasing Concentration of TT1:TEGDVE

b) Polymers with Increasing Concentration of Thiol (wt%)

Figure 2. a) Graph of front velocity and front temperature vs increasing concentration of TT1:TEGDVE. b) Resulting polymers of increasing concentration of thiol in increasing wt%.

Study of Front Velocity vs Initiator Concentration

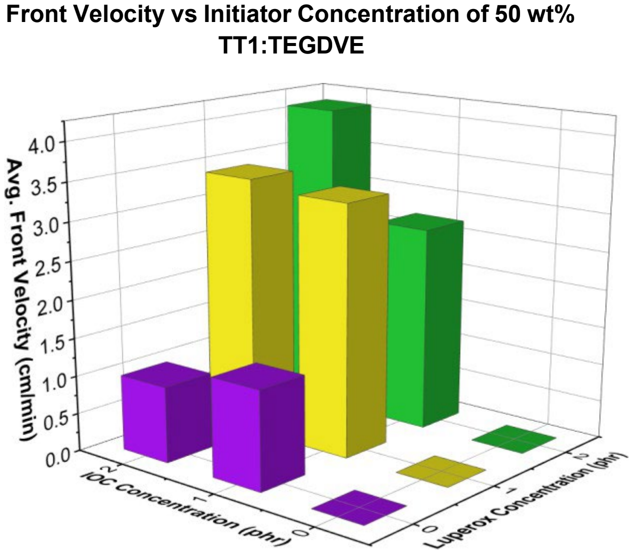
Front Velocity vs Initiator Concentration of 50 wt% TT1:TEGDVE

\

Figure 3. Front velocity vs. varying initiator concentrations (0, 1, & 2 phr) of Luperox 231 & IOC-8 on 50 wt% TT1:TEGDVE with 10 wt% FS

.Mechanical Testing – 3-point Bending

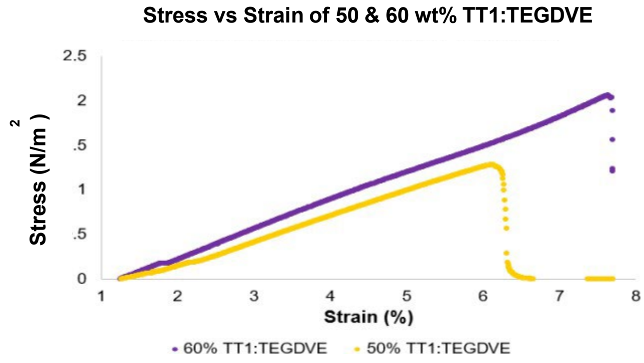

Figure 4. Stress vs. strain of 50 wt% & 60 wt% TT1:TEGDVE with 1 phr L231, 1 phr IOC-8, and 10 wt% FS.

4. Conclusion

Figure 2a depicts how the addition of thiol to a pure vinyl ether system drastically reduces both the front velocity and front temperature of the system. This suggests that the thiol is copolymerizing with the vinyl ether as opposed to just acting as an inert diluent. Figure 2b shows the change in color of the polymer as thiol concentration is increased. Figure 3 confirms that increasing initiator concentration increases front velocity and front temperature and implies front velocity depends mostly on IOC-8. Lastly, Figure 4 demonstrates that increasing thiol concentration increases polymer flexibility. Although it is an interesting system, TT1:TEGDVE is not currently suitable for industrial applications due to its poor pot-life.

5. Acknowledgments

This work is supported by the U.S. National Science Foundation under grant number OIA-1946231 and the Louisiana Board of Regents for the Louisiana Materials Design Alliance (LAMDA).

6. References

[1]] N. M. Chechilo, R. J. Khvilivitskii, N. S. Enikolopyan. *Dokl. Akad. Nuak SSSR*. **1972**, *204*, 1180-1181.
[2]] J. A. Pojman. J. Am. Chem. Soci. **1991**, *113*, 6284-6286.
[3] R. Washington, O. Steinbock. *Polym. News*. **2003**, *28*, 303-310.
[4] J. A. Pojman,. *Polym. Sci. Comp. Ref.* **2012**, *4,* 957-980.
[5] B.A. Suslick, J. Hemmer, B. R. Groce, et al. Chem Rev. **2023**, *123*, 6, 3237-3298.
[6] H. Wei, Q. Li, M. Ojelade, et al. *Macromolecules*. **2007**, *40*, 8788-8793.

High Frequency Tension-Compression Fatigue Testing of Al Alloys Prepared by Additive Friction Stir Deposition

Noushin Adibi, Ehsan Bagheri, Shengmin Guo

Department of Mechanical and Industrial Engineering, Louisiana State University

Abstract: The aim of this study is to investigate the high frequency tension-compression fatigue life of high-strength aluminum alloys. Modal analysis is first performed to study the mode shapes and natural frequencies of the materials and find the optimum specimen design for the fatigue specimens. Next, Al 2050 and 7075 parts are 3D printed by additive friction stir deposition (AFSD). Finally, the fatigue specimens are cut based on the designs obtained by the finite element analysis and are subjected to high cycle fatigue testing to evaluate the durability and reliability of the parts prepared by the AFSD technique.

Keywords: High-cycle fatigue; Additive manufacturing; Aluminum alloys

1. Introduction

Fatigue testing is employed to evaluate the durability and reliability of components subjected to cyclic loads, particularly in scenarios where safety and performance are paramount. The accumulation of small cracks due to repetitive loading leads to fatigue failures, potentially causing catastrophic outcomes. There are various types of fatigue testing methods, chosen based on factors like the intended application, loading conditions, and the test's objective [1]. High cycle fatigue testing involves exposing a component to a large number of cycles (ranging from thousands to millions or even billions) at relatively low stress amplitudes. Typically, the test specimen is standardized and shaped like a bar, wire, or disc. The goal is to determine the fatigue strength, fatigue life, and potential failure modes of the specimen under cyclic loading. The specimen undergoes alternating stress levels, causing repeated deformation and accumulation of microstructural damage, which eventually initiates and propagates cracks, leading to failure. Test parameters include stress amplitude, mean stress, and frequency, selected based on the application and conditions of the specimen. The results are plotted as stress amplitude against the number of cycles to failure, known as the stress-life curve, which provides valuable insights into the fatigue behavior and endurance limits of the material. This test is widely used in industries such as aerospace, automotive, and construction [2].

However, high cycle fatigue testing presents several challenges and limitations. Testing specimens to failure over a large number of cycles can be time-consuming and impractical for applications requiring quick results. The test duration depends on factors like the applied loading frequency, the number of cycles to failure, and the rate at which cycles are applied. Higher cycle counts necessitate lower frequencies, extending the testing time. Additionally, testing time varies by material type, with some materials failing quickly and others exhibiting longer fatigue lives. Accelerated testing methods, such as applying higher stress amplitudes or increasing the testing frequency, can reduce testing time while still providing useful fatigue data [3]. Ultrasonic fatigue testing is one such accelerated method, using ultrasonic vibrations to perform fatigue testing at high frequencies (20 kHz to several hundred kHz).

In this method, ultrasonic waves propagate through the specimen, inducing alternating compressive and tensile stresses to simulate cyclic loading. Introduced in 1950 for uniaxial tension-compression mode, it has since been developed for torsional and three-point bending multiaxial loadings.

Additive friction stir deposition (AFSD) is an innovative and promising additive manufacturing technique. As a solid-state method akin to friction stir welding, AFSD employs friction forces to generate material flow for printing. The process involves feeding a metallic rod into a rotating tool, which is then plunged onto the surface of a substrate. The heat and pressure produced by the tool cause the material to flow, enabling the part to be printed layer-by-layer. AFSD can achieve fully dense structures due to the significant pressure and heat generated during the printing process. Moreover, it results in minimal residual stress and distortion, thanks to the absence of the high thermal gradients found in other additive manufacturing techniques like powder bed fusion. One of the primary advantages of AFSD is its high deposition rate, making it an ideal manufacturing technique for reducing both time and cost. Additionally, the absence of a restrictive printing chamber allows for the production of large prints. The heat-affected zone in AFSD is smaller, and the occurrence of porosity and cracks is much lower compared to other techniques. Consequently, the physical and structural properties of parts printed using AFSD are generally superior to those produced by other methods [4, 5].

In this study, Al 2050 and Al 7075 parts were 3D printed by AFSD. Next, high frequency bending fatigue specimens are designed for both materials to align the natural frequencies with the desired testing frequency (20 kHz) using finite element analysis. The as-deposited specimens are then subjected to the test to find the durability and reliability of components. Finally, the parts are heat treated and tested to compare the properties with the as-deposited and base material.

2. Materials and methods

Wrought Al7075 and Al2050 feedstock rods, each with a cross section of 9.5×9.5 mm² and a length of 500 mm, were prepared from plates using a water jet. To prevent jamming in the tool during the process, the rods were coated with graphite prior to deposition. An AFSD machine (L3, MELD Manufacturing Co.) was used for the deposition. The material was deposited onto a substrate plate measuring 304×102×13 mm³, made of the same material as the feedstock, following the parameters listed in Table 1. Each deposited layer had a thickness of 1.5 mm, resulting in a final block with dimensions of 152.4×38.1×42.7 mm³ (length × width × height). High cycle fatigue testing was conducted using a Shimadzu USF-2000A ultrasonic fatigue tester. This machine generates tension/compression stress in a tapered/straight rod-shaped specimen through 20 kHz longitudinal wave oscillation. It includes a power supply, an ultrasonic oscillator, a booster, and a horn. The specimen is placed between the horn and a straight rod-shaped tension-compression specimen. An eddy current sensor is used to measure the amplitude at the free end of the straight rod. The ultrasonic fatigue testing setup used in this study and the principles of the test are shown in Figure 1.

Table 1. Deposition parameters used in this study

Printing Parameter	Range
Feed rate (IPM)	4-7
Traverse speed (IPM)	5-7
Spindle speed (rpm)	150-200
Substrate temperature (ºC)	Room temperature
Layer thickness (in)	0.06

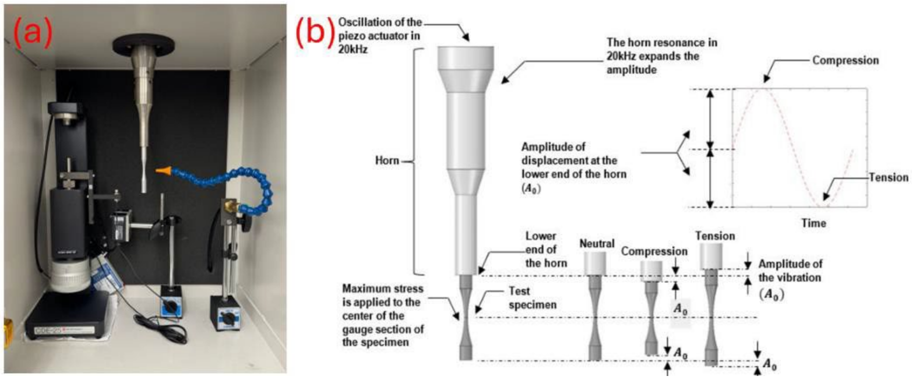

Figure 1.a. Photo of the testing setup, b. Principles of the fatigue testing [2]

3. Results and discussion

Figure 2.a shows the deposited Al 2050 part. The cross-section of the part was polished and is indicated in Figure 2.b. No defects could be found on the cross-section. The specimen arrangement for the fatigue testing is also illustrated in Figure 2.c. The specimens were cut based on this design and utilized for testing. Modal analysis was performed to study the mode shapes and natural frequencies of the specimen. The length (L) of the two sides of the specimen was changed to find out the optimum length and reach 20 kHz natural frequency. The density of Al 2050 and Al 7075 specimens were set to 2.7 and 2.81 g/cm^3, respectively. The Young's Modulus were assumed to be 76 and 71.7 GPa, respectively.

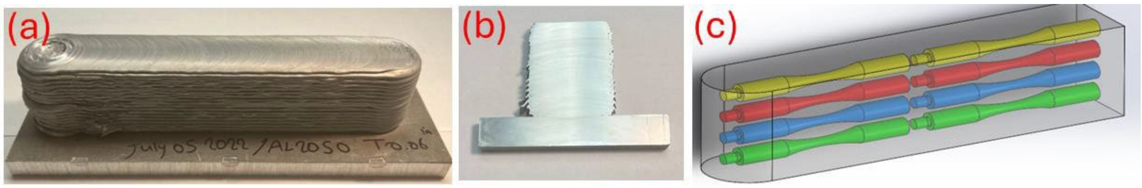

Figure 2. Photo of the as-deposited Al 2050 part, b. Polished cross section of the Al 2050 part, c. Specimen arrangement for fatigue testing

Figure 3 indicates the final element analysis results for Al 2050 and Al 7075. As can be observed, the frequencies for both alloys were close to 20 kHz. The designs display the intended and appropriate bending mode shape at the system testing frequency based on the findings from the finite element analysis. The displacement distribution throughout the specimen's length is also indicated. The corresponding designs for each alloy are depicted in Figure 4.

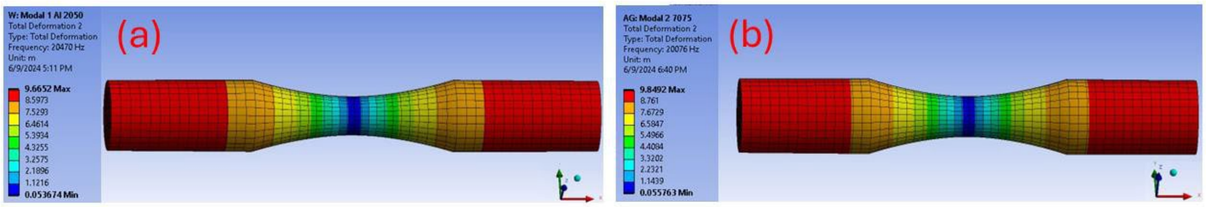

Figure 3. FEA simulation results for a. Al 2050 and b. Al 7075

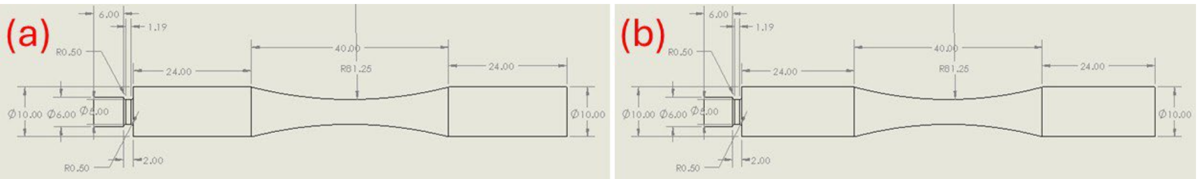

Figure 4. Final design for a. Al 2050 specimens and b. Al 7075

4. Conclusion

The purpose of this study is to explore the high-frequency tension-compression fatigue life of high-strength aluminum alloys. First, a modal analysis is performed to determine the mode shapes and natural frequencies of the materials, identifying the optimal design for the fatigue specimens. Subsequently, Al 2050 and 7075 parts are fabricated using additive friction stir deposition (AFSD). Finally, the fatigue specimens, cut based on the designs derived from finite element analysis, are subjected to high cycle fatigue testing to assess the durability and reliability of the components produced by the AFSD process.

5. Acknowledgments

This work is supported by the U.S. National Science Foundation under grant number OIA-1946231 and the Louisiana Board of Regents for the Louisiana Materials Design Alliance (LAMDA).

6. References

[1] E. Santecchia *et al.*, "A Review on Fatigue Life Prediction Methods for Metals," *Advances in Materials Science and Engineering,* vol. 2016, no. 1, p. 9573524, 2016, doi: https://doi.org/10.1155/2016/9573524.

[2] H. Ghadimi, A. P. Jirandehi, S. Nemati, and S. Guo, "Small-sized specimen design with the provision for high-frequency bending-fatigue testing," *Fatigue & Fracture of Engineering Materials & Structures,* vol. 44, no. 12, pp. 3517-3537, 2021, doi: https://doi.org/10.1111/ffe.13589.

[3] S. Stanzl-Tschegg, "Very high cycle fatigue measuring techniques," *International Journal of Fatigue,* vol. 60, pp. 2-17, 2014/03/01/ 2014, doi: https://doi.org/10.1016/j.ijfatigue.2012.11.016.

[4] H. Ghadimi *et al.*, "Hardness Distribution of Al2050 Parts Fabricated Using Additive Friction Stir Deposition," *Materials,* vol. 16, no. 3, p. 1278, 2023. [Online]. Available: https://www.mdpi.com/1996-1944/16/3/1278.

[5] J. Shao *et al.*, "Additive friction stir deposition of metallic materials: Process, structure and properties," *Materials & Design,* vol. 234, p. 112356, 2023/10/01/ 2023, doi: https://doi.org/10.1016/j.matdes.2023.112356.

High Temperature Compression Testing of Novel Complex Concentrated Alloys

Abdelrahman Garbie[1], **Jonathan R. Raush**[1]

[1]Department of Mechanical Engineering, University of Louisiana at Lafayette

Abstract: This study investigates the high-temperature mechanical performance and compositional characteristics of two newly designed Complex Concentrated Alloys (CCAs), $Cu_{42}Ni_{42}Cr_5$ and $Cu_{48.6}Ni_{36.5}Cr_{14.9}$, particularly for their suitability in additive friction stir deposition (AFSD). High-temperature compression testing revealed that $Cu_{48.6}Ni_{36.5}Cr_{14.9}$ exhibits superior yield strength and hardness across a range of temperatures compared to $Cu_{42}Ni_{42}Cr_5$, attributed to its higher chromium content which enhances solid solution strengthening and thermal stability. Energy Dispersive Spectroscopy (EDS) analysis indicated significant deviations from predicted compositions, highlighting challenges in achieving uniform elemental distribution during arc melting. The results emphasize the importance of optimizing alloy processing parameters to ensure consistent material properties. The robust performance of $Cu_{48.6}Ni_{36.5}Cr_{14.9}$, with its gradual decline in mechanical properties at elevated temperatures, demonstrates its potential for high-performance AFSD applications. This study provides insights critical for the development and practical implementation of next-generation CCAs with tailored properties for specific industrial applications.

Keywords: Complex Concentrated Alloys, CuNiCr, High Temperature Testing

1. Introduction

In this study, high temperature compression testing of newly designed Complex Concentrated Alloys (CCAs), $Cu_{42}Ni_{42}Cr_5$ and $Cu_{48.6}Ni_{36.5}Cr_{14.9}$, is conducted to explore their mechanical performance, microstructural evolution, and underlying mechanisms contributing to their exceptional properties. These alloys were selected for their suitability in additive friction stir deposition (AFSD), which combines additive manufacturing and friction stir processing to produce components with superior mechanical properties and enhanced microstructural characteristics [1]. The $Cu_{42}Ni_{42}Cr_5$ alloy, with its balanced combination of copper and nickel, provides excellent mechanical strength, ductility, and thermal conductivity. Chromium addition enhances oxidation and corrosion resistance, crucial for high-temperature applications [2]. Similarly, the $Cu_{48.6}Ni_{36.5}Cr_{14.9}$ alloy, with a higher chromium content, improves resistance to oxidation, corrosion, and wear. The higher nickel content in both alloys contributes to toughness and thermal fatigue resistance, while copper ensures good electrical and thermal conductivity. Focusing on these alloys in the context of AFSD aims to maintain structural integrity and performance at elevated temperatures. By subjecting $Cu_{42}Ni_{42}Cr_5$ and $Cu_{48.6}Ni_{36.5}Cr_{14.9}$ to high temperature compression testing, we aim to understand their deformation behavior, phase stability, and failure mechanisms under AFSD-like conditions. This understanding is crucial for optimizing compositions and processing parameters, advancing CCA-based technologies in various industrial applications. The findings will enhance knowledge of these novel CCAs and guide their practical implementation in AFSD, paving the way for next-generation materials with tailored properties for high-performance applications.

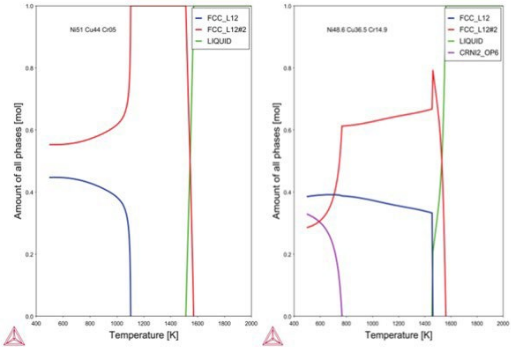

Figure 1: Volume of Phase Fraction vs Temperature for $Cu_{42}Ni_{42}Cr_5$ and $Cu_{48.6}Ni_{36.5}Cr_{14.9}$

2. Methodology

The samples for this study were synthesized at Louisiana State University (LSU) using an Edmund Buhler Arc Melter AM 500. High-purity elemental constituents were arc-melted under an inert argon atmosphere to ensure homogeneity and prevent contamination. Each sample was repeatedly melted and solidified to achieve uniform composition, then sectioned into smaller specimens for mechanical testing. A thorough inspection protocol was implemented to identify and eliminate any samples with surface defects, ensuring test result integrity. Initial mechanical properties were assessed through microhardness testing using the Buehler Micromet 5000 series in Vickers hardness mode. Each sample, prepared to a uniform height of 4mm, was subjected to a 500g load for 30 seconds, with five measurements per sample to ensure consistency. Following microhardness testing, samples were prepared for high-temperature compression testing using the MTS Alliance RF/100 system, capable of exerting up to 100kN of force. Temperature control was managed by the MTS 653.2 furnace and MTS 409.83 temperature controller, with precise measurements ensured by two Type-K Inconel 600 Flexible Thermocouples (1.6mm diameter). The furnace temperature was increased at 100°C per minute until the target temperature was reached, maintaining samples in the furnace throughout. Compression testing was conducted at the target temperature with a strain rate of 10^{-4} s^{-1}, in accordance with ASTM E9 standards. For a sample height of 4mm, this corresponded to a deformation speed of 0.024mm/min, ensuring accuracy and consistency. Post-compression, samples were carefully extracted and stored in labeled vials for further analysis. Stress and strain data were collected from the MTS system and analyzed using Excel to assess mechanical behavior. For comprehensive analysis, selected samples were sent to the Louisiana Accelerator Center (LAC) for Scanning Electron Microscopy (SEM) and Energy Dispersive Spectroscopy (EDS) using the JOEL 6460LV SEM. EDS analysis included square EDS for surface characterization, line EDS for elemental concentration variations, and EDS mapping for detailed elemental distribution, providing an in-depth understanding of the microstructural features and composition of the tested alloys.

3. Results

The yield strength of the $Cu_{42}Ni_{42}Cr_5$ alloy showed significant temperature dependence, as seen in **Figure 2-A**. At ambient temperatures, yield strength remained high across both measurement sets. However, a steep decline.

occurred as temperatures approached 600°C, then stabilized at higher temperatures. The second set showed a similar trend but with a less pronounced decrease, suggesting variance in sample processing or experimental conditions. Compression test results overlaid on this plot confirm the temperature's effect on yield strength. **Figure 2-B** shows yield strength data for the $Cu_{48.6}Ni_{36.5}Cr_{14.9}$ alloy. Initially, yield strength was high and consistent across the first three measurement sets at low temperatures. Unlike $Cu_{42}Ni_{42}Cr_5$, the decline in yield strength with increasing temperature was more gradual. The first and second sets showed a steady decrease, while the third set revealed more variability, possibly due to experimental variability or intrinsic material response heterogeneity. Yield strength values were significantly higher for $Cu_{48.6}Ni_{36.5}Cr_{14.9}$ compared to $Cu_{42}Ni_{42}Cr_5$ across all temperatures, highlighting the impact of chemical composition on thermal stability of mechanical properties. Comparing the two alloys, it is evident that the addition of higher chromium content in $Cu_{48.6}Ni_{36.5}Cr_{14.9}$ contributes to an increased yield strength at elevated temperatures, indicating an enhancement in high-temperature mechanical stability. The decline in yield strength with temperature is more pronounced for $Cu_{42}Ni_{42}Cr_5$, suggesting that the alloy composition plays a crucial role in thermal resistance. Moreover, the variance within the data sets for each alloy suggests that further investigation into processing conditions and experimental repeatability is warranted.

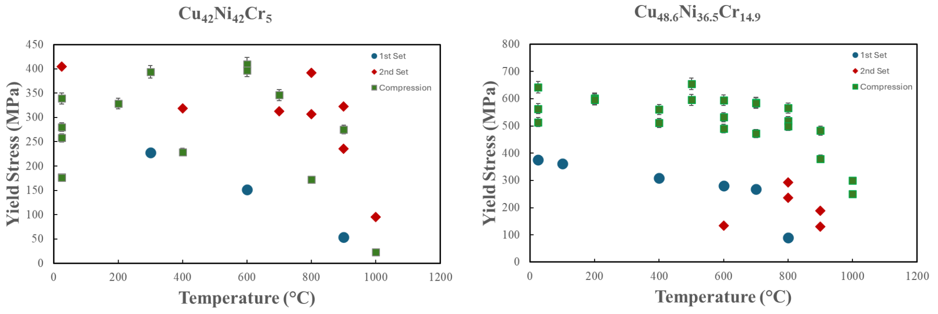

Figure 2: Yield Strength vs Temperature, including previous tensile tests (1st and 2nd Sets) for A) $Cu_{42}Ni_{42}Cr_5$ and B) $Cu_{48.6}Ni_{36.5}Cr_{14.9}$

The $Cu_{48.6}Ni_{36.5}Cr_{14.9}$ alloy consistently exhibits higher hardness values (200-270 HV) compared to $Cu_{42}Ni_{42}Cr_5$ (100-150 HV), as seen in **Figure 3**. The higher chromium content in $Cu_{48.6}Ni_{36.5}Cr_{14.9}$ enhances hardness due to increased solid solution strengthening and possible formation of harder phases. This suggests that alloy composition significantly impacts mechanical properties, with higher chromium content correlating with increased hardness. This insight is crucial for tailoring alloy compositions for applications requiring higher hardness and wear resistance.

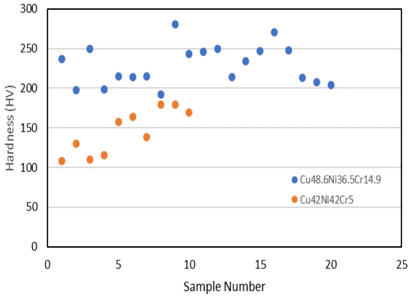

Figure 3: Averaged Hardness vs Sample (5 Hardness tests per sample)

The Energy Dispersive Spectroscopy (EDS) analysis table (**Table 1**) shows significant deviations from the predicted compositions. $Cu_{42}Ni_{42}Cr_5$, particularly in copper content ranges from 60.4% to 73.9%. This variation indicates challenges in achieving uniform composition during arc melting, potentially impacting alloy performance. For example, Sample 8 shows higher.

copper content at the top (69.0%) and side (68.3%) compared to the bottom (60.4%), suggesting segregation during solidification. Nickel content also varies, with Sample 8 (Bottom) at 35.2% and Sample 1.800 (Top) at 17.2%. Chromium content deviates from the predicted 5%, ranging from 4.3% to 9.0%. These variations highlight the need to refine the manufacturing process for more consistent alloy compositions.

Table 1: Atomic Weights of Predicted vs Actual for $Cu_{42}Ni_{42}Cr_5$

		Atomic Weights (%)		
		Cu	**Ni**	**Cr**
	Predicted	**42.0**	**42.0**	**5.0**
Actual	Sample 8 (Top)	69.0	23.4	7.6
	Sample 8 (Bottom)	60.4	35.2	4.3
	Sample 8 (Side)	68.3	23.2	8.5
	Sample 1.25 (Top)	67.8	27.6	4.6
	Sample 1.25 (Bottom)	64.8	26.9	8.3
	Sample 1.800 (Top)	73.9	17.2	9.0

6. Conclusion

The findings from this study highlight the superior high-temperature mechanical performance of the $Cu_{48.6}Ni_{36.5}Cr_{14.9}$ alloy compared to $Cu_{42}Ni_{42}Cr_5$, emphasizing its suitability for demanding applications. The higher chromium content in $Cu_{48.6}Ni_{36.5}Cr_{14.9}$ enhances solid solution strengthening and thermal stability, resulting in higher yield strength and hardness, with a more gradual decline at elevated temperatures. Conversely, $Cu_{42}Ni_{42}Cr_5$ exhibits a more pronounced decrease in yield strength with temperature, underscoring the critical role of composition in thermal resistance. Energy Dispersive Spectroscopy (EDS) analysis revealed significant deviations from predicted compositions, indicating the need for optimized processing to achieve uniform elemental distribution. These results suggest that $Cu_{48.6}Ni_{36.5}Cr_{14.9}$, with its robust mechanical properties and thermal stability, is well-suited for high-performance applications, including those requiring the precise and reliable material characteristics achievable through additive friction stir deposition (AFSD). Further research should focus on refining synthesis techniques and exploring microstructural mechanisms to enhance these alloys' properties for specific industrial uses.

5. Acknowledgments

This work is supported by the U.S. National Science Foundation under grant number OIA-1946231 and the Louisiana Board of Regents for the Louisiana Materials Design Alliance (LAMDA).

6. References

[1] "Additive friction stir deposition of metallic materials: Process, structure and properties - ScienceDirect." Accessed: Jul. 15, 2024. [Online]. Available: https://www.sciencedirect.com/science/article/pii/S0264127523007712

[2] J. Kumar, S. R. Jha, N. P. Gurao, and K. Biswas, "An Odyssey from High Entropy Alloys to Complex Concentrated Alloys," in *New Horizons in Metallurgy, Materials and Manufacturing*, A. Shrivastava, A. Arora, C. Srivastava, N. Dhawan, and S. Shekhar Singh, Eds., Singapore: Springer Nature, 2023, pp. 159–180. doi: 10.1007/978-981-19-5570-9_10.

High Pressure Study on High Entropy Alloys

Kennedy Morgan

Department of Physics, Southern University and A&M College

Abstract: High entropy alloys (HEAs) are solid, multi-elemental solution alloys with unique characteristics and a variety of projected applications. The versatile nature of HEAs has undoubtedly impacted other fields of research and continues to grow in interest as more applications and methodologies are developed, and understanding of fundamentals is refined. Over the recent decade, especially in recent years, more publications and findings are being shared and propelling more in-depth work. As the overall topic of High-entropy alloys is branching out from being an overall, abstract field, there is still much more to discover, understand and apply. This paper will give a brief summary of some recent findings and developments involving high-entropy alloys. We are also presenting some of our high-pressure study results on MoNbTaV.

Keywords: High-Entropy Alloys, X-ray Diffraction, High-pressure study

1. Introduction

High entropy alloys (HEAs) have been the subject of various studies due to their unique characteristics and applications. There have been studies done about many distinct types of alloys, such as nano-high-entropy alloys and magnetic-high energy alloys. As knowledge of high-entropy alloys continues to grow, so do the various methods utilized to study or design alloys. This paper will discuss a few of the methods that have been used within the recent climate of research. Recently, high entropy alloys (HEAs) have attracted significant worldwide attentions from researchers in materials science and engineering due to their promising applications in high temperature under extreme conditions [1-4]. As the properties of HEAs under extreme pressure are still unclear, we employed synchrotron X-ray diffraction (XRD) in conjunction with a diamond anvil cell to investigate the properties of HEAs including MoNbTiVW, MoTaTiVW, AlCoCrFeMn, etc. Here we will present some of our results on high pressure study of MoNbTaV.

2. Development in Design and Methodology

HEAs and materials exhibit behavior that is familiar to the pure materials and simple binary mixtures that we know. However, they possess convolutions that make them fascinatingly distinct. The amount of studies involving HEASs has been growing in interest since the 2010's. As studies produce findings about HEAs, the applications of these findings have impacted and involved other fields as well. There are various methods that are used in HEAs study/design, including: molecular dynamics (MD) simulations; calculation phase diagrams (CALPHAD); machine learning; and parametric approach. These methods can be used to receive valuable results, but they also have some distinct constraints. MD simulations are a set of tools used to predict the properties of simulated alloys. It is especially beneficial when studying nucleation and defect developments in the crystal lattice, however, its capacity of accuracy and predictability are countered with the high computational cost. Machine learning describes the usage of computational tools to model viable solutions in alloy design space using statistical methods. Machine learning is able to manage large databases, but the quality of the model, data and proper values directly impact the accuracy of the projections. The parametric approach is the determination of a set of parameters within quantum physical laws and assessment of a collection of criteria that prospectively leads to stable solid solutions. This method does not need experimental data, and it has high predictive capacity, in contrast, this method is computationally costly when dealing with large alloy design space. The CALPHAD method geometrically demonstrates alloys at thermal equilibrium that restrict their phase transformations in terms of particular characteristics. It is remarkably practical for studying crystal formation and solidification, which is favorable for alloy design as the minimization of the Gibbs free energy is done with the composition, temperature, and pressure. However, this method relies on a competent thermodynamic database being available. Also, lack of these databases restrain accuracy, and causes the usage of CALPHAD to be computationally expensive [5].

3. Application of Methodology

A recent paper discussed investigations of metastable high-entropy alloys, the relationship between strain rate and temperature, and phase transformation pathways. The XGBoost (extreme gradient boosting) ML model is an ML model that was developed to predict the hardness of Ti-Zr-Nb-Ta HEAs. This model combined CALPHAD method with data collected experimentally to produce a guide for the structure-property design of HEAs [6]. Like mentioned, the characteristics involved with the CALPHAD method are composition, temperature, and pressure. Investigating the nature and ability of HEAs is important, and due to lack of certainty about the effects of high pressure, the effects of high pressure were observed on the MoNbTaW alloy. By only manipulating certain characteristics of the environment, the CALPHAD method was utilized in research to investigate the formation of carbides with this compositionally complex alloy (CCA), and what would happen to the alloy, if anything [7].

Investigations were done to observe C-MoNbTaW alloy under elevated temperature and high pressure, and it was found that the sample had phase stability under elevated temperatures and pressures up to 870 C and 3.1 GPa respectively. X-ray diffraction (XRD) patterns were used to observe the phase stability of C-MoNbTaW under high pressure and temperature, and by using DAC XRD at room temperature under 3.1 GPa of pressure, it was shown to have BCC and FCC phases, thus supporting that the Carbon doped alloy was stable under these extreme conditions [7]. The FCC phases were found to be the carbides of the MoNbTaW alloy, resulting from the interaction between the refractory metals and carbon in stearic acid during the high-entropy mixing, ball milling process [7-8]. Understanding the nature of HEAs in extreme conditions is important, especially if one wants to use the alloy to produce materials [9]. By learning that the alloy can withstand elevated temperatures, it gives room to investigate the nature of the alloy in high pressure.

As far as our research on HEAs is concerned, we employed the BL-12-2-2 facility in Lawrence Berkley National Laboratory (LBNL) to investigate our samples. The BL-12-2-2 facility is equipped with state-of-the-art equipment such as high-resolution synchrotron X-ray, diamond-anvil cell, resistor and laser heating, IR/Raman/Brillouin spectroscopy, sample assembling lab, alignment tools and Oxford Laser Micro Drilling to help our experiment in LBNL. Figure 1 shows the beamline 12.2.2 (BL-12-2-2) endstation in LBNL, Berkeley, California, USA. Figure 2 shows the diamond-anvil cell (DAC) device used to get the x-ray diffraction in our experiments. Figure 3 shows the XRD setup control of the facility. We investigated the XRD pattern of MoNbTaV under the pressure of up to 41.8 GPa (Figures 4(a)-(c) shows the XRD we obtained under 9.8 GPa, 19.4 GPa and 41.8 GPa, respectively). Detailed data analysis and discussion will be presented in a separate paper.

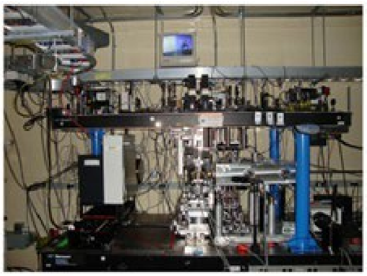

Figure 1. The Beamline 12.2.2 endstation.

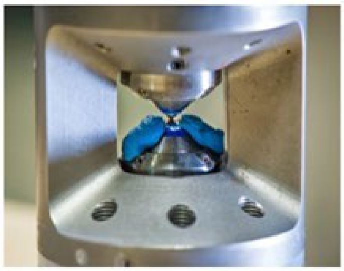

Figure 2. A radial diamond-anvil cell.

Figure 3. XRD setup control

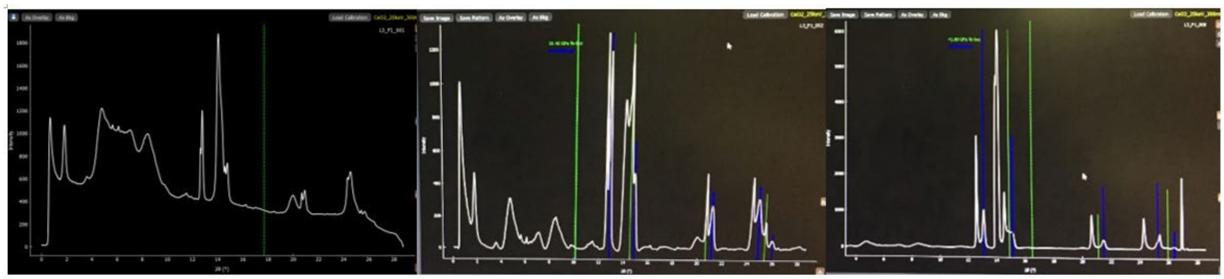

(a) (b) (c)

Figures 4 XRD of MoNbTaV under (a) 9.8 GPa, (b) 19.4 GPa and (c) 41.8 GPa, respectively.

4. Conclusion

HEA research is an extremely broad field where new applications and understandings are developing. As interest in this topic grows, scientists are able to better refine the understanding, projections, and usage of HEAs. As practices and findings continue to come out, molecular dynamics (MD) simulations, the CALPHAD method, machine learning, and parametric method are all commonly used within research into alloy design, characteristics and more. Each of these methods has their strengths and weaknesses and are being further explored as increasing interest in the properties and applications of high entropy alloys continues to grow. We performed XRD study on MoNbTaV under a high pressure of up to 41.8 GPa. In this paper, we presented the XRD pattern of MoNbTaV under the pressure of 9.8 GPA, 119.4 GPA and 41.8 GPA, respectively. Detailed results and discussions on the high pressure study of MoNbTaV will be presented separately.

5. Acknowledgments

This work is supported by the U.S. National Science Foundation under grant number OIA-1946231 and the Louisiana Board of Regents for the Louisiana Materials Design Alliance (LAMDA).

6. References

[1] Cantor B., Chang I.T.H., Knight P., Vincent A.J.B., Microstructural development in equiatomic multicomponent alloys, Mater. Sci. Eng. A, 375–377 (2004), 213-218.
[2] Chen T.K., Shun T.T., Yeh J.W., Wong M.S., Nanostructured nitride films of multi-element high-entropy alloys by reactive DC sputtering, Surf. Coat. Technol., 188–189 (2004), 193-200.
[3] Hsu C.Y., Yeh J.W., Chen S.K., Shun T.T., Wear resistance and high-temperature compression strength of FCC $CuCoNiCrAl_{0.5}Fe$ alloy with boron addition, Metall. Mater. Trans. A, 35A (2004), 1465-1469.
[4] Huang P.K., Yeh J.W., Shun T.T., Chen S.K., Multi-principal-element alloys with improved oxidation and wear resistance for thermal spray coating, Adv. Eng. Mater., 6 (2004), 74-78.
[5] Nonato, R. B. P., & Restivo, T. A. G.. A Brief Review on High Entropy Alloys (HEAs). V Seven International Multidisciplinary Congress (2024).
[6] Liu, X., Banerjee, R., Vitos, L., & Wang, Y., Metastable high entropy alloys. Applied Physics Letters, 120(12) (2021).
[7] Zhang, C.; Bhandari, U.; Lei, J.; Zeng, C.; Guo, S.; Choi, H.; Nam, S.; Yan, J.; Yang, S.; Gao, F., Performance of Carbide Alloy Compounds in Carbon Doped MoNbTaW. Crystals 11, (2021), 1073.
[8] Yonggang Yao et al., Carbothermal shock synthesis of high-entropy-alloy nanoparticles. Science 359, (2018) 1489-1494.
[9] Gao, M., Qiao, J.. High-Entropy Alloys (HEAs). Metals, 8(2), (2018), 108.

Integrated Computational Material Engineering Study of Flexural and Tensile Properties of Cu-Ni-Cr Alloy

Abyaz Abid, Hamid Sharifi, Chowdhury Sadid Alam, Pouria Nourian, Collin Wick, M Shafiqur Rahman

Department of Mechanical Engineering, Louisiana Tech University

Abstract: Copper-nickel-chromium alloys are highly valued for their versatile properties such as corrosion resistance, electrical conductivity, thermal stability, and mechanical strength, making them essential in marine engineering, electronics, and aerospace applications. However, there exists a major research gap in mechanical characterization of the 3D-printable Cu-Ni-Cr alloy due to its novelty and lack of experimentation. This study focuses on the characterization of a novel Cu(51)Ni(44)Cr(5) alloy, particularly its mechanical properties under bending and tensile tests. Utilizing an Integrated Computational Material Engineering (ICME) approach, the study combines Molecular Dynamics (MD) simulations and mesoscale finite element (FE) modeling to predict the alloy's behavior. The results provide insights into the alloy's potential applications in various manufacturing industries, aiming to enhance its utilization in additive manufacturing.

Keywords: Additive Manufacturing, Integrated Computational Mechanical Engineering, Molecular Dynamics, Finite Element, Tensile, Flexural

1. Introduction

The Cu-Ni-Cr alloy is extensively used in many manufacturing industries such as aerospace, automotive, and electronics to produce engine components, heat exchangers, structural elements, circuitry, heat sinks, and electrical connectors and contacts due to its exceptional properties such as high strength, excellent thermal and electrical conductivity, and wear and corrosion resistance. The alloy's compatibility with AM processes enables the production of complex, high-performance components across all these industries, thus enhancing product design, reliability, and cost-effectiveness [1]. There is a significant research gap in the mechanical characterization of the alloy due to its recent development and limited experimentation. A physics-based computational analysis, utilizing an accurate material model and a well-defined mechanical characterization model, is needed to address this. This study aims to explore the mechanical properties of a newly proposed Cu(51)Ni(44)Cr(5) alloy, which has shown potential for use in additive friction stir deposition (AFSD), using bending and tensile tests. This is done via an Integrated Computational Material Engineering (ICME) approach [2] supported by MD simulations and FE modeling. The combination of MD and FE simulations facilitates the design and optimization of materials by providing a detailed understanding of the relationships between atomic-level structures and macroscopic properties, allowing for the targeted design of materials with desired properties.

2. Material and Methods

The study employs MD simulations to predict the mechanical properties of the Cu(51)Ni(44)Cr(5) alloy. Two systems containing 11,520 atoms with FCC crystal structures were created: one for the composition with available experimental data, Cu(75)Ni(19)Cr(6), and the other for the proposed composition, Cu(51)Ni(44)Cr(5). These systems were minimized using a Monte Carlo scheme [3] to develop secondary phases and obtain stable structures. Afterwards, by subjecting the materials to shear stress (Figure 1.b), the yield strength and elastic modulus of Cu(51)Ni(44)Cr(5) was found to be 5.844 and 230 GPa, respectively. The simulations were conducted using LAMMPS. The yield strength and elastic modulus of Cu(75)Ni(19)Cr(6) was compared with those found in the literature [4] to ensure the accuracy of the simulations. The stress-strain curves for both systems were analyzed to determine the yield strength and elastic modulus (Figure 1.a).

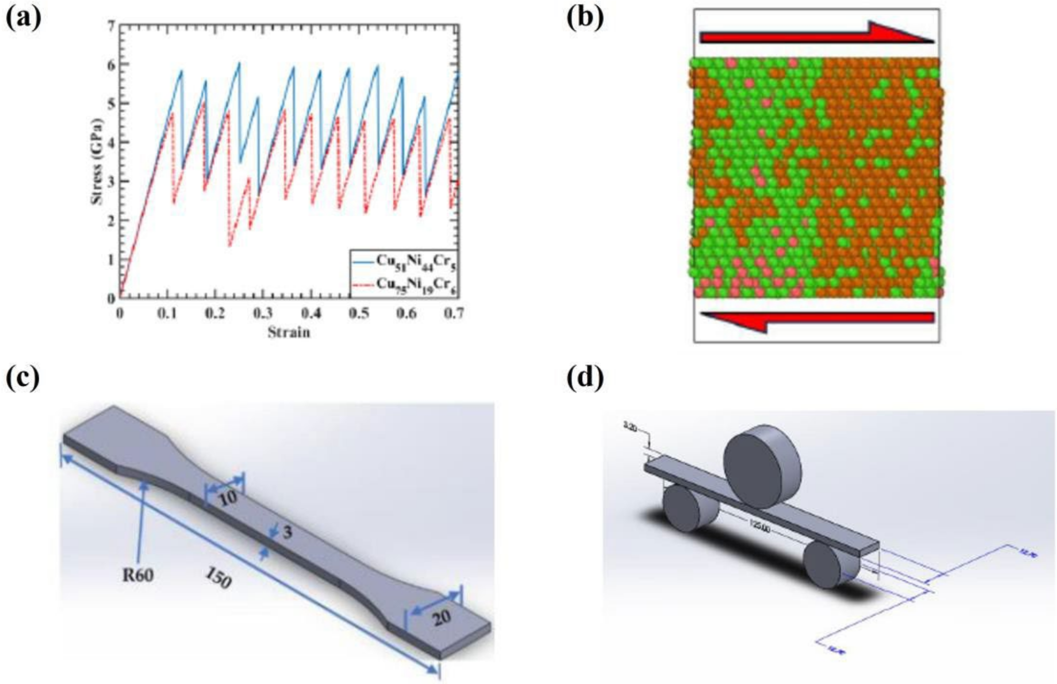

Figure 1. (a) Shear stress-strain curve for curve Cu(75)Ni(19)Cr(6) and Cu(51)Ni(44)Cr(5), and (b) schematic of the structures under shear loading (c) physical domain of an ASTM D3039M subsize flat dog bone specimen, and (d) physical domain of an ASTM D790 three point bending specimen

Two 3D computer-aided design (CAD) models based on the ASTM D3039M and ASTM D3039M standards were created using SolidWorks 2022 (Figures 1.c and 1.d, respectively) and imported into ANSYS Workbench 2021 R2 for FE analysis. The physical and computational domains were defined, and boundary conditions were applied. The tensile test simulation involved applying axial force to a dog bone-shaped specimen, while the three-point bending test used a roller to apply force. Mesh convergence studies were conducted by plotting the ultimate tensile strength vs the number of elements to find the plateau and consequently, the optimal number of elements, ensuring the accuracy of the simulations. The ultimate tensile strength and yield strength of alloy at room temperature obtained from the simulations are compared with numerical results from previous research [1][5], and the discrepancies were less than 10% in both cases.

3. Results and discussion

The simulations provided data on total deformation, stress-strain outcomes, and safety factors.

3.1 Tensile Properties

The tensile test results (Figure 2) showed the distribution of equivalent von Mises stress in the specimen, with stress concentrations near the middle or points of imperfections, with a maximum of 524.45 MPa. The equivalent elastic strain distribution indicated high strain areas around the middle of the specimen. The total deformation plot showed maximum deformation around the middle, where the tensile stress was concentrated.

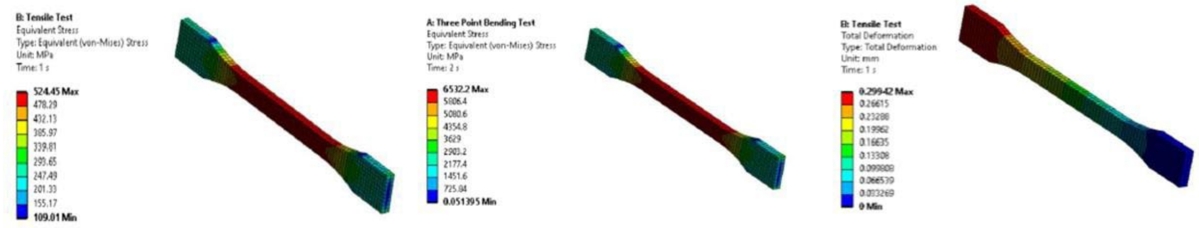

(a) (b) (c)

Figure 2. Representative FE results for the (a) equivalent von Mises stress, (b) equivalent elastic strain, and (c) equivalent total deformation in tensile test of the ASTM D3039M specimen

3.2 Flexural Properties

The three-point bending test results (Figure 3) depicted the von Mises stress distribution, with high stress concentrations near the load application point. The equivalent elastic strain distribution showed high strain areas near the bending points. The total deformation plot indicated maximum deformation at the center, where the bending moment was highest.

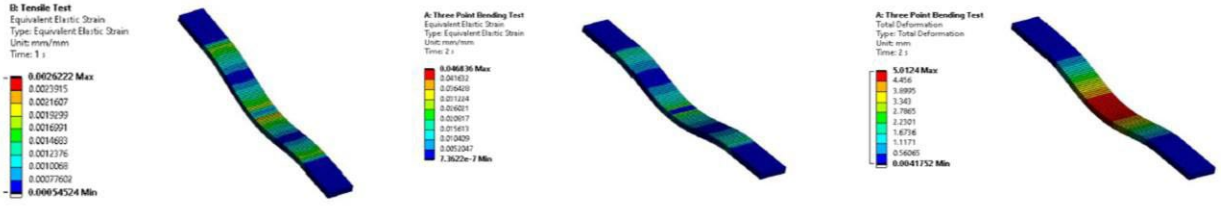

(a) (b) (c)

Figure 3. Representative FE results for the (a) equivalent von Mises stress, (b) equivalent elastic strain, and (c) equivalent total deformation in bending test of the ASTM D3039M specimen

3.3 Safety Factor Analysis

The safety factor analysis for the tensile test showed a steep decline in the safety factor with increasing force in both tensile and bending tests, indicating high sensitivity to initial stress applications. The safety factor approached near-zero values beyond 60 kN in tensile test.

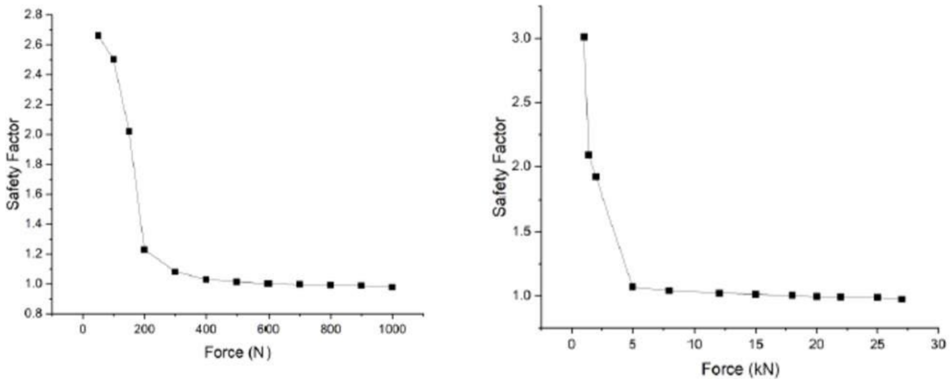

Figure 4. Safety factor analysis results for the (a) tensile test and (b) bending test specimens

3. Conclusion

In this study, an integrated computational mechanical engineering approach, which combines the MD simulations with FE method, is successfully employed provides to systematically analyze the stress distribution, deformation characteristics, and safety factors for the 3D-printable Cu(51)Ni(44)Cr(5) alloy under tensile and flexural loads. The results highlight critical stress concentrations and deformation patterns, guiding material formulation and structural design improvements. The findings offer valuable insights into the alloy's mechanical performance, paving the way for its optimized use in additive manufacturing. Future research should focus on experimental validation of the computational results and explore further applications in industry.

4. Acknowledgments

This work is supported by the U.S. National Science Foundation under grant number OIA-1946231 and the Louisiana Board of Regents for the Louisiana Materials Design Alliance (LAMDA).

5. References

[1] Z. Fu, X. Tian, W. Chen, B. Hu, and X. Yao, “Analytical modeling and numerical simulation for three-roll bending forming of sheet metal,” Int. J. Adv. Manuf. Technol., vol. 69, no. 5–8, pp. 1639–1647, 2013

[2] W. Y. Wang, J. Li, W. Liu, and Z. Liu, ‘Integrated computational materials engineering for advanced materials: A brief review,” Comp. Mat. Sci., vol 158, p 42-48, 2019

[3] K. T. Chen et al., “Mechanical properties and deformation mechanisms in CoCrFeMnNi high entropy alloys: A molecular dynamics study,” Mater. Chem. Phys., vol. 271, p. 124912, 2021

[4] S. I. B. Syed Abdullah, S. K. Bokti, K. J. Wong, M. Johar, W. W. F. Chong, and Y. Dong, “Mode II and mode III delamination of carbon fiber/epoxy composite laminates subjected to a four-point bending mechanism,” Compos. Part B Eng., vol. 270, p. 111110, Feb. 2024

[5] J. W. Nader, H. J. Dagher, R. Lopez-Anido, F. El Chiti, G. N. Fayad, and L. Thomson, “Probabilistic finite element analysis of modified ASTM D3039 tension test for marine grade polymer matrix composites,” J. Reinf. Plast. Compos., vol. 27, no. 6, pp. 583–597, 2008

Inverse Machine Learning Framework for Optimizing Plate-lattice Structures

Amir Teimouri[1], Guoqiang Li[1]

[1] Department of Mechanical & Industrial Engineering, Louisiana State University

Abstract: Shape memory polymers (SMPs) are a class of smart materials that due to their advantages like shape recovery, high deformability, and high strength have considerable applications in various engineering fields. In this study, a novel inverse design framework has been developed to optimize thin-walled lattice structures (TWLSs) with superior stress recovery. This framework is a combination of a deep neural network and conditional generative adversarial networks. The developed deep neural network has 98% and 99% accuracy in predicting the compression strength and mass of TWLSs, respectively. Moreover, through twenty iterations the inverse design framework optimized the average specific compression strength (SCS) of TWLSs by 68%. The inverse design framework has the potential to be utilized in optimizing the structure of diverse designs and applications.

Keywords: Plate-lattice structures, Metamaterials, Machine learning, shape memory polymer, Conditional generative adversarial networks

1. Introduction

In recent years, the field of 4D printing has emerged as a revolutionary technology in the realm of polymers (1, 2). Unlike traditional 3D printing, which focuses on creating static objects, 4D printing adds an extra dimension of time, enabling printed structures to transform and adapt to their environment. This transformative capability is achieved through the integration of shape memory polymers (SMPs). SMPs possess a unique property that allows them to "remember" a particular shape and then revert back to that shape when subjected to certain stimuli, such as heat or light (3).

The shape memory effect in polymers opens up a myriad of possibilities for applications ranging from biomedical devices to aerospace engineering (4, 5). Several strategies have been developed to improve stress recovery in SMPs. As a case in point, the incorporation of nanoparticles/fillers such as carbon nanotubes or silica can significantly increase stress recovery (6). Furthermore, the effect of thermal cycling on stress recovery was also studied, outlining that shape recovery improves by 9% through three thermomechanical cycles (7). Since having high-stress recovery has a decreasing effect on the strain recovery of SMPs, discovering novel lightweight metamaterials with high specific shape recovery has become a captivating focus of research. Metamaterials can be divided into various types based on their functionality, structural design, and composition. Since material distribution in thin-walled structures is efficient, these structures have light weight and high load-carrying capacity while maintaining structural integrity.

In this study, a novel inverse design framework has been developed to optimize thin-walled lattice structures (TWLSs) with superior stress recovery. This framework is a combination of a deep neural network and conditional generative adversarial networks. The developed deep neural network has 98% and 99% accuracy in predicting the compression strength and mass of TWLSs, respectively. Moreover, through twenty iterations the inverse design framework optimized the average SCS of TWLSs by 68%.

2. Methods

2.1 Automated simulations

FEM using ABAQUS has been utilized in this investigation to simulate thin-walled structures. The aim of this numerical analysis is to take fingerprints as input, generate the model based on the present walls in the lattice structure, and calculate the SCS and mass of each structure. The amount of data plays a crucial role in machine learning as it directly impacts the model's performance and generalization ability. Adequate data is essential to capture the underlying patterns and relationships, reducing the risk of overfitting and improving the model's accuracy. Insufficient data can lead to poor model performance, while a larger and more diverse dataset can enhance the model's robustness and enable more reliable predictions. Therefore, 2000 randomly generated fingerprints using the Mersenne Twister algorithm have been given as an input file to a novel PYTHON script to generate, submit, and post-process each TWLS to print the calculated mechanical properties in an output file.

2.2 Dataset generation and fingerprinting for TWLSs

Using deep neural networks is a powerful technique in predicting the output, based on the given input parameters. Based on the number of independent variables affecting the output, the number of required training data changes. Deep neural networks need larger training datasets as the number of independent variables increases. In this section, we outline the strategy employed to generate our dataset for predicting the mechanical properties of thin-walled lattice structures.

In the proposed TWLS, there are 20 various kinds of walls with different orientations. Each of these walls has a specific position in its fingerprint array. Fingerprints are arrays of 20 binary digits that indicate 20 walls in one-eighth of a representative volume element (RVE). As the position of the walls in the RVE is fixed, each TWLS can have a unique fingerprint. After one-eight of the RVE is ready, it must be mirrored with respect to various directions of the 3D coordinate system.

2.3 Deep neural network prediction

To improve the shape recovery of SMPs, structures should have high stress recovery which leads to high stiffness in the rubbery state. The goal of this study is to find optimum TWLSs with high recovery stress. Due to the substantial size of the dataset involved in this investigation, experimental and numerical analysis of each structure is an expensive and time-consuming project as discussed earlier. Consequently, a deep neural network has been developed to predict the compressive strength and mass of each structure. Fingerprints are given as the input parameters to the network and their corresponding compressive strength and mass are the output of the network. The DNN architecture was constructed using the Keras library, with sequential layers consisting of dense units. Several activation functions were examined to train the model and finally, ReLu function was selected due to the enhanced level of accuracy. The input features were processed and normalized using the MinMaxScaler from the scikit-learn library to ensure consistent scaling across the dataset. The dataset was then divided into training (85%) and testing (15%) sets for model evaluation.

To facilitate the learning process, the DNN model utilized the mean squared error loss function and the Adam optimizer with a learning rate of 0.0001. The model was trained over 800 epochs with a batch size of 100, enabling it to capture complex relationships within the data and optimize the prediction accuracy. Throughout the training process, the model was evaluated using various metrics such as mean squared error, mean absolute error, and R-squared score. The R-squared score of the DNN for predicting compression strength and mass of TWLSs were 98% and 99%, respectively.

2.4. Optimization using CGANs

CGANs are a class of deep learning models that combine the power of generative models with the ability to control their output. They introduce a conditional component, allowing users to specify desired attributes or characteristics for the generated samples. CGANs consist of a generator and a discriminator that engage in a game-theoretic competition. The generator aims to produce authentic fingerprints that match the specified conditions (superior SCS), while the discriminator learns to distinguish between real and generated fingerprints. CGANs try to find the optimum structures in an iterative process, while gradually getting better fingerprints in terms of SCS as input parameters. In the first iteration, the CGANs were given 10000 unique fingerprints to be trained and generate new fingerprints. Then, the SCS of each new fingerprint is predicted using the trained DNN. Fingerprints are sorted in terms of SCS and for the next iteration, the framework is given by the top 30% of the fingerprints with higher SCS. In every iteration, the average SCS of the generated fingerprints are calculated. Optimization will continue until reaching a stable range of SCS. Fig. 1 indicates that after 20 iterations the average SCS of TWLSs was increased by 68%.

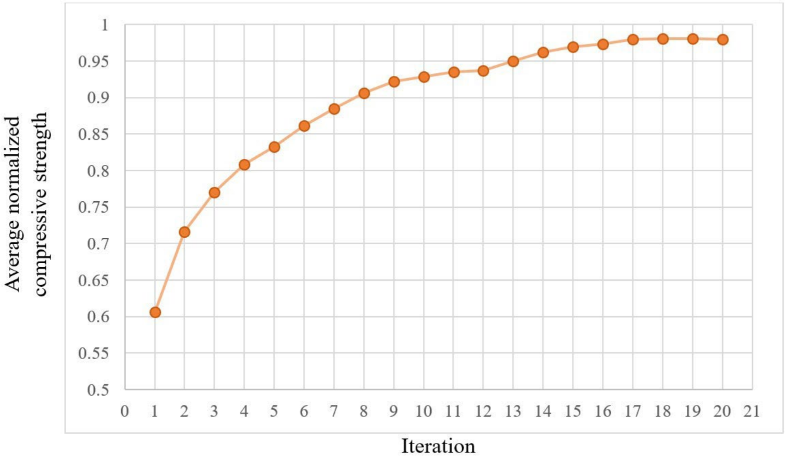

Fig. 1. The normalized average specific SCS with respect to number of iterations.

3. Conclusion

In this study, the SCS of shape memory TWLSs have been investigated. A DNN and CGANs were combined to develop a novel inverse design framework to find the optimum TWLSs with superior compressive strength. An automated ABAQUS Python script was developed to simulate 2000 structures to extract input (fingerprints) and outputs (compression strength and mass) for the machine learning models. Using the manual method, it takes approximately thirty days to simulate 2000 TWLSs, while the novel Python script decreased this time by 88% to roughly 84 hours. Moreover, the inverse design framework was used to optimize the SCS of TWLSs. After twenty iterations, the average SCS of the fingerprints reached a stable range. Results indicate that after 20 iterations the average SCS of TWLSs was in increase by 68%.

5. Acknowledgments

This work is supported by the U.S. National Science Foundation under grant number OIA-1946231 and the Louisiana Board of Regents for the Louisiana Materials Design Alliance (LAMDA).

6. References

1. Momeni F, Liu X, Ni J. A review of 4D printing. Materials & design. 2017;122:42-79.
2. Sydney Gladman A, Matsumoto EA, Nuzzo RG, Mahadevan L, Lewis JA. Biomimetic 4D printing. Nature materials. 2016;15(4):413-8.
3. Meng H, Li G. A review of stimuli-responsive shape memory polymer composites. polymer. 2013;54(9):2199-221.
4. Zhao W, Yue C, Liu L, Liu Y, Leng J. Research progress of shape memory polymer and 4D printing in biomedical application. Advanced Healthcare Materials. 2023;12(16):2201975.
5. Singh M, Gulamabbas T, Ahumuza B, Singh N, Mishra V. Electroactive Polymeric Shape Memory Composites for Aerospace Application. Aerospace Polymeric Materials. 2022:189-210.
6. Subbaroy Sarma G, Chavali M, Nikolova MP, Tripati GK. Effect of Nano and Hybrid Fillers on Shape-Memory Polymers Properties. Shape Memory Composites Based on Polymers and Metals for 4D Printing: Processes, Applications and Challenges: Springer; 2022. p. 213-51.
7. Staszczak M, Nabavian Kalat M, Golasiński KM, Urbański L, Takeda K, Matsui R, et al. Characterization of polyurethane shape memory polymer and determination of shape fixity and shape recovery in subsequent thermomechanical cycles. Polymers. 2022;14(21):4775.

Investigating the Effect of Hydrogen Concentration on Hydrogen-assisted Cracking of Boiler Material Using a Simple Yet Robust 2D Phase-field Model.

Edem Doe Honu[1], Congyuan Zeng[1], Patrick Mensah[1]

[1]Department of Mechanical Engineering, Southern University and A & M College

Abstract: The phase-field modeling approach supplants conventional discrete finite element modeling by providing a robust approach for modelling arbitrarily complex crack topologies based on Griffith's theory and continuum mechanics. In this study, a robust phase-field method is implemented by means of Abaqus user subroutines to investigate the effect of hydrogen concentration on the crack evolution and mechanical properties of boiler steel subjected to uniaxial tension. Deformation, phase field fracture, and hydrogen mass transport problems are modeled accordingly and solved in a staggered scheme for displacement, phase field evolution, and hydrogen concentration. The results showed that hydrogen concentration can result in a drastic reduction in the notched tensile properties of a material. Additionally, the accumulation of hydrogen in the fracture process zone was also consistent with theoretical models. Future works seek to explore the effect of temperature, meshing (in the fracture process zone), and varying mechanical loading conditions on crack evolution and mechanical properties.

Keywords: hydrogen embrittlement, phase-field model, boiler materials, hydrogen, Abaqus user subroutine.

1. Introduction

Phase-field modeling has garnered significant attention as a powerful computational tool, providing a diffuse-interface approach for simulating complex crack topologies. This method excels at accurately simulating phenomena such as crack branching and microcracks, addressing the shortcomings of discontinuity-based methods that rely on conventional discrete finite element methods [1]. It employs a variational mathematical approach that builds upon the fundamental understanding of crack formation based on Griffith's formulation and on continuum-based damage mechanics by defining a damage variable called the phase field parameter [2]. The model has shown great promise for modeling hydrogen-assisted fractures, showing remarkable agreement with experimental data [2-3].

In this study, we present a straightforward yet robust 2-dimensional (2D) implementation of the phase field model using the ABAQUS user subroutine. This work adapts the previous research of Martinez-Paneda [2] to parametrically determine the effects of hydrogen concentration on the evolution of hydrogen-assisted cracks and the notched tensile properties of a selected steel-based material commonly used for critical boiler drums. For our investigation, the material surface and diffuse crack topology are numerically modeled in terms of the phase field variable and displacement variable. Similarly, governing balanced equations regarding bulk stored and surface energies of the material are also modelled as functions of the displacement variable and the phase field parameter. Fick's diffusion law is extended to model the hydrogen diffusion into the material. Lastly, the mechanical deformation, the phase-field fracture, and the hydrogen transport problems are solved for displacement, phase field evolution, and hydrogen concentration.

2. Numerical Formulation

Considering that a physical crack in a solid (Ω) is an internal discontinuity expressed as Γ, the diffused crack functional in multi-dimensions (describing the crack surface) over the entire volume of the solid, can be expressed as function of the phase field parameter as

$$\Gamma(p)=\int_{\Omega}\left(\frac{1(p)2}{2l}+\frac{l}{2}|div|^{2}\right)dv \tag{1}$$

where p is the smooth phase field crack parameter expressed as: $p(x) = e^{\frac{-|x|}{l}}$ (2)

l represents the length scale parameter, which describes the width of the diffused (smear) phase-field function or, in other words, the degree of diffusion or smoothness of the crack. Hence, as *l* approaches 0, the discrete sharp crack topology approximation is also automatically accounted for [1-2].

The total potential strain energy of the solid can be defined in terms of the displacement (u) and p as the sum of the bulk energy of the solid and the surface energy associated with the crack formation. This is expressed mathematically as:

$$\psi(u,p) = \int_{\Omega}\{[(1-p)^{2} + k)](\Psi)_{0}(\varepsilon) + G_{c}(\theta)(\frac{1(p)2}{2l} + \frac{l}{2}|\Delta|^{2})\}dv \tag{3}$$

G_c is the critical energy release rate and θ describes the hydrogen concentration coverage that drives the critical energy release rate. $(\Psi)_{0}(\varepsilon)$ represents the strain density of an undamaged solid (virgin strain density), and k represents a stability parameter chosen as a small number to condition the solution.

The equilibrium of the work done on the solid undergoing a quasi-static deformation process in the presence of an external force can be decomposed into deformation (equilibrium) and phase field contribution as follows:

$$div[((1-p)^{2} + k)(\sigma)_{0}] + b = 0 \tag{4}$$

$$G_{c}(\theta)[\frac{(p)}{l} + l\Delta p] - 2(1-p)(\Psi)_{0}(\varepsilon) = 0 \tag{5}$$

Lastly, the conservation of mass requirement based on the continuity equation is extended to model the hydrogen diffusion into the solid. Upon further assumption and complex mathematical derivation, the hydrogen transport equation over the entire volume of the solid can be expressed as:

$$\int_{\Omega}[\delta C(\frac{1}{D}\frac{dC}{dt}) + div\delta C div C - div\delta C(\frac{V_{h}C}{RT}div\sigma_{h})]dv = -\frac{1}{D}\int_{\vartheta\Omega q}\delta C q ds \tag{6}$$

where C is the hydrogen concentration, D is the diffusion coefficient, σ_h is the hydrostatic stress, V_h is the partial molar volume of hydrogen in a solid solution, and q is the concentration flux across the surface of the solid.

From the simple form in equation 7, the deformation, phase field fracture, and mass transport problems are discretized, weakly coupled, and solved iteratively using a Newton-Raphson approach.

$$K^{s}S+\overline{M}S = F$$

where S represents the solution variable (u, p, and C), K represents the stiffness Jacobian matrix, M represents the hydrogen concentration capacity matrix, and F represents the hydrogen diffusion matrix. The weakly coupled model is implemented using the Abaqus user element (UEL) and user material (UMAT) subroutines written in Fortran, which allow one to define materials, properties, loads, and elements that are not available in Abaqus built-in models. For simplicity, a 2D square plate is considered for analysis, with a horizontal crack placed at the midpoint of the left side of the plate. The geometric setup and boundary conditions are illustrated in Fig. 1a. Figure 1b also depicts the finite element meshing of the plate, with an element size (h) of 0.005 mm along the fracture process zone and a global element size of 0.05. *l* is chosen to be at least five times greater than the element size along the fracture process zone to resolve the solution along the fracture path. The load is applied by prescribing a constant total u of 0.01 mm, as done in experimental uniaxial tensile testing. Considering high-carbon steel (an iron-based material used typically for boiler drums), the material properties are chosen as: Young's modulus of E = 200 GPa, Poisson's ratio of $\nu = 0.3$, and critical energy release rate of $G_c = 27$ MPa·mm. An initial C (in wt ppm) is prescribed and kept constant along the boundaries of the plate to mimic laboratory-scale testing. For an iron-based material, the additional parameters are also defined as: a partial molar volume of $V_h = 2000$ mm^3/mol, a diffusion coefficient of D = 0.0127 mm^2/s and a damage coefficient of $\chi = 0.89$ based on past empirical density functional theory analysis (DFT) analysis [4]. The gas constant is also given by R = 8314 N·mm/(mol·K).

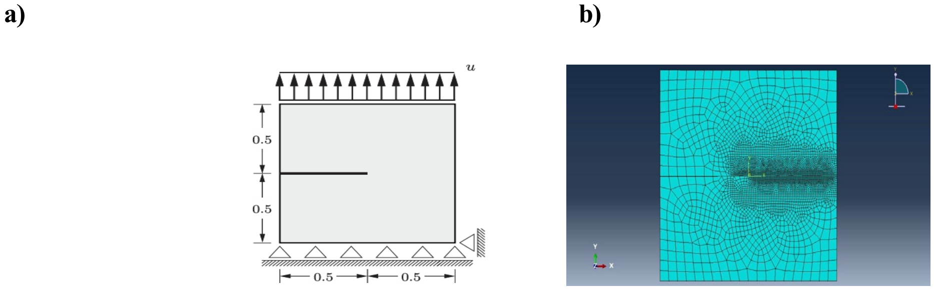

Figure 1. a) A notched square plate subjected to tensile loading [2]. b) A finite element mesh of the plate with element size (h) = 0.005 along the fracture process zone.

3 Results and Discussion

Figure 2a shows the contours of the evolution of the phase field fracture at failure, predicting the potential location of crack growth on a notched plate subjected to uniaxial tension. At the extremes, the blue and red contours represent fully intact and broken material states, respectively. As expected, one can observe diffuse crack growth, as shown in the fracture process zone, because of the definition of the *l.* Figure 2b also depicts the hydrogen concentration contours at the start of crack growth in the fracture process zone. At the extremity, the red and blue contours also, respectively, depict the highest and lowest hydrogen concentration levels in the material. One can observe the highest hydrogen accumulation at the location of the crack tip, where hydrostatic stresses are high. This observation is consistent with the widely accepted hydrogen-enhanced localized plasticity (HELP) theoretical model, which postulates that hydrogen atoms tend to accumulate near dislocation buildup (crack tip), leading to a reduction in resistance to dislocation movement [5]. Figure 3 depicts force displacement curves from the unixial tensile testing of the square plates subjected to varying hydrogen concentration levels. Figure 3 is consistent with laboratory-scale testing [6], showing the reduction in notched tensile strength of a solid under uniaxial load with increasing hydrogen concentration. One can also observe the drastic drop in load with damage and crack growth.

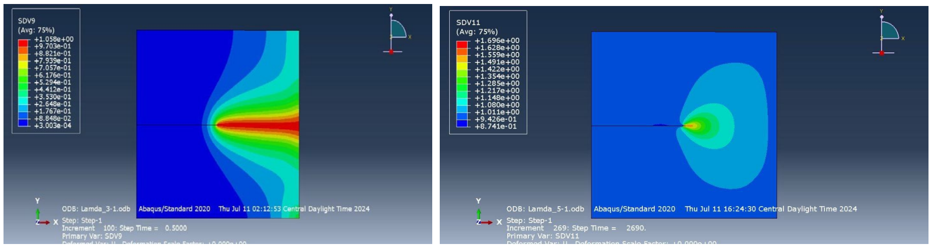

Figure 2. a) Phase-field fracture evolution of a square plate under uniaxial tension; b) hydrogen concentration evolution in the fracture process at crack growth. (Initial and boundary hydrogen concentration = 1 wt ppm)

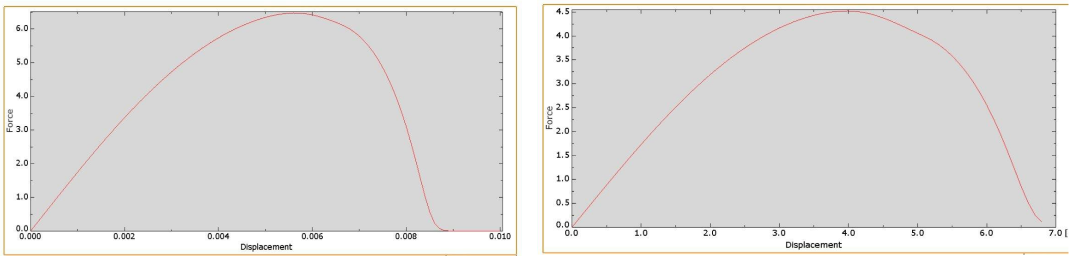

a)

b)

Figure 3. Force displacement curve of notched square plate under tension (a) 0.1 wt ppm; (b) 0.5 wt ppm

4. Conclusion

A simple 2D yet robust phase-field model has successfully been implemented for simulating hydrogen-assisted crack growth and for investigating the effect of hydrogen concentration on the notched tensile strength properties of high-carbon steel. The results have clearly depicted that increasing hydrogen concentration can result in a significant reduction in the mechanical strength of the material, causing it to be severely brittle. Further studies would explore the effect of temperature, different crack topologies, length scale parameters, and mechanical loading conditions on crack growth and mechanical properties in the presence of hydrogen.

5. Acknowledgments

This work is supported by the U.S. National Science Foundation under grant number OIA-1946231 and the Louisiana Board of Regents for the Louisiana Materials Design Alliance (LAMDA). We would like to acknowledge Dr. Emilio Martinez-Paneda (University of Oxford, United Kingdom, England) for his insights and discussions.

6. References

[1] G. Molnár and A. Gravouil, *Finite Elem. Anal. Des.*, vol. 130, pp. 27–38, Aug. 2017
[2] E. Martínez-Pañeda et al. *Comput. Methods Appl. Mech. Eng.*, vol. 342, pp. 742–761, 2018.
[3] R. L. S. Thomas et al. *Metall. Mater. Trans. A*, vol. 34, no. 2, pp. 327–344, Feb. 2003
[4] D. E. Jiang and E. A. Carter, *Acta Mater.*, vol. 52, no. 16, pp. 4801–4807, Sep. 2004.
[5] A. Pradhan et al. *Mater. Today Proc.*, vol. 26, pp. 3015–3019, Jan. 2020
[6] M. Wang et al. *Mater. Sci. Eng. A*, vol. 398, no. 1, pp. 37–46, May 2005

Investigation of the Electrochemical Corrosion Behavior of AFS-D Al6061

Hojun Lee and Erica P. Murray

Institute of Micromanufacturing (IFM), Louisiana Tech University

Abstract: The electrochemical corrosion behavior of aluminum alloy Al6061 fabricated via additive fiction sir deposition (AFS-D) was evaluated during exposure to 3.5% NaCl solution. Linear polarization and cyclic potentiodynamic polarization measurements were collected for samples taken from the top surface of the AFS-D Al6061 part. Although deeper pits were observed within the central region of the AFS-D part, the electrochemical data indicated the edges of the AFS-D Al6061 part had lower corrosion resistance and corroded at a higher corrosion rate.

Keywords: additive friction stir deposition, Al alloy, electrochemical corrosion, localized pitting

1. Introduction

Additive fiction sir deposition (AFS-D) is an additive manufacturing technique where a metal feed stock is deposited rapidly in layers generating a 3D structure. Due to the fabrication speed and scalability, AFS-D is attractive for manufacturing large-scale metal structures that are useful for various industrial and aerospace applications. [1] The microstructural and metallurgical differences between parts made by AFS-D versus traditional manufacturing methods directly impact material properties, and particularly, the corrosion behavior [2]. AFS-D processing of alloys can introduce non-uniform microstructural features due to rotating and traversing the feedstock during deposition. Using aluminum alloy, Al6061, the goal of the present study was to correlate AFS-D processing induced microstructural features with the electrochemical corrosion behavior. This is important for providing insights useful for determining processing parameters that hinder corrosion initiation and localized pitting in alloy materials. Such understanding can contribute towards gathering data that is necessary for AFS-D processing optimization and practical applications of AFS-D.

2. Experimental Methods

A MELD L3 machine was used to fabricate AFS-D Al6061 from feedstock composed of Al-1.63Mg-0.44Si-0.23Cu-0.16Fe (wt.%) according to the following processing parameters: 400 rpm spindle speed, 6 in/min feedstock rate, and 7 in/min tool traverse speed. A moly-spray lubricant was applied to the feedstock rod to facilitate AFS-D processing. Further details are shared elsewhere. **Figure 1** shows a top view of the fabricated part. Samples from regions of the top surface labeled T1, T2, and T3 were selected and cut into 2.5 cm^2 pieces for corrosion testing. The samples were ground using sandpaper from 600 – 1200 grit and polished down to a ~ 0.3 µm surface finish to establish a common surface roughness.

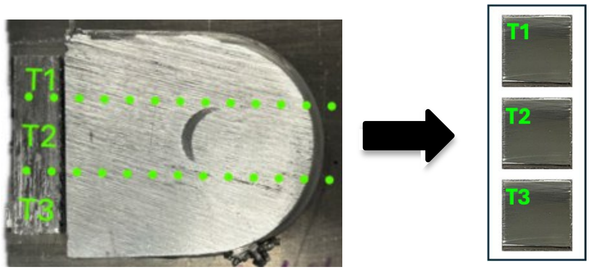

Figure 1. Top view of AFS-D Al6061 and samples cut from sections along the top surface.

Electrochemical corrosion measurements were made using a Gamry Reference 600 potentiostat with a 3-electrode configuration where the sample was the working electrode, a graphite rod was the counter electrode, and the reference electrode was Ag/AgCl. The samples were electrochemically tested in a 3.5% NaCl electrolyte solution, after allowing the open circuit potential to achieve stability for about 30 min. Linear polarization resistance (R_p) and cyclic potentiodynamic polarization (CPP) measurements were performed to gather electrochemical corrosion data. The R_p and CPP measurements were taken at a scan speed of 0.167 mV/s. Following corrosion testing, the samples were exposed to a Keller's etch to remove the passive oxide layer thereby enabling microscopic analysis of localized pitting. Scanning electron microscopy (SEM) was carried out to determine the location, distribution, and morphology of corroded surface features. Confocal microscopy enabled evaluation of the pit size, depth, and profile.

3. Results

Figure 2 shows cyclic potentiodynamic polarization curves for samples from the top surface of the AFS-D Al6061 sample. For each sample, the corrosion potential, E_{corr}, and pitting potential, E_{pit}, were indistinguishable. This indicated that localized pitting initiated upon introducing the sample to the 3.5% NaCl solution. This suggested that stable pitting proceeded before a substantial passive oxide layer formed. Once the potential was reversed, repassivation occurred for all of the samples as indicated by the overlap of the CPP curve below -0.85 V. The bump in the repassivation path occurring around -0.75 V may indicate an initial attempt for repassivation that was possibly hindered or delayed due to the extent of localized pitting. For T1 and T3 samples, E_{corr} and E_{pit} were approximately -705 mV, which suggested the edges of the AFS-D Al6061 sample were slightly less prone to corrosion initiation than the center region, as T2 samples tended to have a more negative E_{corr} /E_{pit} value near -720 mV. However, corresponding corrosion current density, I_{corr}, values suggested the central region of the AFS-D Al6061 sample corroded at a lower corrosion rate than the edges. This finding was based on Tafel fits of the CPP curves that determined I_{corr} for T2 samples was ~ 0.4 μA/cm^2, whereas significantly higher I_{corr} values of about 2.8 and 1.0

μA/cm2 were obtained for T1 and T3 samples, respectively. So, overall the CPP data suggested that the AFS-D processing parameters in this study, caused the center of the Al6061 part to be more resistant to corrosion.

Figure 2. Typical cyclic potentiodynamic polarization curves for top surface regions (T1, T2, and T3) of the AFS-D Al6061 alloy sample.

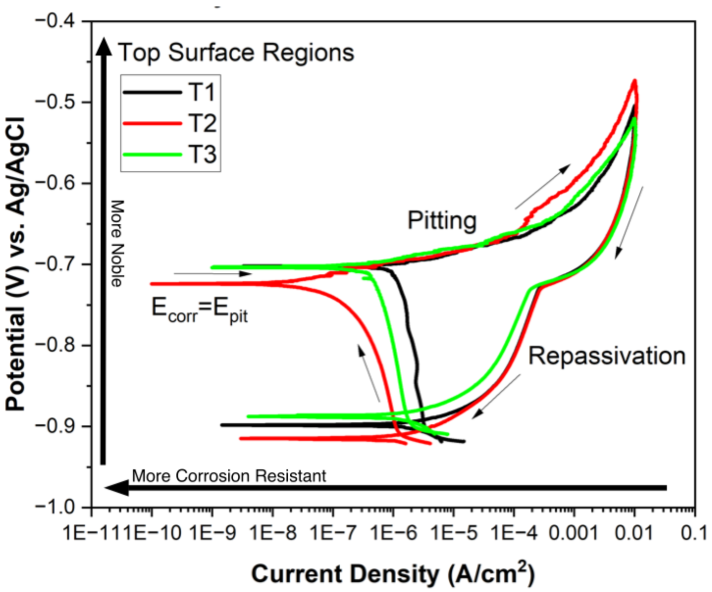

Linear polarization resistance measurements of edge and center AFS-D Al6061 samples were in agreement with the CPP data as measurements taken for the T2 region measured higher resistance. **Table 1** summarizes the linear polarization and cyclic polarization data.

Table 1: Cyclic potentiodynamic polarization and linear polarization parameters.

Samples	E_{corr}/E_{pit} (mV)	I_{corr} (μA/cm^2)	Rp (kΘ)
T1	-707.6 ± 5.9	2.80 ± 0.94	10.68 ± 4.26
T2	-717.2 ± 0.9	0.36 ± 0.04	73.11 ± 7.13
T3	-704.2 ± 0.4	0.97 ± 0.01	26.98 ± 0.38

Scanning electron microscopy and confocal microscopy was carried out to evaluate the pit morphology of the various sections of the AFS-D Al6061 samples. In general, T2 samples had significantly fewer pits compared to T1 and T3 samples, which explains why T2 samples were more corrosion resistant as shown in the CPP data. The pits shown in **Figure 3** were typical SEM images of pits observed over T1, T2, and T3 samples. **Figure 4** summarizes the confocal data, which indicated T2 samples from center region of the AFS-D part tended to have deeper pits, in comparison to the outer edges of the part. This is possible due to the tendency of the AFS-D part to begin corroding for at the center and then progressing to the outer edges. **Figure 4** also shows that the size of the pits over the part surface were generally between 0.05 – 0.2 µm with occasional outliers greater than 0.6 µm.

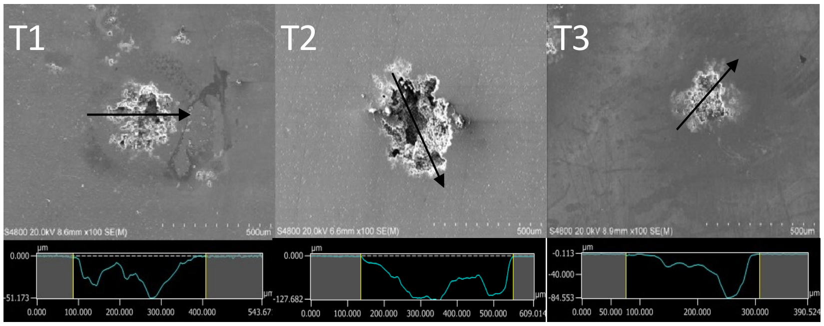

Figure 3. SEM images of pits with corresponding depth profile of samples from regions T1, T2, and T3. Arrows indicate line scan direction.

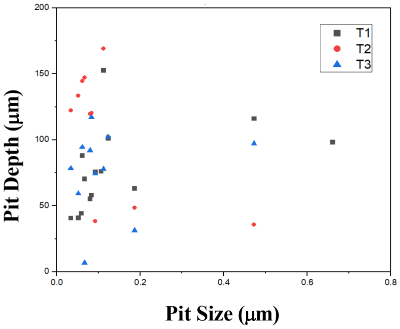

Figure 4. Scatter plot describing the pit morphology.

4. Conclusion

The electrochemical corrosion measurements of the AFS-D Al6061 top surface samples fabricated as described indicated corrosion initiated in the central region of the part but proceeded at a faster rate at the edges of the fabricated surface. Pit morphologies had similar characteristic features, however the pit depth for the central region of the part was greater despite the lower corrosion rate. The electrochemical corrosion measurements were effective in identifying where corrosion began, to what extent, and at what rate corrosion would proceed. Thus, further studies on Al alloys and other alloy materials can enable identification of electrochemically optimal manufacturing specifications for AFS-D components and parts.

5. Acknowledgments

Special thanks to Dr. Shengmin Guo's group for providing the AFS-D Al6061 samples. This work is supported by the U.S. National Science Foundation under grant number OIA-1946231 and the Louisiana Board of Regents for the Louisiana Materials Design Alliance (LAMDA).

6. References

[1] de Carvalho, M.G.M., Cavalcante, D.F., Dreilich, V., Brandolin, G., de Sousa, F.V.V., Alves, F.P., "Electrochemical Behavior under Artificial Seawater and Intergranular Corrosion Performance of 6XXX Aluminum Alloys Series", NACE International, 2020.

[2] Griffiths, R.J., Perry, M.E.J, Sietins, J.M., Zhu, Y., Hardwick, N., Cox, C.D., Rauch, H.A. and Yu, H.Z., "A Perspective on Solid-State Additive Manufacturing of Aluminum Matrix Composites Using MELD". *J. of Materi Eng and Perform* **28**, 648–656 (2019). https://doi.org/10.1007/s11665-018-3649-3

Large Vision Model Adaptation for 4D Fracture Detection in X-ray Material Tomography

Kiran Shrestha, Jihun Hamm, Zhengming Ding*

Department of Computer Science, Tulane University

Abstract: Automatic fracture detection in X-ray material tomography using machine learning represents a significant advancement for intelligent material monitoring. This challenge can be approached as salient object detection (SOD), which focuses on identifying the most prominent regions in an image according to human perception. Recent advancements in AI-based object detection in natural images, powered by sophisticated deep neural networks and extensive well-annotated datasets like the Segment Anything Model, have demonstrated remarkable success. These advancements prompt the question: "How can we leverage such large-scale models for our specific tasks?" This project aims to investigate the potential application of large-scale models for X-ray material tomography. Our objective is to design an efficient pipeline to adapt these models to our specific needs. The successful completion of this project promises significant benefits for smart material design by accurately identifying fractures, in alignment with the LAMDA Strategic Plan.

Keywords: X-ray material tomography, Large-Scale Models

1. Introduction

Fractures visible in X-ray material tomography are inherently three-dimensional (3D) features that significantly influence material flow properties at specific moments. Over time, this influence evolves into a four-dimensional (4D) property, as fractures generally expand rather than shrink. The irregular and uneven nature of fractures dictates that flow typically follows a meandering path determined by local pressure gradients and fracture topography. Automated fracture detection is crucial for swiftly and accurately identifying fracture regions and monitoring changes, yet detailed annotations pose challenges due to the complexity and high resolution of fracture textures [1]. Utilizing pre-trained AI models, such as the Segment Anything Model (SAM) [2], presents a viable solution.

This study aims to evaluate SAM's application in 3D X-ray material tomography for effective fracture detection. Initial findings on 2D images illustrate SAM's capability to delineate intricate fracture boundaries without annotated data, underscoring its potential for 3D applications. However, two critical questions persist:

(a) *How can we minimize or eliminate the need for prompt inputs when employing SAM?*
(b) *How can we accurately refine complex boundaries based on SAM's outputs?*

To address these queries, this study will first evaluate SAM's performance in detecting fractures in 3D X-ray material tomography from multiple perspectives. By integrating SAM's deep learning capabilities with frequency

Proceedings of Louisiana NSF EPSCoR RII LAMDA 2024 Symposium

domain analysis, specifically Fourier Transformation [3], we aim to overcome inherent challenges in X-ray material tomography. Ultimately, this research aims to advance smart material design through enhanced automatic fracture detection methodologies.

2. Method

The success of the Segment Anything Model (SAM) [2] in natural image segmentation is primarily attributed to two factors: leveraging massive deep learning models with billions of parameters and access to high-quality, well-annotated image data. However, in the domain of X-ray material tomography, several challenges necessitate a tailored approach. Unlike natural images, X-ray tomography data are less accessible, and their complex textures and boundaries complicate annotation.

Due to the intricate textures and boundaries in X-ray material tomography, SAM alone may struggle to capture detailed fracture regions effectively. To address this limitation, we propose integrating Fourier Transformation with SAM. Fourier Transformation [3] converts images from the spatial domain to the frequency domain, facilitating the identification of crucial high-frequency patterns associated with fractures. Initial findings indicate that Fourier Transformation can effectively highlight fractured boundaries by filtering out less relevant low-frequency patterns.

SAM, pretrained on a vast and diverse dataset, is then applied to the transformed frequency domain images. This pretrained model demonstrates robust segmentation capabilities without requiring additional training. Enhanced by the frequency domain transformation, SAM generates pseudo annotations for fractures. These annotations reduce the dependency on extensive human input, offering a more efficient method for data labeling. The constructive collaboration between SAM and Fourier Transformation forms a potent approach for automatic fracture detection in X-ray material tomography. By combining their strengths, this methodology produces reliable pseudo annotations that enhance the performance of deep learning models trained on this data.

3. Experimental Results

We have successfully employed foundational AI models such as the Segment Anything Model (SAM) to automatically generate coarse crack annotations. Specifically, Fourier Transformation techniques have been utilized to identify potential crack points, which are then input into the SAM model to produce crack masks.

In the Figures 1 and 2 below, we report some fracture detection results we obtain. (a) shows the raw inputs, (b) presents the FFT (Fast Fourier Transform) segmentation results with bounding boxes covering the blue crack region, (c) displays the FFT segmentation results with green points indicating the center points, (d) shows the SAM segmentation results with box prompts from (b), (e) presents the SAM segmentation results with point prompts from (c). These figures demonstrate the application of FFT-guided SAM for accurate crack detection in X-ray material tomography, highlighting the integration of Fourier Transformation techniques with SAM to enhance fracture identification.

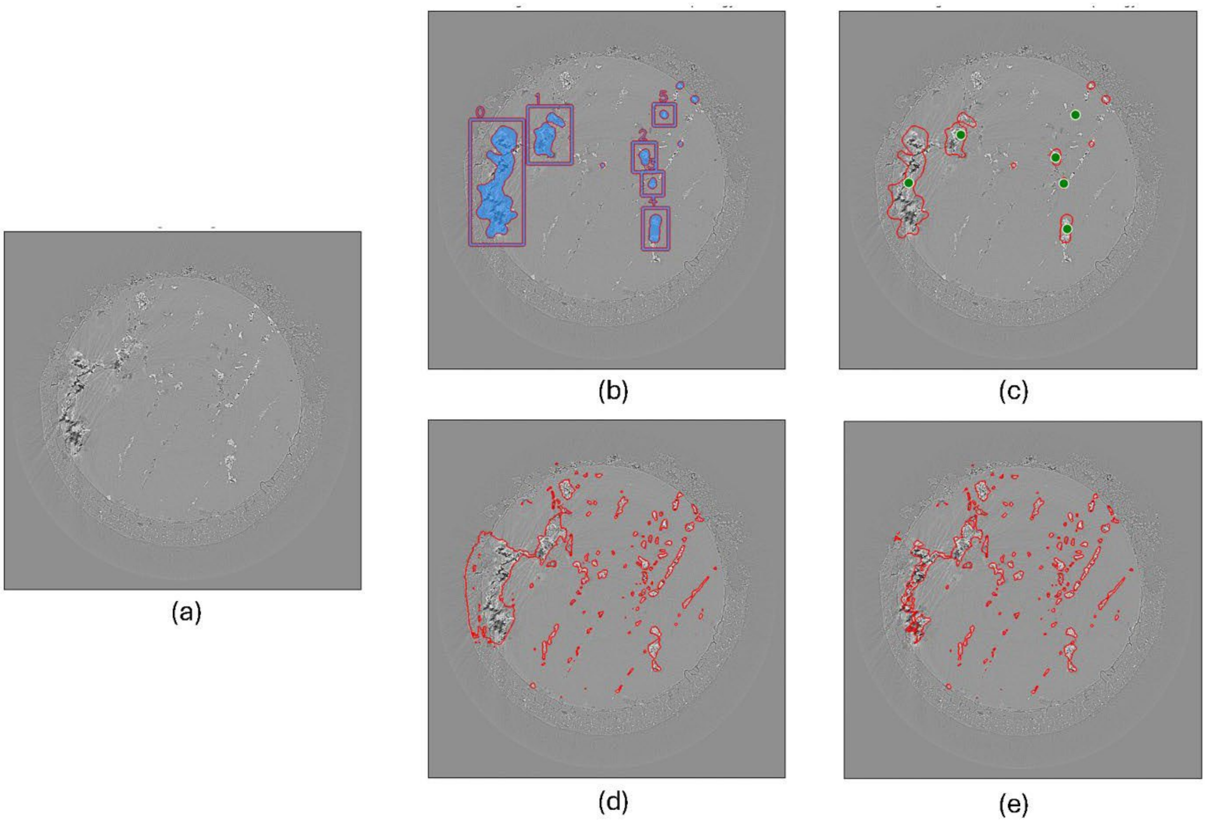

(a) (b) (c) (d) (e)

Figure 1. Results of our proposed model.

4. Conclusion

In conclusion, integrating Fourier Transformation with SAM enhances X-ray material tomography for fracture detection by leveraging SAM's deep learning capabilities and Fourier Transformation's focus on high-frequency fracture patterns. This approach improves automatic fracture detection efficiency, reduces human input in annotation, aligns with the LAMDA Strategic Plan for smart material design advancement, and holds promise for broader applications in materials science and engineering.

5. Acknowledgments

This work is supported by the U.S. National Science Foundation under grant number OIA-1946231 and the Louisiana Board of Regents for the Louisiana Materials Design Alliance (LAMDA).

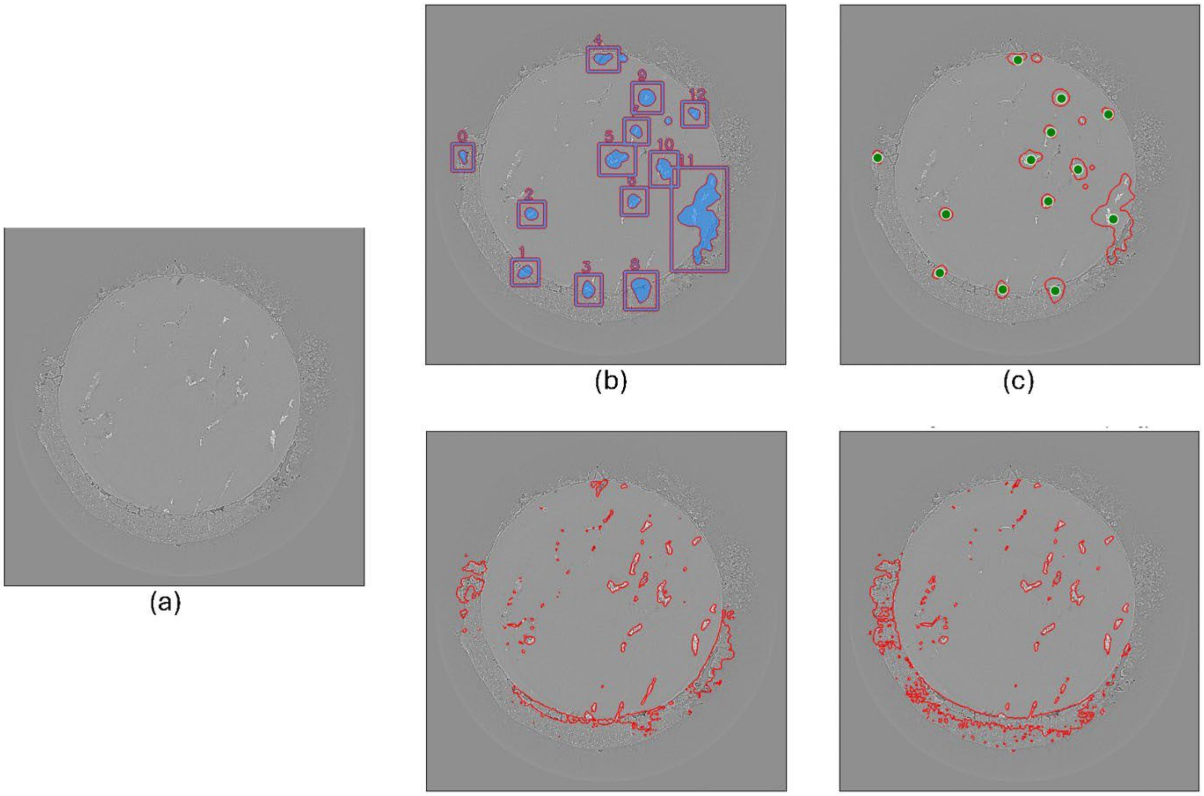

(a) (b) (c) (d) (e)

Figure 2. Results of our proposed model.

6. References

[1] Fatimah Alzubaidi, Patrick Makuluni, Stuart R Clark, Jan Erik Lie, Peyman Mostaghimi, and Ryan T Armstrong. Automatic fracture detection and characterization from unwrapped drill- core images using mask r–cnn. Journal of Petroleum Science and Engineering, 208:109471, 2022.

[2] Alexander Kirillov, Eric Mintun, Nikhila Ravi, Hanzi Mao, Chloe Rolland, Laura Gustafson, Tete Xiao, Spencer Whitehead, Alexander C. Berg, Wan-Yen Lo, Piotr Doll´ar, and Ross Girshick. Segment anything, 2023

[3] Sangrok Lee, Jongseong Bae, and Ha Young Kim. Decompose, adjust, compose: Effective normalization by playing with frequency for domain generalization. ArXiv, abs/2303.02328, 2023.

Laser Hot-Wire Direct Energy Deposition: Data Fusion of X-ray and Neutron Images

Saber Nemati[1], Shengmin Guo[1], Gerry Knapp[2], Kyungmin Ham[3], Leslie G. Butler[4]

[1]Department of Mechanical and Industrial Engineering, Louisiana State University
[2]Oak Ridge National Laboratory,
[3]Center for Advanced Microstructures and Devices, Louisiana State University
[4]Department of Chemistry, Louisiana State University

Abstract: Laser hot-wire direct energy deposition additive manufacturing has the advantage of speed, but also the potential for incorporation of oxide impurities. The detection and quantification of two light elements is difficult with X-ray imaging but is possible with neutron grating-based interferometry. The interferometry dark-field images are sensitive to neutron scattering from structural features too small to be seen with conventional X-ray or neutron tomography. Herein, two wire arc samples are studied the X-ray, neutron attenuation, and neutron dark-field imaging with the goal of establishing an clustering procedure for characterizing and quantifying the oxide impurities.

Keywords: (Laser hot-wire direct energy deposition, data fusion, X-ray tomography, neutron interferometry)

1. Introduction

Laser hot-wire additive manufacturing is a closely related to wire-arc additive manufacturing as both are wire-fed feedstock versus powder blown. Both Laser hot-wire and wire-arc share the advantages of a large build size, less costly feedstock, graded composition, and build/repair options. A disadvantage of wire-arc is a complex thermal history [1], a problem which may be resolved with direct energy deposition via a laser [2]. In the case of aluminum laser hot-wire as studied here, contamination with aluminum oxides can also occur.

Herein, a novel nondestructive evaluation was used to determine contamination distribution in three-dimensions. Two samples of Al laser hot-wire were studied with neutron interferometry tomography and then with laboratory X-ray tomography to yield three datasets with these characteristics:

- The X-ray tomography dataset has a high image contrast-to-noise ratio and is useful for defining the aluminum WAAM structure.
- The neutron attenuation tomography dataset has a medium image contrast-to-noise ratio and shows both aluminum and hydrogen content.
- The neutron dark-field tomography dataset has a low image contrast-to-noise ratio and shows neutron scattering from air-solid interfaces such as internal pores and contamination deposits.

Together, these three 3-D datasets are used to locate and characterize the aluminum laser hot-wire contamination.

Combined X-ray and neutron imaging is finding applications in electrochemical devices (batteries, fuel cells) [3] and in geochemical applications such as envisioned for the Mars sample return missions [4]. The addition of interferometry adds value to the image [5]. For the battery work, Shrestha and co-workers use the combination of X-ray and neutron data at two stages in the data processing. First, the high contrast-to-noise ratio X-ray data is used to support the tomographic reconstruction of the lower contrast-to-noise ratio neutron data. Second, the X-ray and neutrons have different image contrast mechanisms, a feature which allows spatial assessment of metal electrodes (X-ray) simultaneous with the location of lithium and hydrogen distributions (neutrons).

2, Experimental Section

Two examples, labeled M1003 and M1005, of aluminum laser hot-wire were prepared from 1.2 mm diameter wire with a composition of 6.5-7.5 wt.% Si, 0.3-0.45 wt.% Mg and remainder Al. The processing parameters were 4200 W laser, 17 L/min shielding gas, and a wire feed speed of 140 in/min. The relative geometry of the laser, wire, and substrate are shown here.

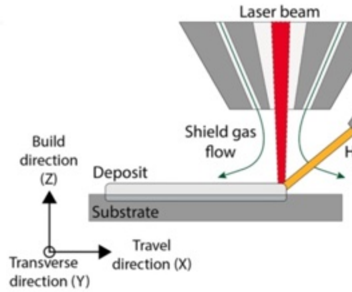

X-ray tomography was performed with a Zeiss Versa 620 at the ORNL Manufacturing Demonstration Facility. Neutron interferometry was performed at the ORNL High-Flux Isotope Reactor MARS beamline configured in a Talbot-Lau geometry as shown here. The neutron attenuation and dark-field datasets are acquired simultaneously in the stepped-grating interferometry process. The effective pixel size at the neutron imaging detector was 42 µm. A rigid-body affine transformation was used to convert the X-ray dataset into the coordinate system of the neutron attenuation and dark-field datasets. A photo (a) and slice views–(b) neutron attenuation, (c) neutron dark-field, and (d) X-ray–of sample M1005 are shown here.

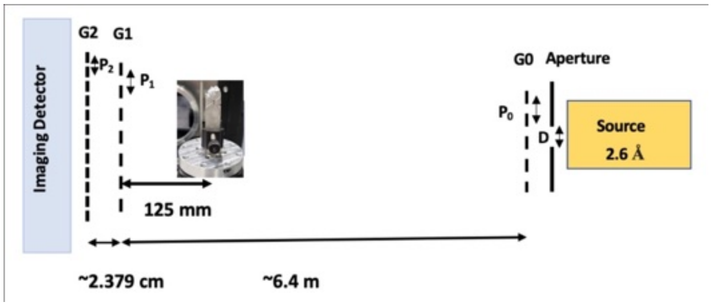

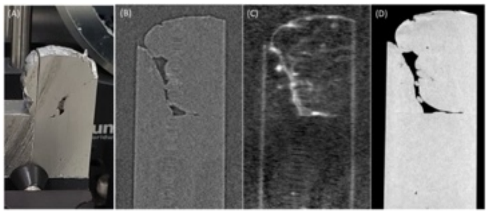

The workflow is shown on the following page. The central feature is the unsupervised machine learning used to detect and locate the contamination deposits. A Gaussian mixture model was used to classify the imaging data into four or five classes where the clusters were assessed with the Calinski-Harabasz metric. The workflow before clustering includes scaling of intensity values into approximate a 0-100 range and the masking for all datasets to exclude air and bulk aluminum from the clustering. Clustering operated only on the voxels having a scaled X-ray intensity between the air and bulk aluminum; a histogram of scaled X-ray intensity values is shown in the workflow. The mask accepted the voxels containing corrosion as well as partially-filled voxels at the air-aluminum edges. The X-ray, neutron attenuation, neutron dark-field intensities, and an index representing the {width, depth, height} voxel positions were reshaped into an 4xN matrix where N is the number of non-zero entries in the mask. The clustering required on the order of 12 hours of workstation, hence the datasets were downsampled by a factor of two for exploration with 3 hour computations.

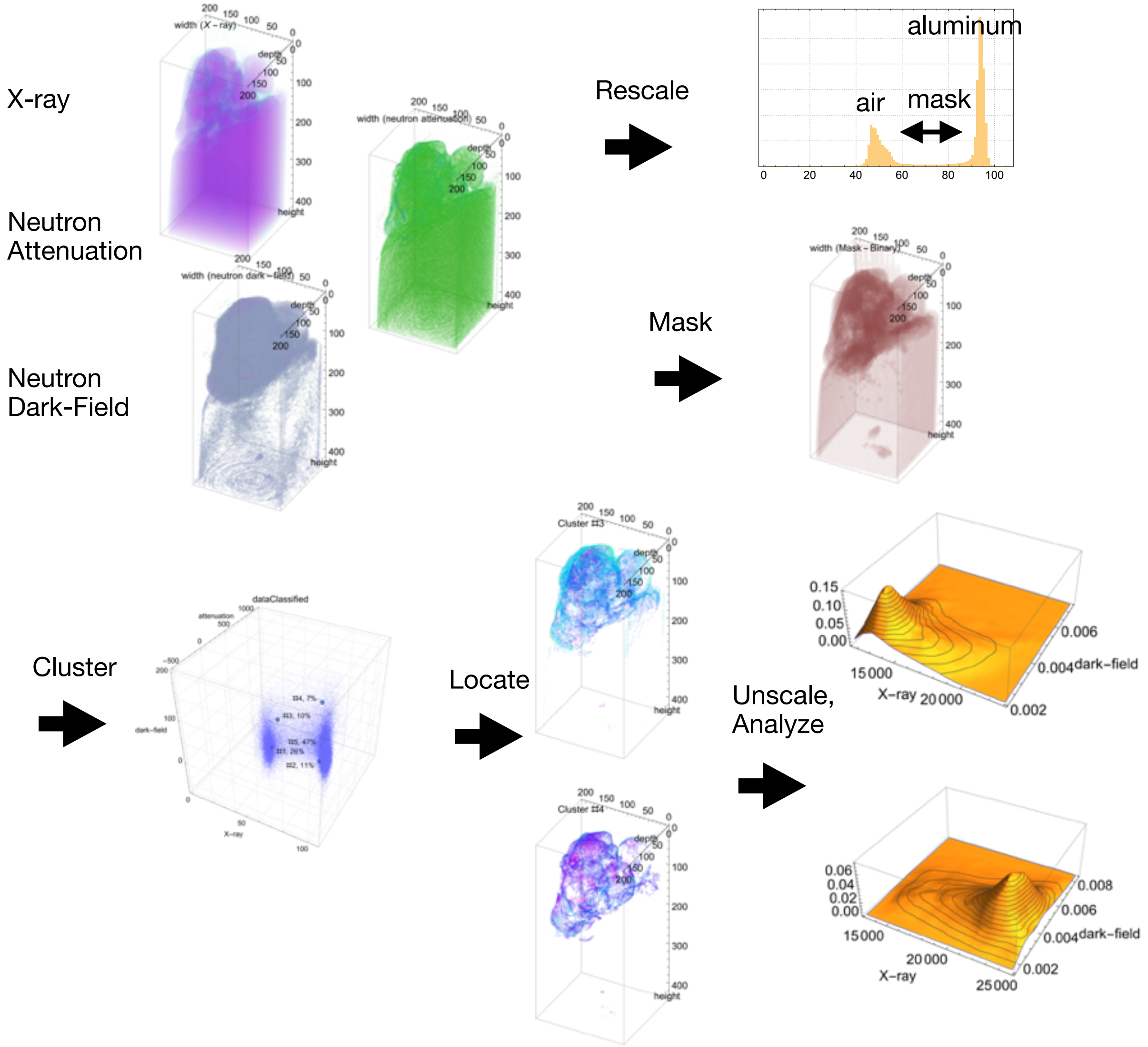

3. Results

Both samples show two clusters for the corrosion, with the clusters differing by their X-ray absorption as well as by neutron dark-field values as shown with the 3-D histograms in the workflow. The chemical suspects for the corrosion are corundum, Al_2O_3, d= 4.05 g/cm^3, and perhaps a blend of boehmite and diaspore, AlO(OH), d= 3.035 g/cm^3 and 3.4 g/cm^3, respectively.

4. Conclusion

A workflow for data fusion of X-ray, neutron attenuation, and neutron dark-field 3-D datasets has been developed, a workflow which preserves spatial information. This workflow is expected to have widespread applications in combined X-ray and neutron imaging experiments due to its combination of high spatial resolution X-ray imaging with the feature scattering information from dark-field imaging.

5. Acknowledgments

This work is supported by the U.S. National Science Foundation under grant number OIA-1946231 and the Louisiana Board of Regents for the Louisiana Materials Design Alliance (LAMDA). This research used resources at the High Flux Isotope Reactor, a DOE Office of Science User Facility operated by Oak Ridge National Laboratory.

6. References

[1] Shah, A., Aliyev, R., Zeidler, H., Krinke, S., 2023. A Review of the Recent Developments and Challenges in Wire Arc Additive Manufacturing (WAAM) Process. JMMP 7, 97. https://doi.org/10.3390/jmmp7030097

[2] Gibson, B.T., Mhatre, P., Borish, M.C., Atkins, C.E., Potter, J.T., Vaughan, J.E., Love, L.J., 2022. Controls and process planning strategies for 5-axis laser directed energy deposition of Ti-6Al-4V using an 8-axis industrial robot and rotary motion. Additive Manufacturing 58, 103048. https://doi.org/10.1016/j.addma.2022.103048

[3] Shrestha, P., Lamanna, J.M., Fahy, K.F., Kim, P., Lee, C., Lee, J.K., Baltic, E., Jacobson, D.L., Hussey, D.S., Bazylak, A., 2023. Simultaneous multimaterial operando tomography of electrochemical devices. Sci. Adv. 9, eadg8634. https://doi.org/10.1126/sciadv.adg8634

[4] Martell, J., Alwmark, C., Woracek, R., Alwmark, S., Hall, S., Ferrière, L., Daly, L., Koch, C.B., Hektor, J., Johansson, S., Helfen, L., Tengattini, A., Mannes, D., 2024. Combined Neutron and X-Ray Tomography—A Versatile and Non-Destructive Tool in Planetary Geosciences. JGR Planets 129, e2023JE008222. https://doi.org/10.1029/2023JE008222

[5] Gustschin, A., Neuwirth, T., Backs, A., Viermetz, M., Gustschin, N., Schulz, M., Pfeiffer, F., 2020. Comparison of Thermal Neutron and Hard X-ray Dark-Field Tomography. J. Imaging 7, 1. https://doi.org/10.3390/jimaging7010001

Mechanical Property Characterization of Hybridized Laminate Composites

Abubakar Sumaila[1], Patrick Mensah[1], Maryam Jahan[2]

[1]Mechanical Engineering, Southern University And A&M College
[1]Mechanical Engineering, Southern University And A&M College

Abstract: This work has been able to produce a strong, thermally stable composite through the incorporation of sugarcane bagasse fibers into carbon fibers and a vitrimer matrix. Bagasse purification was carried out using water, sonication, drying, grinding, sifting, carbonization in the oven at 600°C for 4 hours, alkali activation, and oven- drying. Hand layup was carefully made for the composite, involving eight carbon fiber films that were laid and later carefully cured for 24 hours and then thermally post-cured at 100°C and 150°C. Subsequent to this, the samples were ground, polished, and subjected to testing. X-Ray Diffraction Analysis Tests were carried out to compare and analyze critically all three different states of the bagasse particulate samples. Scanning Electron Microscope was also use to visually inspect and compare the microscopic surface of all three different states of the bagasse samples. Three-point flexural strength and modulus were done with great stringency by bending tests. After which a Fractography analysis were carried out to visually inspect and characterize the exact failure modes observed on the fractured surface of the 3 point bending test.

Introduction

This research solves some prime environmental and economic problems by utilizing natural fibers in composite materials. Basically, natural fibers have provided a sustainable alternative for non-renewable resources to help protect the environment. Due to being biodegradable with low carbon footprint, they are cost-effective since it is agriculture waste-based, hence reducing material cost while providing waste management.

Mechanical properties: natural fibers improve, increasing toughness and impact resistance by reducing brittleness. Improved flexural properties mean processed materials can apply to many uses in structural applications. Thermal stability: natural fillers improve thermal resistance of the material, enhance thermal insulation, and control temperature changes. It is due to the synergistic effect of both natural fillers and other additives that brings examples of fantastic improvement in the mechanical robustness and structural integrity, thereby allowing property adjustment by varying the ratio among others of natural fillers and carbon fibers.

Typical limitations in conventional carbon fiber-reinforced laminate composites include high material and manufacturing costs, brittleness, and sensitivity to the environment. It is also highly expensive to produce and fabricate carbon fibers, having low ductility and fracture toughness, which makes them prone to sudden failure. Moreover, moisture absorption and UV exposure can degrade carbon fiber composites.

The research will aim at plugging these gaps through determining the optimum hybridization configuration to bridge dissimilar fiber types and matrix materials and promote interfacial bonding between fibers and matrices to avert delamination, which has adverse effects on mechanical performance. It will establish the working temperature range, flexural strength, and modulus of the hybridized composite while making a critical analysis of the modes of fracture failure reported during the 3-point bending test. This research aims to develop sustainable, cost-effective, and high-performance composite materials.

2.0 Materials Used and Methodology

2.1 Materials

The hybridized laminate composite was formed using raw sugarcane bagasse fiber, which was further subjected to purification and interface enhancement. All compounds used in this work are compounds of commerce and were all utilized as received from the market without additional purification. Sigma Aldrich, USA supplied DCN-PEI Vitrimer 3:1 branched polyethylenimine, PEI; average Mw~800 by LS, average Mn ~600 by GPC. Diglycidyl 1,2, cyclohexanedicarboxylate, DCN, was supplied by Ambeed, IL, USA.

2.2 Methodology

Natural Fiber Treatment & Laminate Formation

Sugarcane Fibers were washed and sonicated for further purification. After which the washed fibers were dried and grinded to attain the particulate state. Then the bagasse fibers were further sifted to attain a consistent particle size afterwards carbonized at 600ºC for 4 hours in a nitrogen-blanketed furnace and allowed to cool overnight. After which the carbonized sample was mixed with 0.1M Potassium hydroxide solution and allowed to stir for 24 hours to ensure complete activation. Samples of the Raw, Carbonized and Activated Bagasse were analyzed with an X-Ray Diffraction Machine and a Scanning Electron Microscope.. 8.25g of activated sugarcane bagasse was mixed with 165g of polymer matrix consisting of 123.75g Diglycidyl 1,2-Cyclohexane-Dicarboxylate , 41.25g Branched Polyethylenimine and 8 films of intermediate carbon fiber were used by the hand layup laminate method with the help of a mold, Teflon sheets, paint bush and a roller to create a mechanically robust and thermally stable hybridized carbon fiber reinforced laminate composite. After which the Hybridized Carbon Fiber reinforced laminates sample was left in the mold to cure under room temperature while being cooled by a fan for 24 hours. Post thermal curing was done in an oven at an elevated temperature of 100ºC for 2 hours. After which another post thermal curing was carried out consecutively at 150ºC for 2 hours. The sample was taken out of the mold and was cut and polished into standardized sizes for the necessary tests.

Scanning Electron Microscope (SEM) Characterization of Bagasse particulate fibers

The raw, carbonized and activated bagasse particles were visually inspected using the SEM to analyze the surface of the particulate fibers.

X-Ray Diffraction Analysis (XRD) XRD analysis Test was carried out on the Raw, Carbonized and Activated sample to determine and analyze the phases

3-Point Bending Test

A three point Bending test was carried out on 4 Activated sugarcane bagasse laminate samples. All 4 samples were of the same standardized geometry with regards to thickness (h) and width (b). A constant Span of Length value (L) = 77.04mm was maintained throughout all 4 experiments.

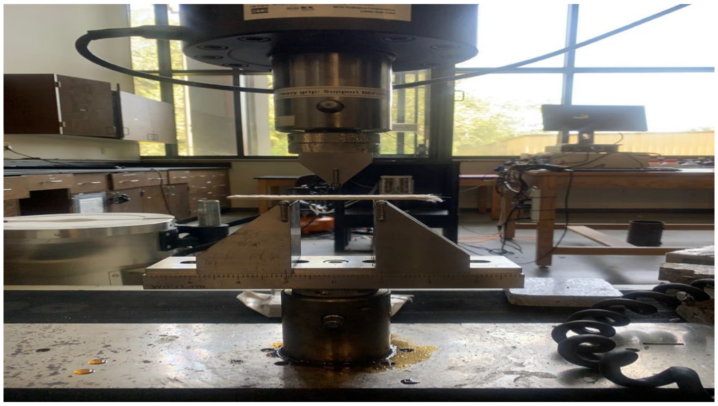

3-Point Bending Test Set-up

The scanning Electron Microscope was used to analyze the fracture surface of the Activated Sugarcane Bagasse sample after it fractured.

Overview of natural fiber treatment & Laminate Formation

3.0 Results & Discussion

XRD Analysis Graphs

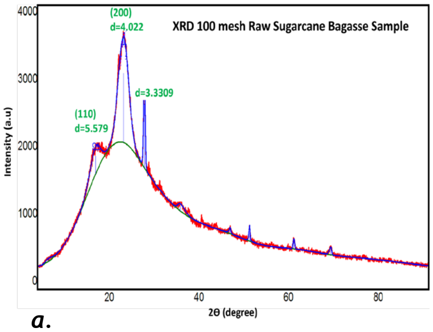

a.

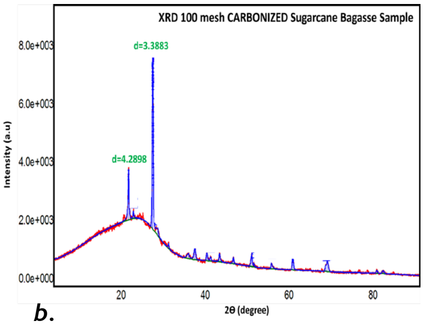

b.

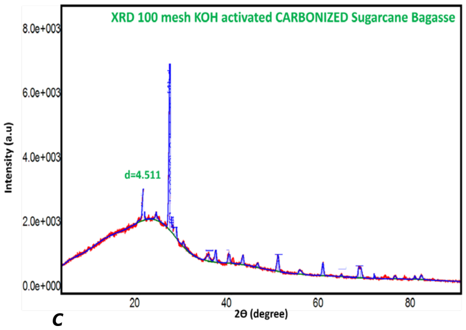

c

SEM Images of Raw, Carbonized & Activated particulate Fibers

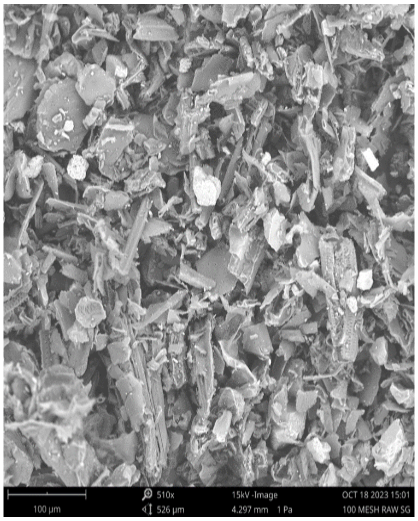

a.

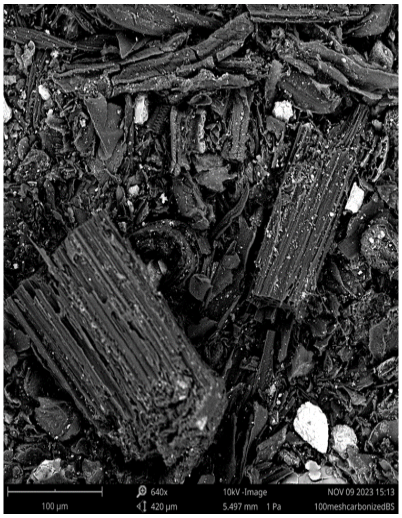

b.

c

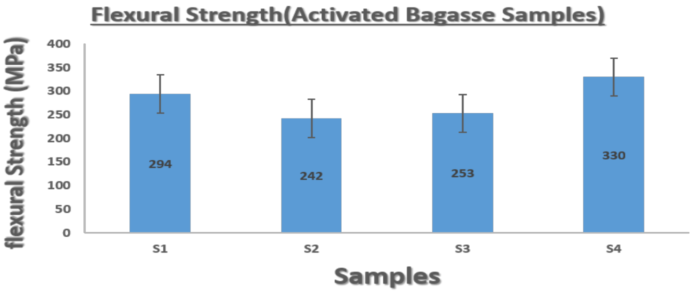

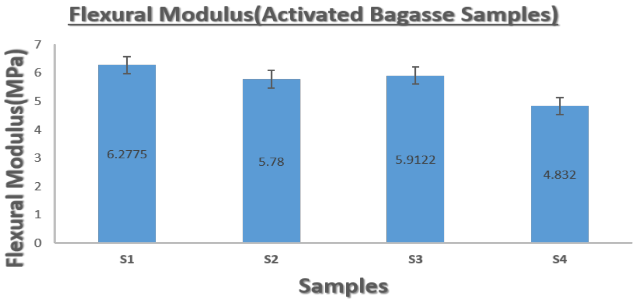

Fractography analysis of Fractured Surface from 3-Point Bending Test

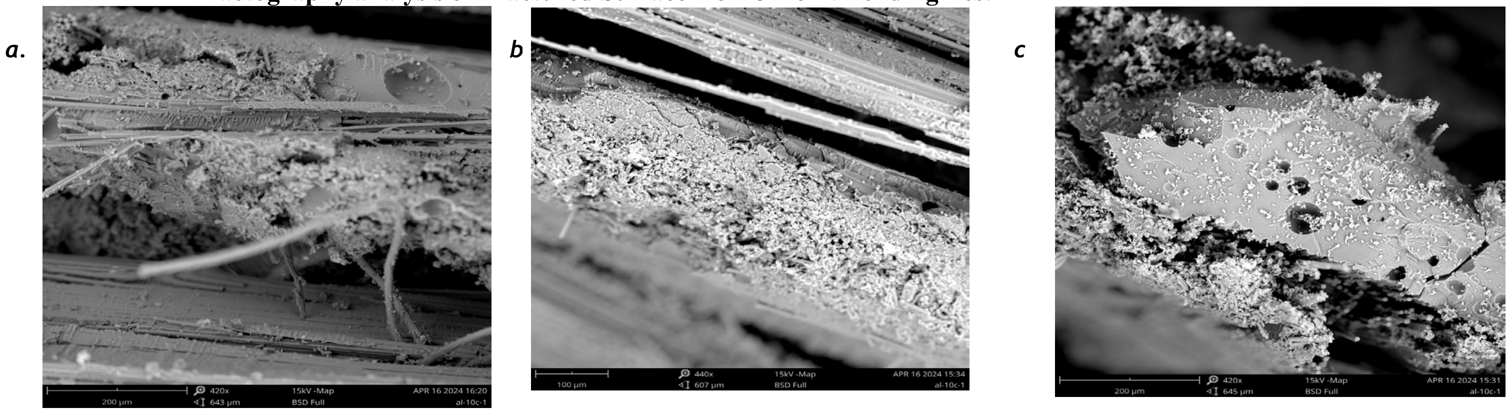

Discussion & Conclusion

Conclusion

XRD Images have an incresed number of Peaks(Crystallographic Phases) from 9(a) to 20(b) to 23(c)and that affacts samples reactivity and bonding Ability. ***SEM Analysis*** of Images(b) and Image(c) in comparison to Image(a). 'b' has rill and gulley like structures which serve as points of attachment inthe Polymer matrix. 'c' appears to have pores, honeycomblike structures,rills and gulleys which seem to be a more enhanced surface for increased interfacial bonding in the Polymer Matrix. ***Fractography Analysis*** (a) shows a fully pulled out fiber meaning strong interfacial bonding.'b' shows delamination in the strata hence a rittle material. 'c' shows voids within the sample which serve as stress concentration points.

5. Acknowledgments

This work is supported by the U.S. National Science Foundation under grant number OIA-1946231 and the Louisiana Board of Regents for the Louisiana Materials Design Alliance (LAMDA).

.

6. References

Usta, F., Türkmen, H. S., & Scarpa, F. (2021). *"Low-velocity impact resistance of composite sandwich panels with various types of auxetic and non-auxetic core structures."* Thin-Walled Structures.

Goldstein, J. I., et al. (2017). "Scanning Electron Microscopy and X-ray Microanalysis."

Denissen, W., Winne, J. M., & Du Prez, F. E. (2016). "Vitrimers: permanent organic networks with glass-like fluidity."

Mentoring the Next Generation of Mentors: Guided Student Teaching to Provide Undergraduate Training in Additive Manufacturing

Mynmayh Khamvongsa[1], William Chirdon[1]

[1]Institute for Materials Research & Innovation (IMRI), Department of Chemical Engineering, University of Louisiana at Lafayette

Abstract: 3D printing is a rapidly expanding field with increasing demand in industry and growing interest from students. With 3D printing becoming more accessible, it can provide STEM students with valuable hands-on experience and technical skills benefiting their future careers. It takes an abstract concept of an idea and makes it more concrete and tangible. It also encourages creativity, experimentation, and innovation. Students are given a hands-on approach in designing a project, identifying design flaws, and finding solutions to fix them.

This project represents a novel approach to training undergraduate students in low teacher-ratio environment by utilizing a graduate student mentor. Oftentimes, graduate students do not get meaningful teaching experiences through their research-based graduate program. The novelty of this project is that the graduate student mentor is closely mentored by an experienced faculty member, and in turn, the graduate student receives course credit after quantifying the effectiveness of their course through student assessment and by writing a reflective summary of their experience.

Keywords: 3D printing, STEM education, teacher training, additive manufacturing, mentorship program

1. Introduction

With 3D printing becoming more accessible, it can provide STEM students with valuable hands-on experience and technical skills benefiting their future careers [1]. It takes an abstract concept of an idea and makes it more concrete and tangible. It also encourages creativity, experimentation, and innovation. Students are given a hands-on approach in identifying design flaws and coming up with solutions to fix them [2]. Furthermore, it can foster collaboration and help develop stronger professional relationships with peers. This report is separated into three parts: design method, results and discussion, and conclusions. The design method lists the course objectives and class structure. The results and discussion state how the course fared throughout the semester and the students' feedback on the effectiveness of the course in teaching them 3D printing. The conclusions state the lessons learned teaching the course: CHEE 412: ADVANCE: 3D Printing Workshop.

2. Design Method

CHEE 412: ADVANCE: 3D Printing Workshop is a 3-hour credit course and aims to have students be at an intermediate proficiency in 3D modeling/design and 3D printing. The student teacher has geared this course towards beginners to serve as an introduction to 3D modeling and 3D printing. Students are assumed to have little or no experience in 3D modeling and 3D printing.

The course is structured to be 20% 3D modeling and 80% 3D printing focused. Even though this course focuses on 3D printing, there is a focus in 3D modeling in the beginning of the course since to be able to 3D print an object, that object will first need to be created in a computer program. It will also serve as a good technical skill for the students to have to further develop their career. The main software used in this class is Fusion360, a 3D modeling software, and Cura, a 3D slicing software. Classes during the semester have been split between lectures and labs to give ample time for students to learn and obtain hands-on experience with 3D printers. The 3D printers available for students to use are Flashforge Guider II and Creality Ender 3; both are FDM (fused deposition modeling) 3D printers. Filament available for students to use are poly-lactic acid (PLA) and thermoplastic polyurethane (TPU).

In this undergraduate course, students are graded in five categories: attendance, homework, quizzes, mini-projects, and a final project. Assigned homework involves students using their creativity to draw an object they will 3D model and eventually 3D print. This develops their ability to conceptualize an idea and determine how best to solve any difficulties to achieve the product they envision. Quizzes test students on their knowledge of 3D printing. 3D printers have associated safety hazards (i.e, hot electrical components) and it is important that students are aware of the equipment they are working with, so they do not hurt themselves or damage the 3D printers. Mini-projects and the final project test the students' ability to design a 3D model from scratch and obtain a 3D print with no to little flaws. The graduate student mentor met weekly with the faculty mentor starting a month before the semester to discuss and develop the syllabus, course plan, policies, and activities. The graduate student met with the faculty instructor throughout the semester to discuss updates, issues, and progress. The graduate student was primarily responsible for managing the projects and keeping within the budget thereby giving the graduate student project management experience similar to leading a small research group.

3. Results & Discussion

The course had several undergraduates interested in enrolling and was listed with a max class size of 15 students. However, due to conflicting meeting times with other courses, only four students registered for this course. The small size became more of a benefit throughout the semester since it provided the student teacher to be able to help each individual student more effectively. The students were taught the parts of a 3D printer, the differences between the FDM 3D printers available and how they differ from resin 3D printers, and how to troubleshoot the most common 3D printing issues. In addition, students were given plenty of opportunities during the semester to use the 3D printers and develop their 3D modeling and 3D printing skills. At the end of the semester, an online course survey was given to the students and Table 1 displays the results and the students' feedback on the effectiveness and value of the course. The additional essay questions students were asked in the survey are shown in Table 2 where S1 refers to Student 1, S2 is Student 2, S3 is Student 3, and S4 is Student 4.

Table 1
Results from End of Semester Course Survey

#	Question:	Strongly Disagree	Disagree	Neutral	Agree	Strongly Agree	Average
1	Did you have prior knowledge about 3D printing? (no experience is strongly disagree and lots of experience is strongly agree)	2	0	2	0	0	2.00
2	Did you have prior knowledge about 3D modeling? (no experience is strongly disagree and lots of experience is strongly agree)	2	1	1	0	0	1.75
3	I understood the course objectives.	0	0	0	0	4	5.00
4	I enjoyed the teaching style in this course.	0	0	0	1	3	4.75
5	The teacher provided prompt and helpful feedback.	0	0	0	0	4	5.00
6	The teacher was available for assistance.	0	0	0	0	4	5.00
7	Lecture slides were helpful in learning the course material.	0	0	0	0	4	5.00
8	Quizzes given were helpful in learning the course material.	0	0	0	1	3	4.75
9	This course has improved my oral presentation skills.	0	0	2	1	1	3.75
10	This course allowed me to develop stronger professional relationships with my peers.	0	0	0	1	3	4.75
11	This course helped deepen my understanding of 3D modeling and 3D printing.	0	0	0	0	4	5.00
12	I now feel confident in my 3D printing skills.	0	0	0	0	4	5.00
13	This course has given me confidence in my ability to learn independently.	0	0	0	1	3	4.75
14	Overall, I found this course to be a valuable experience.	0	0	0	0	4	5.00
15	I feel this course should be continued in future semesters.	0	0	0	0	4	5.00
16	This course has helped me prepare for a career in engineering.	0	0	1	0	3	4.50
17	I will be able to list the technical skills learned in this course on my resume.	0	0	0	0	4	5.00

18	I will be able to mention my work in this course during interviews for a job or graduate school.	0	0	0	0	4	5.00
19	This course has motivated you to continue 3D modeling and 3D printing.	0	0	0	0	4	5.00

Based on Table 1 and the students' feedback, this course taught valuable skills that greatly benefit them and their careers. In addition, every student has an interest in continuing to further develop their 3D modeling and 3D printing skills beyond the course. The lowest average on the survey was the course helping students improve their oral presentation skills which is understandable since this course did not have a big focus on oral assignments. The survey showed what worked and what did not in teaching the course and what areas should be focused on if this course was offered again in the future. The core structure of the class seems to be effective and will most likely keep the same format in future classes. The difficulty of the 3D printing projects could be increased, and more quizzes and exams be given to better develop the students' skills to a more intermediate proficiency to help them stand out more as they seek employment after college.

4. Conclusion

The objective is for the Student Teacher to teach an undergraduate 3D printing course from scratch to gain teaching experience under the guidance of a Supervising Instructor for a college semester. There were several lessons learned teaching the course: CHEE 412: ADVANCE: 3D Printing Workshop, a 3-hour credit course aimed to give students an intermediate proficiency in 3D modeling and 3D printing. If the course is offered again in the future and the student teacher remains the one to teach it, she has learned of what worked better for the students to grasp the course material and what she would change for future classes. As a graduate student who is interested in growing a career in the academic field, teaching undergraduates for a semester is invaluable for gaining experience. In addition, this course has made seeking employment in a teaching position a strong possibility.

5. Acknowledgments

This work is supported by the U.S. National Science Foundation under grant number OIA-1946231, the Louisiana Board of Regents for the Louisiana Materials Design Alliance (LAMDA), and the University of Louisiana at Lafayette's Advance Student Research initiative.

6. References

[1] Cheek, L. R., & Carter, V. (2021) STEM Integration Through 3D Printing and Modeling. *Elementary STEM Journal, 26*(1), 6.

[2] Khurma, O. A., Ali, N., & Khine, M. S. (2023). Exploring the impact of 3D printing integration on STEM attitudes in elementary schools. *Contemporary Educational Technology, 15*(4), 458.

Microstructural Analysis of As-deposited and Heat-treated Al 7075 Parts Fabricated by Additive Friction Stir Deposition

Ehsan Bagheri, Huan Ding, Saeid Zavari, Noushin Adibi, Shengmin Guo

Department of Mechanical and Industrial Engineering, Louisiana State University, Baton Rouge, LA 70803

Abstract:
Additive friction stir deposition (AFSD) is a promising metal additive manufacturing technique that offers many advantages over fusion-based methods. Despite recent advancements, research on AFSD is still in its early stages, and processing hard and strong materials like Aluminum 7075 remains challenging. In this study, the microstructure of the as-deposited parts by AFSD were analyzed. Compared to the base material, the precipitations were larger and aggregated for the as-deposited specimens. However, the secondary phases became smaller and more uniformly distributed in the matrix after the heat treatment.

Keywords: Additive manufacturing, Aluminum alloy, Microstructure

1. Introduction

Metal additive manufacturing (AM) is a transformative technology that offers significant advantages across various industries, including enhanced design freedom, reduced production lead time and waste, custom fabrication, and rapid prototyping. Fusion-based metal AM, one of the first commercial techniques, continues to dominate the market. However, this method has inherent constraints that create a gap between production capabilities and industrial demands. Issues such as porosity, residual stress, distortion, hot cracking, elemental segregation, and elemental loss are common in fusion-based AM and compromise the quality of the produced parts. Consequently, it is essential to develop AM techniques that process metallic alloys in the solid state, rather than melting and solidifying them, to avoid these problems [1, 2].

AFSD has been successfully employed for the deposition of various aluminum alloys, ranging from the softer 5xxx and 6xxx series to the harder 2xxx and 7xxx series [3-5]. Numerous studies have explored the relationships between processing parameters and the properties of the printed parts. For instance, Philips et al. [4] reported successful deposition of Al 5083 using AFSD and investigated the mechanical properties and microstructure of the as-deposited part. Ghadimi et al. [6] studied the AFSD of Al 6061, examining the impact of different deposition parameters on the tensile properties of the fabricated parts. A common phenomenon reported in AFSD studies is grain refinement, attributed to dynamic recrystallization caused by the high temperature (above half of the melting temperature) and significant plastic deformation during the process. However, many studies have found that the hardness, strength, and corrosion resistance of as-deposited aluminum parts are often inferior to those of the feedstock material. This degradation in properties is due to changes in the strengthening mechanisms and the loss of hardening precipitates after AFSD, underscoring the importance of post-deposition heat treatment to recover these properties. For example, Zeng et al. [5] subjected as-fabricated Al 6061 parts to T6 heat treatment, resulting in hardness comparable to that of the feedstock due to the changes in the microstructure.

The 7xxx series of aluminum alloys are extensively utilized in the aerospace and military sectors due to their high specific strength, excellent fatigue properties, and machinability. Given the challenges associated with fusion-based additive manufacturing for this series, including hot cracking due to their non-weldable nature, it is essential to employ solid-state techniques such as AFSD. There is a relative scarcity of research on the multilayer AFSD of these alloys. The higher hardness and strength of Al 7075 make the AFSD process particularly challenging. In the present work, two Al 7075 blocks were deposited using AFSD, with one block subjected to heat treatment. Microstructural including X-ray diffraction analysis (XRD), scanning electron microscopy (SEM), and energy dispersive analysis (EDS) were conducted on both parts to evaluate the microstructural changes before and after heat treatment.

2. Materials and methods

Al 7075 square rods with dimensions of 9.5×9.5×457.2 mm^3 were cut from Al 7075-T651 square bars (OnlineMetals) using a waterjet cutter and used as feedstock material. A MELD L3 machine, equipped with a standard tool featuring two pairs of teardrop-shaped protrusions, was employed for 3D printing. An Al 7075-T651 plate (304.8×101.6×12.7 mm^3) was used as the substrate for 3D printing. The substrate was preheated to 250°C to facilitate the printing of the initial layers. To prevent jamming inside the tool during AFSD, the feedstock rods were coated with a thin layer of graphite as a dry lubricant before being fed into the machine. The process began by pushing the rods against the substrate to generate sufficient heat for material flow, and the parts were deposited layer-by-layer based on a G-code. Two large blocks, each with lengths and heights of 165.1 mm and 40.6 mm, respectively, were successfully fabricated. XRD analysis was performed to investigate the phase structure of Al 7075 after AFSD and the effect of heat treatment for the top and bottom layer regions. A Pananalytical Empyrean diffractometer equipped with Pre-FIX (pre-aligned, fast, interchangeable X-ray) modules with monochromatic CuKα radiation was employed for this purpose. The patterns were collected from 10 to 90^0 with a scan step size of 0.01. A ThermoFisher Helio G5 Xe PFIB/SEM machine was utilized in the backscatter electron (BSE) mode for general inspection of the surface of the cross section for top and bottom layers before and after the heat treatment. The composition distribution of the specimens was also studied using the same instrument equipped with EDS.

3. Results and discussion

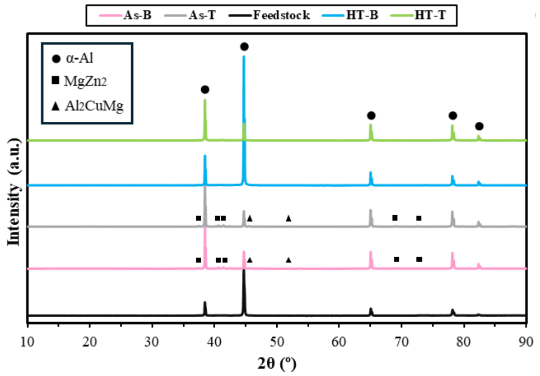

Fig. 1 XRD patterns of the feedstock, as-deposited and heat-treated specimens

The XRD patterns of the feedstock and the top and bottom layers of the as-deposited and heat-treated blocks are shown in Fig. 1. From Fig. 1.a, the feedstock exhibited only the peaks attributed to α-Al (FCC) at 2θ = 38.46, 44.69, 65.10, 78.12, and 82.13° [7]. However, weak peaks corresponding to the η/η' phase ($MgZn_2$) and S phase (Al_2CuMg) were also detected in the as-deposited top and bottom layers. The temperature and pressure applied during the AFSD process caused the precipitates, especially metastable ones, to dissolve into the Al matrix, reprecipitate, and coarsen according to their thermal cycle history. As a result, the precipitates grew larger and became detectable by XRD after the process. The formation of larger secondary phases may deteriorate the mechanical properties of the parts. Similar XRD results have been reported after the AFSD of other Al alloys [5]. The peaks attributed to the secondary phases almost disappeared after the heat treatment. During the T73 treatment of the as-deposited parts, the alloying elements first dissolved back into the matrix and then formed fine and uniformly distributed precipitates after artificial aging.

BSE imaging and EDS mapping were used to further analyze the secondary phases and composition distribution in the matrix. The results for the feedstock and the as-deposited specimens are shown in Fig. 2, while those for the heat-treated samples are depicted in Fig. 3. In the BSE image of the feedstock (Fig. 2.a), a smooth surface with almost no apparent particles was observed. Additionally, the uniform distribution of Mg, Zn, and Cu, attributed to the η/η' and S phases, was detected in the raw material. However, many large particles appeared on the surface of the as-deposited samples, as seen in the BSE images (Fig. 2.b and 2.c). These particles were attributed to secondary phases that reprecipitated non-uniformly during the AFSD process. Furthermore, the precipitates were larger in the bottom layers compared to the top layers, as confirmed by the EDS mapping. This difference is due to the higher number of heating cycles the bottom layers experienced during the deposition of the entire block, leading to precipitation coarsening. After heat treatment, the number of large secondary phases significantly decreased in both the bottom and top specimens. However, the bottom layers still contained more, and larger particles compared to the top layers. These results are consistent with the XRD data, which showed a reduction in the size and number of secondary phases after heat treatment.

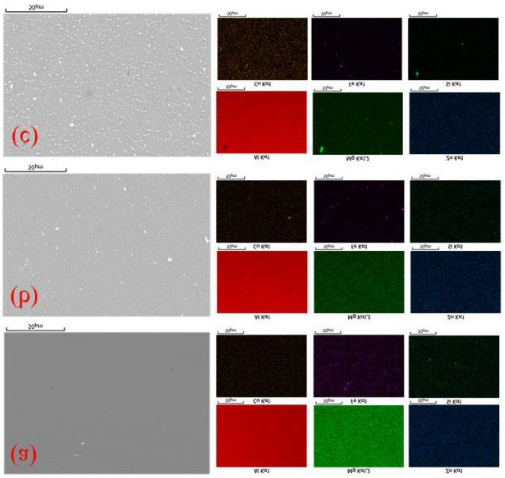

Fig. 2 BSE images and EDS mapping of a. feedstock, b. as-deposited top layers, and c. as-deposited bottom layers specimens

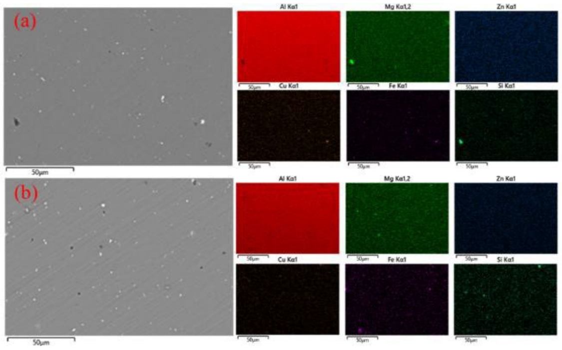

Fig. 3 BSE images and EDS mapping of heat-treated a. top layers, and b. bottom layers specimens

4. Conclusion

In this study, the microstructure of the as-deposited parts by AFSD was analyzed. Compared to the base material, the precipitates in the as-deposited specimens were larger and more aggregated. However, after heat treatment, the secondary phases became smaller and more uniformly distributed in the matrix.

5. Acknowledgments

This work is supported by the U.S. National Science Foundation under grant number OIA-1946231 and the Louisiana Board of Regents for the Louisiana Materials Design Alliance (LAMDA).

6. References

[1] A. Kar, S. Kumar, and S. V. Kailas, "Developing multi-layered 3D printed homogenized structure using solid state deposition method," *Materials Characterization,* vol. 199, p. 112770, 2023/05/01/ 2023, doi: https://doi.org/10.1016/j.matchar.2023.112770.

[2] A. K. Kushwaha *et al.*, "1 - Powder bed fusion–based additive manufacturing: SLS, SLM, SHS, and DMLS," in *Tribology of Additively Manufactured Materials*, P. Kumar, M. Misra, and P. L. Menezes Eds.: Elsevier, 2022, pp. 1-37.

[3] H. Ghadimi *et al.*, "Hardness Distribution of Al2050 Parts Fabricated Using Additive Friction Stir Deposition," *Materials,* vol. 16, no. 3, p. 1278, 2023. [Online]. Available: https://www.mdpi.com/1996-1944/16/3/1278.

[4] B. J. Phillips, C. J. Williamson, R. P. Kinser, J. B. Jordon, K. J. Doherty, and P. G. Allison, "Microstructural and Mechanical Characterization of Additive Friction Stir-Deposition of Aluminum Alloy 5083 Effect of Lubrication on Material Anisotropy," *Materials,* vol. 14, no. 21, p. 6732, 2021. [Online]. Available: https://www.mdpi.com/1996-1944/14/21/6732.

[5] C. Zeng *et al.*, "Microstructure Evolution of Al6061 Alloy Made by Additive Friction Stir Deposition," *Materials,* vol. 15, no. 10, p. 3676, 2022. [Online]. Available: https://www.mdpi.com/1996-1944/15/10/3676.

[6] H. Ghadimi, M. Talachian, H. Ding, S. Emanet, and S. Guo, "The Effects of Layer Thickness on the Mechanical Properties of Additive Friction Stir Deposition-Fabricated Aluminum Alloy 6061 Parts," *Metals,* vol. 14, no. 1, p. 101, 2024. [Online]. Available: https://www.mdpi.com/2075-4701/14/1/101.

[7] S. M. Bayazid, H. Farhangi, H. Asgharzadeh, L. Radan, A. Ghahramani, and A. Mirhaji, "Effect of cyclic solution treatment on microstructure and mechanical properties of friction stir welded 7075 Al alloy," *Materials Science and Engineering A,* vol. 649, 01/01 2016.

Nanofiber-in-Microfiber Carbon/Silicon Composite Anode with High Silicon Content for Lithium-ion Batteries

Yuxin Wang[1,2], Yixin Liao[2], Le Wang[2], and Shengnian Wang[2]

[1] Chemical Engineering, West Virginia University, [2] Chemical Engineering, Institute for Micromanufacturing, Louisiana Tech University

Abstract: Silicon-rich anodes are desired to leverage the energy capacity of lithium-ion batteries (LIBs) towards critical markets. We prepared new silicon-rich composite anodes with a nanofiber-in-microfiber architecture using a co-axial electrospinning setup. A polyvinyl alcohol (PVA) solution that allows high silicon content serves as the central stream, which holds silicon nanoparticles into short, branched composite nanofibers. These nanofibers were wrapped by long, ductile microfibers made of polyacrylonitrile (PAN) that is supplied in the sheath fluid. After carbonization, the received carbon/silicon composites were tested as the anode of LIBs, in which the silicon-rich nanofibers host the majority of lithium ions while their thin carbon skin originated from PVA promotes the conductivity and charge transfer. The outside PAN-derived microfibers provide needed structural support for those encapsulated silicon-rich nanofibers, making the final composites also an integrated, three-dimensional current collector. The nanofibrous morphology and the void space in between help accommodate the notorious volume expansion issues during lithiation/delithiation. The new composites were confirmed on their nanofiber-in-microfiber configuration. With a Si content of 40%, this unique fibrous anode material achieves ~900 mAh g^{-1} specific capacity and ~90% capacity retention from cycle 50 to cycle 250 by effectively balancing some major challenges associated with silicon-rich anodes.

Keywords: Silicon-rich anode; Nanofiber; Microfiber; Lithium-ion Batteries; Composites

1. Introduction

Rechargeable lithium-ion batteries (LIBs) dominate current mobile electronics market because of their high energy density, long cycle life, and promising power performance. However, commercial LIBs have been stretched to nearly their capacity limit with current metal oxide cathodes and graphite anodes while not yet meet the need on energy density (energy/volume) and specific capacity (energy/weight) from other critical energy storage applications such as electric transportation or stationary power storage that need much large energy/power capacity. Tremendous efforts have been made in the past decade in the search for new active materials and/or desired configurations of electrodes for LIBs. The adoption of silicon/carbon composites seems a natural solution of challenges on the anode materials for their potential heritage of merits from carbon (high electrical conductivity) and silicon (high lithium capacity). Despite their successful proof-of-concept, the silicon/carbon composite anodes still face great challenges in their processing and manufacturing for high throughput and desired performance. High solid content is essential for silicon-based anode materials of large energy capacity while their continuous addition in polymer contributes to a dramatic increase of the viscosity of the processing fluid after passing a critical solid percentage. Beyond the maximum silicon mass allowance in a particular polymer solution, fiber production becomes very challenging, which leads to collapsed nanofibers or nanofibers that lose ductility.

To achieve composite nanofibers with high silicon content and ductility of long fiber network, we present here a nanofiber-in-microfiber composite configuration with rich silicon content and ductile fiber mat morphology [1]. The new silicon/carbon composites were prepared through a coaxial electrospinning process (Fig 1a). A PVA aqueous solution was used as the middle electrospinning fluid in which silicon nanoparticles (25-50% content) were dispersed prior to electrospinning. A PAN/DMF (5-10 wt%) solution was introduced in the sheath stream to wrap up the silicon-rich nanofibers, serving as ductile shell to help hold the fibrous structure of inside silicon-rich composites after the great mass loss of PVA during later carbonization in N_2 gas. In these fibrous silicon/carbon composites (Fig 1b), silicon serves as the active materials for Li ion host; PVA helps hold silicon nanoparticles in a short nanofiber format; PAN works as the outer support layer to retain the fibrous morphology to provide the essential electron conductivity and flexibility needed as collector-free anodes. The produced nanofiber-in-microfiber carbon/silicon composite were further assembled and tested for their battery performance.

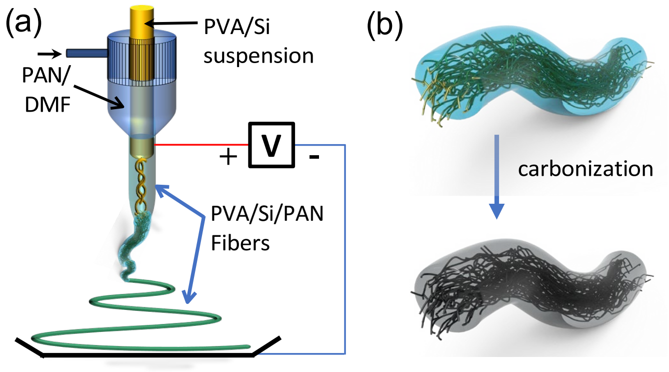

Fig 1. Schematic of the coaxial electrospinning process in the manufacture of nanofiber-in-microfiber composite fiber mat (a) and the 3D anode configuration with Si/PVA nanofiber bundles in PAN microfiber before and after carbonization (b).

2. Nanofiber-in-Microfiber Carbon/Silicon Composite Preparation

The morphology of PVA/Si/PAN composites fibers are shown in Fig 2. As the PAN outer layer is thick enough to fully wrap up the inside PVA/Si nanofibers, the composite microfibers have taut and smooth surface (Fig 2a). The average diameter of these fibers varies from 5-9 µm, on which silicon nanoparticles or polymer nanofibers scattered. Inside microfibers, porous structures made of PVA/Si nanofibers can be clearly seen (Fig 2b). To reveal how PVA/silicon nanofibers are wrapped inside PAN microfibers, TEM images of the composite microfibers were taken. As shown in Fig 2c, PVA/Si nanofibers with an average diameter 300-600 nm present with well-reserved nanofiber morphology. Silicon nanoparticles are encapsulated in individual PVA nanofibers like bead chains (Fig 2c). Occasional aggregations are found inside nanofibers at entangled locations (inset of Fig 2c). Element mapping was done using EDS to further reveal the dispersion status of silicon nanoparticles in composite microfibers. As shown in Fig 2d, silicon nanoparticles are distributed uniformly in the carbon domains of the composite microfibers.

During carbonization, a large percentage of carbon in PVA/Si nanofibers is lost, which helps leverage the silicon/carbon ratio in the final C/Si composites. Although carbonization raises the eventual silicon percentage, it costs the ductility of those nanofibers on many occasions. This disqualifies their use as flexible 3D current collector and makes them not much different from those composite anodes that were made by physically mixing conductive carbon and silicon nanoparticles. After introducing a layer of PAN to wrap up the PVA/Si nanofiber bundles, the produced silicon-rich composite microfibers become ductile again after carbonization. With nearly 40-60% of the original carbon molecules is retained after cyclization of carbon atoms, this PAN-derived fibrous shell provides mechanical strength to the composite microfiber mat while protect the thin silicon/carbon nanofibers insides to hold their morphology to avoid pulverization.

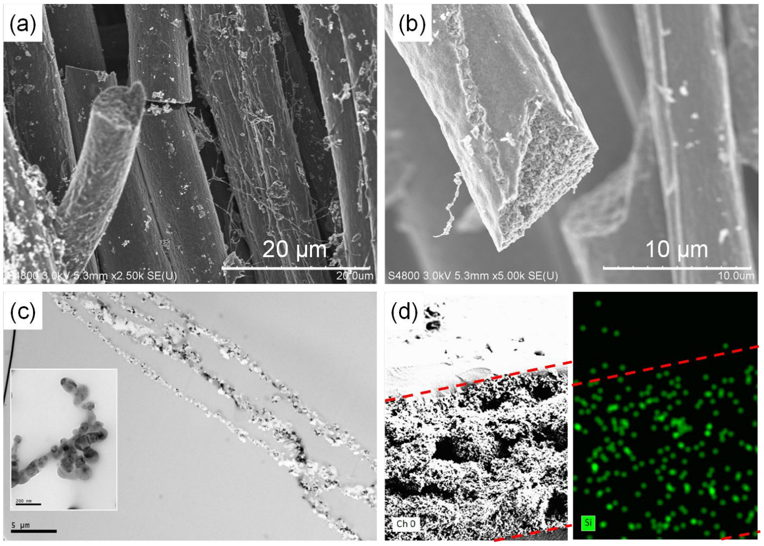

Fig 2. Images of SEM (a, b), TEM (c), and EDS elemental mapping (d) of PVA/Si/PAN fibers with an original Si/PVA ratio of 1:3 (or 25 wt%). Panel d has the boundary of a microfiber outlined in dashed red line.

3. Battery Testing

The electrochemical performance of these nanofiber-in-microfiber composite anodes was done via galvanostatic charge/discharge experiments. Fig 3a shows the voltage profiles (plot of potential against specific capacity) at the end of 1st, 2nd, 10th, 50th, and 100th galvanostatic charge/discharge cycles of the composite nanofibers with silicon/carbon ratios of 40 wt%. For the first cycle, composite fiber anodes show 2458 mAh g^{-1} (charge) and 1749 mAh g^{-1} (discharge). Here the capacity is calculated based on the total mass of the anode material (i.e., including both carbon and Si). Starting from the second cycle, a second plateau appears on the charge and discharge curves of these Si-rich anodes at a voltage of ~ 0.25 V (charge) and ~0.50 V (discharge), respectively, attributed to the phase transformations between different Si-Li states during lithiation and delithiation processes. After the establishment of stable SEI, the coulombic efficiency quickly recovers to nearly 100% and remains high afterwards (Fig 3b). The composite fibrous anode with 50 wt% Si has the fastest fading rate on the voltage plateau and percentage loss of the specific capacity. Its specific capacity value drops below that of the anodes with 40 wt% Si after 75 cycles and even below the anodes with 25 wt% Si after 125 cycles. The anodes with 25 wt% and 40 wt% Si show a similar plateau shrinkage and capacity decay dynamics, despite their different specific capacity values. After 10 cycles, the retention ratio of the specific capacity is 87% for the anodes with 40 wt% Si and 88% for the ones with 25 wt% Si, respectively. After 50 cycles, the retention capacity drops to 65% (for anodes with 40 wt%

Si) and 64% (for anodes with 25 wt% Si). Nonetheless, similar decay rates for these two composites anodes sustains with only minor variations. This suggests that the lithiation/delithiation situations in them are similar. For over 250 cycles, the specific capacity of the composite fibrous anode with 40 wt% Si retains ~900 mAh g^{-1} (with only additional 10% loss from cycle 50 to cycle 250).

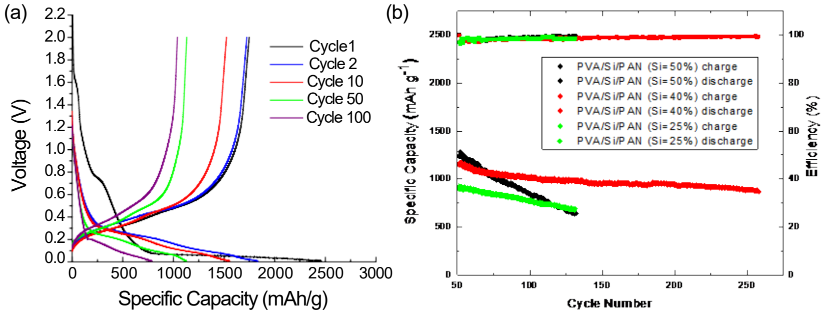

Fig 3. (a) The voltage profiles for galvanostatic charge/discharge cycles of nanofibers-in-microfibers composite anodes with a Si ratio of 40%. (b) Cycling performances and coulombic efficiency of those PVA/Si/PAN fibers of various Si contents.

4. Conclusion

A new nanofiber-in-microfiber, Si-rich composite anode was prepared through a coaxial electrospinning, in which PVA/silicon suspension flows in the middle and a PAN/DMF solution serves as the sheath stream. The high-quality, nonwoven carbon microfibers derived from PAN outer shell provide structural protection for short, silicon-rich nanofibers inside and prevent further oxidation of silicon during fiber processing. Together with the thin carbon skin over silicon/carbon nanofiber bundles inside, the microfiber mats form an electrically conductive network to serve as the 3D current collector to promote Li ion transport and charge transfer during charge/discharge processes. Simultaneously, short silicon nanofibers and the mesoporous buffering spaces among them help effectively mitigate the induced stress in Si nanoparticles initialized by the volume change during Li insertion and extraction. All these features of this nanofiber-in-microfiber composite anode together effectively balance issues between electrode pulverization and high reversible capacity, leading to promising electrochemical performance and capacity retention for silicon-rich anodes to move forwards their commercialization. The unique processing strategy involved in this work also suggests a new route to manufacture composite nanomaterials with high solid content in broad applications beyond LIBs.

5. Acknowledgments

This work is supported by the U.S. National Science Foundation under grant number OIA-1946231 and the Louisiana Board of Regents for the Louisiana Materials Design Alliance (LAMDA). We acknowledge additional financial support from Louisiana Board of Regent, ITRS [LEQSF(2019-20)-RD-D-07].

6. References

[1] Y Pei, Y. Wang, A. Chang, Y. Liao, G. Zhang, X. Wen, S. Wang, Nanofiber-in-Microfiber Carbon/Silicon Composite Anode with High Silicon Content for Lithium-ion Batteries, ***Carbon***, 2022, 203, 436 – 444.

Numerical Modeling of Additive Friction Stir Deposition of AA6061-T6 Alloy Using Coupled Eulerian Lagrangian Technique

Chowdhury Sadid Alam[1], Saied Zavari[2], Pouria Nourian[1], Shengmin Guo[2], M Shafiqur Rahman[1]

[1]Department of Mechanical Engineering, Louisiana Tech University
[2]Department of Mechanical & Industrial Engineering, Louisiana State University

Abstract: Additive Friction Stir Deposition (AFSD) is a unique method for making solid metal structures that are very strong and have properties like wrought materials. A computational model was created in this research to analyze the thermal and mechanical behavior of aluminum alloy AA6061, using a plastic deformation-based finite element (FE) approach. This model considers important factors of the AFSD process such as tool speeds and material flow, predicting temperature, cooling, and stress in different scenarios. The model's accuracy was confirmed by comparing its results with the AFSD experimental data obtained from the MELD L3 machine. This computational model offers a cost-effective way to foresee results and determine the best conditions for material deposition in the AFSD process.

Keywords: Additive Friction Stir Deposition, Plastic Deformation, Johnson-Cook Plasticity Model, Coupled Eulerian Lagrangian Model, Eulerian Volume Fraction

1. Introduction

Additive Friction Stir Deposition (AFSD) is a solid-state additive manufacturing (AM) method for creating dense metallic 3D structures, advancing the traditional AM techniques. A rotating tool deposits material onto a substrate, generating heat through friction that deforms the material without melting it. This process produces fine microstructures and mechanical properties like wrought metals, with minimal defects. AFSD uniquely achieves wrought-like mechanical characteristics in the as-printed state. [1-3]. In the past decade, researchers have pursued AFSD analysis with various metals and alloys to understand the process-material interplay focusing heavily on the experimental studies. However, numerical modeling of the thermo-mechanical response of AFSD remains underexplored, despite their potential to save time and cost in experiments. The full potential of AFSD including material choice, scalability, and design flexibility is yet to be unlocked, and therefore, more rigorous studies are required to investigate the thermo-mechanical aspects of AFSD.

This study aims to numerically simulate the process-material interplay in AFSD using AA6061-T6 feed material replicating the experiments conducted by the MELD L3 machine. A computational model, using the coupled Eulerian-Lagrangian (CEL)-based finite element (FE) approach (Fig. 1), is developed and experimentally validated to examine the effects of various process parameters on the thermal and mechanical properties of deposition layers, including material flow and temperature distribution [4]. The CEL model for AFSD uses independent Lagrangian material within the Eulerian boundary, with the substrate in the Eulerian domain and the rotating tool in the Lagrangian formulation. The model incorporates key AFSD parameters like tool rotation speed, traverse speed, and material deposition rate. Transient thermo-mechanical simulations with various process parameters generate reliable results for temperature distribution, cooling rate, equivalent stress, and material flow behaviors in AFSD.

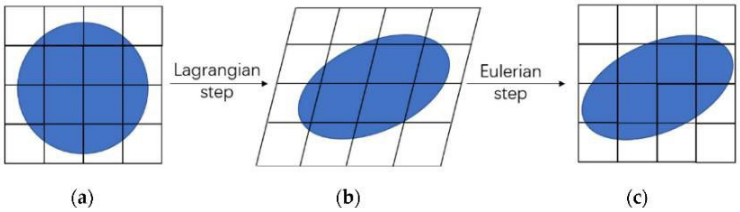

Figure 1. Steps in the Coupled Eulerian-Lagrangian (CEL) method for dynamic analysis [4]

2. Materials and Method

A coupled Eulerian-Lagrangian (CEL) approach is developed in ABAQUS to simulate the thermo-mechanical response of the AFSD process [4]. The CEL formulation is implemented by combining the Johnson-Cook material law and Coulomb's frictional law [5, 6]. Figure 2(a) shows the processing of an Al6061-T6 block using the MELD L3 machine at LSU. Following the experimental set-up, a full-length model is created as shown in Fig. 2(b), where the substrate measures 304.8 mm × 101.6 mm × 12.7 mm. The hollow circular tool carries the solid and square rod-shaped feed material with a cross section of 9.5 mm × 9.5 mm. A rigid circular piston drives geometry that pushes material onto substrate. AFSD layer height is determined by the tool-substrate gap (1.5 mm). Fig. 2(c) shows the Eulerian mesh assembly of the AFSD process having a total of 66,682 elements. The top surface was exposed to convection and radiation with an ambient temperature of 293 K. After plastic deformation, layers are deposited at temperatures around 90% of the feed material's melting point. The optimum deposition condition is achieved by configuring the tool's spindle speed, traverse speed, and material feed rate.

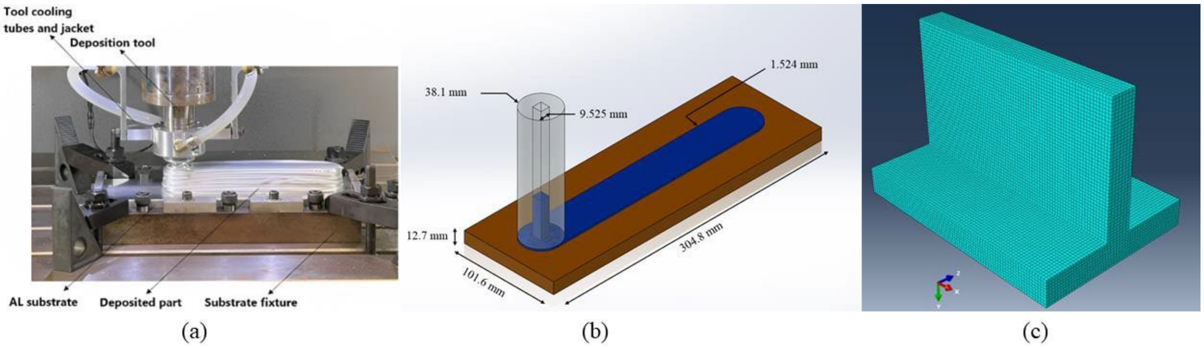

Figure 2. (a) AFSD experiment, (b) physical domain of the CEL model, and (c) computational domain

3. Results and Discussion

Results for the material flow and temperature distribution from the CEL model are discussed in this section.

3.1 Material Flow

The CEL model can incorporate the thermal and physical properties of any suitable materials and can predict the material flow behavior for various AFSD process parameters [7]. An optimum case of AA 6061-T6 deposition is shown in Fig. 3 with 300 rpm tool rotation speed, 6 inch/mm actuator push speed, and 7 inch/mm tool traverse speed. The distribution of materials is determined by the Eulerian volume fraction (EVF) using the CEL model, where an element is capable of existing in any state. When an element is completely full of the material, EVF of void equals zero (blue), but when the element is completely empty, EVF equals one (red). The Lagrangian object can move around in the zone without encountering any resistance from the Eulerian substance. A time step that is sufficiently small is used so that there is no element distortion caused by the Lagrangian phase. Explicit integrations are carried out so that the solution is dependent solely on the outcomes of the most recent time step. In this study, the AFSD modeling is conducted using the CEL method in ABAQUS. This is done so that large deformations can be considered while the thermo-mechanical conditions are calculated with the increment of the involved time steps. Figure 3 shows the material flow from the hollow tool of MELD machine in AFSD process for the AA 6061-T6 feed material. It depicts the deposition of the feed material in the horizontal layer of elements with an estimation of the missed depositions and defects at the top of the layer.

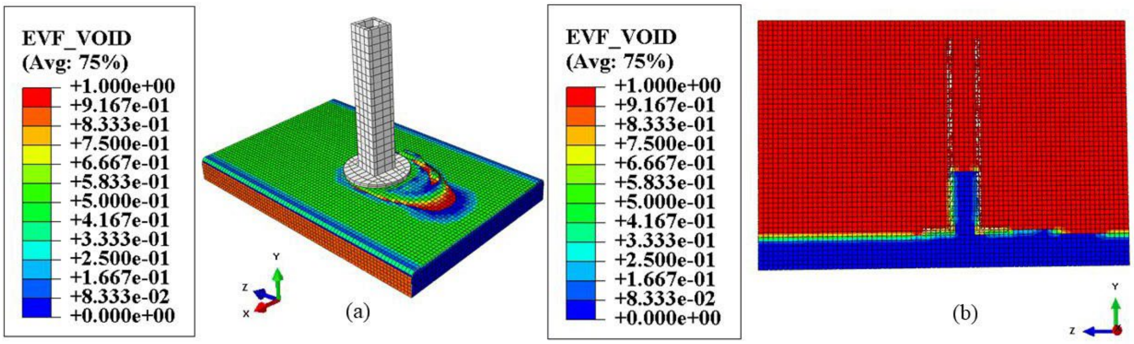

Figure 3. Eulerian Volume Fraction at 20.45 s during AFSD with 300 rpm tool rotation speed, 6 inch/min actuator push speed, and 7 inch/min tool traverse speed, where the blue zone indicates 100% material

3.2 Temperature Distribution

The CEL model can predict temperature at any point in the model geometry at any time. Figure 4 (a, b) shows a case of temperature distribution for 300 rpm tool rotation speed, 6 inch/min actuator push speed, and 7 inch/min tool traverse speed. The white marked dot at the top of the substrate at Fig. 4(b) is selected to extract the temperature history with respect to time plotted in Fig. 4(c).

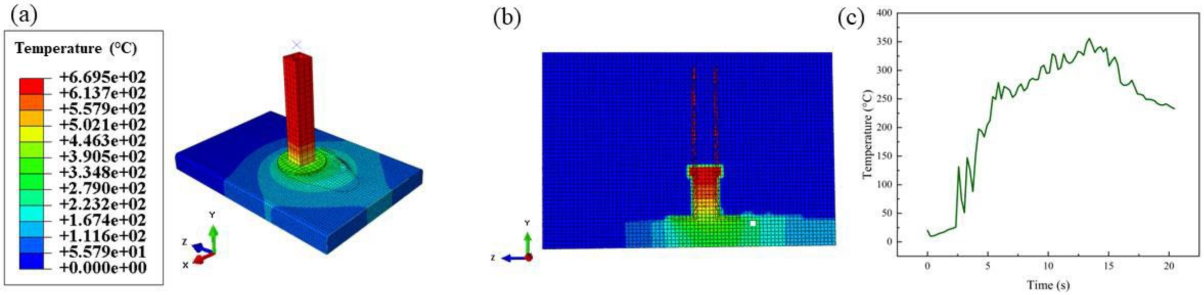

Figure 4. (a) Temperature distribution during AFSD at 20.45 s (isometric view), (b) cross-sectional view of the temperature distribution at 20.45 s, and (c) temperature history at an element at top of substrate (white marked) with 300 rpm tool rotation speed, 6 inch/min actuator push speed, and 7 inch/min tool traverse speed

Experimental approaches lack the ability to record in-layer temperature information during the AFSD process whereas the current model can offer accurate predictions within the solution boundary. The peak temperature in the AFSD layer is also obtained successfully using the CEL model with the change of processing parameters. The CEL model is validated by comparing with experimental data obtained by thermocouples fit under the substrate during the AFSD process, which shows a maximum deviation of 14.7 % for the peak temperature at a given condition [7]. The peak temperature changes with the variations of the three major parameters. The increase of actuator push speed and the tool rotation speed leads to an increase in the peak temperature when other input parameters are kept as constants. However, the peak temperature decreases with the increase of tool traverse speed initially and then starts increasing after a specific value, leaving an optimum range for the tool rotation speed. This phenomenon is observed from both the CEL model and the AFSD experiments with the Al alloy.

4. Conclusion

Numerical simulation of the AFSD process is conducted using an AA 6061 specimen to analyze the thermal and mechanical characteristics of the deposited layer. The study investigates the impact of process parameters on AFSD-produced parts, examining material flow, temperature distribution, stress generation, and thermal properties under various conditions. Experimental findings on substrate temperatures closely match the simulation results, validating the model as a useful tool for predicting the quality of deposited layers based on specified process parameters. Future research will extend AFSD modeling to high entropy alloys with conformal substrates and applications at smaller scales, aiming to establish a comprehensive dataset for future Machine Learning studies on AFSD process parameters and outcomes.

5. Acknowledgments

This research is supported by the National Science Foundation through cooperative agreement OIA-1541079 and the Louisiana Board of Regents.

6. References

[1] Tuncer, N. and Bose, A. (2020) “Solid-state metal additive manufacturing: A Review,” JOM, 72(9), pp. 3090–3111.

[2] Shao, J. et al. (2023) “Additive friction stir deposition of metallic materials: Process, structure and properties”, Materials & Design, 234, p. 112356.

[3] Rivera, O.G. et al. (2017) “Microstructures and mechanical behavior of Inconel 625 fabricated by solid-state additive manufacturing,” Materials Science and Engineering: A, 694, pp. 1–9.

[4] Xu, H. et al. (2023) “3D simulation of debris flows with the coupled Eulerian–Lagrangian method and an investigation of the runout”, Mathematics, 11(16), p. 3493. doi:10.3390/math11163493.

[5] Salloomi, K.N. and Al-Sumaidae, S. (2021) “Coupled Eulerian–Lagrangian prediction of thermal and residual stress environments in dissimilar friction stir welding of aluminum alloys,” Journal of Advanced Joining Processes, vol. 3, p. 100052.

[6] K. Kuykendall, T. Nelson, and C. Sorensen, “On the selection of constitutive laws used in modeling friction stir welding,” Int. J. Mach., vol. 74, pp. 74–85, 2013.

[7] Alam, C. S. (2024) “Additive Friction Stir Deposition: Thermo-mechanical Simulation and Materials Characterization,” MS Thesis, Louisiana Tech University, Ruston, LA, USA.

Numerical Study on SMP Beam-Column Actuators

Alireza Ostadrahimi[a*], Guoqiang Li[a]

[a]Department of Mechanical and Industrial Engineering, Louisiana State University

Abstract: The present paper focuses on studying the anti-buckling behavior of prismatic shape memory alloy (SMA) beam-columns. It combines analytical and semi-analytical approaches to investigate the process of column straightening for anti-buckling. We try to comprehensively describe this phenomenon and develop a mathematical model to formulate each step of the anti-buckling problem. Due to the complex stress-strain behavior of SMA material, nine different cases of stress-height diagrams may potentially occur during this effect; thus, for facilitating the design process of SMA structures, corresponding forces and moments to each case, are analytically derived. We also conduct an experimental test to validate the analytical model and then compare it with existing numerical results. Our demonstration establishes that the primary cause of beam-column straightening is not the uniformity of stress, but rather the achievement of uniform strain across all fibers of the cross section. This uniform strain distribution implies that the curvature of the beam-column diminishes to zero.

Keywords: Anti-buckling, Shape memory alloy, Actuators, Beam-column

1. Introduction

Displacement (angle or stroke), load (or force) as well as bandwidth (frequency or speed) are three main technical objectives needing to be addressed in designing SMA actuators for any industrial application. There always exists a challenge between the constraints of a specific application or design and potentially satisfying its conflicting objectives based on their requirements. As an example, thicker actuators generate higher force but actuate more slowly than thinner ones, shorter length of actuators may require less triggering in energy, however it provides less stroke or displacement. Moreover, environmental conditions, permissible weight and size, positional control and stability, cost, durability, and maintenance can be added to the available constraints [1-5].

The Souza model, developed in 1998, is a three-dimensional framework that effectively describes the unique effects of both pseudoelasticities (PE) and shape memory effect (SME) within the realm of small deformations. This model, rooted in the theory of irreversible thermodynamics, provides a general reduced one-dimensional representation when considering a uniaxial test. Let s , e, E and e^{tr} be, respectively, the normal stress, strain, Elasticity modulus, and transformation strain, then

$$s = E\left(e - e^{tr}\right) \tag{1}$$

Figure 1: The stress-strain characteristics and the material parameters associated with the Souza model [32]

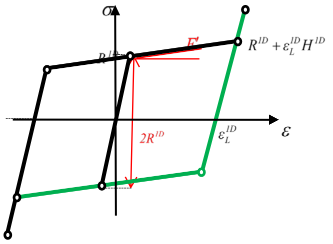

---

[*] Corresponding Author: lguoqi1@lsu.edu

Table 1: Stress-strain relationship for different regions [32]

Region / Parameters	Elastic	Detwinning	Twined martensitic twin	Negative martensitic twin
Transformation strain (e^{tr})	0	$\left(\sigma-(R^{1\mathrm{D}}+\tau_{M}^{1\mathrm{D}})\right)\big/H^{1\mathrm{D}}$	ε_{L}^{1D}	$-\varepsilon_{L}^{1D}$
Constitutive relation	$\sigma=E\varepsilon$	$\sigma=E'(\varepsilon+\varepsilon_0)$	$\sigma=E(\varepsilon-\varepsilon_{L}^{1D})$	$\sigma=E\,(\varepsilon+\varepsilon_{L}^{1D})$

Material parameters in the 1D Souza model (Figure 1 and Table 1) can be described below:

$$\varepsilon_0 = \frac{{}^{1\mathrm{D}}\quad {}^{1\mathrm{D}}_{M}}{H^{1\mathrm{D}}},\quad E = \frac{{}^{1\mathrm{D}}}{H^{1\mathrm{D}}+E},\quad \varepsilon_L = \left(\sqrt{2/3}\right)\varepsilon_L \tag{2}$$

$$H^{1\mathrm{D}}=\left(3/2\right)H,\quad R^{1\mathrm{D}}=\left(\sqrt{3/2}\right)R,\quad \tau_{M}^{1\mathrm{D}}=\left(\sqrt{3/2}\right)\tau_{M}$$

where R, H and ε_L are, respectively, elastic domain radius, phase transformation hardening, and transformation strain at its maximum value during a uni-axial loading condition in a 3D model. Furthermore, considering T_0 and β reference temperature and a material parameter, respectively, τ_M may be defined as:

3. Anti-buckling Problem

In this section, we provide a concise description of the material behavior of SMA beam-column and its loading steps to display anti-buckling behavior. This problem consists of two stages: in the first stage, the pre-strained SMA beam undergoes bending stresses caused by transverse loading or bending moment (Figure 2a). After removing the transverse load a residual deflection may remain in the beam. In the second stage, an axially compressive load exerts on this pre-bent beam; thus, in contrast to ordinary materials, beam deflection does not increase and/or buckle (Figure 2b), rather the deflection starts decreasing and eventually it becomes straight (Figure 2c).

Worth to note that when a martensite SMA beam is under bending stress, some fibers on both sides of the beam experience a detwinning process from twinned martensitic variants to positive or negative detwinned variants in tensile or compressive sides, respectively. By removing the transverse loads, a substantial deflection may remain in the beam-column and subsequently, bending stress distributes inhomogeneously across the cross-section. In the second stage as the axial load applies on the beam column, the fibers in the tensile side reorient into negative detwinned martensitic variants; thus, gradually a uniform stress distribution occurs in the beam meaning that residual curvature and deflection reach zero.

In the following discussion, we try to deeply describe the exact process of straightening in the beam and then analytically drive its governing equations to estimate the generated bending moment and required axial load as beam deflection reverts back to its initial shape. The pre-bent beam with length *L* and initial residual deflection will be exposed to a compressive load *F* as shown in Figure 2c.

.1. Stage I: Moment-curvature relationship for SMA beam-column under bending

In this section, to generate bending stress in the pseudo-plastic beam at the first stage, the bending moment-curvature relationship obtained by Ostadrahimi et al. [32] is employed. In the most general case, we can divide the cross-section into three zones, 1: elastic core when stress in these fibers is lower than detwinning start stress (σ_s), 2: detwinning zone when the fibers in this region have the stress in between σ_s and σ_f (detwinning finish stress), 3: saturation zone in which fibers are fully transformed to detwinned martensite. In order to obtain the total moment, bending moments in each region must be calculated and summed across the whole cross-section. The kinematics of a section may be described using two variables of normal strain (ε) and its corresponding curvature (κ). Based on classical beam theory, normal strain varies linearly with the beam height (*z*) as

$$\varepsilon(z) = -\kappa z \tag{4}$$

According to Table 1, the maximum elastic curvature (κ_e^{max}) and maximum detwinning curvature (κ_{de}^{max}) are obtained and presented in Table 2. For the curvature lower than κ_e^{max} , all fibers are located in the elastic zone, and for higher curvature, if some fibers exceed the detwinned zone, then the detwinning process should occur in the middle part (Figure 3). To describe a complete bending moment-curvature relationship, it is necessary to obtain the boundaries of each zone (h_e and h_{de} , Figure 3). Considering the normal strain at points *a* ($\varepsilon_a = \sigma_s / E$) and *b* ($\varepsilon_b = \sigma_s / E + H^{1D}\varepsilon_L^{1D} / E'$) as well as Equation 4, the height of the elastic and detwinning zones are derived and presented in Table 2.

Table 2: Maximum curvature and height of each one [2]

Maximum elastic curvature	Maximum detwinning curvature	Height of elastic zone	Height of detwinning zone
$\kappa_e^{max} = \frac{2\sigma_s}{Eh}$	$\kappa_{de}^{max} = -\frac{2}{h}\left(\frac{\sigma_f}{E'} - \varepsilon_0\right)$	$h_e = \frac{\sigma_s}{E\kappa_l}$	$h_{de} = \frac{H^{1D}\varepsilon_L^{1D}}{E'\kappa_l}$

2. Results

In this example, to proceed more deeply in the anti-buckling behavior and extract all cases of stress distributions in Figure 5 (a, b), a square beam with a dimension of 1×1mm, length of 10 mm, and material parameters presented in Table 7 are considered. For the occurrence of all cases, it is required to induce saturation region in both compression and tension sides of the column. Due to the initial compression of about 210 kN, all fibers will be in the negative saturation region and then the pre-strain reaches -0.058. Subsequently, the length of the beam reduces about 0.5 mm from its initial value, and then upon unloading the stress uniformly comes back to zero (Figure 19a). By imposing a bending moment of about 90 Nmm, the beam fibers at different positions may follow different paths due to the different amounts of generated strain in each fiber. As shown in Figure 19 b, the outmost fibers at both sides (-0.5 and 0.5), respectively, might be endured being in negative and positive saturation regions. Moreover, due to the reverse phase transformation in tensile sides, some fibers seem to have been loaded in this region (-0.125, 0.125, 0.25). Regarding different moduli of elasticity in saturation and phase transformation regions, there must be a relocation for beam-neutral fiber to satisfy force equilibrium. Thus, the beam is under applied load whereas some fiber similar to -0.3125 strain has an initial loading and then unloading path attributing to the movement neutral fiber. Regarding Figure 19c, upon unloading the stress could be reduced elastically and/or through reverse phase transformation. Once the axial load is applied it is expected to have a stress reduction throughout the beam, however, the compressive side may release its stress and some portions go to the tensile side as illustrated for the fiber at -0.5 mm in Figure 19d. Given further axial load gradually causes all fibers to experience negative reverse phase transformation (Figure 19e, f) and eventually in this example both stress and strain of the fibers converge into a specific amount (Figure 19g), consequently the curvature and deflection return to zero.

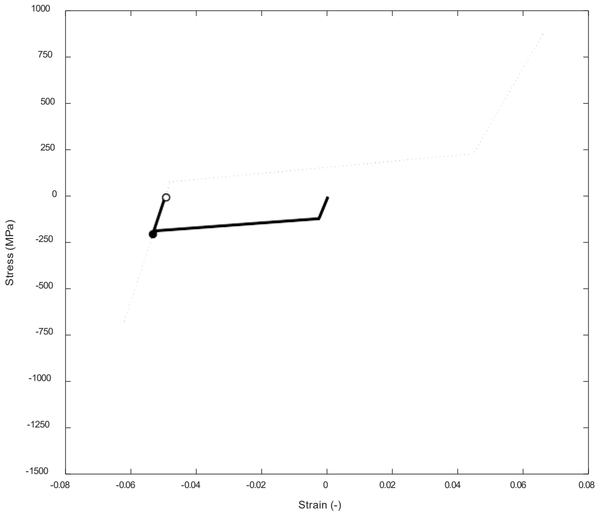

a: loading and unloading of the axially compressive load at the first stage

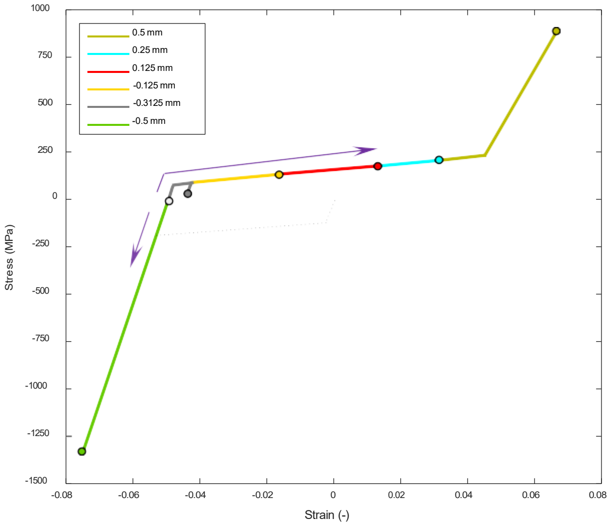

b: applying a bending moment at the second stage

3. Conclusions:

The present paper aims to provide an analytical and experimental investigation into the anti-buckling behavior of prismatic shape memory alloy (SMA) beam-columns. The paper begins by thoroughly describing the process of column straightening during anti-buckling and develops a mathematical model based on this concept. The analytical modeling approach considers nine distinct cases of loading and unloading stages that occur during anti-buckling. Each stage is step by step formulated, and the corresponding force and moment values are derived and presented, primarily for the purpose of designing SMA beam-columns.

4. Acknowledgments

This work is supported by the U.S. National Science Foundation under grant number OIA-1946231 and the Louisiana Board of Regents for the Louisiana Materials Design Alliance (LAMDA).

5. References

[1]. Billah, A. H. M. M., Rahman, J., & Zhang, Q. (2022). Shape memory alloys (SMAs) for resilient bridges: A state-of-the-art review. Structures, 37, 514–527.

[2]. Fang, C. (2022). SMAs for infrastructures in seismic zones: A critical review of latest trends and future needs. Journal of Building Engineering, 57, 104918.

[3]. Rastjoo, S., Fechner, R., Bumke, L., Kötz, M., Quandt, E., & Kohl, M. (2020). Development and co-integration of an SMA/Si bimorphnanoactuator for Si photonic circuits. Microelectron. Eng., 225, 111257.

Optimizing Processing Parameters for Additive Friction Stir Deposition of Al 7075 Components

Ehsan Bagheri, Saeid Zavari, Noushin Adibi, Shengmin Guo

Department of Mechanical and Industrial Engineering, Louisiana State University

Abstract: Additive friction stir deposition (AFSD) is a relatively new metal additive manufacturing technique that offers numerous advantages over fusion-based methods. Despite recent advancements, research on AFSD is still in its early stages, and processing hard and strong materials like Aluminum 7075 remains challenging. This study introduces and optimizes a set of processing parameters for the AFSD of defect-free Al 7075 parts. The continuity equation is used as the basis for the process and modified to remove defects. Focusing on the need for a faster deposition rate, which is crucial for industrial applications, this research aims to establish higher deposition parameters than those found in existing literature.

Keywords: Additive manufacturing, Additive friction stir deposition, Processing parameters, Al 7075

1. Introduction

Additive friction stir deposition (AFSD) is an emerging and promising additive manufacturing technique that offers several advantages over traditional methods. Similar to friction stir welding, AFSD uses friction forces to generate material flow for 3D printing. A metallic rod is fed into a rotating tool and plunged onto a substrate's surface. The resulting heat and pressure cause the material to flow, allowing the part to be printed layer-by-layer. This process produces fully dense structures with minimal residual stress and distortion, thanks to the absence of the high thermal gradients typical of other additive manufacturing techniques like powder bed fusion. One of the significant benefits of AFSD is its high deposition rate, making it an ideal manufacturing technique to reduce time and costs. Additionally, there are no limitations on the size of the print chamber, allowing for the production of large parts. The heat-affected zone is smaller in AFSD, and the occurrence of porosity and cracks is significantly reduced compared to other techniques. Consequently, the physical and structural properties of parts printed using AFSD are generally superior [1, 2].

There are many potential applications for AFSD, such as repairing, joining, and prototyping. Damaged or worn parts can be repaired using AFSD, reducing manufacturing costs by repairing expensive structures rather than replacing them. AFSD can also be employed for rapid tool and die production, as well as rapid prototyping and the creation of free-form designs and intricate structures. Furthermore, it is a suitable process for joining different alloys, particularly those that cannot be joined using conventional welding methods. Given its numerous advantages, AFSD has the potential to become a primary manufacturing technique in many industries [3, 4].

Al7075 is widely used in aerospace, marine, and automotive industries due to its excellent properties, such as high specific strength and corrosion resistance. However, few studies have investigated the fabrication of Al7075 block by AFSD. This study aims to assess the feasibility of building an Al7075 block with AFSD and optimization of the processing parameters. The continuity equation is used as the basis for the process and modified to remove defects.

2. Materials and methods

Wrought Al7075-T651 feedstock rods, each with a cross section of 9.5×9.5 mm² and a length of 500 mm, were prepared from plates using a water jet. To prevent jamming in the tool during the process, the rods were coated with graphite before deposition. An AFSD machine (L3, MELD Manufacturing Co.) was used for the deposition. The material was deposited onto a substrate plate measuring 304×102×13 mm³, made of the same material as the feedstock. The relation between the processing parameters is given by the continuity equation (Equations 1and 2) [5].

$$\dot{m}_{in} = \dot{m}_{out} \tag{1}$$

$$a^2\dot{y} = wt\dot{x} \tag{2}$$

where a is the side of the feedstock cross section, $\dot{y}$ is the feedstock feed rate, w is the deposited layer width, t is the deposited layer thickness, and $\dot{x}$ is the traverse velocity. The range of the processing parameters used in this study are summarized in Table 1. The thickness of each layer was set to 1.5 mm and a total of 26 layers were deposited. The final block's dimensions were 152.4×38.1×42.7 (length × width × height) mm^3.

Table 1 Processing parameters used in this study

Parameter	Value
Feedstock feed rate (mm/min)	138.4
Traverse velocity (mm/min)	138.4-194
Tool rotational speed (rpm)	100-200
Initial substrate temperature (^{0}C)	250
Layer thickness (mm)	1.5

3. Results and discussion

The processing parameters for the initial attempt were 138.4 mm/min feed rate, 194 mm/min traverse velocity, and 200 rpm rotational speed. The surface of the first deposited layer, shown in Fig. 1.a, exhibited an obvious lack of material due to insufficient feedstock feeding. In subsequent attempts, the traverse velocity was reduced to 138.4 mm/min while maintaining the same feed rate and rotational speed. This adjustment resulted in a successful deposition of the first layer without any apparent surface defects, as shown in Fig. 1.b. However, defect-free surfaces were only observed for the initial layers. As the process continued, excessive material flash became evident (Fig. 1.c). This material flash led to a lack of material on the surface, which is highlighted and magnified in two regions marked by red circles in Fig. 1.c. The defects observed after depositing subsequent layers in the AFSD process are due to the deformation behavior of Al 7075 at elevated temperatures. Specifically, undesired surface tearing has been reported in hot extrusion of Al 7075, particularly at temperatures above 460°C. It has been noted that this tearing can be controlled by reducing the processing temperature [6].

The peak temperature in the AFSD process can be estimated using the Equation 3 [7].

$$\frac{T}{T_m} = K \left(\frac{\omega^2}{v \times 10^4}\right)^{a} \tag{3}$$

where T_m is the melting temperature of the material, K and α are constants in the ranges of 0.65-0.75 and 0.04-0.05,

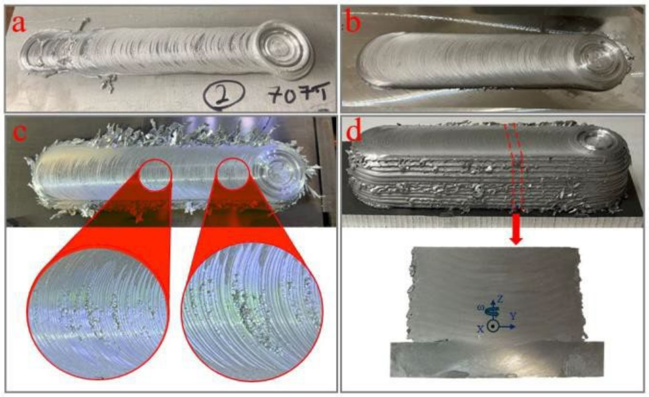

Fig 1. Photographs of the depositions: a. the first layer at F= 138.4 mm/min, V= 194 mm/min, and ω= 200 rpm, b. the first layer at F= 138.4 mm/min, V= 138.4 mm/min, and ω= 200 rpm, c. multiple layers at F= 138.4 mm/min, V= 138.4 mm/min, and ω = 200 rpm, and d. final block at F= 138.4 mm/min, V= 138.4 mm/min, and ω= 150 rpm

respectively, and ω is the rotational speed. Based on this equation, the tool rotational speed was reduced from 200 to 150 rpm to lower the peak temperature. As illustrated in Fig. 1.d, this change significantly reduced the excessive material flash. Consequently, the final block was 3D printed with a feed rate of 138.4 mm/min, a traverse velocity of 138.4 mm/min, and a rotational speed of 150 rpm. For further macroscopic inspection, the polished and etched cross section of the block is shown in Fig. 1.d. The part's layered structure is evident by the alternating bright and dark layers. This color contrast is attributed to the different crystalline morphology and texture resulting from the process. The repetitive arrangement of the layers indicates the consistent thermo-mechanical process in AFSD [5]. Unlike commonly observed arrangements, the structure is altered by the tool protrusions that restir the layers. This restirring distorts the layer boundaries, resulting in intertwined structures. Additionally, all the interfaces between the layers, including the one between the substrate and the first layer, exhibit a curved profile due to the mutual plastic deformation of the depositing layer and the underlying layer.

The data recorded by the AFSD machine during the deposition of the 26-layer blocks are processed and presented in Fig. 2. These data include process parameters, downward force, torque, and substrate temperature. The axial downward force, shown in Fig. 2.b, represents the vertical force applied to the material being deposited. It is crucial to maintain this force within a specific range during deposition. The force must be high enough to generate sufficient heat and pressure for material flow and to ensure good bonding between layers. However, it must also be below a certain threshold (~22 kN for the machine used in this study) to avoid damaging the machine. The average force recorded for the block deposition was approximately 8.6 kN, which was within the acceptable range for successful deposition. Additionally, the actuator torque variations are depicted in Fig. 2.c. Torque, applied by the tool to the material, is another critical parameter in AFSD that affects deposition quality. The average torque recorded was 212.2 N·m. This torque value was used to calculate the heat input for the block deposition according to Equation 3, resulting in a heat input of 24,071.9 J/m. Fig. 2.d illustrates the temperature changes during the process. Although the process began with a substrate temperature of 250°C, the actual temperature at which the deposition of the first layer started, based on the G-code, was around 330°C. This increase was due to the initial feeding of the feedstock rod and its subsequent pressure against the substrate, which generated extra heat for the material's plasticization. The average temperature recorded by the thermocouple during deposition was 317.4°C.

The fluctuations in the temperature diagram indicate the heating and re-heating cycles experienced during deposition.

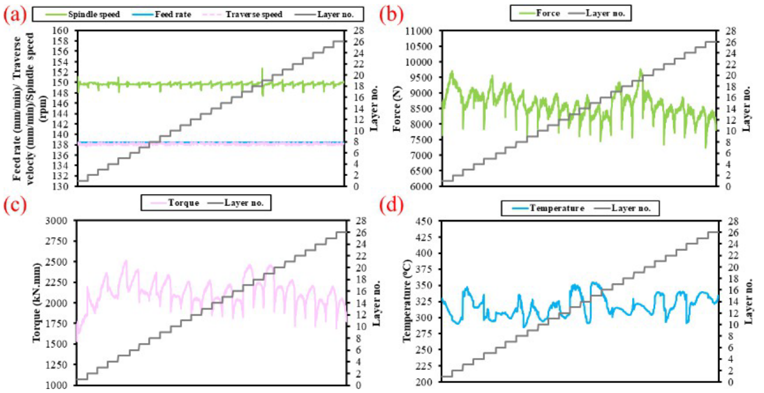

Fig 2. The processed data recorded by the machine during the deposition of 26 layers: a. Processing parameters, b. axial force, c. actuator torque, d. substrate temperature

4. Conclusion

AFSD is a relatively new metal additive manufacturing technique that provides numerous advantages over fusion-based methods. However, research on AFSD is still in its early stages, and processing hard and strong materials like Aluminum 7075 remains challenging. This study introduces and optimizes a set of processing parameters for producing defect-free Al 7075 parts using AFSD. By modifying the continuity equation to eliminate defects, this research focuses on achieving a faster deposition rate, which is essential for industrial applications. The goal is to establish higher deposition parameters than those reported in existing literature.

5. Acknowledgments

This work is supported by the U.S. National Science Foundation under grant number OIA-1946231 and the Louisiana Board of Regents for the Louisiana Materials Design Alliance (LAMDA).

6. References

[1] H. Dong *et al.*, "A Review on Solid-State-Based Additive Friction Stir Deposition," *Aerospace,* vol. 9, no. 10, p. 565, 2022. [Online]. Available: https://www.mdpi.com/2226-4310/9/10/565.

[2] Y. Li, M. Zhang, H. Wang, R. Lai, B. Yang, and Y. Li, "Microstructure and mechanical properties of Al–Li alloy manufactured by additive friction stir deposition," *Materials Science and Engineering: A,* vol. 887, p. 145753, 2023/11/06/ 2023, doi: https://doi.org/10.1016/j.msea.2023.145753.

[3] D. A. P. Prabhakar *et al.*, "A comprehensive review of friction stir techniques in structural materials and alloys: challenges and trends," *Journal of Materials Research and Technology,* vol. 20, pp. 3025-3060, 2022/09/01/ 2022, doi: https://doi.org/10.1016/j.jmrt.2022.08.034.

[4] F. Khodabakhshi and A. P. Gerlich, "Potentials and strategies of solid-state additive friction-stir manufacturing technology: A critical review," *Journal of Manufacturing Processes,* vol. 36, pp. 77-92, 2018/12/01/ 2018, doi: https://doi.org/10.1016/j.jmapro.2018.09.030.

[5] P. Agrawal, R. S. Haridas, S. Yadav, S. Thapliyal, A. Dhal, and R. S. Mishra, "Additive friction stir deposition of SS316: Effect of process parameters on microstructure evolution," *Materials Characterization,* vol. 195, p. 112470, 2023/01/01/ 2023, doi: https://doi.org/10.1016/j.matchar.2022.112470.

[6] T. Funazuka, K. Dohda, N. Takatsuji, K. Takano, and N. Sukunthakan, "Effect of Temperature on Surface Cracking Defects in AA7075 Hot Extrusion," *Key Engineering Materials,* vol. 926, pp. 409-415, 2022, doi: 10.4028/p-6bfd8v.

[7] T. Wang *et al.*, "Extrusion of Unhomogenized Castings of 7075 Aluminum via ShAPE," *Materials & Design,* vol. 213, p. 110374, 2022/01/01/ 2022, doi: https://doi.org/10.1016/j.matdes.2021.110374.

Optimizing The Self-Healing Parameters of DCN-PEI Vitrimer through Welding and Lap Shear Testing

Bernard Mahoney[1], Patrick Mensah[1], Guoquiang Li[2]

[1]Mechanical Engineering, Southern University and A&M College
[2]Mechanical Engineering, Louisiana State University

Abstract: Temperature, time and pressure play a crucial role in the welding and self-healing of vitrimer materials. A strongly welded joint usually results from application of adequate pressure at a temperature that facilitates BERs and for a sufficient period of time. In this work, strips of vitrimer material were welded together at different temperatures, applying 3 MPa pressure for 4 hours. The strength of the welded joints was determined by lap shear tests performed using an MTS Q-test machine at 1mm/min strain rate. Results obtained established a correlation between increasing joint strength and increasing temperature. The strength of the welds was estimated averaging the peak loads over the welded area. Welding was performed at 160 ºC, 170 ºC and 180 ºC at constant pressure and time of 3 MPa and 4 hours respectively. Average joint strengths obtained were 1.68, 2.06 and 4.29 MPa which corresponded to healing efficiencies of 4.8%, 6.04% and 12.26% when juxtaposed with the shear strength of the vitrimer, 35 MPa.

Keywords: BER, vitrimer

1. Introduction

The ability to self-heal is one of the most outstanding qualities of vitrimers. Vitrimers are finding widespread use as the matrix component in composite materials due to their ability to combine good mechanical properties with excellent thermal stability and chemical resistance. Optimizing the self-healing parameters of DCN-PEI vitrimer is vital for prolonging the material's shelf life. In a bid to understand the dynamics of interfacial healing between vitrimers and fibers in composite materials, it is paramount to obtain insights into the healing abilities of the pure vitrimer material.

Welding is an effective means of exploring the self-healing capacity of vitrimers. During welding, there is an interplay between pressure, temperature and time. Pressure applied during welding plays the role of establishing "intimate" contact between the faces to be welded and higher temperature allows for bond exchange reactions (BER) to occur effectively healing the failed material [1].

In this paper, we seek to optimize the self-healing ability of DCN-PEI vitrimer by welding at temperatures above the topology freeze transition temperature, T_v, of the vitrimer which is 160ºC. Bond exchange usually occurs at a greater rate at the T_v, which connotes an energy level higher than the activation energy of the vitrimer. This increases the vitrimer's ability to self-heal and subsequently shortens the time required for accomplish the self-healing process. Applications in industries like aerospace, automotive, and electronics, where materials are regularly exposed to mechanical stress and potentially damaging environmental conditions, require this optimization

2. Materials & Methods

2.1 Raw materials

All the chemicals used are commercially available and were used as received without further purification. DCN-PEI Vitrimer (3:1) branched polyethylenimine (PEI, average Mw~800 by LS, average Mn ~600 by GPC) was purchased from Sigma Aldrich, USA, and diglycidyl 1,2-cyclohexanedicarboxylate (DCN) was obtained from Ambeed, IL, USA.

2.2 Methods

Preparation of Vitrimer. DCN-PEI was mixed in a 3:1 weight ratio in a beaker in a vacuum chamber in order to remove bubbles from the mixture. A total weight of 165 grams was used. The mixture was stirred slowly for about 8 minutes while being cooled by a fan. It was then poured into a 150mm x 150 mm mold and allowed to cure.

Cutting of Vitrimer into strips. The coupon was then cut into rectangular strips of dimensions (50mm ´ 14mm ´ 5mm) fit for the welding process. Figure 2.1 shows measuring the dimension of the cut strips.

Welding of Strips. A Dake carver press was used for the welding procedure. Rectangular strips of material of dimensions 50 mm × 14 mm × 5 mm were used in the welding process.

Lap shear testing. The welding or bonding efficiency was then evaluated by lap shear testing on the welded samples in an MTS Landmark Servohydraulic Test system at room temperature with a cross-head speed of 1 mm/min.

Figure 2.1 Dimensions of the Vitrimer strips

Figure 2.2 Single lap joint

3. Results And Discussion

3.1 Maximum Load Values

	160°C	**170°C**	**180°C**
Average	235.5	287.64	600.75 N

3.2 Strength of The Welded Joint

Sample No.	**160°C**	**170°C**	**180°C**
Average	**1.68** MPa	**2.06 MPa**	**4.293 MPa**

3.3 Healing Efficiency

The healing efficiency is calculated by dividing the average shear strength of the single-lap joint specimen over the shear strength of the vitrimer (35 MPa). The results are summarized in Table 3.

Table 3. Average healing efficiency for various temperatures

160°C	**170°C**	**180°C**
4.8 %	6.04%	12.26%

3.4 Discussion of test results

3.4.1 Effect of Temperature on Maximum Load

Figure 3.4.1 shows the effect of healing temperature on the peak shear force during single-lap shear test. Welding was carried out around the topological freeze transition temperature, 160°C, enabling bond exchange reactions to occur, causing the dynamic covalent nature of the vitrimer to be fully utilized. From the results, it was evident that an increase in the welding temperature from 160°C to 180°C resulted in higher maximum load values. The average maximum load for the samples welded at 160°C was 235.5 N, for the samples welded at 170°C, 287.64 N and for samples welded at 180°C, 600.75 N. Welding at 180°C resulted in a comparably stronger joint than those at 170°C and 160°C, as evidenced by the higher maximum loads and corresponding strength. This can be attributed to faster diffusion of polymer chains across the bonding interface at that temperature. Enhanced transesterification reaction resulted from increasing the welding temperature. Higher temperatures cause an increase in the activity of the tertiary amine catalysts present in the vitrimer, which play a crucial role in facilitating the bond exchange reactions. Also, higher temperatures reduced the viscosity of the vitrimer material allowing for faster diffusion of the chains across the interface, thereby enhancing the strength of the welded joint. The healing efficiency also follows this trend, with higher efficiency observed at the higher welding temperature. The highest healing efficiency value was obtained for welding performed at 180^{o}C with a mean value of 12.26%. The welding done at 160^{o}C and 170^{o}C yielded 4.8% and 6.04% respectively. Overall, the joint shear strength obtained for the various conditions (1.68, 2.06 and 4.29 MPa) were relatively low compared to the shear strength of the vitrimer (35 MPa). This could be attributed to the low pressure applied to the joint during welding. The surface of the specimens is uneven, with a large surface area not in direct contact, making transesterification reaction impossible. Higher pressure would force the surfaces in contact, leading to an increase in healing efficiency. Another reason is that the polymer is hydrophilic. The two substrates may have absorbed some moisture. The water molecules resist the transesterification reaction to occur, leading to reduced healing efficiency. Finally, exposure of the substrate surfaces to air may cause oxidation of the vitrimer molecules, which again may reduce the healing efficiency.

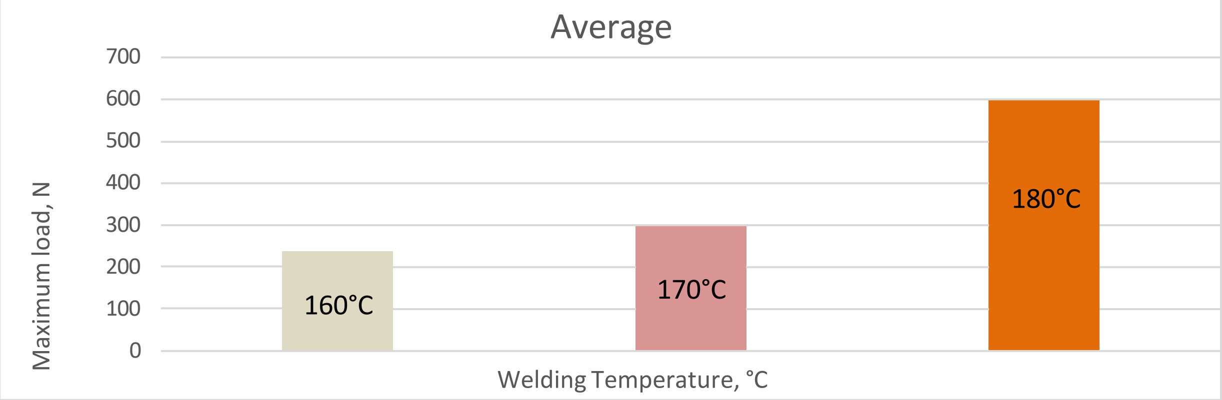

Figure 3.4.1. Plot of average maximum load for various welding temperatures

4. Conclusion

In conclusion, the lap shear tests on vitrimer strips reveal that increasing the welding temperature from 160°C to 180°C improves the joint strength. This is reflected by the higher maximum loads, strengths, and healing efficiencies at the highest healing temperature.

5. Acknowledgments

This work is supported by the U.S. National Science Foundation under grant number OIA-1946231 and the Louisiana Board of Regents for the Louisiana Materials Design Alliance (LAMDA).

6. References

[1] Hafeezullah Memon, Yi Wei. Welding and reprocessing of disulfide-containing thermoset epoxy resin exhibiting behavior reminiscent of a thermoplastic. *Journal of Applied Polymer*, **2020, 9-10.**

[2] Aurelie Legrand, Corinne Soulie Ziakovic. Silica-Epoxy Vitrimer Nanocomposites, *Macromolecules*, **2016,** 5899

[3] Qian Shi, Chenyu Jin, Zhiqian Chen, Le An, Tiejun Wang. On The Welding Of Vitrimers: Chemistry, Mechanics and Applications. *Advanced Functional Materials*, **2023**.

Phase Segregation and Shear Strength of CrCoNi-W Medium Entropy Alloy: A Molecular Dynamics Study

Hamid Sharifi, Collin D. Wick

College of Engineering & Science, Louisiana Tech University

Abstract: This paper investigates the effects of W content on the phase segregation and the shear strength of CrNiCo-W medium entropy alloy using Molecular Dynamics simulations. Three alloys with 3%, 6% and 10% of W content were considered, and the calculations showed that alloy remained single phase at 3% W content, while phase segregation occurred for 6% and 10% cases. To investigate the impact of W on the strength of CrNiCo alloy, both perfect crystal structure and systems with edge dislocations were considered. While the shear strength of CrNiCo was slightly higher for the perfect crystal case, the results showed that CrNiCo-3W had higher shear strength for the cases with edge dislocations.

Keywords: complex concentrated alloys (CCAs); Molecular Dynamics; MEAM potentials; phase formation; compositional segregation

1. Introduction

High entropy alloys (HEAs) are a new generation of metallic alloys that have emerged over the past two decades [1]. While experimental tests are utilized to determine the physical and mechanical properties of materials, they are limited by their expensive and lengthy processes [2]. Computational methods can accelerate the design process by guiding experimental tests [3]. Design procedure and computational framework for enhancing complex concentrated alloys (CCAs) design were introduced previously [4]. The current work is a focus on the phase segregation and the shear strength of CrNiCo-W medium entropy alloy using previously developed MEAM potentials [5]. To perform the simulations, MEAM potentials, a Monte Carlo (MC) scheme and molecular dynamics (MD) in LAMMPS [6], were utilized and effects of W content on the phase segregation and the shear strength of CrNiCo-W were studied.

2. Phase segregation

Wu et a. [7] used Thermocalc to predict the phase formation in CrNiCo-W as a function of W content and validated the results with experimental tests. Table 1 compares the prediction of the current work using MC and MD simulations and results of Thermocalc for selected W concentrations.

Table 1. Phase segregation in CrNiCo-3W, CrNiCo-6W and CrNiCo-10W MEAs based on MC simulations.

Systems		Elements Percentages				Phase Composition	
Alloys	Phases	Cr	Ni	Co	W	This work	Ref. [7]
CrNiCo-3W		33	32	32	3	100%	100%
CrNiCo-6W		32	31	31	6	100%	100%
	Phase 1	11.3	32.9	18.2	37.5	9%	11%
	Phase 2	34.2	29.3	30.2	6.3	91%	89%
CrNiCo-10W		31	31	28	10	100%	100%
	Phase 1	57.5	23.1	16.2	3.2	23%	27%
	Phase 2	33.4	31.0	29.0	6.6	77%	73%

3. Shear strength of perfect crystal structure

To study the shear strength of CrNiCo-3W using the prepared MEAM models, the composition presented in the first line of Table 1 was used and a system of 11,520 atoms with a cubic fcc structure was prepared. Each side of the system is approximately 5 nm and subjected to two constant loads at the top and bottom of the cube in reverse directions along the X axis. The velocity of the movement was 0.1 Å per step with the schematic shown in Fig. 1 (b). Fig. 1 (a) illustrates comparison between the shear strength of CrNiCo and CrNiCo-3W. While both systems show almost the same behavior in the stress-strain curve, the shear strength of CrNiCo (15.74 GPa) is higher than CrNiCo-3W (15.21 GPa) by 3.5%.

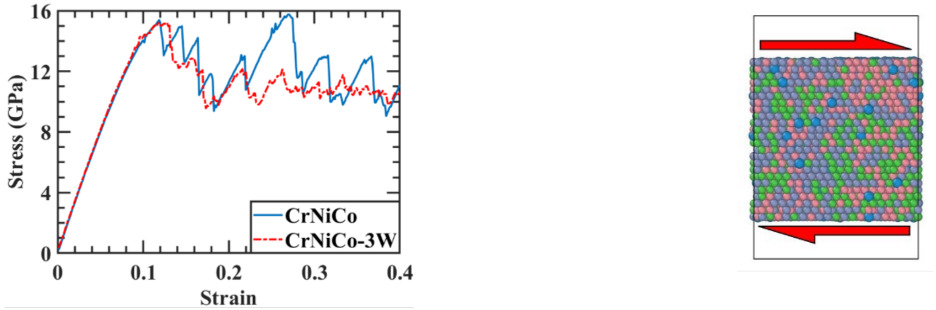

(a)

(b)

Fig. 1. a) Shear Stress-strain curve of CrNiCo and CrNiCo-3W b) CrNiCo-W under shear load

4. Effects of dislocations on the shear strength

Based on the traditional solid solution strengthening theories, mobility of a dislocation in dilute solutions is affected by solute atoms. However, new theories were proposed for the solid solution strengthening mechanisms in HEAs, since there is no real solute-solvent due to equiatomic composition [8]. To study the interaction of tungsten atoms with dislocations and investigate their impacts on the shear strength of materials, an edge dislocation consisting of two Shockley partials (1/6<112>) was introduced to the system (see Fig. 2). As is seen in Fig. 2 (a), the strength of CrNiCo and CrNiCo-3W decreased to 13.14 GPa and 13.98 GPa, respectively. While for the perfect crystal cases the shear strength of CrNiCo was higher than CrNiCo-3W by 3.5%, by introducing an edge dislocation, CrNiCo-3W showed higher strength by 6.4%.

Following the same procedure and to further investigate the effects of dislocations on the shear strength of CrNiCo-3W, two edge dislocations were introduced to the systems and shear loadings were applied to both systems and in the same directions (see Fig. 2 (d)). Fig. 2 (c) compares the shear strength of two systems, where CrNiCo-3W (13.25 GPa) is higher than CrNiCo (12.11 GPa) by 9.4%.

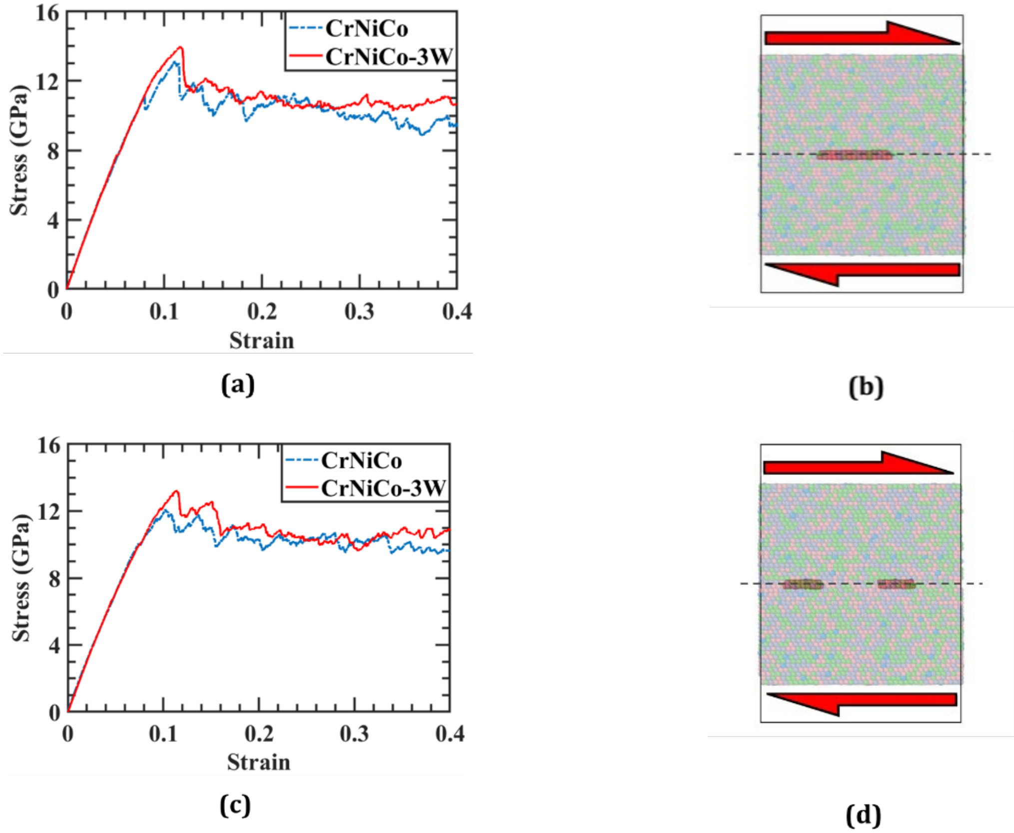

Fig. 2. a) Shear Stress-strain curve of CrNiCo and CrNiCo-3W with one edge dislocation b) CrNiCo-3W system with one edge dislocation under shear load c) Shear Stress-strain curve of of CrNiCo and CrNiCo-3W with two edge dislocations d) CrNiCo-3W system with two edge dislocations under shear load

Increasing the shear strength of CrNiCo-3W by 9.4% is in good agreement with the experimental results by Chang et al. [9], where it was shown that the solid solution hardening and grain boundary hardening have the same contributions on the increasing the yield strength of CrNiCo-W in comparison with CrNiCo, and incorporating 3 at. % W to CoCrNi improves its yield strength by ∼33%. Table 3 shows the different cases that were investigated in this work.

Table 2. Summary of maximum shear strength of different cases in this study

Case	Definition	Dislocations	Dislocation Energy (mJ/m^2)	Max. Shear Strength (GPa)
CrNiCo	No dislocations	0	-	15.74
CrNiCo-3W	No dislocations	0	-	15.21
CrNiCo	1 edge dislocation	1	278.21	13.14
CrNiCo-3W	1 edge dislocation	1	419.04	13.97
CrNiCo	2 edge dislocations	2	779.57	12.11
CrNiCo-3W	2 edge dislocations	2	992.21	13.25

5. Conclusion

Using MC and MD simulations, phase segregation of CrNiCo-W with 3%, 6% and 10% of W was investigated. The results showed that CrNiCo-W remained single phase at 3% but for 6% and 10% it was segregated into two phases. Concentrations of the created secondary phases were in good agreement with the Thermocalc results available in the literature. The effects of considering dislocations on the shear strength of the alloys were studied and it was observed that by adding 3% of W to the CrNiCo system with two edge dislocations, the strength was increased up to 9.4% which was in accordance with experimental data from literature.

6. Acknowledgments

This work is supported by the U.S. National Science Foundation under grant number OIA-1946231 and the Louisiana Board of Regents for the Louisiana Materials Design Alliance (LAMDA). The high-performance computing resources provided by the Louisiana Optical Network Infrastructure (https://loni.org) were used for this work.

7. References

[1] Cantor B, Chang ITH, Knight P, Vincent AJB. Microstructural development in equiatomic multicomponent alloys. Mater Sci Eng A 2004;375–377:213–8.

[2] Feng R, Zhang C, Gao MC, Pei Z, Zhang F, Chen Y, et al. High-throughput design of high-performance lightweight high-entropy alloys. Nat Commun 2021;12:4329.

[3] Elgack O, Almomani B, Syarif J, Elazab M, Irshaid M, Al-Shabi M. Molecular dynamics simulation and machine learning-based analysis for predicting tensile properties of high-entropy FeNiCrCoCu alloys. J Mater Res Technol 2023;25:5575–85.

[4] Sharifi H, Wick CD. Design Procedure and Modeling of Complex Concentrated Alloys Using DFT Calculations and Molecular Dynamics. Proc. Louisiana EPSCoR RII LAMDA 2022 Symp., 2022.

[5] Sharifi H, Wick CD. A combined DFT / MD / MC study on the Stability , Phase Formation and Shear Strength of CrNiCo , CrNiCu and CuNiCo Ternary Systems. Proc. Louisiana EPSCoR RII LAMDA 2023 Symp., 2023, p. 15–8.

[6] Plimpton S. Fast parallel algorithms for short-range molecular dynamics. J Comput Phys 1995;117:1–19.

[7] Wu Z, Guo W, Jin K, Poplawsky JD, Gao Y, Bei H. Enhanced strength and ductility of a tungsten-doped CoCrNi medium-entropy alloy. J Mater Res 2018;33:3301–9.

[8] Wu Z, Troparevsky MC, Gao YF, Morris JR, Stocks GM, Bei H. Phase stability, physical properties and strengthening mechanisms of concentrated solid solution alloys. Curr Opin Solid State Mater Sci 2017;21:267–84.

[9] Chang R, Fang W, Bai X, Xia C, Zhang X, Yu H, et al. Effects of tungsten additions on the microstructure and mechanical properties of CoCrNi medium entropy alloys. J Alloys Compd 2019;790:732–43.

Quantification of Wettability and Surface Tension of Liquid Aluminum 7075 Alloy on Various Substrates

Chukwudalu U. Uba [1]*, Jonathan R. Raush [2]

[1]Department of Mechanical Engineering, University of Louisiana at Lafayette
[2]Department of Mechanical Engineering, University of Louisiana at Lafayette

Abstract: Herein, the wettability and surface tension of Al 7075 alloy were characterized from 923–1073 K under argon on porous alumina, tungsten, and nonporous alumina substrates using sessile drop experiments. The contact angle results revealed the alloy's poor wettability on all substrates. The surface tension data ranged from 675.67–975.78 mN·m^{-1} in decreasing order of tungsten, porous alumina, and nonporous alumina. The results of this study will aid in computational design and optimization improvement of processes that necessitate using thermophysical properties, such as wettability and surface tension.

Keywords: Wettability; surface tension; contact angle; sessile drop; Aluminum 7075 alloy

1. Introduction

Surface tension is the interfacial tension at a liquid–gas boundary that causes the liquid to form a droplet. This droplet formation behavior affects the fluid flow behavior of molten metals and melt pool shape, making it a key property for welding and additive manufacturing process optimization.

High-strength Al alloys, such as Al 7075 alloy, are known for their remarkable mechanical properties, lightweight characteristics, relatively low melting temperature characteristics, and various aerospace and automotive applications. Despite its various applications, its wettability and surface tension characteristics are uncertain. The available surface tension data are limited to pure Al and a few examined Al-based alloys [1].

To the best of our knowledge, only two studies have investigated the surface tension of Al 7075 alloy. Bainbridge *et al.* measured the surface tension of molten Al and its alloys, including Al 7075 alloy, under vacuum using the sessile drop (SD) method [1]. Their measurement comprised four steps: melting and stabilizing the sample at $T_{\mathrm{Liquidus}} + 50$ K in an evacuated tube furnace; the first fracture of the droplet's surface using a probe; introducing a controlled gas atmosphere; second fracture of the droplet's surface using a probe. The experiments were conducted under four conditions (1–4): as-melted (vacuum), as-melted + fractured, exposure to dry air, and dry air + refractured, with mean surface tension values of 0.809, 0.843, 0.777, and 0.607 N·m^{-1}, and standard deviations of 0.041, 0.018, 0.061, and 0.083 N·m^{-1}, respectively, with a minimum of $n = 5$ samples. Also, Momeni *et al.* [2] engineered the surface melt for the in-space manufacturing of Al parts by developing a phase-field model of surface melting, where the surface energy can directly be implemented from the experimental measurements. In their study, they measured the surface tension of Al 7075 alloy on porous alumina substrates under vacuum using the SD technique from T_{m} up to 1023 K. They reported a mean surface tension value of 0.134 J·m^{-2}, with a standard deviation of 3.45×10^{-3} J·m^{-2}. However, these abovementioned studies did not report the surface tension–temperature relationship of Al 7075 alloy as a function of the testing conditions.

To support the computational design and optimization improvement of processes that necessitate using temperature-dependent thermophysical properties, this study characterized the wettability and surface tension of liquid commercial Al 7075 alloy from 923–1073 K under 100% argon atmosphere on three substrates: porous high-refractory alumina, tungsten, and nonporous high-refractory alumina substrates using the SD technique.

domain analysis, specifically Fourier Transformation [3], we aim to overcome inherent challenges in X-ray material tomography. Ultimately, this research aims to advance smart material design through enhanced automatic fracture detection methodologies.

2. Method

The success of the Segment Anything Model (SAM) [2] in natural image segmentation is primarily attributed to two factors: leveraging massive deep learning models with billions of parameters and access to high-quality, well-annotated image data. However, in the domain of X-ray material tomography, several challenges necessitate a tailored approach. Unlike natural images, X-ray tomography data are less accessible, and their complex textures and boundaries complicate annotation.

Due to the intricate textures and boundaries in X-ray material tomography, SAM alone may struggle to capture detailed fracture regions effectively. To address this limitation, we propose integrating Fourier Transformation with SAM. Fourier Transformation [3] converts images from the spatial domain to the frequency domain, facilitating the identification of crucial high-frequency patterns associated with fractures. Initial findings indicate that Fourier Transformation can effectively highlight fractured boundaries by filtering out less relevant low-frequency patterns.

SAM, pretrained on a vast and diverse dataset, is then applied to the transformed frequency domain images. This pretrained model demonstrates robust segmentation capabilities without requiring additional training. Enhanced by the frequency domain transformation, SAM generates pseudo annotations for fractures. These annotations reduce the dependency on extensive human input, offering a more efficient method for data labeling. The constructive collaboration between SAM and Fourier Transformation forms a potent approach for automatic fracture detection in X-ray material tomography. By combining their strengths, this methodology produces reliable pseudo annotations that enhance the performance of deep learning models trained on this data.

3. Experimental Results

We have successfully employed foundational AI models such as the Segment Anything Model (SAM) to automatically generate coarse crack annotations. Specifically, Fourier Transformation techniques have been utilized to identify potential crack points, which are then input into the SAM model to produce crack masks.

In the Figures 1 and 2 below, we report some fracture detection results we obtain. (a) shows the raw inputs, (b) presents the FFT (Fast Fourier Transform) segmentation results with bounding boxes covering the blue crack region, (c) displays the FFT segmentation results with green points indicating the center points, (d) shows the SAM segmentation results with box prompts from (b), (e) presents the SAM segmentation results with point prompts from (c). These figures demonstrate the application of FFT-guided SAM for accurate crack detection in X-ray material tomography, highlighting the integration of Fourier Transformation techniques with SAM to enhance fracture identification.

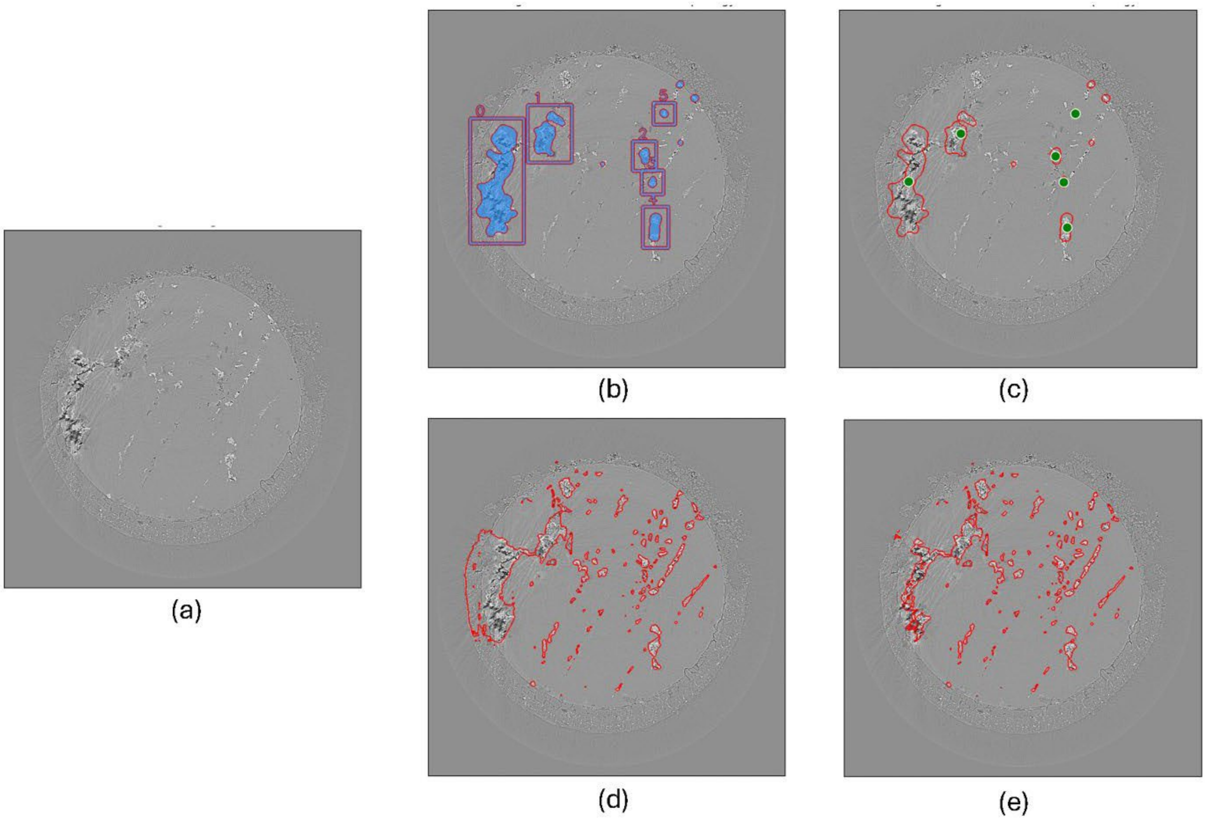

Figure 1. Results of our proposed model.

4. Conclusion

In conclusion, integrating Fourier Transformation with SAM enhances X-ray material tomography for fracture detection by leveraging SAM's deep learning capabilities and Fourier Transformation's focus on high-frequency fracture patterns. This approach improves automatic fracture detection efficiency, reduces human input in annotation, aligns with the LAMDA Strategic Plan for smart material design advancement, and holds promise for broader applications in materials science and engineering.

5. Acknowledgments

This work is supported by the U.S. National Science Foundation under grant number OIA-1946231 and the Louisiana Board of Regents for the Louisiana Materials Design Alliance (LAMDA).

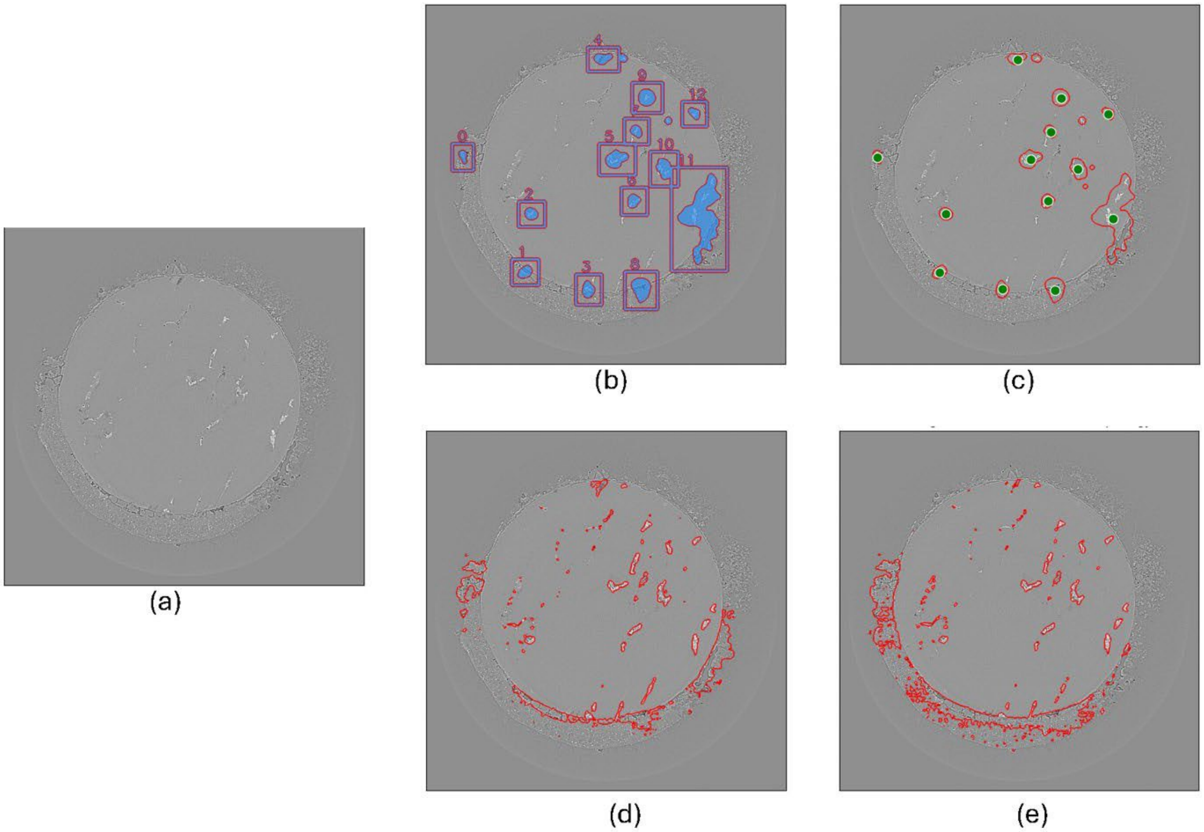

(a) (b) (c) (d) (e)

Figure 2. Results of our proposed model.

6. References

[1] Fatimah Alzubaidi, Patrick Makuluni, Stuart R Clark, Jan Erik Lie, Peyman Mostaghimi, and Ryan T Armstrong. Automatic fracture detection and characterization from unwrapped drill- core images using mask r–cnn. Journal of Petroleum Science and Engineering, 208:109471, 2022.

[2] Alexander Kirillov, Eric Mintun, Nikhila Ravi, Hanzi Mao, Chloe Rolland, Laura Gustafson, Tete Xiao, Spencer Whitehead, Alexander C. Berg, Wan-Yen Lo, Piotr Doll´ar, and Ross Girshick. Segment anything, 2023

[3] Sangrok Lee, Jongseong Bae, and Ha Young Kim. Decompose, adjust, compose: Effective normalization by playing with frequency for domain generalization. ArXiv, abs/2303.02328, 2023.

Self-healing of Macroscopic Cracks in Concrete by Cellulose Fiber Carried Microbes

Emmanuel Igbokwe[1,2], Samuel Ibekwe[1], Patrick Mensah[1], Ogad Agu[1], Guoqiang Li[1,2, *]

[1]Department of Mechanical Engineering, Southern University
[2]Department of Mechanical & Industrial Engineering, Louisiana State University

Abstract: This research introduces a method to heal millimeter-scale concrete cracks using Lysinibaccilus Sphaericus Bacteria (LSB) encapsulated in cellulose fibers. While previous studies focused on microscopic cracks, this study targets larger cracks, integrating LSB's biocalcification abilities with renewable cellulose fibers. Preliminary tests with a 3D-printed scaffold showed promising calcite precipitation. The optimal cellulose fiber concentration of 0.45% by volume improved concrete's mechanical properties, increasing compressive and split tensile strength by up to 25% compared to controls. Cracks up to 2.5 mm in wet and 1.5 mm in wet-dry conditions healed within 30 days. This approach ensures the bacteria's resilience in harsh environments, offering a durable and maintenance-free solution for concrete structures.

Keywords: Self-healing concrete, Lysinibaccilus Sphaericus Bacteria, Cellulose fibers, 3D-printed polymeric scaffold, Bio-mineralization, Macroscopic cracks, Mechanical properties, Sustainable infrastructure.

1. Introduction

Concrete is dominant in global construction due to its affordability, durability, high compression strength, and stiffness. However, it has low tensile strength and is prone to cracking from fatigue, extreme temperatures, loading, and moisture loss [1]. These cracks can compromise structural integrity, leading to issues like moisture infiltration, reinforcement corrosion, and material degradation. The American Association of State Highway and Transportation Officials (AASHTO) estimates that repairing substandard bridges, excluding inspections and traffic restrictions, costs over $140 billion nationally. Financial constraints often hinder immediate repairs, necessitating long-term solutions to reduce infrastructure maintenance costs. Traditional repair methods, such as external bonding of fiber-reinforced polymer (FRP) sheets and applying engineered cementitious composite (ECC) layers and steel plates, are effective but require intensive preparation and may disrupt usage [2]. Consequently, there is growing interest in self-healing solutions for concrete. Self-healing concrete proactively reduces permeability and restores strength and stiffness. Autonomous capsule-based mechanisms in polymer-modified concrete, similar to microencapsulation in polymer self-healing, have been explored, using epoxy drops that harden upon release to repair cracks [3].

Recent years have seen an increase in using bacteria for self-healing, with various studies exploring different bacteria and carriers. One approach embeds nutrients and bacteria within capsules that release their contents upon encountering fractures, initiating precipitation for crack healing. However, challenges include low capsule concentration and issues with vitamin release in cylindrical capsules. Traditional methods for producing microcapsules require sophisticated equipment, and released healing agents can result in new defects [4].

An alternative involves adsorption methods, embedding microbes and minerals in permeable fabric saturated with bacterial suspension. This provides support for bacteria growth and necessary conditions for calcite precipitation. Despite benefits, the complexity and cost have limited use in construction [5]. Using fibers as bacteria carriers offers a protective environment and reinforcement, enhancing concrete strength and reducing crack openings. Polypropylene (PP) fiber has shown high healing efficiency, but previous studies have not focused on healing wide, millimeter-scale cracks. Singh and Gupta investigated cellulose fibers as bacteria carriers, showing enhanced self-healing but decreased compressive strength and limited physical self-healing. This research uses Lysinibacillus Sphaericus Bacteria (LSB) encapsulated within cellulose fibers for autonomous healing of millimeter-scale cracks in concrete. LSB is chosen for its biocalcification capabilities, while cellulose fibers provide a biodegradable, supportive environment, reducing bacterial leakage and maintaining healing agents. This approach leverages cellulose fibers' properties to reinforce concrete and facilitate bacterial-induced calcite precipitation, essential for healing macroscopic cracks. Our experimental design includes rigorous testing to assess healing efficiency and mechanical properties. Initial tests using calcite precipitation on a 3D-printed polymer scaffold demonstrated the approach's potential. Subsequent experiments ensured successful translation to concrete applications. This research advances microbial loading technologies and cellulose fibers as bacteria carriers, offering a comprehensive solution for self-healing concrete, setting a new standard for sustainable, resilient infrastructure.

2. Material and Methods

Cellulose Fiber, Lysinibaccilus Sphaericus Bacteria (LSB), 3D Polymer scaffold, Cement and Aggregate. A range of chemicals was used in the study to provide nutrients and calcium sources while also promoting bacterial growth and biomineralization. All the chemicals utilized in this research, such as Yeast extract, BatoTM Peptone, calcium chloride anhydrous, calcium nitrate, sodium bicarbonate, urea broth, and ethanol, were purchased from Sigma-Aldrich. To promote microbial activity, the investigation utilized yeast extract as the growth medium, urea as the nitrogen source, and calcium nitrate as the calcium source. The experiments involved culturing Lysinibacillus Sphaericus bacteria (LSB) in nutrient broth and absorbing them into cellulose fibers for self-healing concrete applications. A 3D polymer scaffold was utilized to observe bacterial calcification potential before application to concrete. SEM analysis confirmed calcite precipitation on fibers and scaffolds. Mechanical testing of 3D printed polymer specimens was conducted to assess the impact of calcification. Four types of concrete specimens were prepared: control, with cellulose fibers, with bacteria, and with bacteria in cellulose fibers. These were tested for strength, water absorption, acid resistance, and thermal stability. Concrete fracture and self-healing were evaluated using wet and dry techniques, and structural morphology was analyzed using SEM and X-ray diffraction. Compression and split tensile strength tests were conducted to assess strength recovery post-healing.

3. Results

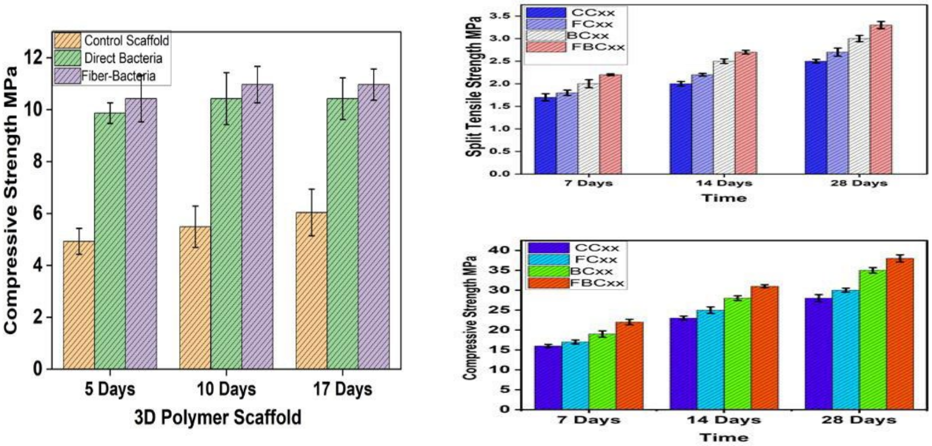

Figure 1. Mechanical properties of 3D printed polymeric scaffold and the four types of concrete.

Figure 1 shows that adding cellulose fiber and bacteria enhances the compressive strength of polymeric scaffolds, with FBCxx samples (bacteria carried by cellulose fiber) showing the highest strength. This study demonstrates that bacteria can enable self-healing and strengthen polymer scaffolds through $CaCO_3$ precipitation. The optimal cellulose fiber content was 0.45% by volume of cement mortar. FBCxx concrete exhibited split tensile strengths of 2.2 MPa, 2.7 MPa, and 3.3 MPa, which were 29.4%, 35%, and 32% higher than control concrete (CCxx) on days 7, 14, and 28. The compressive strengths of FBCxx were 22.0 MPa, 31.0 MPa, and 38.0 MPa, 37.5%, 34.8%, and 35.7% higher than CCxx concrete on the same days.

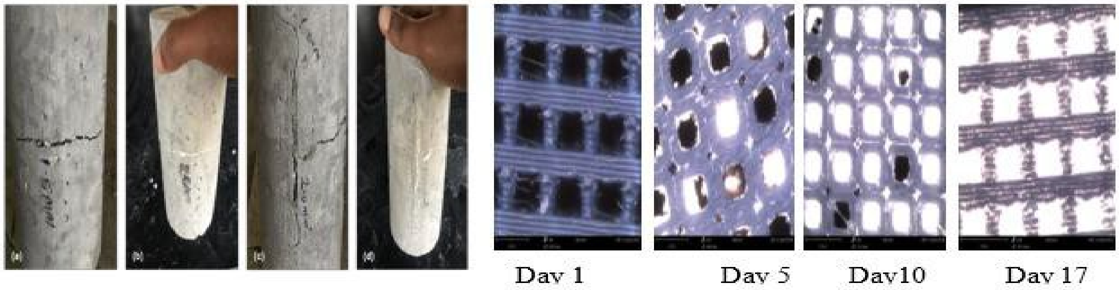

Figure 2 Visualization of self-healing of the concrete and SEM Self-healed 3D Polymeric scaffold

Figure 2 indicates that incorporating bacteria in BCxx and using cellulose fiber as a bacteria carrier in FBCxx successfully healed concrete fractures with crack widths from 1.5 mm to 2.5 mm. This healing, achieved through wet-dry and fully wet methods over 30 days, doubled and tripled previously studied crack widths. By day 30, complete healing and calcium carbonate precipitation were observed. Also, 3D-printed polymeric scaffold self-healed within 17 days through CaCO3 precipitation.

4. Conclusion

This research introduces a method for autonomously healing macroscopic concrete cracks using Lysinibaccilus Sphaericus Bacteria (LSB) encapsulated in cellulose fibers. Using a 3D-printed polymeric scaffold for initial observations, this approach significantly enhanced concrete's mechanical properties, with a 25% increase in split tensile and compressive strength compared to controls. Post-healing, FBCxx and BCxx samples maintained higher strength than undamaged controls. Cracks up to 2.5 mm in wet and 1.5 mm in wet-dry conditions healed within 30 days, doubling or tripling the results of previous studies. This validates the potential of bacteria-laden cellulose fibers for sustainable, self-healing concrete constructions.

5. Acknowledgments

This work is supported by the U.S. National Science Foundation under grant number OIA-1946231 and the Louisiana Board of Regents for the Louisiana Materials Design Alliance (LAMDA).

.

6. References

[1] Puranik, S.A., Jain, S., Sritam, G., and Sandbhor, S. (2019). Bacterial Concrete- a sustainable solution for concrete maintenance. *International Journal of Innovative Technology and Exploring Engineering*, *8*(11S), 227–232.
https://doi.org/10.35940/ijitee.k1046.09811s19

[2] Ganesh, S. (2020). Experimental Study on Self-healing Concrete with the Effect of Bacillus Subtilis Bacteria to Improve the Strength and Sustainability of Concrete. *Journal of Green Engineering*, *10*(4), 1909–1923. https://www.researchgate.net/publication/341804025_Experimental_Study_on_Self-healing_Concrete_with_the_Effect_of_Bacillus_Subtilis_Bacteria_to_Improve_the_Strength_and_Sustainability_of_the_Concrete

[3] American Society of Civil Engineers News Release. (1999). *Public Works Management & Policy*, *4*(1), 58–80. https://doi.org/10.1177/1087724x9941007

[4] Li, G., Pang, S., Helms, J. E., Mukai, D., Ibekwe, S., and Alaywan, W. (2002). Stiffness degradation of FRP strengthened RC beams subjected to hygrothermal and aging attacks. *Journal of Composite Materials*, *36*(7), 795–812.
https://doi.org/10.1177/0021998302036007614

[4] Wang, J., Soens, H., Verstraete, W., and De Belie, N. (2014). Self-healing concrete by use of microencapsulated bacterial spores. *Cement and Concrete Research*, *56*, 139–152.
https://doi.org/10.1016/j.cemconres.2013.11.009

[5] Singh, H., and Gupta, R. (2020). Influence of cellulose fiber addition on self-healing and water permeability of concrete. *Case Studies in Construction Materials*, *12*, e00324.
https://doi.org/10.1016/j.cscm.2019.e00324

Shape Recovery Form-stable Phase Change Materials for Generating the Electrical Energy Harvesting

Chengbin Yu[1], Guoqiang Li[1,2]

[1]Department of Mechanical and Industrial Engineering, Louisiana State University
[2]Department of Mechanical Engineering, Southern University and A &M College

Abstract: Over the years, thermoelectric energy harvesting has been becoming a topic of intensive research and thermoelectric power generator has been utilized in various energy harvesting applications. However, a thermoelectric device is required to collect the electrical energy, which has relatively low energy conversion efficiency and high cost. To overcome such a common problem, the objective of this study is to generate electrical energy without using thermoelectric devices. A stable electrical energy output would be feasible without a thermoelectric device, by directly connecting two types of phase change materials with different electrical conductivities and different phase transition temperatures. Two types of polydimethylsiloxane open-cell foams were prepared by embedding single walled carbon nanotubes, leading to different electrical conductivities. Two types of phase change materials with different phase transition temperatures were selected as working materials by infiltrating into the polydimethylsiloxane open-cell foams. Based on the test results, it is found that direct connection of 1-tetradecanol and polyethylene glycol composites can produce stable electrical voltage and current under the change of external temperature from 25 °C to 80 °C, through the light-on/-off process, and through heat flow treatment. Moreover, we report a new solar energy harvesting under a moist environment with dissolved carbon dioxide (CO_2). A 3D printed hydrophilic shape memory vitrimer (SMV) was utilized as a supporting container, and two types of PCM composites were obtained. This study shows that greenhouse gases can be effectively employed to harvest energy and it is believed that this study provided new opportunities for clean energy harvesting.

Keywords: Energy harvesting, Phase change material, open-cell foams, shape memory vitrimer

1. Introduction

Developing renewable energy is one of the challenges especially replacing fossil fuel by clean energy. Solar energy is a well-qualified candidates to produce converted electrical and mechanical energy, which mitigates the climate change without any negative environmental impact[1]. For utilization of solar energy, Ricardo et at. Summarized the background of solar energy conversion systems and current analysis on some typical research areas to demonstrate the importance of solar energy technology[2]. Surface modification of 2D materials as solar panels is crucial to produce solar-to-electrical conversion and is utilized in various photocatalytic energy harvesting systems. The common method is to employ the Seebeck effect which can generate electrical energy output due to the existence of temperature difference between two sides of a thermal device[3]. The practical solar-to-thermal design for a thermoelectric power generator (TEG) is to produce electrical energy under temperature difference between two sides of a device. Additionally, opposite P and N types of semiconductors can be connected to compose an effective TEG for obtaining solar-to-electrical energy harvesting while absorbing the solar energy. Based on the previous studies, reliable thermal energy storage (TES) is required by collecting the external solar energy to generate a stable and continuous electrical energy. The TES capacity is proportional to the pure PCM mass ratio and it is indispensable to keep a high weight fraction of the pure PCM in the final composite[4]. Thus, a 3D porous material has been selected as an advanced supporting material due to its high porosity and large surface area which can maintain high TES of form stable PCM composites[5]. The carbon based material is easy to absorb sunlight and facilitate the pure PCM to store thermal energy after fabricating a porous structure. The carbon aerogel supported PCM composites showed a highly efficient thermal and sunlight-driven energy storage for harvesting electrical energy. To validate the new concept, a polydimethylsiloxane (PDMS) is utilized to fabricate a 3D porous foam structure, and single-walled carbon nanotube is dispersed into the PDMS skeletons to increase the electrical conductivity. Compared with aerogel structure, PDMS foam exhibits much higher flexibility and mechanical property to construct excellent internal skeletons as electrical carriers. The concentration of single-walled carbon nanotube is different in each PDMS foam in order to observe the thermoelectric energy harvesting under the melting and cooling processes. Sunlight is also utilized to produce electrical energy during the light-on/-off process and the effect of heat flow on the energy harvesting is investigated. Moreover, unlike previous studies, we propose the usage of a 3D printed hydrophilic shape memory vitrimer (SMV) as a supporting material to prepare form stable PCM composites. One reason for using SMV to manufacture the supporting container is that under cyclic thermal loading, fatigue failure may occur in the container of the form stable PCM composites. The cracks, if not healed, will lead to a leakage of the PCM. As a result, the energy harvesting would be stopped working Particularly, a combination of the shape memory effect and intrinsic self-healing capability can help heal wider opened cracks per the biomimetic close-then-heal (CTH) strategy[6]. Although most of SMVs exhibit low electrical conductivities, these can be increased significantly in a moisture environment with high concentrations of carbon dioxide (CO_2). The increase in ion concentration at the cold side promotes the generation of carbonic acid and recombination into carbon dioxide (CO_2). In a word, the CO_2 enters the hot side, decomposes into ions, moves to the cold side, and recombines into CO_2. Thus, the greenhouse gas is only used as a medium to produce electricity. To produce a continuous electricity output, we use the light-on/-off cycles to maintain a constant temperature gradient between the two SMV-supported PCM composites. The reason is that during the light-on process, both the PCMs change from a solid to a liquid, absorbing a large amount of heat, but almost keeping the temperature at their corresponding phase transition temperature, thus maintaining a constant thermal gradient, which is one critical requirement for the Seebeck effect. The light-on/-off process completes one cycle, the subsequent cycles will repeat the first cycle, a light-on branch, followed by a light-off branch. Therefore, a continuous and constant temperature gradient will be maintained, leading to continuous electricity production. The polyethylene glycol (PEG) and 1-tetradecanol (1-TD) are also utilized as two kinds of pure PCMs. The SMV container, which is a rectangular hollow box, is obtained by 3D printing using a digital light processing (DLP) type of 3D printer. These two PCM composites are connected with each other and water is sprayed on the surface under the different concentrations of CO_2, which can produce the output electrical energy harvesting.

2…. New Section

For PDMS foam supported PCM composites, we can obtain the output electrical energy without TEG device. This is a novel concept for energy harvesting. To validate this concept, the Seebeck effect was utilized by directly connecting two PCM composites with different phase transition temperatures and different electrical conductivities.

The PDMS open-cell foam embedded with single-walled carbon nanotubes was utilized to fabricate the form stable PCM composites. Two PCMs, PEG and 1-TD, which have different phase change temperatures, were employed to fill in the pores in the PDMS open-cell foam, creating conductive PCM composites with different phase change temperatures. It is found that the change of external temperature from 25 °C to 80 °C led to electrical energy harvesting by directly connecting these two PCM composites without the TEG device, which validated the hypothesis. It was found that the maximum output voltage was up to 1.18 mV with a 50 % energy harvesting efficiency. This study validates a new concept in thermoelectric energy harvesting without any TEG device, which may lay a solid foundation for harvesting electrical energy. While conventional electrical energy harvesting has limitations due to the use of the TEG devices, the PCM composites do not have this limitation. It has potential applications in aerospace structures, buildings, and vehicles, which have the natural inside and outside environments with temperature differences, facilitating effective energy harvesting.

3….. New Section

For SMV supported form stable PCM composites, we obtained both PEG and 1-TD included SMV containers showed excellent form-stability during the phase transition process without any leakage. The energy harvesting efficiency was increased by change the relative humidity (RH) and carbon dioxide (CO_2) concentrations on the surface of the SMV containers. It was found that high RH conditions promoted the dissolving ability of CO_2, and the electrical resistivity was decreased significantly. Although the CO_2 dissolving ability changed based on the temperature variation, the difference in electrical resistivity between two sides of the PCM composites can induce the Seebeck effect and produce electrical energy during the light-on/-off process. The assembly made of RH 70% 1-TD and RH 90% PEG composites were employed and obtained the highest voltage and current outputs up to 2.73 mV and 500 nA, respectively. The PCM composites showed high energy harvesting efficiency at 700 ppm and 1200 ppm CO_2 concentrations which indicated that greenhouse gases can be utilized to help harvest electrical energy. This has high potential for application in industry, vehicles, aerospace, households, and agriculture to produce a large amount of electrical energy from solar energy simply and easily.

4. Conclusion

In this work, we demonstrated a new concept of thermoelectric energy harvesting without TEG device. Both open-cell foam and SMV supported PCM composites showed excellent form-stability during the phase transition process. The PDMS with different weight fractions of single-walled carbon nanotubes can infiltrate two kinds of pure PCMs and conducted the stable and continuous thermoelectric energy harvesting according to the Seebeck effect. Three conditions such as heating/cooling, light-on/-off, and hot/cold air flow were considered and electrical energy has collected while the PCMs were under melting and cooling processes. Furthermore, the hydrophilic SMV can absorb plenty of moisture on the surface which can dissolve the carbon dioxide (CO_2) to generate the electrical energy harvesting. Different relative humidity (RH) with high concentrations of CO_2 can achieve the solar-to-electrical energy harvesting and it was also repeatable to maintain the thermoelectric energy harvesting during the PCM phase transition process. It is noted that the mention of CO_2 is to demonstrate a greenhouse gas can be utilized to do something benefits. Other organic or inorganic compounds, whether solids, liquids, or gases, can be employed as long as they can be dissolved in water to produce ions and generate the output electrical energy.

5. Acknowledgments

This work is supported by the U.S. National Science Foundation under grant number OIA-1946231 and the Louisiana Board of Regents for the Louisiana Materials Design Alliance (LAMDA).

The US National Science Foundation under grant number 1736136, and the US National Science Foundation under grant number 2051050. The authors would like to thank the Advanced Manufacturing and machining Facility (AMMF) at Louisiana State University for providing the facilities to cut our samples.

6. References

[1] F. Creutzig, P. Agoston, J.C. Goldschmidt, G. Luderer, G. Nemet, R.C. Pietzcker. The underestimated potential of solar energy to mitigate climate change. Nature Energy. 2 (2017) 1-9.
[2] R. Conceicao, J. Gonzalez-Aguilar, A.A. Merrouni, M. Romero. Soiling effect in solar energy conversion systems: A review. Renewable and Sustainable Energy Reviews. 162 (2022) 112434.
[3] C.-T. Hsu, G.-Y. Huang, H.-S. Chu, B. Yu, D.-J. Yao. An effective Seebeck coefficient obtained by experimental results of a thermoelectric generator module. Applied energy. 88 (2011) 5173-9.
[4] C. Yu, Y. Song. Modified Supporting Materials to Fabricate Form Stable Phase Change Material with High Thermal Energy Storage. Molecules. 28 (2023) 1309.
[5] Y. Luo, F. Zhang, C. Li, J. Cai. Biomass-based shape-stable phase change materials supported by garlic peel-derived porous carbon for thermal energy storage. Journal of Energy Storage. 46 (2022) 103929.
[6] G. Li, D. Nettles. Thermomechanical characterization of a shape memory polymer based self-repairing syntactic foam. Polymer. 51 (2010) 755-62.

Sintering Process of Silver Nanoparticles with a Combination of Laser Irradiation

Rajib Chowdhury, Thomas Poche, Seonhee Jang

Department of Mechanical Engineering, University of Louisiana at Lafayette

Abstract: Silver (Ag) nanoparticle (NP) ink was employed for fabrication of conductive Ag patterns on flexible polyimide substrates using thermal sintering process with a combination of laser irradiation. The printed Ag NP ink patterns were processed by four different sintering conditions with laser irradiation only (LO), thermal treatment only (TO), thermal treatment then laser irradiation (TL), and laser irradiation then thermal treatment (LT). For laser irradiation, Nd:YAG with a wavelength of 1064 nm was used. For thermally treatment, the printed Ag NP ink patterns were processed at 140 °C for 1.5 min in formic acid vapor gas. Sintered Ag NP ink patterns showed different microstructure, chemical structure, hardness, and sheet resistance depending on sintering process conditions.

Keywords: Silver, Nanoparticle, Thermal sintering, Laser

1. Introduction

Printing techniques are used to create electrical devices in the field of printed electronics, which has attracted significant attention from the materials science community [1-3]. The selection of printing methods, flexible substrates, and conductive ink materials is crucial to the effective fabrication of printed flexible electronic 2D and 3D devices that meet specified performance and characteristic criteria. The primary inkjet-printed conductive inks include silver (Ag), copper (Cu), nickel (Ni), tin (Sn), and gold (Au) nanoparticle (NP) inks [4-8]. Post processing is essential for the removal of solvents and additives from the ink so that the optimal properties of the printed electronic device can be achieved. This process results in different microstructure, chemical structure, and mechanical and electrical properties of the printed metal patterns.

2. Experimental Details

Ag conductive patterns were printed using Ag NP ink and processed by four different sintering conditions with laser irradiation only (LO), thermal treatment only (TO), thermal treatment then laser irradiation (TL), and laser irradiation then thermal treatment (LT). For laser irradiation on the printed Ag NP patterns, a laser fluence of 0.15 J cm^{-2} and a laser exposure time of 15 s were used. For thermal treatment, an N_2-bubbled formic acid (FA, CH_2O_2, ACS 96+%, Fisher Scientific) vapor was used as the thermal treatment environment. The printed Ag NP patterns were thermally treated at 140 °C for 1.5 min. The sintered Ag NP patterns were characterized for microstructure, organic residue, crystallinity, surface morphology, chemical composition, Vickers hardness, and electrical sheet resistance using SEM, TGA, XRD, AFM, FTIR, Vickers micro-indentation, and four-point probe, respectively.

3. Results and Discussion

Fig. 1(a)-(d) presents the SEM microstructures of the Ag NP patterns sintered using LO, TO, TL, and LT conditions, respectively. For all of the sintered patterns, the microstructure analysis revealed the presence of pores and dispersed unsintered particles. Notably, after sintering the Ag patterns using the TL and LT, the patterns exhibited a greater degree of agglomeration than those sintered using the LO and TO. All of the Ag NP patterns had a granular structure. Grain growth, pore distribution, the presence of unsintered particles, and traces of organic residues were significant factors that influenced the properties of Ag NP patterns.

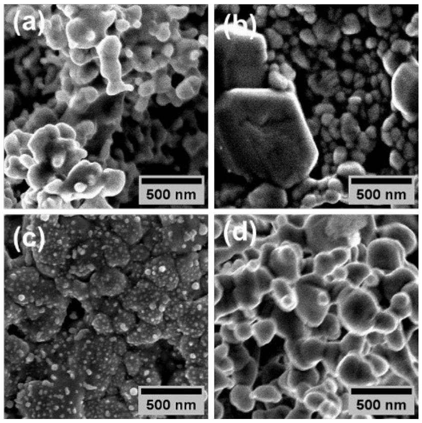

Fig. 1 SEM microstructures of the Ag NP patterns sintered using (a) LO, (b) TO, (c) TL, and (d) LT.

Fig. 2 shows the TGA analysis of the Ag NP patterns sintered using LO, TO, TL, and LT conditions. The weight losses were measured as 11.34, 6.58, 11.59, and 4.71 wt% for the sintering conditions of LO, TO, TL, and LT, respectively. It is demonstrated that the organic substances were removed most effectively by the TO and LT conditions because the smallest drop in weight loss was observed for these conditions before the plateau. In comparison, a relatively large amount of organic substance remained in the Ag NP patterns sintered using the LO and TL.

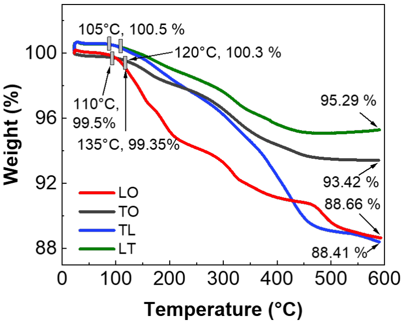

Fig. 2 TGA analysis of the Ag NP patterns sintered in various sintering conditions of LO, TO, TL, and LT.

Fig. 3 presents the XRD analysis of the Ag NP patterns sintered in various sintering conditions of LO, TO, TL, and LT. Five distinct diffraction peaks were identified, corresponding to the diffracted planes of the face-centered cubic (FCC) crystalline structure of Ag, including (111), (200), (220), (311), and (222) planes. These peaks were associated with their respective 2θ angles of 38.2°, 44.4°, 64.5°, 77.5°, and 81.6°. The crystallite size was determined by employing the Scherrer equation, $DD = \frac{KKKK}{\beta\beta\cos\theta\theta}$, where D is the average crystallite size, λ is the X-ray wavelength, β represents the width of the X-ray peak on the 2θ axis, typically denoted as the full width at half maximum (FWHM), and θ denotes the diffracted Bragg angle. The calculated average crystallite sizes for LO, TO, TL, and LT were found to be 19.29, 19.57, 19.42, and 20.11 nm, respectively.

Fig. 4 shows the AFM surface morphology images of the Ag NP patterns sintered using LO, TO, TL, and LT conditions, respectively. Scanning was performed across an area that was 5 μm×5 μm for each sintering condition. The scale bar within each image depicts the difference between the highest and lowest points on the scanning surface, which reflects variations in grain boundaries caused by the interaction between grain growth and residual unsintered Ag NPs. The RMS roughness values were derived from the AFM morphological scan. The measured

RMS roughness values for LO, TO, TL, and LT conditions were 32.58, 25.11, 27.56, and 48.00 nm on average, respectively.

Fig. 5 shows the electrical sheet resistance values of the Ag NP patterns sintered in various sintering conditions of LO, TO, TL, and LT. The average sheet resistances for the Ag NP patterns sintered using LO, TO, TL, and LT were measured as 49.6179, 0.0065, 0.0063, and 0.0031 Ω Sq^{-1}, respectively. It is known that electrical conductance is closely related to the amount of organic substance remaining in the conductive patterns after sintering. From the TGA analysis, a relatively small amount of organic substance remained for the patterns sintered under the TO and LT. A reduced amount of organic substance in the conductive patterns contributed to the smaller electrical sheet resistance. Conversely, the LO condition exhibited a relatively large amount of organic residue, resulting in a higher electrical sheet resistance.

Fig. 6 shows the FTIR spectra of the Ag NP patterns sintered in various sintering conditions of LO, TO, TL, and LT. The FTIR spectra were utilized to identify organic residues present in the Ag NP patterns. The spectra displayed distinct chemical bonding configurations, including C—H stretching, C—O stretching, C—O stretching, and C—H bending modes, which were observed within specified wavenumber ranges of 3000–2800, 1300–1200, 1100–1000, and 850–750 cm^{-1}, respectively. The formation of these bonds could be associated with the undecomposed capping molecules and additives that were present in the ink. The O—H bending mode observed at 1400–1395 cm^{-1} was absent following the sintering procedure, indicating that the aqueous-based portion was removed. Nevertheless, the presence of various chemical bonds such as C—H stretching, C—H bending, and C—O stretching modes, which were expected to derive from organic residues, was still detected after the sintering process.

Fig. 7 presents the Vickers hardness (HV) of the Ag NP patterns sintered in various sintering conditions of LO, TO, FTL, and LT. The HV values are calculated using the equation, $HHHH = kk\frac{FF}{SS}$, where HV is the Vickers hardness, k is the constant ($k = 1/g_n \approx 0.102$, g_n is the standard acceleration due to gravity), F is the test force (N), and S is the surface area of the indentation (mm^2) found by applying the force to a sample using a quadrangular

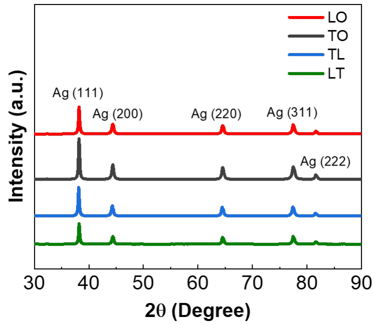

Fig. 3 XRD analysis of the Ag NP patterns sintered in various sintering conditions of LO, TO, TL, and LT.

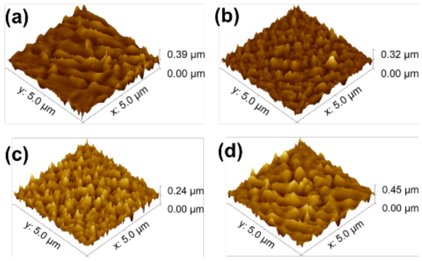

Fig. 4 AFM surface morphology images of the Ag NP patterns sintered using (a) LO, (b) TO, (c) TL, and (d) LT.

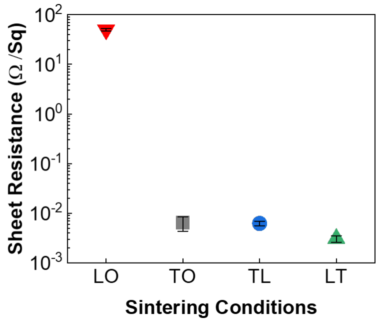

Fig. 5 Sheet resistances of the Ag NP patterns sintered in various sintering conditions of LO, TO, TL, and LT.

pyramid diamond indenter. The average *HV* values for the patterns sintered using LO, TO, TL, and LT were measured as 0.70, 3.62, 4.28, and 3.82 Nmm^{-2}, respectively. The low hardness of 0.70 Nmm^{-2}, high sheet resistance of 49.6179 Ω Sq^{-1}, and high weight loss of 11.34 wt% were observed for the Ag NP patterns sintered using the LO condition.

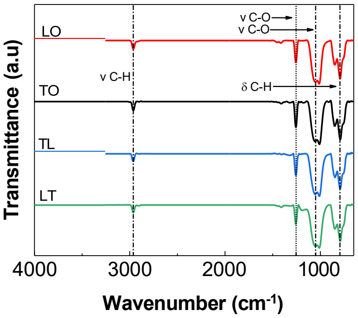

Fig. 6 FTIR spectra of the Ag NP patterns sintered in various sintering conditions of LO, TO, TL, and LT.

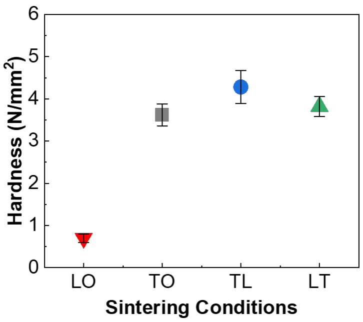

Fig. 7 Vickers hardness of the Ag NP patterns sintered in various sintering conditions of LO, TO, TL, and LT.

4. Conclusion

The study evaluated the physical, chemical, electrical, and mechanical properties of Ag NP patterns using four distinct sintering methods. Different parameters, such as laser irradiation power, laser irradiation duration, sintering temperature, and atmosphere, affected the properties of the sintered patterns. The Ag NP patterns sintered using the LT demonstrated the lowest electrical sheet resistance of 0.0031 Ω Sq^{-1}. From the microstructure analysis, it was demonstrated that the Ag NP pattern sintered using the LT showed better grain growth through necking and grain boundary diffusion compared with the rest of the sintering conditions. As there was more connectivity between the Ag NPs, the electrical conductivity was improved. Additionally, the efficient removal of organic residues using the LT condition, identified from TGA, and helped in producing the highest crystallite size of 20.11 nm. Among the four sintering conditions for the Ag NP patterns, the TL condition led to the highest mechanical hardness with a value of 4.28 Nmm^{-2}.

5. Acknowledgments

This work is supported by the U.S. National Science Foundation under grant number OIA-1946231 and the Louisiana Board of Regents for the Louisiana Materials Design Alliance (LAMDA).

6. References

[1] C. H. Rao, K. Avinash, B. K. S. V. L. Varaprasad, S. Goel, J. Electron. Mater. 2022, 51, 2747.
[2] G. Grau, J. Cen, H. Kang, R. Kitsomboonloha, W. J. Scheideler, V. Subramanian, Flex. Print. Electron. 2016, 1, 023002.
[3] J. Perelaer, P. J. Smith, D. Mager, D. Soltman, S. K. Volkman, V. Subramanian, J. G. Korvink, U. S. Schubert, J. Mater. Chem. 2010, 20, 8446.
[4] M. Nishimoto, R. Tokura, M. T. Nguyen, T. Yonezawa, Mater. Trans. 2022, 63, 663.
[5] K. A. Ohiri, N. M. Nowicki, T. J. Montalbano, M. Presley, N. S. Lazarus, Adv. Eng. Mater. 2021, 23, 2100362.
[6] D. Li, Y. Mei, Y. Xin, Z. Li, P. K. Chu, C. Ma, G.-Q. Lu, IEEE Trans. Power Electron. 2020, 35, 12646.
[7] K. Andritsos, I. Theodorakos, F. Zacharatos, I. Zergioti, Appl. Surf. Sci. 2020, 506, 144968.
[8] R. Tokura, H. Tsukamoto, T. Tokunaga, M. T. Nguyen, T. Yonezawa, Mater. Adv. 2022, 3, 4802.

Spatial Thermal Characterization of AFSD printed Al 6061-T6 by Transient Thermoreflectance Method

Mst. Nusrat Yasmin[1], Rifat-E-Nur Hossain[1], and Arden L. Moore[1,2,*]

[1] Institute for Micromanufacturing, Louisiana Tech University
[2] Mechanical Engineering Dept., Louisiana Tech University

Abstract: In additive friction stir deposition (AFSD), the change in grain structure of the materials affects the thermal properties of materials. This study shows the thermal characterization of the Al 6061-T6 printed by AFSD using transient thermoreflectance method. This ultra-fast method is a combination of an experimental set up and a 2-D heat conduction model that measures and compares the thermal conductivity of substrate, print layer (PL) PL-1, and PL-3 of the AFSD sample.

Keywords: Transient thermoreflectance, thermal conductivity, additive friction stir deposition, grain size, printed layer, 2D heat conduction model.

1. Introduction

Thermal transport properties of materials play a critical role in additive manufacturing. Efficient optimization of any additive manufacturing process that involves heat requires a comprehensive understanding of the thermal transport properties of printed material, which may differ from bulk properties. Thermal conductivity (κ), specifically, is vital for understanding the thermal management and cooling kinetics of the process, which has a strong influence on the inter-layer bonding strength, defect formation, and overall quality of print. Studies have shown that change in thermal conductivity strongly relates to microstructure evolution. A decrease in thermal conductivity has been observed when grain size is reduced [1]. This is because grain boundaries are considered as an obstacle for heat transmission; phonon mean free path reduces due to increased phonon scattering with decreasing grain size. Therefore, smaller grain size will facilitate a decrease in thermal conductivity value [2]. In additive manufacturing, microstructure evolution can take place because of the printing technique, process parameter influence and heat treatment. Additive friction stir deposition (AFSD), which is a high strain rate thermo-mechanical additive manufacturing process for metals, has similar fundamental physics as the friction stir welding process.

When measurement of thermal conductivity is a requirement for thermal characterization of additive manufacturing materials, a non-contact nanosecond transient thermoreflectance is a fast and effective method to consider. This study presents a nanosecond transient thermoreflectance method to determine the change in thermoreflectance of the additive manufacturing friction stir materials and a heat transfer model to extract the spatially varying thermal properties using the experimental data. The thermal conductivity of Al6061-T6 alloy substrate, AFSD printed layer (PL)-1, and AFSD PL-3 are measured and discussed here.

2. Methodology

a) Sample Preparation

Polished and etched cross-section of Al 6061-T6 from additive friction stir deposition machine is used as the sample for this work. The sample consists of a substrate and five printed layers of Al 6061-T6 alloy. The nanosecond pump-probe technique is an optical technique which requires good optical properties of the sample. To enhance the optical reflectivity and absorptivity of the sample, a 100 nm gold layer is deposited on the sample surface. This gold coating works as a metal transducer during measurement.

b) Heat Transfer Model

As the pump-probe technique represents a cylindrical heat conduction phenomena, this study implements a two-dimensional heat conduction equation in cylindrical coordinates for thermal simulation of the measurement. This model considers the in-plane heat conduction in radial (r) direction and cross-plane heat conduction in axial (z) direction. The heat equation is solved numerically by using finite difference method considering the spatial domain as electrical circuit of thermal resistance and thermal capacitance.

Our developed thermal model is validated by Au-coated Si substrate. The thermal conductivity, density, specific heat capacity of the transducer layer, and density, specific heat capacity of the targeted material is considered as the fixed parameter and thermal conductivity of material as the free parameter while fitting. Table 1 shows the input parameters used in the heat transfer model for both silicon substrate and our material of interest.

Table 1: Fixed Parameters for Heat Transfer Model

Material	Density	Specific Heat	Thermal Conductivity
Gold (100 nm)	19000 kg/m^3	129 J/kg-K	158 W/m-K
Silicon	2330 kg/m^3	712 J/kg-K	fitted
Al6061-T6	2700 kg/m^3	896 J/kg-K	fitted

For curve fitting, the decay part of the thermoreflectance curve is considered as thermal properties of the material is dominated by the nature of the cooling curve [6]. The most used thermal conductivity for silicon is 148 W/m-K. [4]. Using the input parameters from Table 1, we obtained thermal conductivity for Si substrate 138 W/m-K with the best correlation coefficient of 0.99. The best fitted experimental thermoreflectance data and simulated temperature data is shown in Figure 1a). The fitted thermal conductivity is very close to the reported value. This validation result substantiates the effectiveness of our two dimensional heat transfer model.

3. Results and Discussion

For the experimental set up, a 532 nm pulsed pump laser is used to heat up the sample and a 635 nm continuous wave laser is used to probe the thermoreflectance response. The thermoreflectance response is captured with a high-throughput photodetector. The output of the photodetector is connected with an oscilloscope which shows thermal response of the sample as a thermoreflectance signal. The calculated heating spot size is 86$\mu\mu\mu\mu$ whereas the probe spot is 17$\mu\mu\mu\mu$ in diameter. This study reports a thermal penetration depth of 90 $\mu\mu\mu\mu$ that is nearly the same as the heating diameter. The pulse width of the pump laser is 20 ns. The obtained pump laser power is 1200mW and single pulse energy is 20$\mu\mu\mu\mu$.

The measurement is taken across the substrate, PL-1, and PL-3 under the same experimental condition to avoid experimental uncertainty. Figure 1b) shows the change in reflectance at various positions. It is shown that the thermoreflectance response of substrate and PL-3 are very similar to one other and overlap after 130 ns. In contrast, the PL-1 gives a faster decay than either the substrate or PL-3. Using these experimental data to our heat transfer model we obtained thermal conductivity 172 W/m-K for substrate, 188 W/m-K for PL-1, and 168 W/m-K for PL-3. Ref. [5] reports the thermal conductivity of 167 W/m-K value for traditionally processed Al6061-T6 alloy, which is in good agreement with our substrate and PL-3 values within experimental uncertainty.

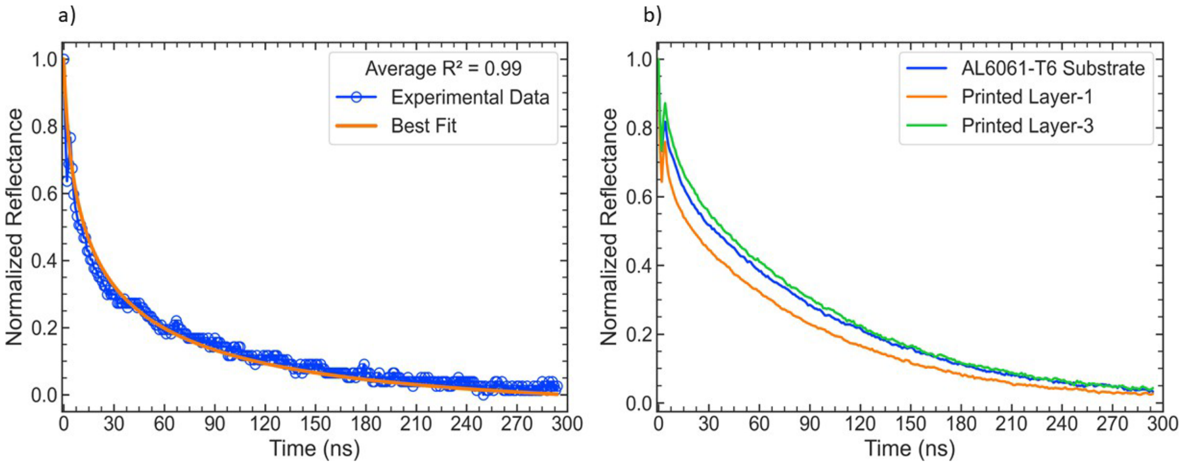

Figure 1. a) Heat transfer model validation with Silicon and b) shows experimental thermoreflectance decay curve for substrate and printed layers.

AFSD printed layers can be fully-dense even though the feed materials of the AFSD machine are not fully-dense due to intense material deformation [7]. As PL-1 shows the highest thermal conductivity, it may have denser atomic packing or have a microstructure that facilitates superior thermal transport. Additional microstructure analysis is required to confirm this hypothesis.

4. Conclusion

In this study, we have demonstrated the use of the transient thermoreflectance method to measure the location-specific thermal conductivity of Al6061-T6 alloy in various conditions: as a substrate, and in printed layers produced by AFSD. The results highlight the significant impact of the AFSD process on microstructure-influenced thermal properties. These findings underscore the importance of understanding and controlling microstructural evolution during additive manufacturing to optimize thermal properties. Future work involves investigating the change in thermal conductivity of Al6061-T6 for varying AFSD printing parameters and linking our property observations to microstructure.

5. Acknowledgments

This work is supported by the U.S. National Science Foundation under grant number OIA-1946231 and the Louisiana Board of Regents for the Louisiana Materials Design Alliance (LAMDA).

6. References

[1] J. Crocombette and L. Gelebart, “Multiscale Modeling of the Thermal Conductivity of Polycrystalline Silicon Carbide Multiscale Modeling of the thermal conductivity of polycrystalline silicon,” vol. 106, no. 8, October, 2009, doi: 10.1063/1.3240344.

[2] H. Dong, B. Wen, and R. Melnik, “Relative importance of grain boundaries and size effects in thermal conductivity of nanocrystalline materials,” pp. 1–5, 2014, doi: 10.1038/srep07037.

[3] D. Zhao, X. Qian, X. Gu, S. A. Jajja, and R. Yang, “Measurement Techniques for Thermal Conductivity and Interfacial Thermal Conductance of Bulk and Thin Film Materials,” vol. 138, no. December 2016, pp. 1–19, 2017, doi: 10.1115/1.4034605.

[4] El-Cat website
https://www.el-cat.com/silicon-properties.htm

[5] MatWeb website
https://www.matweb.com/search/datasheet_print.aspx?matguid=1b8c06d0ca7c456694c7777d9e10be5b

[6] R. Garrelts, A. Marconnet, and X. Xu, “Assessment of Thermal Properties via Nanosecond Thermoreflectance Method,” Nanoscale Microscale Thermophys. Eng., vol. 19, no. 4, pp. 245–257, 2015, doi: 10.1080/15567265.2015.1078425.

[7] H. Yu and R. Mishra, “Additive friction stir deposition: a deformation processing route to metal additive manufacturing,” Materials Research Letter. Eng., vol. 9, no. 2, pp. 71–83, 2020, doi: 10.1080/21663831.2020.184721

SS316 Fabrication with Preheated Substrate by MELD and Microstructure Comparison

Selami Emanet[1], Saeid Zavari[1], Hamed Ghadimi[1], Huan Ding[1], Shengmin Guo[1] Carl Schmidt [2]

[1]Department of Mechanical and Industrial Engineering, Louisiana State University
[2] Bechtel Plant Machinery, Inc.

Abstract: The utilization of additive manufacturing methodologies shows promising potential for the rapid fabrication of high-performance parts made of aluminum alloys and hard metal alloys, including 1018 carbon steel and SS 316 components. These techniques facilitate efficient production by enabling the facile design of the deposition path. In this study, the additive friction stir deposition (MELD) technique was employed to generate multilayer deposits of Stainless Steel 316 on a heated substrate, utilizing various printing parameters. Extensive efforts were made to identify optimal parameters and enhance the quality of the printed components. Post-printing, a microstructural evaluation was conducted to assess the bonding quality between layers along the z-axis direction. The findings of this study are encouraging, providing a comprehensive analysis of the mechanical and thermal properties of the produced components.

Keywords: Additive Manufacturing, Additive Friction Stir Deposition, Hard Metals, SS316

1. Introduction

Due to their low density, high strength, exceptional corrosion resistance, fracture toughness, and plastic formability, aluminum alloys are among the most widely used structural materials in industrial manufacturing [1]. Concurrently, additive manufacturing technologies represent a rapidly evolving field, with new production techniques emerging swiftly. Advances in metal additive manufacturing technology now allow for the quick and easy design and creation of complex, lightweight aluminum structures [2].

Additive Friction Stir Deposition (AFSD), also known as MELD, is a layer-by-layer solid-state additive manufacturing technique. The process relies on the friction generated between the rotating feedstock material bar, the deposition tool, and the printing substrate. Initially, the feeder rod is directed towards the substrate, creating significant frictional heating upon contact. This frictional heat initiates the plastic flow of the material, filling the void between the tool and the substrate. The resulting frictional heat and substantial plastic deformation form a metallurgical bond between the feeding rod and the substrate. Once the deposition process stabilizes, the tool follows the predetermined G-code to complete the manufacturing. This technique is highly advantageous and capable of large-scale additive manufacturing [3][4].

With these developments, the production of many different alloys such as stainless steel and carbon steels with MELD attracts the attention of organizations in different fields. The MELD technique is highly advantageous and possesses substantial production capacity for large-scale additive manufacturing. Based on the preceding information, this investigation aims to fabricate SS316 using specific printing parameters, including spindle speed, feed rate, and travel speed, in conjunction with the MELD machine, which employs the AFSD technique. Subsequently, an analysis of the material's microstructure will be conducted, with the anticipation that it will provide valuable insights for future research endeavors. Additionally, this study will explore the effect of different layer thicknesses on the microstructure of the printed parts.

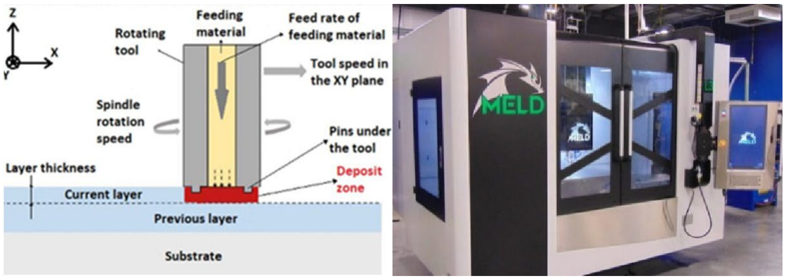

Figure 1. AFSD mechanism and the MELD L3

As MELD fabrication is a novel technology, the production of key alloys is significant, and the investigation into the production of various hard metals will be essential in this field [5]. From this perspective, this study will fundamentally guide our future research.

In this study, the preheated substrate design previously utilized in the production of aluminum alloys was further developed and redesigned to accommodate the production of hard metals, with its capacity increased to 650 degrees Celsius. Our previous study highlighted the significant importance of this design in the manufacturing process.

2. Material and Method

The AFSD of SS316 was conducted using a MELD-L3 machine equipped with a MELD-based tungsten tool. Figure 1 presents the schematic of the AFSD process, the tool used, and the resulting SS316 deposits. Commercial grade SS316 rods, with dimensions of 9.525 mm in thickness and width and 508 mm in length, were utilized as feedstock material and fed through a hollow rotating tungsten tool. The solid feedstock material was plasticized at high temperatures due to the combined effect of friction stir heating and deformation-induced (adiabatic) heating [6]. The AFSD process parameters significantly impact the microstructure of the printed samples. Consequently, the parameters were adjusted according to the track width, the specific parameter combinations illustrated in Table 1.

Table 1. ASFD SS 316 Process Parameters

Sample	Layer Thickness (inch)	Feed Rate (ipm)	Spindle Speed (RPM)	Traverse Rate (ipm)
1	0.03	1.5	400	7
2	0.06	2	400	5.2

All parameter calculations were made according to the calculation method specified below.

$$Track\ Width(IN) = \frac{Feed\ Rate(IPM) * Area\ of\ bar(IN^2)}{Tool\ Speed(IPM) * Layer\ Height(IN)}$$

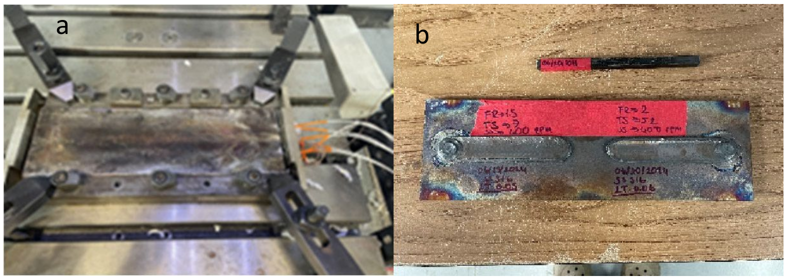

Figure 2. a) Heated Substrate b) SS316 Deposited Parts

All parameters were calculated, and the G-codes were set according to the specified parameters. After determining the zero positions for the x, y, and z axes, the substrate was preheated to 650 degrees Celsius. Following the depositions, the samples were cross sectioned to examine the microstructure. Subsequently, a milling machine was used to clean the surface, and the samples were polished. Additionally, the hardness of the samples was measured for comparative analysis.

3. Results

The SS316L samples, fabricated with a layer thickness of 0.03 inches, a travel speed of 7 ipm, and a feeding rate of 1.5 ipm, demonstrated a consistent hardness distribution. The hardness at the interface was consistently higher than that of the substrate, indicating strong metallurgical bonding. Specifically, the microhardness measurements were 230 HV – 250 HV between layers, 215 HV – 225 HV at the interface, and 195 HV – 205 HV for the substrate. These results suggest the presence of metallurgical bonding at the interface.

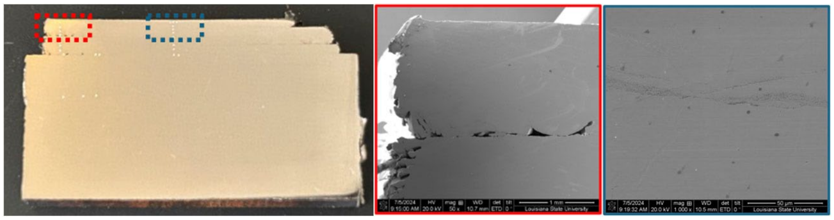

Figure 3. Microstructures analyze of SS316 Deposited part (Layer Thickness 0.03)

SS316L samples fabricated with a layer thickness of 0.06 inches, a travel speed of 5.2 ipm, and a feeding rate of 2 ipm exhibited an irregular distribution in hardness. Microhardness measurements revealed values ranging from 175 HV to 270 HV between layers, with the interface maintaining a stable hardness between 215 HV and 225 HV, and the substrate showing values between 195 HV and 205 HV. Interestingly, some interlayer regions displayed hardness lower than that of the substrate. Overall, these samples demonstrated lower hardness compared to those with a 0.03-inch layer thickness. The results indicate the presence of metallurgical bonding at the interface.

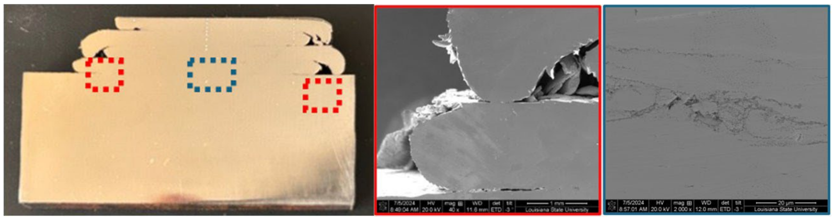

Figure 4. Microstructures analyze of SS316 Deposited part (Layer Thickness 0.06)

4. Conclusion

In conclusion, the study of SS316L samples with varied layer thicknesses and printing parameters revealed distinct hardness distributions. Samples with a 0.03-inch layer thickness, produced at 7 ipm travel speed and 1.5 ipm feeding rate, showed consistent hardness and clear metallurgical bonding at the interface. Conversely, samples with a 0.06-inch layer thickness, manufactured at 5.2 ipm travel speed and 2 ipm feeding rate, exhibited irregular hardness distribution, with some interlayer regions displaying lower hardness than the substrate, despite stable interface hardness. These findings highlight the significant influence of layer thickness and printing parameters on overall hardness and microstructural integrity. Moreover, opting for a reduced layer thickness enhances bonding quality, demonstrating the clear impact of parameters on hard metals.

5. Acknowledgments

This work is supported by the U.S. National Science Foundation under grant number OIA-1946231 and the Louisiana Board of Regents for the Louisiana Materials Design Alliance (LAMDA).

6. References

[1] Tang, W., Yang, X. & Tian, C. Influence of rotation speed on interfacial bonding mechanism and mechanical performance of aluminum 6061 fabricated by multilayer friction-based additive manufacturing. Int J Adv Manuf Technol 126, 4119–4133 (2023).
[2] Shimizu S, Fujii HT, Sato YS, Kokawa H, Sriraman MR, Babu SS (2014) Mechanism of weld formation during very-high-power ultrasonic additive manufacturing of Al alloy 6061. Acta Mater 74:234–243
[3] Dong, H.; Li, X.; Xu, K.; Zang, Z.; Liu, X.; Zhang, Z.; Xiao, W.; Li, Y. A Review on Solid-State-Based Additive Friction Stir Deposition. Aerospace 2022, 9, 565
[4] Ghadimi, H.; Ding, H.; Emanet, S.; Talachian, M.; Cox, C.; Eller, M.; Guo, S. Hardness Distribution of Al2050 Parts Fabricated Using Additive Friction Stir Deposition. Materials 2023, 16, 1278.
[5] Priyanshi Agrawal, Ravi Sankar Haridas, Surekha Yadav, Saket Thapliyal, Abhijeet Dhal, Rajiv S. Mishra, Additive friction stir deposition of SS316: Effect of process parameters on microstructure evolution, Materials Characterization, Volume 195, 2023
[6] Williams, M.B.; Zhu, N.;Palya, N.I Towards Understanding the Relationships between Processing Conditions and Mechanical Performance of the Additive Friction Stir DepositionProcess. Metals 2023, 13, 1663. https://doi.org/10.3390/met13101663

Structural Condition Assessment of Concrete Beams Utilizing Aerial Vehicles (UAVs) and Computer Vision

Nazila Jamshidighadikolaei[1], Hadi Salehi[2]

[1]Phd Student, Department of Civil Engineering and Construction Engineering Technology, Louisiana Tech University
[2]Assistant Professor, Department of Civil Engineering and Construction Engineering Technology, Louisiana Tech University

Abstract: Concrete is a widely used material in civil infrastructure due to its durability, strength, and versatility. Regular monitoring of concrete structures is essential to ensure safety and serviceability due to aging. Traditional crack detection methods mainly suffer from drawbacks such as human error, time constraints, and accessibility issues. This study proposes a smart monitoring platform using a computer-vision based approach and unmanned aerial vehicles (UAVs) to tackle noted challenges. Two concrete beams were fabricated and tested under shear dominant loading and 2000 images were captured by a UAV. The proposed approach employing deep learning analyzes images collected from experiments for crack detection. Through the integration of deep learning architectures, namely, convolutional neural networks (CNNs) for spatial feature extraction and long short-term memory (LSTM) for temporal analysis, the computer vision-based approach achieved a high accuracy of 99.80%. The results demonstrate the effectiveness of the smart monitoring platform for enhanced structural health monitoring of concrete members, with a potential for further improvements by using larger datasets and optimized UAV deployment.

Keywords: Crack detection, Real-time monitoring, Computer vision, Convolutional neural networks (CNN), Long Short-term memory (LSTM), Unmanned aerial vehicles (UAVs)

1. Introduction

Concrete is a fundamental construction material widely used in critical civil infrastructures due to its durability, strength, longevity, and versatility [1], [2]. Regular and reliable monitoring of concrete infrastructure is essential to ensure safety and serviceability, as concrete surfaces experience various types of damage over time, including cracks, corrosion, delamination, and spalling. Cracks are particularly important as they indicate structural integrity, yet conventional crack detection methods relying on human visual inspection are limited by inspector experience, time constraints, access issues, high costs, labor intensity, and safety hazards [3], [4].

To address these limitations, this research introduces an innovative computer vision-based method integrated with unmanned aerial vehicles (UAVs) to improve the accuracy and efficiency of detecting cracks in concrete structures. Computer vision techniques analyze, and process images or videos collected by UAVs to identify patterns and detect anomalies. Deep learning methods, such as Convolutional Neural Networks (CNN) and Long Short-Term Memory (LSTM), are employed to enhance the automated analysis of images, enabling consistent, accurate, and efficient crack detection. Despite advancements in crack detection using computer vision, existing research often overlooks temporal analysis, is time-consuming, computationally expensive, and lacks scalability. This paper proposes a real-time computer vision technique combining CNN and LSTM architectures for crack detection, leveraging UAVs for automated data collection and analysis. The proposed method was trained and evaluated using images from experimental studies on beams [5].

The results demonstrate the capabilities and limitations of UAV-assisted inspections, validating the effectiveness of the CNN-LSTM framework in accurately detecting and classifying cracks. This research contributes to the development of an advanced structural health monitoring method for concrete infrastructures, reducing failure rates and ensuring the durability and reliability of critical civil structures. The paper is structured as follows: Section 2 outlines the methodology, including data collection and the CNN-LSTM architecture. Section 3 presents the results and discussion, and Section 4 concludes the research.

2. Methodology

The dataset for this study was obtained from laboratory experiments involving two reinforced concrete beams subjected to shear-dominant loading. The beams, measuring 8 feet in length, 9 inches in width, and 12 inches in depth, were fabricated with high-strength concrete and varied in concrete mix composition and stirrup spacing. One beam included steel fibers along with longitudinal and transverse reinforcements. A four-point loading setup applied incremental shear loading via a 120 KN capacity MTS machine, and crack propagation was monitored at different load levels. Data collection was performed using an EVO II Pro V3 UAV equipped with a Sony 20-megapixel camera. The UAV, manually operated and maintained approximately 2 meters from the beams, captured around 5000 images in both cracked and uncracked conditions. Figure 1 illustrate the beam casting process, experimental setup, and data acquisition, and employed UAV.

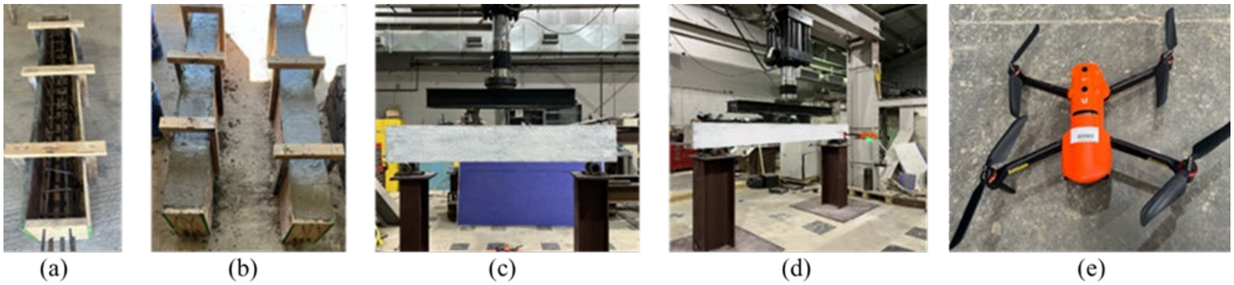
(a) (b) (c) (d) (e)

Fig. 1 (a) Reinforced concrete mold for casting beams (b) Casting beams (c) Test setup (d) Data acquisition utilizing UAV (e) Autel Evo II pro V3 for image acquisition

This study employs a CNN-LSTM architecture for crack classification and object detection, combining spatial feature extraction and temporal sequence modeling. The CNN model consists of three convolutional layers with 32, 64, and 128 filters respectively, each using a 3×3 kernel size. Each layer includes a ReLU activation function and a 2×2 max pooling layer to reduce spatial dimensions and enhance feature extraction. The CNN-extracted features are flattened and input into the LSTM model. The LSTM consists of two layers with 128 and 64 units, using ReLU activation to capture temporal dependencies and sequential patterns. The final dense layer with a sigmoid activation function outputs a binary classification, predicting cracked or intact structural conditions. Figure 2 depicts the CNN-LSTM model architecture, and Table 1 details each layer.

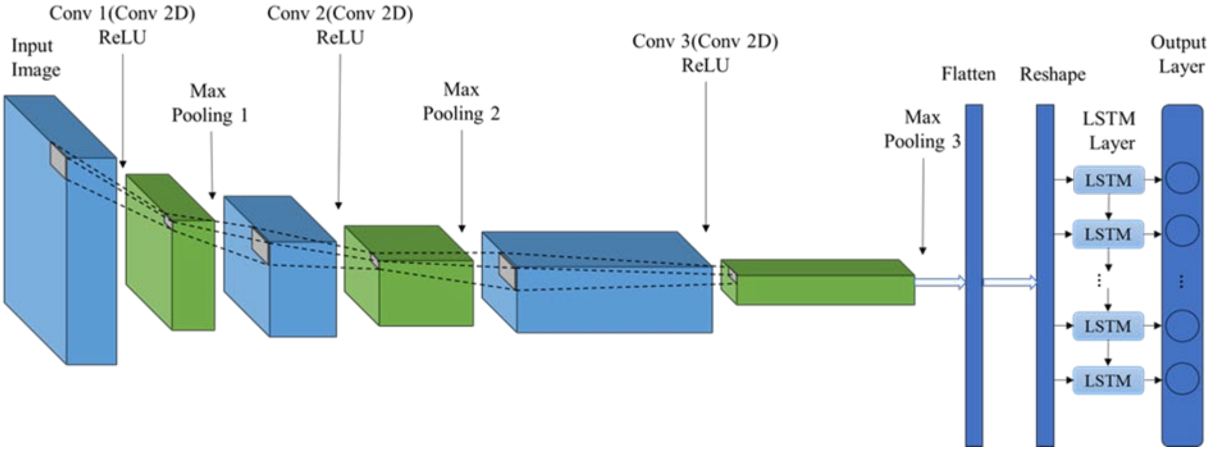

Fig. 2 Schematic of the CNN-LSTM architecture

Table 1. Information regarding each layer within the deep learning architecture

Layer	**Operator**	**Output Shape** **(Height × Width × Depth)**	**Kernel** **(Height × Width)**	**Number of Parameters**
Layer 1	Conv 1 (Conv2D) / ReLU	98 × 98 × 32	3 × 3	896

Layer 2	Max Pooling 1	49 × 49 × 32	2 × 2	0
Layer 3	Conv 2 (Conv2D) / ReLU	47 × 47 × 64	3 × 3	18496
Layer 4	Max Pooling 2	23 × 23 × 64	2 × 2	0
Layer 5	Conv 3 (Conv2D) / ReLU	21 × 21 × 128	3 × 3	73856
Layer 6	Max Pooling 3	10 × 10 × 128	2 × 2	0
Layer 7	Flatten	12800	-	0
Layer 8	Reshape	1 × 12800	-	0
Layer 9	LSTM 1 / ReLU	1 × 128	-	6619648
Layer 10	LSTM 2 / ReLU	64	-	49408
Layer 11	Dense / Sigmoid	1	-	65

The dataset comprised 3000 images, with 1500 images each of cracked and intact instances, split into training and test sets. Data preprocessing and augmentation techniques, such as cropping, resizing, shuffling, splitting, and normalization, were used to enhance the model's robustness. The CNN-LSTM model was evaluated using metrics like accuracy, ROC curve, F-1 score, and result visualization to assess its effectiveness. Hyperparameters were optimized using the control variable method, focusing on the optimizer, learning rate, and test size. The Adam optimizer with a learning rate of 0.0001 yielded the best results. The model was developed using the TensorFlow framework and Python, and simulations were conducted on a desktop with an Intel Core i7-13700 CPU, Intel UHD Graphics 770 GPU, and 32 GB of RAM, running Windows 11, TensorFlow 2.16.1, and Python 3.11.5 in a Jupyter notebook via Anaconda.

3. Crack Detection Results

The overall performance of the proposed CNN-LSTM model for structural health monitoring was assessed using UAV-captured images from experiments conducted on two beams. The dataset was split randomly into training and test sets in five different scenarios: (1) 85% training set and 15% test set, (2) 80% training set and 20% test set, (3) 75% training set and 25% test set, (4) 70% training set and 30% test set, and (5) 65% training set and 35% test set. Model performance was measured and presented by using accuracy, ROC curve, F1 score, and visualizations of classification and object detection results. The performance of the model for each case is illustrated in Table 2. The highest performance was observed in Case 3. The model demonstrated excellent accuracy in detecting cracks, with a confusion matrix showing 99.6% accuracy for cracked beams and 99.9% for intact beams resulting in an overall accuracy of 99.80% in Case 3. The ROC curve, with an AUC of 1 for almost all cases, further confirmed the model's robustness and efficiency in distinguishing between cracked and intact surfaces.

Table 2. Performance of the proposed CNN-LSTM model across five cases with varying test set size

Data subset	Test size	Accuracy (%)	AUC	f-1 score
Case 1	15%	99.66	0.99	0.98
Case 2	20%	99.50	1.00	0.99
Case 3	25%	99.80	1.00	0.99
Case 4	30%	99.50	1.00	0.99
Case 5	35%	99.71	1.00	0.98

Visualizations in Figure 3 (a) shows the model's effectiveness in correctly identifying cracked and intact instances, with cracked surfaces labeled as 1 and intact surfaces as 0. Figure 3 (b) depicts the results of object detection, highlighting cracks with rectangular bounding boxes. Enlarging the dataset and incorporating more diverse data are expected to enhance the model's performance further.

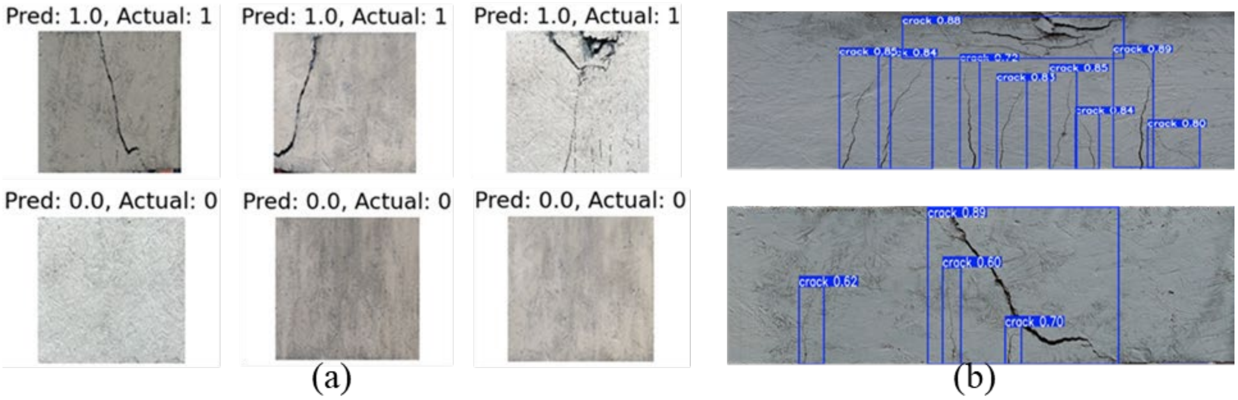

(a) (b)

Fig. 3 (a) Visualization results for crack classification: 0 refers to intact (negative), and 1 refers to cracked (positive) surfaces (b) Object detection for concrete surfaces of the beams

4. Conclusion

In this research, a novel method for structural condition assessment of concrete beams was presented by integrating a CNN-LSTM computer vision model with the utilization of UAV for data collection. The proposed method employs CNN to extract high-dimensional spatial features from the input and LSTM to extract time-series features of the dataset. A total number of 2000 images of cracked and non-cracked concrete surfaces were captured in laboratory and were randomly split to train and test the proposed CNN-LSTM architecture. Various test sizes were evaluated, with the best performance achieved using 75% of the data for training and 25% for testing. The model demonstrated an accuracy of 99.50% on the testing dataset.

The implemented framework effectively utilized the well-trained model and showed great performance in accurately detecting cracks, despite being trained on a limited dataset. Confusion matrix, ROC curve, f-1 score, and visual representation of object detection and classification were implemented to validate the results. Although the proposed deep learning model achieved good performance, its performance could be further enhanced by incorporating more training data to improve generalization to unseen cases. Future research could aim to develop models utilizing larger and more diverse datasets or integrating other deep learning methods to achieve better performance. Moreover, while UAVs offer significant benefits for data collection, they also present limitations such as difficulties in accessing hard-to-reach areas and dependence on weather conditions. Future studies could explore optimizing the use of UAVs to overcome these limitations and achieve the best results in data collection.

5. Acknowledgments

This work is supported by the start-up fund provided by the College of Engineering and Science at Louisiana Tech University and the Louisiana Board of Regents for the Louisiana Materials Design Alliance (LAMDA).

6. References

[1] Z. Li, X. Zhou, H. Ma, and D. Hou, *Advanced concrete technology*. John Wiley \& Sons, 2022.

[2] B. Han, L. Zhang, and J. Ou, *Smart and multifunctional concrete toward sustainable infrastructures*. Springer, 2017.

[3] R. Solhmirzaei, H. Salehi, and V. Kodur, “A computer vision-based approach for crack detection in ultra high performance concrete beams,” *Comput. Concr.*, vol. 33, no. 4, p. 341, 2024.

[4] H. J. Jung, J. H. Lee, S. S. Yoon, I. H. Kim, and S. S. Jin, “Condition assessment of bridges based on unmanned aerial vehicles with hybrid imaging devices,” in *Proceedings of the 2017 World Congress on Advances in Structural Engineering and Mechanics (ASEM17), Ilsan, Korea*, 2017.

[5] B. F. Spencer, V. Hoskere, and Y. Narazaki, “Advances in Computer Vision-Based Civil Infrastructure Inspection and Monitoring,” *Engineering*, vol. 5, no. 2, pp. 199–222, 2019, doi: https://doi.org/10.1016/j.eng.2018.11.030.

Structural Stability of Ni38Co33Cr29 Alloy at High Temperatures

Frank McKay[1], Brianna C. Simon[1], Kane Bergeron[2], S. Thomas Britt[3], David P. Young[1], Jonathan Raush[2], Phillip T. Sprunger[1]

[1]Department of Physics & Astronomy, Louisiana State University
[2]Department of Mechanical Engineering, University of Louisiana at Lafayette
[3]Jacobs Space Exploration Group, NASA Marshall Space Flight Center

Abstract: The structural stability of the novel alloy $Ni_{38}Co_{33}Cr_{29}$ is tested using the method of energy-dispersive X-ray diffraction (XRD) at high temperatures and 2D XRD at room temperature (RT). These measurements are compared to a CALPHAD structural phase diagram and show an additional *fcc* phase appearing at room temperature, and an additional unknown structural phase appearing at high temperatures.

Keywords: Complex concentrated alloys, high-temperature, X-ray diffraction, additive manufacturing, CALPHAD, structural phase stability

1. Introduction

The investigation of the dynamic structural evolution of metal alloys at high temperatures is vital to understanding their potential use in additive manufacturing (AM) processes. All AM techniques require exposure to high temperatures. In some cases, all the way to the melting point. For example, in select laser melting processes,[1] a solid metal powder is rapidly liquified by a laser and then allowed to solidify layer-by-layer, forming a 3d geometry. In other processes, such as friction-stir additive manufacturing[2] and fused deposition modelling[3] subsequent layers are heated to near their melting point, to allow easy flow of the feedstock material. A thorough understanding of the structural evolution of prospective alloys is critical to determining if they are viable for AM.

Given recent interest in the AM applications of 3d transition metal alloys,[4-6] there is a demand for different alloy compositions to be tested. In this paper, we investigate the structural stability of $Ni_{38}Co_{33}Cr_{29}$ by performing X-ray diffraction (XRD) measurements at high temperatures and comparing to phase diagrams generated by CALculation of PHAse Diagram (CALPHAD) methods.[7] The structural changes of the sample at high temperatures are measured using energy-dispersive X-ray diffraction (ED-XRD) on electrostatically levitated (ESL) samples. These results are then compared to room temperature (RT) measurements in a typical 2D-XRD setup.

2. Methods

This sample was manufactured by mixing pure powders (99.99%) at the desired elemental concentration and arc-melting in a water-cooled copper hearth in an argon atmosphere. A larger ingot was re-melted and turned over several times to ensure a homogenous sample. A small piece was then removed and re-melted to form a small spherical bead approximately 2 mm in diameter

In brief, our ED-XRD experiments were conducted at LSU's synchrotron facility (Center for Advanced Microstructures and Devices-CAMD) using NASA Marshall Space Flight Center's (MSFC) mobile ESL chamber. After the sample was manufactured, it was then loaded into the ESL chamber and ED-XRD measurements were taken at several temperatures. Each measurement was performed after the sample was at a stable temperature and position, recorded over a period of 180 seconds. The sample, exposed to polychromatic light from the synchrotron, generated X-ray scattering[8] emissions which provided structural information according to Bragg's law. These, as well as X-ray fluorescence (XRF) emissions, are measured with a Ketek™ AXAS-M1 Si-drift detector, which is sensitive to energies up to 20 keV. The sample was levitated in the ESL chamber and measured at a variety of temperatures from room temperature (RT ~25°C) to near its predicted melting point. Heating was provided by a 600W 810 nm diode laser focused on the sample and temperature monitored using an Impac IGA 140 optical pyrometer (300 – 2000°C).

Two aspects of this measurement process are important to note. Only an area in the near-surface region (<15 µm)[9] of these samples are being measured. Secondly, since the synchrotron light was of sufficient energy, XRF emissions are measured as well. At times, this can cause artifacts to appear in the spectra which originate from the "double counting" of two characteristic XRF emissions within the duty cycle of the detector.[10] This can cause peaks to appear at energies that are the sum of any two XRF emissions, which may interfere with X-ray scattering peaks.

For this sample composition a CALPHAD phase diagram was generated for temperatures from 200°C to the melting point. The CALPHAD software generates these phase diagrams by calculating the Gibbs free energy for all compositional configurations at a specific temperature. This phase diagram provides a comparison of the possible structural phases for this alloy composition to the crystal structure measured by ED-XRD.

After the sample was processed in the ESL chamber, 2D XRD measurements were performed with a Bruker D8 GADDS in Bragg-Brentano geometry with a Cu Kα (λ=1.5406 Å) source at RT. Prior to 2D-XRD measurements, the sample was polished down through half its diameter to provide a cross-section of the sample.

3. Results

CALPHAD (Figure 1) predicts that this alloy has two *fcc* + a single *bcc* phase up to 400°C, a single *fcc* + *bcc* phase up to 800°C, and then a single *fcc* phase above 800°C. An initial inspection of our ED-XRD results (Figure 2a) revealed an *fcc* phase through all temperatures with three peaks labelled (111), (200), and (220) in Figure 2a. However, the behavior of the (200) peak does not follow the same trend of the (111) and (220) peaks at 799°C and higher. Specifically, it does not shift as expected due to thermal expansion. This could be due to the presence of an additional phase, contrary to CALPHAD predictions in Figure 1. Unfortunately, any additional peaks associated with this unknown phase cannot be found, so the identification of the structural symmetry cannot be determined from ED-XRD data alone.

To illustrate the behavior of this unknown phase, the change in the lattice spacing as determined by Bragg's law[8] is shown in Figure 2b. The blue line in Figure 2b shows the lattice constant from the primary *fcc*

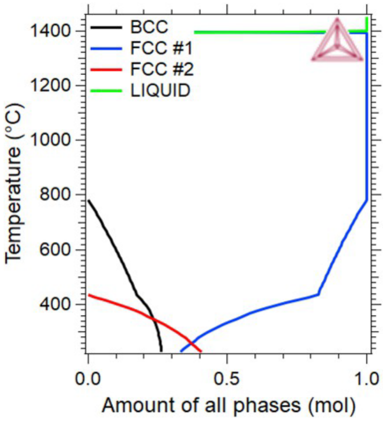

Figure 1: CALPHAD predictions showing predicted structural phases as function of temperature.

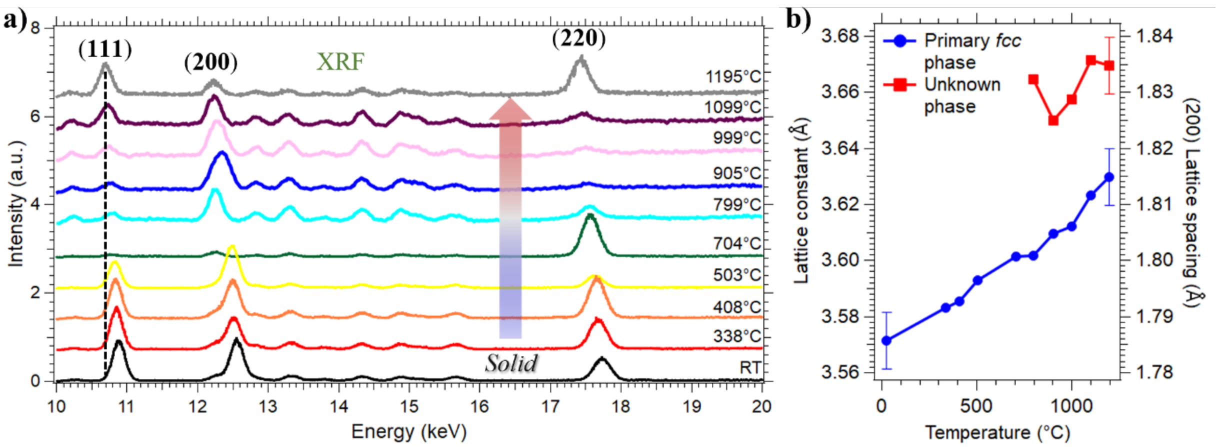

Figure 2: a) ED-XRD results shows one *fcc* phase at all temperatures, and another unidentified phase from 799°C to 1195°C. b) Temperature-dependent lattice constant of the primary *fcc* phase (blue circles) and lattice spacing of unknown phase (red squares).

phase, as determined by the locations of the (111), (200), and (220) peaks, plotted on the left-axis. Plotted on the right-axis on that same line is the lattice spacing from the (200) peak of that phase. The red line in Figure 2b shows the lattice spacing of the unknown phase plotted on the right-axis.

The inability to see this additional phase at low temperatures is likely due to the limited resolution (± 0.01 Å) of this ED-XRD technique and interference between the (200) scattering peak and fluorescence artifacts, such as from the Ni Kα + Cr Kα artifact (@12.3 keV). Examples of other artifacts combinations can be seen in Figure 2 in the region labelled "XRF".

Results from 2D-XRD data taken at RT can be seen in Figure 3. As seen in the inset, additional peaks can be seen at higher angles. The highlighted sets of peaks correspond to the (220) and (311) peaks of two different *fcc* phases with lattice constants 3.56 Å & 3.55 Å. Considering that the error in lattice constant from our ED-XRD measurements is ±0.01 Å, it is unsurprising that this additional phase cannot be resolved at RT with ED-XRD.

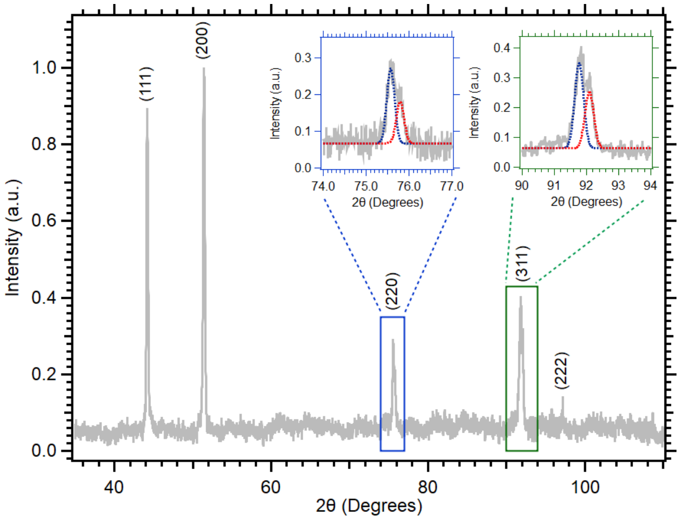

Figure 3: 2D-XRD on $Ni_{38}Co_{33}Cr_{29}$ sample in spinning mode at RT. The insets highlight fits for (220) peaks (2θ = 75.6° & 75.8°) and (311) peaks (2θ = 91.8° & 92.1°).

4. Conclusion

In this paper, we've looked at the structural evolution of a particular alloy,

$Ni_{38}Co_{33}Cr_{29}$, by taking XRD measurements at RT and high temperatures. The XRD measurements are compared to phase diagrams generated by CALPHAD. While there is some agreement with CALPHAD at RT, it fails to predict the high temperature behavior of this alloy. Our 2D-XRD measurement reveals that a dual *fcc* phase does in fact exist at RT but is unable to see the *bcc* phase predicted by CALPHAD. Our high temperature ED-XRD measurements reveal another unknown phase, contrary to the single *fcc* phase predicted by CALPHAD at high temperatures. This additional unknown phase appears near the same temperatures in which CALPHAD predicts secondary *fcc* and *bcc* phases are supposed to be absent. This ultimately shows that CALPHAD predictions are only partially accurate for this ternary alloy configuration. It is apparent that additional measurements, with increased resolution, will need to be performed to fully understand the structural evolution of this alloy at high temperatures and its viability for AM applications.

5. Acknowledgments

This work is supported by the U.S. National Science Foundation under grant number OIA-1946231 and the Louisiana Board of Regents for the Louisiana Materials Design Alliance (LAMDA).

6. References

[1] Yap, C.Y., et al., *Review of selective laser melting: Materials and applications.* Applied physics reviews, 2015. **2**(4).

[2] Palanivel, S., H. Sidhar, and R. Mishra, *Friction stir additive manufacturing: route to high structural performance.* Jom, 2015. **67**: p. 616-621.

[3] Rajan, K., et al., *Fused deposition modeling: process, materials, parameters, properties, and applications.* The International Journal of Advanced Manufacturing Technology, 2022. **120**(3-4): p. 1531-1570.

[4] Hosseini, E. and V. Popovich, *A review of mechanical properties of additively manufactured Inconel 718.* Additive Manufacturing, 2019. **30**: p. 100877.

[5] Karmuhilan, M. and S. Kumanan, *A review on additive manufacturing processes of inconel 625.* Journal of Materials Engineering and Performance, 2021: p. 1-10.

[6] Konieczny, B., et al., *Challenges of Co–Cr alloy additive manufacturing methods in dentistry—The current state of knowledge (systematic review).* Materials, 2020. **13**(16): p. 3524.

[7] Andersson, J.-O., et al., *Thermo-Calc & DICTRA, computational tools for materials science.* Calphad, 2002. **26**(2): p. 273-312.

[8] Marschilok, A.C., et al., *Energy dispersive X-ray diffraction (EDXRD) for operando materials characterization within batteries.* Physical Chemistry Chemical Physics, 2020. **22**(37): p. 20972-20989.

[9] Henke, B.L., E.M. Gullikson, and J.C. Davis, *X-ray interactions: photoabsorption, scattering, transmission, and reflection at E= 50-30,000 eV, Z= 1-92.* Atomic data and nuclear data tables, 1993. **54**(2): p. 181-342.

[10] Goldstein, J.I., et al., *Energy dispersive X-ray spectrometry: physical principles and user-selected parameters.* Scanning Electron Microscopy and X-Ray Microanalysis, 2018: p. 209-234.

Synthesis and Characterization of CoCrFeNi HEA (110) Single-crystal

Frank McKay[1], David P. Young[1], Phillip T. Sprunger[1]

[1]Department of Physics & Astronomy, Louisiana State University

Abstract: As high-entropy alloys are being developed for a variety of different applications, chemisorption studies of these alloys are of particular interest. In preparation for these studies a large (~20mm^3) single crystal, quaternary *fcc* CoCrFeNi sample was synthesized via a modified Czochralski technique. The size and orientation of the crystal was determined by low-energy electron diffraction measurements, X-ray diffraction, and electron backscattered diffraction to be oriented along the (110) direction. The equimolar composition was also verified by energy-dispersive x-ray spectroscopy.

Keywords: X-ray diffraction, Low-energy electron diffraction, High-entropy alloys, single-crystal synthesis

1. Introduction

Chemisorption on metal alloy surfaces can be complex, yet it continues to provide a playground for understanding and developing unique catalytic behaviors. For decades, researchers have conducted fundamental investigations into the adsorption properties of single-crystal, single-element metals, and to a lesser extent, binary alloys.[1, 2] Vibrational studies of the adsorption process on transition metal surfaces have long helped provide a thorough picture of the bonding and structure of adsorbates. Countless examples of studies of adsorption of common gases can be found in the literature.[3-6] However, fundamental studies of more complex model systems, such as quaternary and higher component, high-entropy alloys (HEAs) are nearly nonexistent.[7]

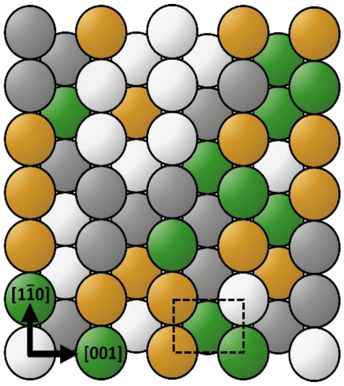

Figure 1: Schematic of the fcc structure of a random (110) quaternary HEA alloy, where different colors indicate different elements.

HEAs are a relatively new class of alloys discovered by Cantor and Yeh.[8, 9] They consist of multiple elements but in nearly equal molar proportions, in which the entropy of mixing favors the formation of solid solutions with a random distribution of elements as illustrated in Figure 1.

However, the study of these alloys requires reliable methods of single-crystal synthesis of these compositionally random, but structurally low-index HEAs. This paper reports on the synthesis of a single-crystal CoCrFeNi(110) surface and characterization by low energy electron diffraction (LEED), X-ray diffraction (XRD) and electron-backscattered diffraction (EBSD).

2. Sample Synthesis

The CoCrFeNi sample containing relatively large (~20 mm^3) single crystal grains of the HEA was grown by a modified Czochralski technique[10] in an RF-induction furnace. Stoichiometric amounts of the constituent elements in the HEA were placed in a large alumina crucible surrounded by a tantalum sleeve that served as a flux susceptor (Figure 2). The crucible was placed inside the RF furnace that was evacuated and backfilled with ultra-high-purity argon gas. The sample was completely melted, and the elements were mixed thoroughly. A 4-mm diameter pure single crystal tungsten rod was lowered into the top of the melt to initiate seed crystal growth. The temperature of the melt was kept just above the melting point of the HEA (T_m= 1861° C).[11] The rod and crucible were counter-rotated at approximately 10 rpm. A Centorr Vacuum Industries Series 3 crystal puller was used to extract the rod at a rate of approximately 3 mm/h. Afterwards, a section was sliced from the tungsten seed rod by electrical-discharge machining (EDM). This EDM-cut ingot was then sanded and polished with a compound of alumina powder (down to 0.2 µm, 99.99%, Alfa Aesar) to preferentially reveal the (110) surface.

Figure 2: Modified Czochralski technique shown. CoCrFeNi single-crystal boule is being grown/pulled in an RF furnace. Seeding W single-crystal rod shown at top.

3. Methods

To reveal the bulk structure, 2D-XRD (Bruker D8 GADDS) with Cu Kα (λ = 1.5406 Å) was employed. During these measurements the (~0.5 mm) X-ray beam was focused on the large (110) grain while the sample was set in spinning mode. Probing the nearer surface structure (10 - 15 nm), EBSD and energy-dispersive X-ray spectroscopy (EDS) measurements (at 20 keV) were performed using a ThermoScientific Helios G5 XVe PFIB at the Shared Instrument Facility at Louisiana State University.

LEED measurements were performed in an ultra-high vacuum (UHV) chamber (10^{-10} Torr base pressure) equipped with Specs ErLEED 1000-A optics and neon ion sputtering gun. Prior to LEED measurements the sample was cleaned by repeated cycles of neon ion sputtering (45 min) at room temperature and annealing (~800°C for 5 mins). The clean sample was then cooled to -190°C. Just prior to LEED measurements, the cooled sample was flash annealed to approximately 800°C to remove any residual adsorbates on the surface.

4. Results

For this single crystal, EBSD measurements (**Error! Reference source not found.**a) show a large single grain at least 2 x 3 mm in area. In addition, EDS confirmed that in the near-surface region (< 80 nm) the sample remained compositionally nearly equimolar (±0.5%), consistent with other HEAs.[8, 9] Lastly, our 2D XRD

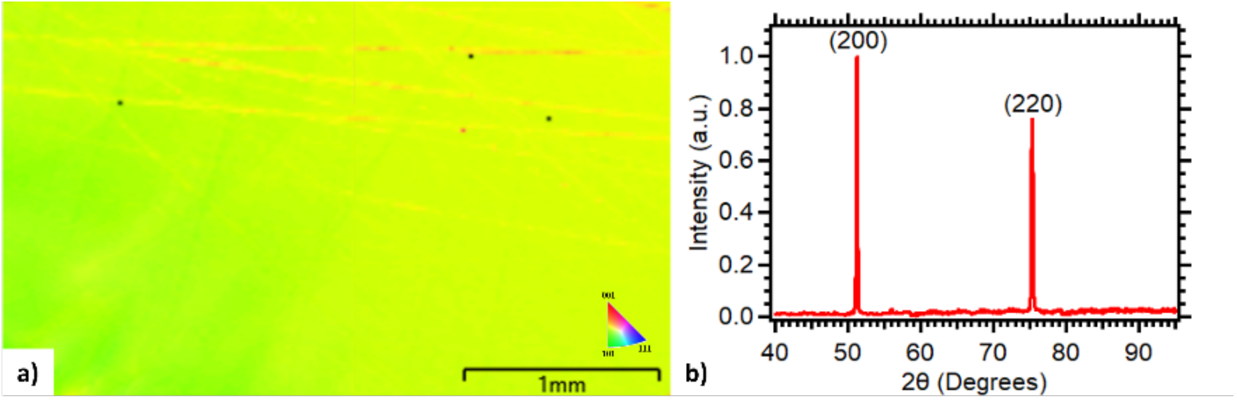

Figure 3: a) 2D EBSD composite image of CoCrFeNi (110) sample; stitched together from two large images, indicates a large, oriented grain. The horizontal lines are remnants of crystal polishing (dark spots are residual diamond polishing particles). b) XRD of CoCrFeNi (110) in sample-spinning mode.

measurements (**Error! Reference source not found.**b) show a single-phase *fcc* structure with a lattice constant of 3.56 Å, consistent with our previous studies.[12, 13]

The LEED pattern of a single-crystal, clean (sputtered & annealed) CoCrFeNi(110) surface is shown in Figure 4. This pattern shows the typical [110] diffraction spots that indicate a large single crystal grain of a *fcc* structure nearly perpendicular to the surface. The size of the crystal grain was confirmed by translating across the crystal (~3×5 mm) without a change in the LEED pattern. As seen in Figure 4, the width of the diffraction spots at -190°C was not as sharp as other single crystal surfaces, due to apparent roughness of the surface, or small local relaxations. A certain amount of in- and out-of-plane surface roughness is expected due to the difference in atomic composition of the surface which causes small local distortions in the lattice.[14]

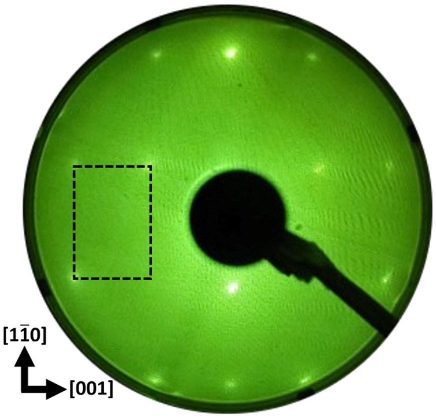

Figure 4: LEED pattern of a clean CoCrFeNi(110) surface at LN_2 temperatures, E_{inc}=221 V. The dashed rectangle represents a multiple of the unit cell.

5. Conclusion

Understanding the adsorption characteristics of multi-component alloys is necessary for exploring their feasibility for catalytic applications. Fundamental studies of structurally symmetric surfaces are necessary as a first step, requiring the synthesis of single-crystal sample surfaces. In this paper, we presented the characterization of a CoCrFeNi sample manufactured via a modified Czochralski technique.

EDS confirmed that this sample maintained the equimolar CoCrFeNi composition intended. The orientation and size of the sample surface was determined by LEED and EBSD measurements to be at least 2 x 3 mm in size and oriented in the (110) direction. This confirms this sample is a good candidate for further chemisorption studies, in particular vibrational measurements such as high-resolution electron energy loss spectroscopy (HREELS).

6. Acknowledgments

This work is supported by the U.S. National Science Foundation under grant number OIA-1946231 and the Louisiana Board of Regents for the Louisiana Materials Design Alliance (LAMDA). The authors wish to thank Brianna C. Simon for acquisition of XRD data, and members of the Shared Instrument Facility at LSU.

7. References

[1] Pantförder, A., et al., Surface segregation and chemisorption of CO and oxygen on Pt25Ni75 (111) studied by XPS and HREELS. Surface science, 1995. **331**: p. 824-830.

[2] Gassmann, P., R. Franchy, and H. Ibach, *Investigations on phase transitions within thin Al2O3 layers on NiAl (001)—HREELS on aluminum oxide films.* Surface science, 1994. **319**(1-2): p. 95-109.

[3] Canning, N. and M. Chesters, *The co-adsorption of H2 and CO on Ni (110).* Surface Science, 1986. **175**(3): p. L811-L816.

[4] Grossmann, A., W. Erley, and H. Ibach, *Entropy-controlled site occupation of CO adsorbed on Ni (100).* Applied Physics A, 1993. **57**: p. 499-505.

[5] Rahman, T.S., et al., *Surface phonons and the c (2× 2) oxygen overlayer on Ni (100): Theory and experiment.* Physical Review B, 1984. **30**(2): p. 589.

[6] Shinn, N.D. and T.E. Madey, *Oxygen chemisorption on Cr (110): I. Dissociative adsorption.* Surface science, 1986. **173**(2-3): p. 379-394.

[7] Schwarz, H., et al., *Fabrication of Single-Crystalline CoCrFeNi Thin Films by DC Magnetron Sputtering: A Route to Surface Studies of High-Entropy Alloys.* Advanced Materials, 2023: p. 2301526.

[8] Cantor, B., et al., *Microstructural development in equiatomic multicomponent alloys.* Materials Science and Engineering: A, 2004. **375**: p. 213-218.

[9] Yeh, J.W., et al., *Nanostructured high-entropy alloys with multiple principal elements: novel alloy design concepts and outcomes.* Advanced engineering materials, 2004. **6**(5): p. 299-303.

[10] Czochralski, J., *Ein neues verfahren zur messung der kristallisationsgeschwindigkeit der metalle.* Zeitschrift für physikalische Chemie, 1918. **92**(1): p. 219-221.

[11] Yang, X. and Y. Zhang, *Prediction of high-entropy stabilized solid-solution in multi-component alloys.* Materials Chemistry and Physics, 2012. **132**(2-3): p. 233-238.

[12] McKay, F., et al., *CoCrFeNi High-Entropy Alloy as an Enhanced Hydrogen Evolution Catalyst in an Acidic Solution.* The Journal of Physical Chemistry C, 2021. **125**(31): p. 17008-17018 DOI: 10.1021/acs.jpcc.1c03646.

[13] McKay, F., et al., *Surface oxidation mechanism of CoCrFeNi high entropy alloy.* Surface Science, 2022: p. 122124.

[14] Tsai, M.-H. and J.-W. Yeh, *High-entropy alloys: a critical review.* Materials Research Letters, 2014. **2**(3): p. 107-123.

The Correlation between Y2O3 Content and Thermal and Mechanical Properties of GRX-810

Yehong Chen[1], Shengmin Guo[1]

Department of Mechanical & Industrial Engineering, [1]Louisiana Stata University

Abstract: NASA recently developed a new oxide-dispersion-strengthened NiCoCr-based alloy, employing a model-driven alloy design methodology and utilizing laser-based additive manufacturing technologies. This innovative alloy, designated GRX-810, was meticulously fabricated using laser powder bed fusion, a sophisticated process that facilitates the homogeneous dispersion of nanoscale Y_2O_3 particles throughout the material's intricate microstructure. Remarkably, rigorous scientific evaluations have revealed that GRX-810 demonstrates a staggering twofold enhancement in tensile strength compared to conventional polycrystalline wrought Ni-based alloys. Inspired by these groundbreaking findings, my current research endeavors are twofold: first, to explore the impact of varying Y_2O_3 content on the thermal properties and mechanical resilience of GRX-810; and second, to delve into the multifaceted effects of the Hot Isostatic Pressing (HIP) process on its thermal and mechanical performance, given its potential to significantly transform the material's characteristics.

Keywords: GRX-810; Thermal conductivity; Additive manufacturing; Thermal diffusivity

1. Introduction

With the development of the material science area, medium-entropy alloys (MEAs) have received more attractions due to their excellent mechanical properties and potential for high performance applications. Among these materials, GRX-810, which is mainly composed of Ni, Co, and Cr is a novel MEA that appears a balance of strength, corrosion resistance, and high temperature resistance. Recent works in material science and engineering have significantly focused on the alloys' capabilities in extreme environments, particularly in high-entropy and medium entropy alloys such as GRX-810. This medium entropy alloys, composed of Ni, Co, and Cr has delivered acceptable results in high temperature applications since the enhanced mechanical properties and oxidation resistance[1-2]. Yttria is well known for its high melting point and exceptional stability, which is the ideal option for strengthening alloys. The incorporation of yttria (Y_2O_3) nanoparticles is the crucial factor in helping improve the performance of GRX-810, which are widely known to refine the microstructures and enhance the extreme temperature stability. The Y_2O_3 nanoparticles acti as pin centers to inhibit the movement of dislocations which is usually the primary reason for material failure under high stress. This dispersion strengthening mechanism significantly extends the serving life and durability of alloys, particularly in the applications that require long term performance in harsh environments. Meanwhile, the integration of Y_2O_3 nanoparticles enhances the alloys' creep resistance, which is the intrinsic property of solid materials deforming permanently under the influence of mechanical stress. This special property is significant crucial to the materials utilized in high temperature environments, where the conventional materials might deform over time. With the improvement of the creep resistance, GRX-810 exhibits the shape and functional stability even with prolonged exposure to high temperatures. The study in this manuscript aims to investigate the correlation between the Y_2O_3 content and the relative thermal conductivities and mechanical properties of GRX-810. With the systematically changing the Y_2O_3 content, this article explores the optimal dispersion levels which can maximize the alloys' behaviors in harsh environments. Since the high potential applications of GRX-810 in aerospace and automotive areas[3], where the materials are normally exposed to severe environments, figuring out the role of Y_2O_3 content can result in the improvement in design the next generation materials. Additionally, this paper will explore the correlation between Hot Isostatic Pressing (HIP) and thermal properties and mechanical properties. HIP is a post-processing technique which applies high temperature and isostatic pressure to heal casting defects and densify materials. The HIP process aims to improve the microstructural homogeneity of alloys, accordingly, to strengthen the mechanical properties. It is crucial to understand how HIP affects the properties of GRX-810 due to the high-demanding superb performance of related applications in adverse environments. The research will also focus on how HIP modifies the thermal properties of GRX-810. Given the alloys' promising prospects, the potential impact on industries that demand reliable performance under harsh working environments is substantial. This research aims to contribute valuable knowledge to the area of advanced materials promoting the development of MEAs designed for severe environments by addressing these two critical directions. The discovery in this article is expected to offer a comprehensive understanding of how adjustments of compositions and advanced manufacturing processes can be utilized to enhance the properties of GRX-810 and set a standard for future research and applications of high performance MEAs.

2. Results

The Yttria contents in GRX-810 samples 1 to 8 provided by NASA are 1wt%, 0.9wt%, 0.7wt%, 0.5wt%, 0.3wt%, 0.45wt%, 0.4wt%, and 0.35wt%, respectively. As shown in Figure 1, the relationship between temperature and the thermal properties such as diffusivities and conductivities demonstrate a consistent increase across the temperature range studied. Notably, the measurements of thermal diffusivity for all samples fall comfortably within the 3% uncertainty provided by the equipment's specifications, suggesting that variations in yttria content do not significantly influence these properties. Since the closed thermal diffusivity values of the samples, the thermal diffusivity value can be curved-fitted to the equation over a temperature range of 25°C to 900°C.

Non-HIP

$$k(T) = -2.69T^3 + 4.0032T^2 + 1.6458T + 2.4111 \tag{1}$$

HIP

$$k(T) = -2.8903T^3 + 4.5553T^2 + 1.1413T + 2.4813 \tag{2}$$

where T is temperature in K/1000.

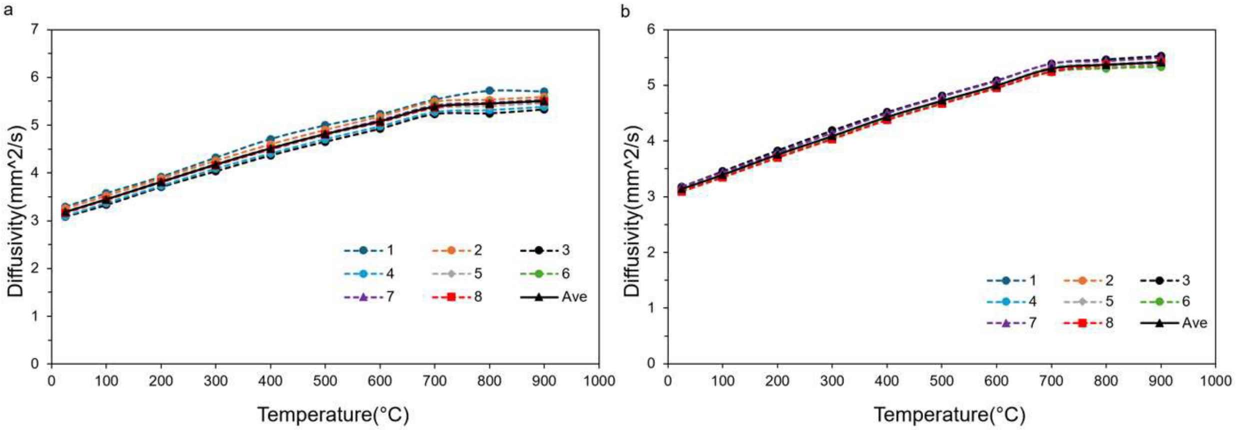

Fig. 1. (a) Thermal diffusivity of non-HIP GRX-810 samples. (b) Thermal diffusivity of HIP GRX-810 samples.

In Figure 2, the data further illustrate that the variance in thermal properties among the samples becomes more pronounced as the temperature escalates. Specifically, at 900°C, non-Hot Isostatic Pressing (non-HIP) sample 8 with the relevantly 0.35wt% yttria contents exhibits the highest recorded thermal conductivity at 30.0 W/(m*K), while sample 3 with the relevantly 0.7wt% yttria contents registers the lowest at 25.9 W/(m*K), marking an approximate increase of 15.8% in thermal conductivity between these two extremes. In comparison, the HIP-processed sample 8 shows a thermal conductivity peak of 31.2 W/(mK), with sample 3 at a minimum of 27.2 W/(m*K), thereby exhibiting a 14.7% increase, which subtly underscores the impact of yttria in marginally reducing the thermal conductivity of the GRX-810 alloys.

When comparing samples subjected to Hot Isostatic Pressing (HIP) with their non-HIP counterparts, a notable difference emerges. Specifically, the thermal conductivity of HIP-treated sample 8 is approximately 4% higher than that of non-HIP sample 8; meanwhile, the thermal conductivity of HIP-treated sample 3 is also 5% higher than non-HIP sample 3. Thus, we can conclude that this process can slightly increase the thermal conductivities of the samples.

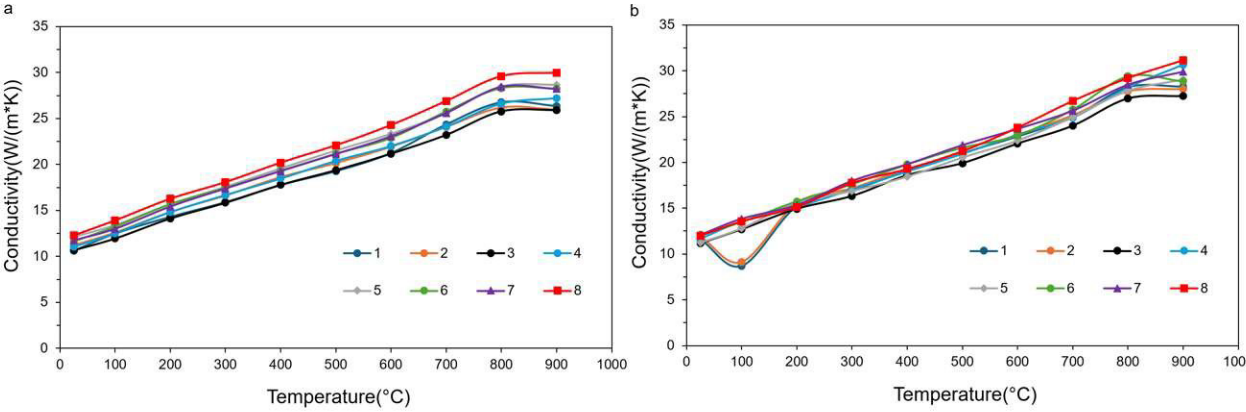

Fig. 2. (a) Thermal conductivity of non-HIP GRX-810. (b) Thermal conductivity of HIP GRX-810.

3. Conclusion

The analysis of GRX-810 alloys demonstrates that yttria content has minimal impact on thermal diffusivities, as all measured values stay within the 3% uncertainty range of the equipment across various samples. However, thermal conductivities show variability with temperature, particularly highlighted by the differences between non-HIP and HIP-treated samples. At 900°C, HIP treatment results in a slight increase in thermal conductivity compared to non-HIP samples, indicating the beneficial effects of the HIP process on the material's thermal properties. These findings suggest that while yttria content does not significantly alter thermal diffusivity, the HIP process can enhance thermal conductivity, offering potential improvements in high-temperature performance of the GRX-810 alloys. This provides a foundational understanding for further material optimization in high-performance applications.

4. Acknowledgments

This work is supported by the U.S. National Science Foundation under grant number OIA-1946231 and the Louisiana Board of Regents for the Louisiana Materials Design Alliance (LAMDA).

5. References

(1) Smith, T. M.; Kantzos, C. A.; Zarkevich, N. A.; Harder, B. J.; Heczko, M.; Gradl, P. R.; Thompson, A. C.; Mills, M. J.; Gabb, T. P.; Lawson, J. W. A 3D printable alloy designed for extreme environments. Nature 2023, 617 (7961), 513-518.
(2) Smith, T.; Kantzos, C.; Gabb, T. NASA High Temperature Alloy Development–GRX-810. In Turbomachinery Technical Conference & Exposition, 2023.
(3) Gradl, P. R.; Smith, T. M.; Tinker, D. C.; Williams, B.; Kantzos, C. Extreme Temperature Additively Manufactured GRX-810 Alloy Development and Hot-fire Testing for Liquid Rocket Engines. In AIAA SCITECH 2024 Forum, 2024; p 0997.

The Effects of Deposition Layer Thickness on the Microstructural Properties of AFSD AA6061 Parts

Hamed Ghadimi, Shengmin Guo

Department of Mechanical & Industrial Engineering, [1]Louisiana Stata University

Abstract: Solid-state additive friction stir deposition (AFSD) is a thermomechanical-based additive manufacturing technique. This study used AFSD to produce aluminum alloy 6061 (AA6061) blocks with varying layer thicknesses (1mm, 2mm, and 3mm). The parts' temperature histories were studied and compared against each other. It showed that the deposition layer thickness influences the temperature histories experienced by the part and acts as a dynamic heat treatment. It also depends on the location of the point being studied in the part, resulting in variations in the microstructure and consequently mechanical properties along the building direction and across the part's width.

Keywords: metal additive manufacturing (AM); additive friction stir deposition (AFSD); AA6061; microstructural properties

1. Introduction

The thermomechanical process of AFSD is an innovative solid-state metal AM technique designed for the efficient production of large-scale pieces under open-air conditions [1]. This process employs a rotating deposition tool to plastically deform feedstock rods, which are subsequently integrated into the deposited layer or a substrate, enabling the gradual deposition of a part, layer by layer. The AFSD procedure starts with the activation of the deposition tool, set into rotation while the feedstock rod is within it. A downward force is exerted by the push rod onto the rotating feedstock rod, generating frictional heat between the rotating rod and the stationary substrate. As the temperature elevates, the feedstock rod undergoes yielding and extrusion, allowing the softened material to flow beneath the rotating deposition tool. As the material continues to flow, the deposition tool follows a predetermined path, forming a new layer in the additive manufacturing process. The gap existing between the tool's lower surface and the previously deposited layer (or the substrate) dictates the deposition's layer thickness. Figure 1 shows the arrangement of the additive friction stir deposition (AFSD) and introduces the different parts.

The deposition tool used for this study is the standard tool provided by the manufacturer. The outside diameter of the deposition tool is 38.1 mm (1.5 in), and it has two pairs of protrusions at the lower face of the tool.

Two pairs of teardrop-shaped protrusions located at the lower surface of the deposition tool help stir the depositing softened material and also generate additional heat due to added friction [2]. Furthermore, protrusions allow for the re-stirring of previously laid materials while depositing a layer while the layer thickness is smaller than the height of the protrusion. For instance, for a layer thickness of 1 mm (0.04 in), the height of the larger protrusion is larger than the sum of two layers' thicknesses, which means that while depositing a new layer, the last two already deposited layers are also re-stirred. It is also feasible to deposit a layer with a thickness that is greater than the height of the larger protrusion. When depositing a part with such a layer thickness, the depositing tool is not stirred into any of the underneath layers.

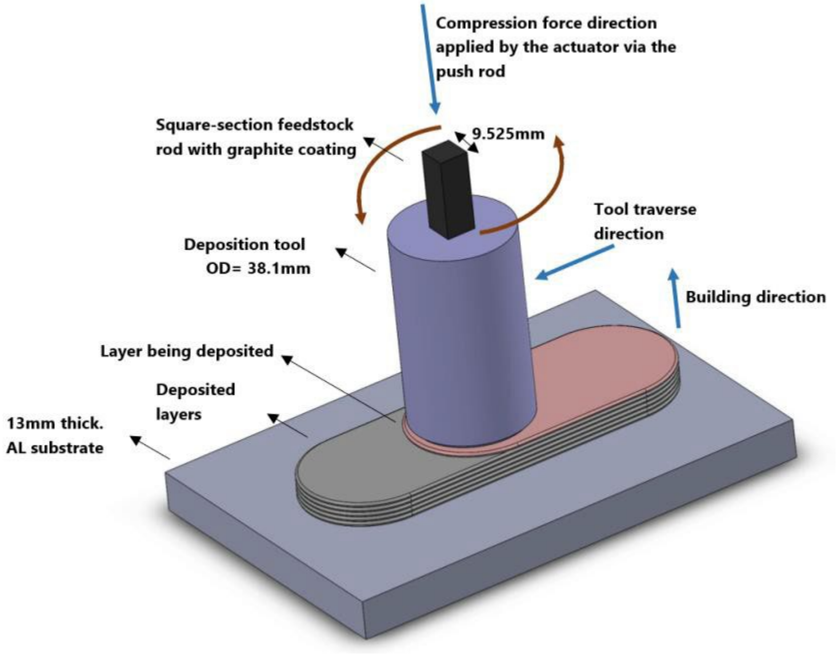

Figure 1. Additive Friction Stir Deposition (AFSD) arrangement

2. Sample Preparation

Three blocks were deposited (with different layer thicknesses) for this study. For the deposition of these blocks, the same deposition parameters of the feedstock material feed rate and the tool's rotation speed were used, while the deposition tool's traverse speed was adjusted for each build with a different layer thickness. The printed blocks were named based on their layer thicknesses: 1mm, 2mm, and 3mm. The deposition parameters for the printed builds are listed in Table 1.

Table 1. Deposition parameters for the samples (1 mm, 2 mm, and 3 mm block).

Part's Name	Deposition Layer Thickness (mm)	Deposition Tool's Rotation Speed (rpm)	Tool's Traverse Speed (mm/min)	Feed Rate (mm/min)
Sample #1 (1 mm block)	1 (0.04 in)	300	279.4 (11.0 in/min)	152.4 (6.0 in/min)
Sample #2 (2 mm block)	2 (0.08 in)	300	127.0 (5.0 in/min)	152.4 (6.0 in/min)
Sample #3 (3 mm block)	3 (0.12 in)	300	96.5 (3.8 in/min)	152.4(6.0 in/min)

3. Results

During the deposition process, the torque exerted on the deposition tool is generated by the spindle motor of the machine. The spindle motor rotates the deposition tool at a predetermined speed as specified in the G-code instructions. In this study, all the deposited materials were processed using a deposition tool with a rotational speed of 300 revolutions per minute (rpm). The average torque values were computed for each layer during the deposition of every block. Figure 2 presents the calculated average torque values for each layer during the deposition of the 1mm, 2mm, and 3mm blocks.

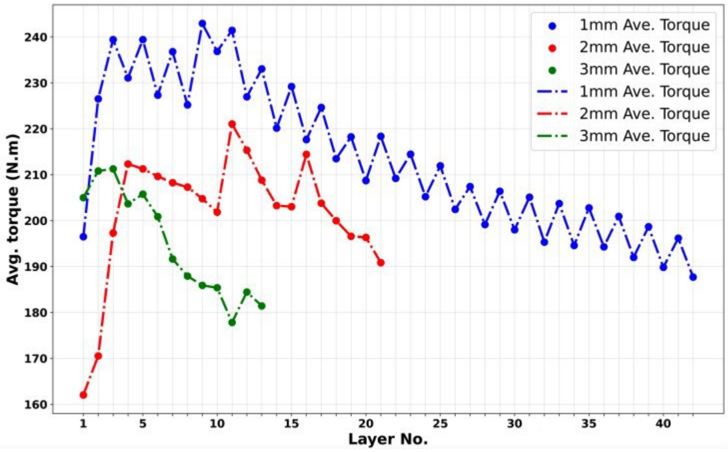

Figure 2. Average torque values applied on the deposition tool during deposition of each layer AFSD blocks.

A thermocouple was positioned on the substrate during the deposition process of the blocks to monitor the temperature at a fixed location. The recorded data provided information on the temperature profile at that specific point. The average substrate temperature values were computed for each layer during the deposition of every block. Figure 3 presents the calculated values for each layer during the deposition of the 1mm, 2mm, and 3mm blocks.

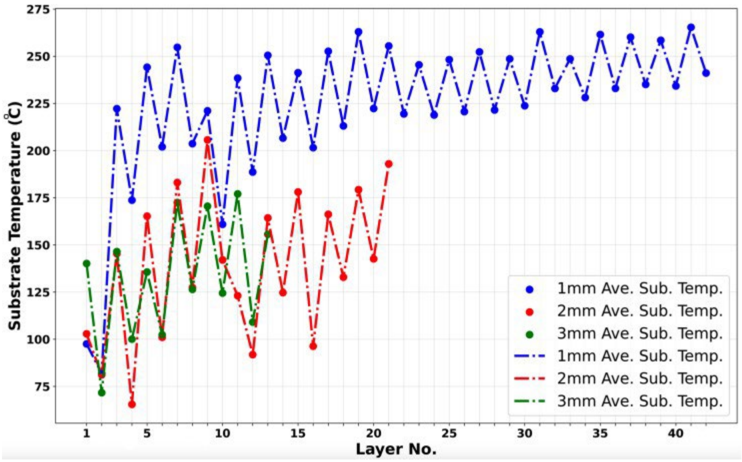

Figure 3. Average substrate temperature values during deposition of each layer for AFSD blocks.

4. Discussion

The height of the larger protrusions is larger than 2mm. In the case of thinner layers (<2mm), the protrusions on the deposition tool make deeper engagements with the previously deposited material or the substrate as the tool traverses. Due to the lower temperature of the previously deposited part or substrate in comparison to the material being deposited, an increase in the torque applied on the deposition tool occurs, resulting in more heat generation. Specifically, for the 1mm block, the larger protrusions penetrate more than 1mm into the deposited layer or substrate, whereas in the case of the 3mm block, the protrusions do not make any contact with the previously deposited layer or substrate. AA6061 is a precipitate-hardened alloy [3]. AFSD components undergo a dynamic heat treatment process throughout their manufacturing process, which significantly influences the size and distribution of precipitates, thereby impacting the microstructural and mechanical properties of the resulting part. This phenomenon is affected by the temperature history experienced by the part during the deposition. Notably, the different deposition layer thicknesses of 1mm, 2mm, and 3mm impart distinct thermal histories to the blocks during the deposition procedure, resulting in different mechanical properties of samples taken from different blocks. Additionally, different regions of a specific part experience varying temperature histories depending on their positioning within the part along the building direction.

5. Conclusion

This study used AFSD to produce AA6061 blocks with varying layer thicknesses (1mm, 2mm, and 3mm). The parts' temperature histories were studied and compared against each other. It showed that the deposition layer thickness influences the temperature histories experienced by the part and acts as a dynamic heat treatment. It also depends on the location of the point being studied in the part, resulting in variations in the microstructure and consequently mechanical properties along the building direction and across the part's width.

5. Acknowledgments

This work is supported by the U.S. National Science Foundation under grant number OIA-1946231 and the Louisiana Board of Regents for the Louisiana Materials Design Alliance (LAMDA).

6. References

[1] Gumaste, A.; Dhal, A.; Agrawal, P.; Haridas, R.S.; Vasudevan, V.K.; Weiss, D.; Mishra, R.S. A Novel Approach for Enhanced Mechanical Properties in Solid-State Additive Manufacturing by Additive Friction Stir Deposition Using Thermally Stable Al-Ce-Mg Alloy. JOM 2023, 75, 4185–4198.

[2] Garcia, D.; Hartley, W.D.; Rauch, H.A.; Griffiths, R.J.; Wang, R.; Kong, Z.J.; Zhu, Y.; Yu, H.Z. In Situ Investigation into Temperature Evolution and Heat Generation during Additive Friction Stir Deposition: A Comparative Study of Cu and Al-Mg-Si. Addit. Manuf. 2020, 34, 101386.

[3] Feng, A.H.; Chen, D.L.; Ma, Z.Y. Microstructure and Low-Cycle Fatigue of a Friction-Stir-Welded 6061 Aluminum Alloy. Metall. Mater. Trans. A 2010, 41, 2626–2641.

Understanding the Composition Distribution and Hardness of AL6061/AL7075 Dissimilar Joints Produced Via AFS-D

Kekeli Doe Agbewornu, Antonio Wells, Patrick Mensah, Congyuan Zeng

Mechanical Engineering, Southern University And A&M College

Abstract: In this study, the composition distribution and hardness of joints fabricated by Additive Friction Stir Deposition (AFS-D) of Al6061/Al7075 and Al7075/Al6061 were investigated. Results showed strong metallurgical bonds with effective intermixing of Zn, Mg, Cu, Cr, and Fe across the interface, as confirmed by EDS mapping. Vickers hardness testing showed varied hardness profiles across the joints, indicating diffusion and mixing effects of alloying elements. This proves the effectiveness of the AFSD process in creating durable dissimilar Aluminum alloy joints with its possible optimization to reduce porosity and increase the quality of the produced joints.

Keywords: Additive Friction Stir Deposition; Composition Distribution; Hardness; Al6061/Al7075 alloys

1. Introduction

Dissimilar metal joining, especially aluminum alloys, has been of interest over the past decades as its application is critical to high-performance industries such as aerospace, automotive, and marine technologies Mehta, K. P. (2019). Among the various joining techniques, additive friction stir deposition (AFSD) has proven to be the most promising solid-state manufacturing process for creating durable and reliable dissimilar joints with minimum complications due to porosity and cracking, as usually produced by fusion-based joining technologies (Mishra & Ma, 2005). Aluminum alloys, specifically Al6061 and Al7075 alloys have a wide range of applications due to their excellent mechanical properties, including a high strength-to-weight ratio and very good corrosion resistance. The intrinsic challenges in joining these two dissimilar alloys have been related to their differences in terms of chemical composition, microstructure, and thermal properties (Hussein & Medraj, 2014). The understanding of the distribution of composition and hardness in joints formed through AFSD is very critical to the improvement of the reliability and performance of such dissimilar joints (Zhang & Zhang, 2014).

The AFSD process, a variant of friction stir welding (FSW), utilizes a non-consumable tool to combine dissimilar materials through frictional heat and plastic deformation that form a solid-state bond. The technique has considerable advantages over other fusion-based methods, with lesser residual stresses and minimum distortion (Mishra & Ma, 2005). Studies conducted previously showed that the AFSD process had demonstrated effectiveness in joining different aluminum alloys, and it had the potential to produce high-quality dissimilar joints. (Scialpi et al., 2007).

Despite such efforts, the microstructural evolution and mechanical properties of AFSD joints, particularly in dissimilar aluminum alloys, remain active areas of research. The interaction of as many alloying elements as possible with each other and the formation of different intermetallic compounds affect the distribution of these phases in the joint interface. This interaction is very important to the general performance of the joint (Yazdipour et al., 2009). As such, comprehensive research in the composition distribution and hardness of AFSD joints will be necessary for process optimization and assurance of mechanical integrity for dissimilar aluminum alloy joints (Chen & Nakata, 2009).

This study aims to investigate the hardness and composition distribution of dissimilar aluminum alloy joints produced by AFSD. This study aims to explain the process-structure-property relationships governing the mechanical integrity and durability of the dissimilar Aluminum alloy joints. It also includes optimization of the AFSD processing parameters, coupled with post-treatment in the form of heat treatment so that the evolution of a microstructure during the joining process of Al6061/Al7075 and its consequences on mechanical properties can be understood comprehensively. The focus of this research is; to analyze the composition distribution across the dissimilar joint interface, and to evaluate the hardness variation within the joint region.

Understanding the composition distribution is very important because it directly impacts the mechanical properties of the joint. Whereas Al6061 and Al7075 have some differences in alloying elements, the dissimilarities could probably result in the formation of brittle intermetallic compounds at the joint interface, greatly reducing the strength and ductility of the joint (Chen & Nakata, 2009). Hence, the study of this distribution in composition will allow gaining an insight into the process parameters of the optimum conditions to reduce the likelihood of undesirable phases being formed (Hussein & Medraj, 2014).

Evaluating the hardness variation within the joint region is equally important. Hardness measurements can provide a quick and reliable assessment of the mechanical properties of a joint. The variations in hardness can be related to changes in the microstructure (grain size and phase composition) relevant to explaining the overall performance of the joints (Scialpi et al., 2007). Hardness measurements can, therefore, be correlated with microstructural features seen in microscopy to provide insight into the various determinants of the mechanical properties of AFSD joints (Yazdipour et al., 2009).

Correlating the findings with the AFSD process parameters and post-treatment conditions will help in identifying optimal conditions for producing high-quality dissimilar aluminum alloy joints. The process parameters of tool rotation speed, traverse speed, and axial force drastically affect the heat input and material flow during AFSD, which affects the microstructural evolution and mechanical properties of the joint. Especially in the post-treatments, including heat treatments, the microstructure can still be modified to reach an enhanced mechanical property of the joint (Zhang & Zhang, 2014).

This study emphasizes bridging this research gap and understanding the distribution of hardness and elemental composition across dissimilar aluminum alloy joints obtained by AFSD. It also seeks to explain process-structure-property relationships to find out the optimum conditions for the AFSD process capable of producing joints with better mechanical integrity and durability thereby enhancing their applications in many high-performance industries.

2. Experiments & Methods

To investigate the interlayer bonding between Al6061 and Al7075 alloys, dissimilar metal joints were fabricated using an additive friction stir deposition process. In this process, a layer of Al6061 alloy was deposited on an Al7075 alloy substrate and vice versa. The deposition parameters remained the same for both configurations to maintain consistency and comparability. The rotational speed of the tool was set to 150 RPM, the tool traversing speed to 152.4 mm/min, and the feedstock feed rate to 139.7 mm/min. The deposition process was successfully done, where the Al6061 alloy bonded well to the Al7075 substrate and the Al7075 alloy bonded well to the Al6061 substrate. A smoother deposition surface of Al6061 compared to that of Al7075 indicated that the Al6061 alloy had better weldability. To gain a deeper understanding of the interfacial bonding between the two alloys, the deposited parts were sectioned, ground, and polished. This was done in preparation for any further microstructural analysis. Images of cross-sections were obtained to ascertain bonding quality and identify probable defects along the interface. The cross-sectional examination was conducted via a Scanning Electron Microscope. These techniques gave clear images of the interfacial regions, which allowed for a proper assessment of the characteristic microstructural features that were present in these regions. For the as-fabricated parts of the Al6061 and Al7075 alloys, it had been proved that the AFSD process parameters used were adequate to obtain strong metallurgical bonds. To assess the mechanical properties of the dissimilar joints, microhardness testing was conducted across the bonded interfaces. The Vickers hardness test was employed, with indentations at regular intervals from one side of Al6061 to the other side of the Al7075 joint. In doing this, it gave a hardness profile across the joint, which is very significant for understanding the mechanical integrity and weld performance under various load conditions during practical applications. The results obtained from microstructural analysis and hardness testing proved the successful bonding of Al6061 and Al7075 alloys. As observed, microstructural images indicated smoother surface finishes for the deposition of Al6061, which agreed with the initial observation. A hardness profile showed a gradient across the interface, reflecting the varying properties of both alloys and the effectiveness of the AFSD process in its joining technique without the introduction of massive defects.

3. Results And Discussion

3.1 Composition Distribution

The composition distribution obtained from the Energy Dispersive Spectroscopy (EDS) for Al6061/Al7075 and Al7075/Al6061 are shown in Figure 1. Based on the measurements, important elements like Al, Mg, Zn, Cu, Cr, and Fe were observed as the alloying elements across the joint interface due to intermixing and diffusion of elements during the AFSD process. The mapping across the Al6061/Al7075 joint indicates that Aluminum (Al), is uniformly distributed, indicating good metallurgical bonding and intermixing between the alloys. Magnesium (Mg), is more concentrated on the Al6061 side and indicates limited diffusion into the Al7075 alloy. On the other hand, Zinc (Zn), indicates very clear separation, with high concentration on the Al7075 side, due to higher Zn content. Cu and Cr are relatively diffuse, indicating some form of interdiffusion across the interface. Fe and Mn showed fairly homogeneous dispersion, again attesting to good mixing during the AFSD process.

The elemental distribution maps of the Al7075/Al6061 joint have also exhibited the same trend that Aluminum is distributed uniformly on the Al6061 side, signifying proper bonding between the alloys. Magnesium represents a more homogeneous distribution than the Al6061/Al7075 joint and diffuses rather well into the Al6061 alloy from the Al7075 side. Zinc remains more enriched in the Al7075 and shows only a very low diffusion into the Al6061 alloy. Copper, Titanium, and chromium show good distribution across the interface, and marks of interdiffusion. Iron and Manganese are very uniform, just like the Al6061/Al7075 joint.

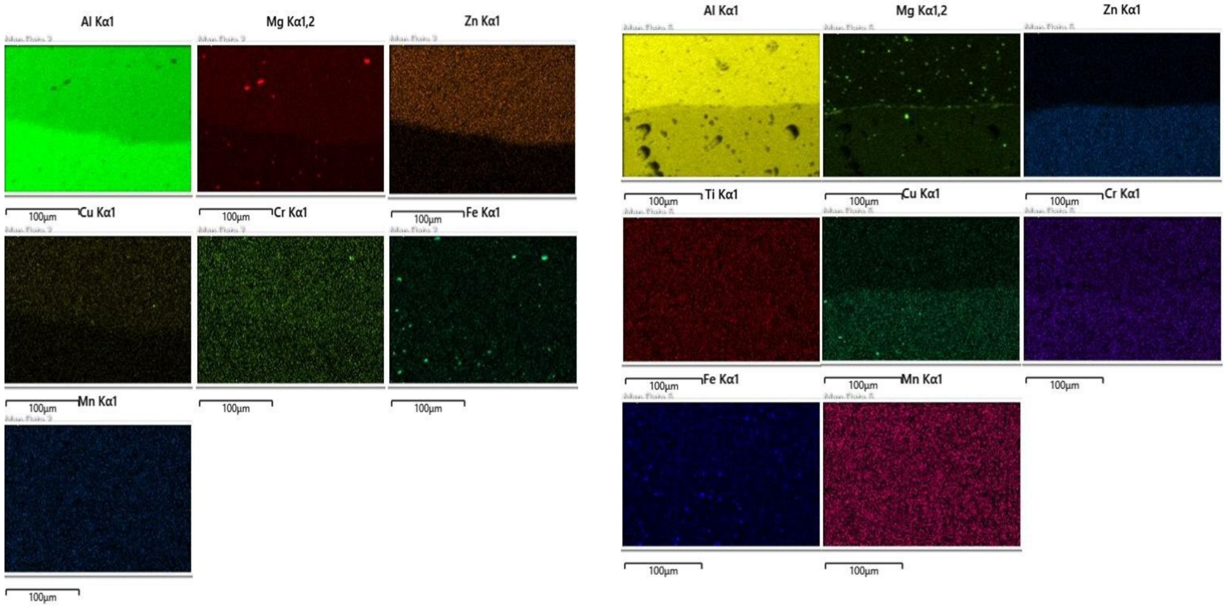

Figure 1. Left: EDS Mapping images for Al6061 deposition on Al7075. Right: EDS Mapping images for Al7075 deposition on Al6061.

3.1 Vickers Hardness

The Vickers hardness images shown in Figure 2 provide insights into how hardness has been distributed through different regions of the Al6061/Al7075 and Al7075/Al6061 joints produced using the AFSD process. In the case of the Al6061/Al7075 joint, the deposition region of Al6061 is approximately 35 HV0.1, very close to the properties known for this kind of alloy. The interface region shows an increased hardness of about 45 HV0.1, which is indicative of some intermixing/diffusion of the alloying elements Zn, Cu, Cr, and Fe, as also supported by the EDS mapping. The Al7075 base region displays a hardness of around 70 HV0.1, which is characteristic of Al7075 because of its increased content of alloying elements, particularly Zn. In contrast, for the Al7075/Al6061 joint, the base Al7075 has the highest hardness of about 70 HV0.1, whereas the interface region is slightly lower in its hardness of approximately 45 HV0.1, reflecting the diffusion and intermixing at the interface, which is also supported by the EDS mapping. The Al6061 deposition region exhibited a much lower value of hardness of about 35 HV0.1. The general trends of the hardness measurement correlating with elemental distribution, as observed in the EDS maps, support effective intermixing and diffusion in the AFSD process. The pores that are visible in the EDS images may act as stress concentrators and can have some effect on the hardness measurements, but general trends are consistent with the material properties expected for the process. These findings demonstrate the AFSD process's effectiveness in making strong joints with good bonding and elemental intermixing, while also pointing out where potential optimization within the process may lead to a reduction in porosity and hence an overall improvement in the quality of joints.

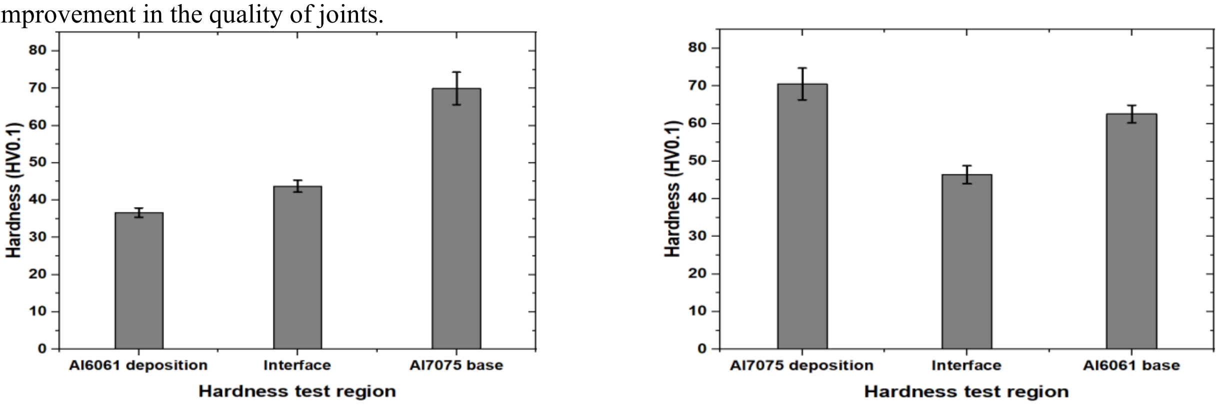

Figure 2. Left: Hardness test results for Al6061 deposition on Al7075. Right: Hardness test results for Al7075 deposition on Al6061.

4. Conclusion

In this study, the composition distribution and hardness of Al6061/Al7075 and Al7075/Al6061 joints produced by Additive Friction Stir Deposition (AFS-D) were evaluated, and the following conclusions were reached:

1. The Additive Friction Stir Deposition (AFSD) method fabricated strong metallurgical bonds between Al6061 and Al7075 alloys, proving its effectiveness in joining dissimilar aluminum alloys.
2. Energy dispersive spectroscopy mapping also showed that the interfaces of both the Al6061/Al7075 and the Al7075/Al6061 joints effectively mixed elements. Key alloying elements like Zn, Mg, Cu, Cr, and Fe were distributed across the joint interfaces.
3. The Vickers hardness testing showed various hardness profiles across the joints. These variations in the hardness at different regions of the joints confirmed the diffusion and mixing of the alloying elements, which was further verified by the EDS mapping.

.

5. Acknowledgments

This work is supported by the U.S. National Science Foundation under grant number OIA-1946231 and the Louisiana Board of Regents for the Louisiana Materials Design Alliance (LAMDA).

6. References

Mehta, K. P. (2019). A review on friction-based joining of dissimilar aluminum-steel joints. Journal of Materials Research, 34, 78-96. https://doi.org/10.1557/jmr.2018.332

Chen, Y. C., & Nakata, K. (2009). Microstructural characterization and mechanical properties in friction stir welding of aluminum and titanium dissimilar alloys. Materials & Design, 30(9), 469-474.

Hussein, M., & Medraj, M. (2014). Review of aluminum-to-steel welding technologies. In The Minerals, Metals & Materials Society 2014 Annual Meeting & Exhibition, 177-187.

Mishra, R. S., & Ma, Z. Y. (2005). Friction Stir Welding and processing. Materials Science and Engineering: R: Reports, 50(1-2), 1-78.

Scialpi, A., De Filippis, L. A. C., & Cavaliere, P. (2007). Influence of shoulder geometry on microstructure and mechanical properties of friction stir welded 6082 aluminium alloy. Materials & Design, 28(4), 1124-1129.

Suhuddin, U. F. H., Mironov, S., Sato, Y. S., & Kokawa, H. (2009). Grain structure evolution during friction stir welding of Al–Mg alloy. Materials Science and Engineering: A, 501(1-2), 140-145.

Yazdipour, A., Heidarzadeh, A., & Simchi, A. (2009). Process-structure-properties in dissimilar friction stir welding of Al alloys: Role of tool geometry and rotational speed. Materials & Design, 30(5), 1211-1221.

Zhang, Z., & Zhang, H. (2014). Microstructural evolution and mechanical properties of friction stir welded dissimilar Al alloys. Journal of Materials Processing Technology, 214(8), 1523-152